Design, Modeling, Optimization and Control of Compliant Mechanisms

Ke Wu

CENTRALE LILLE

THESE

Présentée en vue
d'obtenir le grade de

DOCTEUR

En

Spécialité : Automatique, Génie Informatique,

Traitement du Signal et des Images

Par

Ke Wu

DOCTORAT DELIVRE PAR CENTRALE LILLE

Titre de la thèse :

Conception, Modélisation, Optimisation et Commande de Mécanisme Flexible

Design, Modeling, Optimization and Control of Compliant Mechanisms

Soutenue le 31, Mars 2023 devant le jury d'examen :

Président	Frederic Boyer	Professeur, IMT-Atlantique
Rapporteur	Jiansheng Dai	Professeur, King's College London, UK
Rapporteur	Guillaume Laurent	Maître de Conférences, HDR, ENSMM
Examinateur	Li Zhang	Professeur, Chinese University of Hong Kong
Examinateur	Florence Bertails-Descoubes	Directrice de Recherche, INRIA Grenoble
Directeur de thèse	Gang Zheng	Chargé de Recherche INRIA, HDR, INRIA Lille

Thèse préparée dans le Centre de Recherche en Informatique, Signal et Automatique de Lille,
CRIStAL, CNRS UMR 9189

Ecole Doctorale MADIS-631

Membre du Groupe des Écoles Centrale
Centrale Lille
Cité Scientifique – CS20048 – 59651 Villeneuve d'Ascq Cedex – France
Tél. + 33 (0)3 20 33 53 53 – http://centralelille.fr

Abstract

Doctor of Philosophy

Design, Modeling, Optimization and Control of Compliant Mechanisms

by Ke WU

Compliant mechanisms (CMs), as a novel type of mechanical systems, utilize the elastic deformation of the built-in elementary flexible members to transfer motion, force and energy. Due to their inherent advantages, CMs have been widely used in various mechanical applications. However, in the current literature, researchers still suffer from the lack of efficient tools and a comprehensive analysis framework for designing CMs. To more systematically and efficiently analyze CMs for application-oriented purposes, this thesis aims to propose a comprehensive methodology of designing, modeling, optimizing and controlling CMs. Detailed derivations have been presented on the aforementioned perspectives, followed by both numerical and experimental validation.

Acknowledgements

First of all, I would like to thank my supervisor, Gang Zheng for providing me with the opportunity to work on such an interesting topic during my PhD studies, and also for his patient guidance, professional help, and unreservedly sharing his experience with me. I wouldn't expect a better superior like him at the the first stage of my academic career.

Secondly, I would like also to thank my teammates, Shijie Li, Amehri Walid, Stefan Escaida Navarro, Félix Vanneste, Lingxiao XUN, Yiru Guo, Damien Marchal, and so on for their support and help in both my research and life during my PhD studies.

Thirdly, I would like to thank Christian Duriez, Alexandre Kruszewski, Yinoussa Adagolodjo and Quentin Peyron who effectively manage the team and provide a decent research environment for all team members.

Finally, I would like to thank Region, I-site and ANR for their financial support during my PhD studies.

Contents

List of Figures

List of Tables

List of Abbreviations

ADM	**A**dmoian **D**ecomposition **M**ethod
BVP(s)	**B**oundary **V**alue **P**roblem(s)
BCM	**B**eam **C**onstraint **M**odel
BBCM	**B**ody-frame **B**eam **C**onstraint **M**odel
B.C.	**B**oundary **C**ondition(s)
CM(s)	**C**ompliant **M**echanism(s)
COR	(Reduced-mode) **CO**ssrat **R**od model
COR-GM	**CO**ssrat **R**od-**G**alerkin **M**ethod
COR-WRM	**CO**ssrat **R**od-**W**eighted **R**esidual **M**ethod
CE	**C**omputational **E**xpense
CFM(s)	**C**onstant **F**orce **M**echanism(s)
CTM(s)	**C**onstant **T**orque **M**echanism(s)
CC	**C**onstant **C**urvature
CMG	**G**lobally-implemented **C**ollocation **M**ethod
CML	**L**ocally-implemented **C**ollocation **M**ethod
CBCM	**C**hained **B**eam **C**onstraint **M**odel
CTBCM	**C**hained **T**imoshenko **B**eam **C**onstraint **M**odel
CPPM(s)	**C**ompliant **P**lanar **P**arallelogram **M**echanism(s)
D-H	**D**enavit-**H**artenberg
DOF(s)	**D**egree **O**f **F**reedom(s)
DOC(s)	**D**egree **O**f **C**onstraint(s)
D.E.	**D**iffential **E**quation
ER	**ER**ror
FEM	**F**inite **E**lement **M**ethod
FDM	**F**inite **D**ifference **M**ethod
GM	**G**alerkin **M**ethod
ICB(s)	**I**nitially **C**urved **B**eam(s)
IVP(s)	**I**nitial **V**alue **P**roblem(s)
LSM	**L**east **S**quare **M**ethod
LM	**L**agrange **M**ultiplier
MOM	**M**ethod **o**f **M**oment
MEM(s)	**M**icro**E**lectro**M**echanical **S**ystem(s)
NEB	Geometrically **N**onlinear **E**uler Bernoulli **B**eam theory
NEB-WRM	Geometrically **N**onlinear **E**uler Bernoulli **B**eam theory-**W**eighted **R**esidual **M**ethod

ODE(s)	**O**rdinary **D**ifferential **E**quation(s)
PA	**P**adé **A**pproximant
PRBMs	**P**seudo **R**igid **B**ody **M**odel(s)
PCC	**P**iecewise **C**onstant **C**urvature
RRM	**R**ayleigh **R**itz **M**ethod
SD-FEM	**S**oli**D**-mechanics-based **F**inite **E**lement **M**ethod
SH	**SH**ooting method
SUM	**SU**bdomain **M**ethod
TBCM	**T**imoshenko **B**eam **C**onstraint **M**odel
TSM	**T**aylor **S**eries **M**ethod
WRM(s)	**W**eighted **R**esidual **M**ethod(s)

List of Symbols

$\mathcal{A}$	Adomian polynomial	N/A
A	Area of cross sections	m^2
A_b, B_b, C_b, D_b	Model matrices of BCM	1
A_t, B_t, C_t, D_t	Model matrices of TBCM	1
c	Polynomial coefficients	1
d	Diameter of round-cross-section beam	m
$\mathbf{d_1}, \mathbf{d_2}, \mathbf{d_3}$	Orthogonal unit vectors at each cross section in the body frame	1
E	Young's modulus	Pa
E_p	The stored elastic energy in deflected beams	J
$\hat{E}_p$	Nondimensionalized E_p	1
F_x	The horizontal part of F_o or the beam-end X-axis beam end point load	N
F_y	The vertical part of F_o or the beam-end Y-axis beam end point load	N
F_z	The beam-end Z-axis beam end point load	N
F_o	Beam-end point load	N
F_1, F_2, F_3, F_4	Cable force inputs of the continuum manipulator	N
$\mathbf{f}$	Global distributed force exerted on the rod	N
f_x	Nondimensionalized F_x	1
f_y	Nondimensionalized F_y	1
G	Shear modulus	Pa
h	Depth of the rectangular-cross-section beam	m
Δh	Fixed sampling step of the defined space in Euler' method and Runge-Kutta method	1
I	Second moment inertia of the cross-section area	m^4
I_2, I_3	Second moment inertia of the cross-section area along $\mathbf{d_2}$ and $\mathbf{d_3}$	m^4
i, j, k	Order numbers	1
J_z	Polar moment of inertia at torsional cross section's center of the rod	m^4
K	Stiffness of each revolute joint in chained-PRBM	N m
K^n	Linear stiffness matrix	N
K^m	Angular stiffness matrix	Nm^2
k_t	Timoshenko shear coefficient	1
L	Beam length	m
l	Length of each rigid or flexible beam element in chained-PRBM or chained BBCM	m
$\mathbf{l}$	Global distributed moment exerted on the rod	Nm
Δl	Cable displacement inputs of the continuum manipulator	m

M	The exerted moment along the beam	N m
M^*	Distribute moment along the beam	N m
M_o	Beam-end moment	N m
M_x	Beam-end moment around X axis	N m
M_y	Beam-end moment around Y axis	N m
M_z	Beam-end moment around Z axis	N m
m	Local internal moment along the rod	Nm
m_o	Nondimensionalized M_o	1
$\mathbf{m}$	Global internal moment along the rod	Nm
n	Local internal force along the rod	N
$\mathbf{n}$	Global internal force along the rod	N
P_e	Position of the end effector of the continuum manipulator	m, 1
q_x	X-axis distributed load along the beam	N/m
q_y	Y-axis distributed load along the beam	N/m
q_n	Distributed pressure along the beam	N/m
$\mathcal{R}$	Residual function in weighted residual methods	N/A
$\mathbf{R}$	Rotation matrix	1
$\mathbf{R}_o$	Rotation matrix of the undeformed configuration	1
R	Initial radius of curvature	m
$\mathbf{r}$	Global position vector	m
$\mathbf{r}_o$	Global position vector of the undeformed configuration	m
r	Nondimensionalized R	1
r_a	The radius coordinate in polar coordinate system	m
s	The independent variable along the beam axis	m
$\hat{s}$	Nondimensionalized s	1
$\mathbf{u}$	Global angular strain vector	1/m
$\mathbf{u}_o$	Global angular strain vector of the undeformed configuration	1/m
u	Local angular strain vector	1/m
u_o	Local angular strain vector of the undeformed configuration	1/m
V	Shear force along the beam cross sections	N
$\mathbf{v}$	Global linear strain vector	1
$\mathbf{v}_o$	Global linear strain vector of the undeformed configuration	1
v	Local linear strain vector	1
v_o	Local linear strain vector of the undeformed configuration	1
w	Width of the rectangular-cross-section beam	m
$\mathcal{W}$	Weight function in weighted residual methods	N/A
x	Global X-axis coordinate	m
$\hat{x}$	Nondimensionalized x	1
$\underline{x}$	Lower bound of x	N/A
$\bar{x}$	Upper bound of x	N/A
y	Global Y-axis coordinate	m
$\hat{y}$	Nondimensionalized y	1

Γ	The analytical formulation of BBCM	rad
$\hat{\Gamma}$	The nondimensionalized analytical formulation of BBCM	rad
ν	Poisson's ratio	1
θ	The independent variable (global rotation angle) along the beam axis	rad
θ_o	Global initial rotation angle along the beam axis	rad
ϑ	Numerical approximation to θ	rad
ϑ_o	Numerical approximation to θ_o	rad
$\hat{\theta}$	Nondimensionalized θ	1
ϕ	The angular coordinate in polar coordinate system or in spherical coordinate system	rad
$\underline{\phi}$	Lower bound of ϕ	rad
$\overline{\phi}$	Upper bound of ϕ	rad
ζ	The angular coordinate in spherical coordinate system	rad
κ	Curvature of the beam	1/m
κ_o	Initial curvature of the beam	1/m
$\hat{\kappa}_o$	Nondimensionalized κ_o	1
ε	An infinitesimal	1
ϵ_a	The axial strain of a slender beam	1
ϵ_s	The shear strain of a slender beam	1
$\hat{\epsilon}_a$	Nondimensionalized ϵ_a	1
$\hat{\epsilon}_s$	Nondimensionalized ϵ_s	1

Chapter 1

Introduction

1.1 Motivations

Compliant mechanisms (CMs), as a novel type of mechanical systems, utilize the elastic deformation of the built-in elementary flexible members to transfer motion, force and energy (Howell, 2013a)(Howell, 2013b). This novel and powerful concept has provided many desired properties for CM-based mechanical systems: compliance due to the flexibility of the used elastic material (Howell, 2013a); monolithic design that results in increased motion precision with no concerns about errors from assembly (Farhadi Machekposhti, Tolou, and Herder, 2015), simplified manufacturing process (Howell, 2013a)(Farhadi Machekposhti, Tolou, and Herder, 2015)(Lobontiu, 2020), reduced weight (Howell, 2013a)(Lobontiu, 2020), cost reduction (Howell, 2013a)(Farhadi Machekposhti, Tolou, and Herder, 2015)(Lobontiu, 2020) and less maintenance (Howell, 2013a)(Lobontiu, 2020). These mentioned desired characteristics have made CMs a gradually mature component in many mechanical applications, such as compliant kinematic joints (Farhadi Machekposhti, Tolou, and Herder, 2015; Dong et al., 2014; Tanık et al., 2015), high-accuracy positioning motion stages (Awtar, 2003; Fan, Liu, and Fan, 2018; Wu and Hao, 2020), bi/tri-stable mechanisms (Qiu, Lang, and Slocum, 2004; Pham and Wang, 2011) and other more complex applications that integrate the former three (Trease and Kota, 2009; Song et al., 2010; Qi et al., 2015). However, the challenges of the research area lie in the following parts: the lack of commonly adopting existing and classic beam and rod theories for modeling large deflection of slender structures under different loading conditions (Ling et al., 2020), the lack of using existing reliable numerical methods to implement the aforementioned constitutive theories (Ling et al., 2020) and depending on empirical methods to design CMs rather than following the efficient modern methodology of optimization (Rao, 2019) to design CMs (Howell, 2013a) (which often suffers from the trial-and-error process (Howell and Midha, 1994)(Albanesi, Fachinotti, and Pucheta, 2010)). In this field, researchers are still suffering from using high-dimensional and time-consuming models or methods to solve large deflections of slender structures, such as finite element method (FEM) (Rao, 2017) and chained algorithms (Howell, 2013a). Besides, most of them only consider beam-end loading without touching more complex loading conditions, such as gravity and pressure (Ling et al., 2020).

Therefore, in this chapter, the state-of-the-art literature is first reviewed regarding the existing applications of CMs in academia and industry. Then, we have also reviewed the current constitutive models and theories, such as solid mechanics and rod (beam) theories used for modeling CMs and the commonly-used methods of implementing the adopted theories are presented along with their advantages and limitations. In the end, we summarize the corresponding contributions to handle these limitations and present the outline of the thesis followed by the list of published papers.

1.2 State of the art

1.2.1 Compliant mechanisms

Compliant mechanisms (CMs) have been serving as a promising alternative for the current mechanical applications due to their inherent advantages (Howell, 2013a). Conventional rigid-body mechanisms utilize the cooperation of kinematic pairs and rigid links to provide the transfer of motion, force and energy. CMs, as a unique concept of mechanical systems, can realize the same function merely through the deformation of the built-in elementary flexible and compliant members (Howell, 2013a). This powerful concept has presented many desired characteristics over rigid ones: compliance due to the flexibility of the used elastic material (Howell, 2013a); monolithic design that results in increased motion precision with no concerns about errors from assembly (Farhadi Machekposhti, Tolou,

and Herder, 2015), simplified manufacturing process (Howell, 2013a)(Farhadi Machekposhti, Tolou, and Herder, 2015)(Lobontiu, 2020), reduced weight (Howell, 2013a)(Lobontiu, 2020), cost reduction (Howell, 2013a)(Farhadi Machekposhti, Tolou, and Herder, 2015)(Lobontiu, 2020) and less maintenance (Howell, 2013a)(Lobontiu, 2020). As mentioned above, the major difference between conventional rigid mechanisms and CMs lies in the kinematic joints where the compliant joints as demonstrated in Fig. 1.1 essentially lead to the unique nature of CMs.

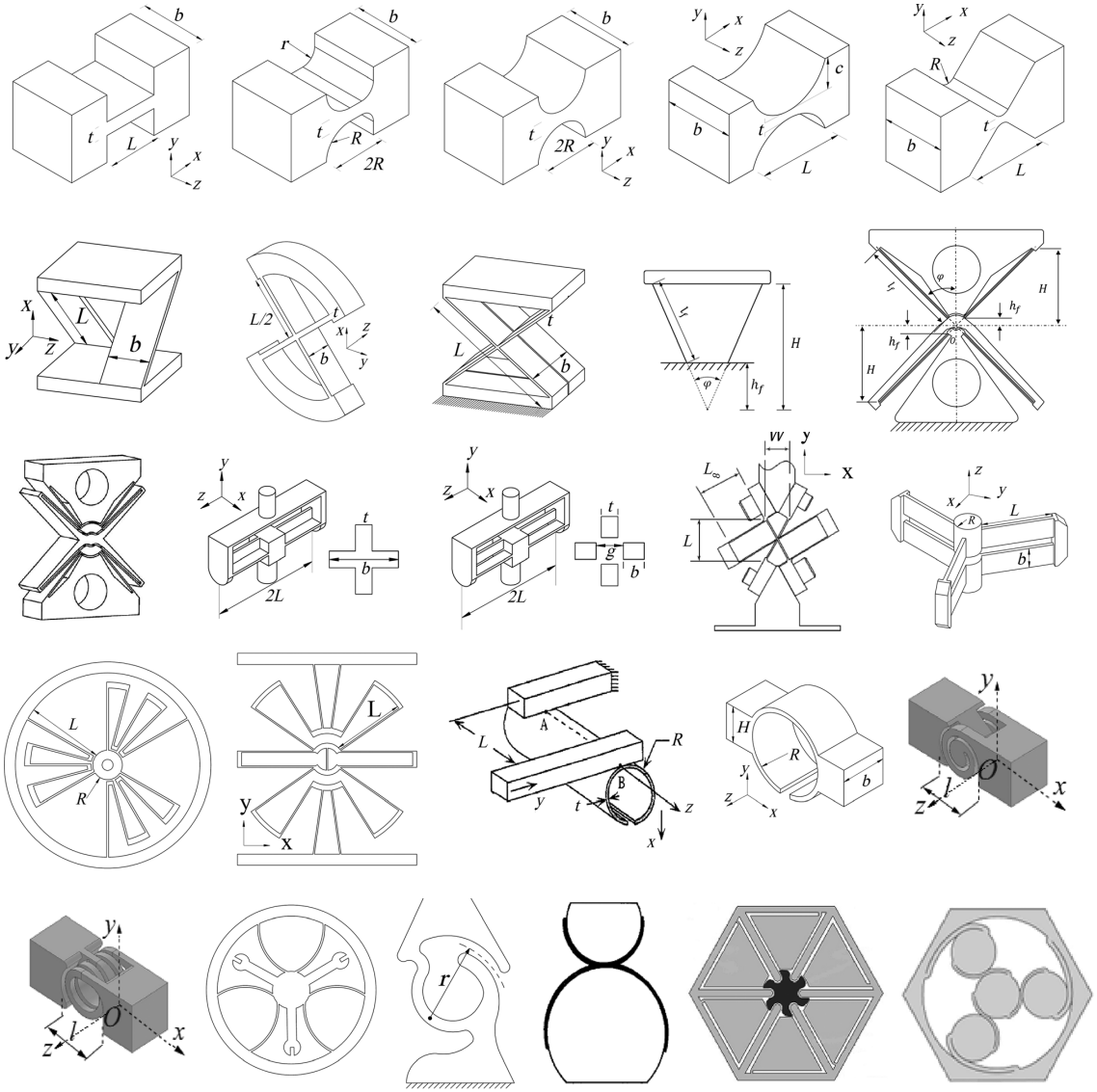

FIGURE 1.1: Compliant kinematic joints (Farhadi Machekposhti, Tolou, and Herder, 2015)

As CMs operate, the elementary built-in compliant joints deform accordingly where the elastic energy will be stored in these flexible members, equivalently, the CMs where they belong. To manipulate the flow of the stored energy, multi-stable mechanisms (Chen and Ma, 2015)(Chen, Ma, and Li, 2016)(Meng et al., 2020) as shown in Fig. 1.2 and Fig. 1.3 are designed where these mechanisms have multiple energy states that represent different modes of the elastic systems (Chen and Ma, 2015)(Chen, Ma, and Li, 2016). Besides, some external energy in our daily lives can be utilized for further use otherwise they may be wasted. CMs can be a suitable choice for storing the energy due to its nature of elasticity. For example, piezoelectric compliant mechanisms are commonly used for energy harvesting (Liang, Hao, and Olszewski, 2021)(Ling et al., 2016)(Ma et al., 2016) as shown in Fig. 1.4. It is worthwhile noting that CMs can be also utilized to isolate the external vibration as resonance filter (Tantanawat, Li, and Kota, 2004), equivalently to avoid the resonance frequency of the protected mechanical system (Fowler, Howell, and Magleby, 2011), such as one of the space applications (Zirbel et al., 2016)(Fowler, Howell, and Magleby, 2011) as shown in Fig. 1.5.

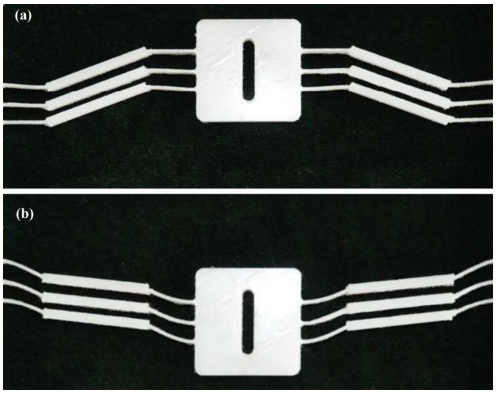

FIGURE 1.2: Bistable mechanisms (Chen and Ma, 2015)

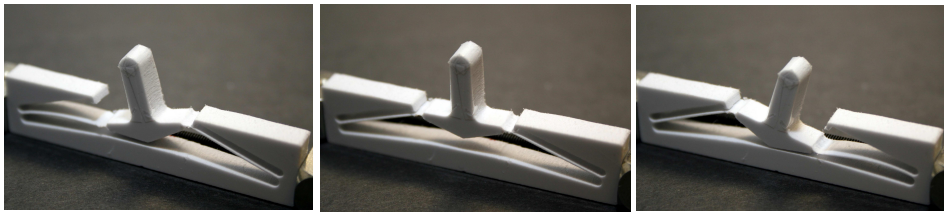

(A) Tri-stable compliant switching mechanisms

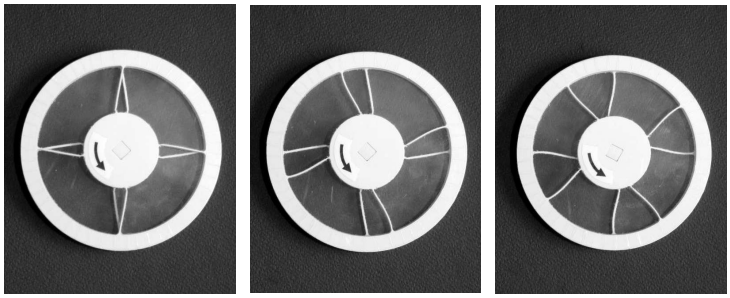

(B) Multi-stable rotational compliant mechanism using RL deformed beams

FIGURE 1.3: Tri-stable mechanisms (Oh and Kota, 2009)

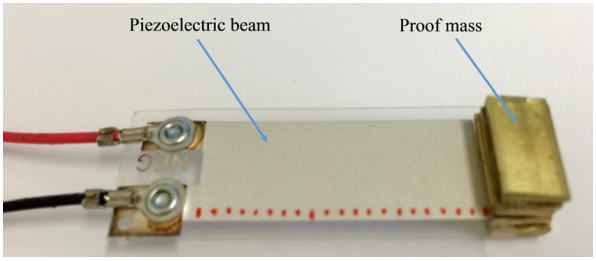

FIGURE 1.4: Piezoelectric compliant mechanisms for energy harvesting (Ma et al., 2016)

Unlike rigid kinematic joints that provide perfect degrees of freedoms and constraints (DOFs, DOCs), the imperfect DOFs and DOCs of the compliant joints offer CMs more diverse displacement outputs (Awtar, 2003). Some remarkable contributions are noted using the concept of symmetry to overcome this imperfection to design compliant positioning stages (Awtar, 2003)(Li, 2016) as shown in Fig. 1.6. Besides, this imperfection can be used to synthesize a CM that amplifies the displacement input to a larger one, which is shown in Fig. 1.7. This type of compliant displacement amplifiers utilize the smart and artful layout of the rigid links and flexible joints to provide this user-designed displacement ratio between the input and the output (Chen, Ma, and Li, 2016)(Hricko and Havlík, 2019).

From the perspective of stiffness and compliance, CMs can also provide desired force outputs. As graphically demonstrated in Fig. 1.8, the constant-force and constant-torque properties offer the CMs self-balancing ability (zero stiffness), bistable states (negative stiffness) and self-locking ability (positive stiffness) (Kuppens et al., 2021) just by adjusting the length of red area as shown in Fig. 1.8a and Fig. 1.8b respectively. The displayed contact-aided

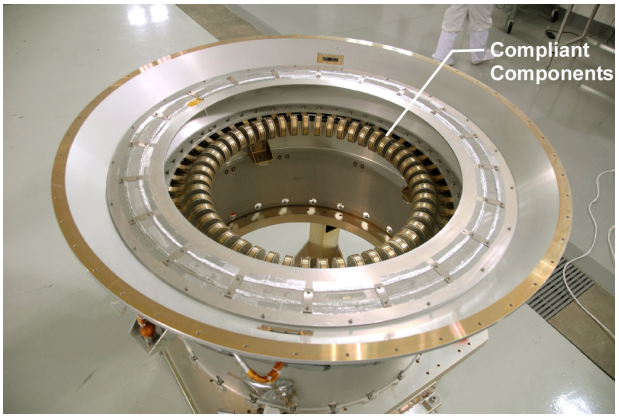

FIGURE 1.5: Vibration isolation mechanism (Fowler, Howell, and Magleby, 2011)

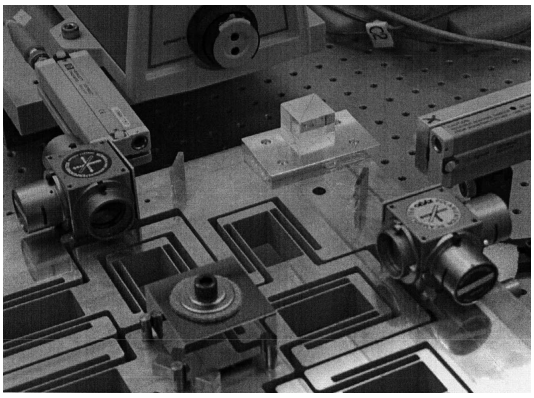

(A) X-Y planar positioning stage (Awtar, 2003)

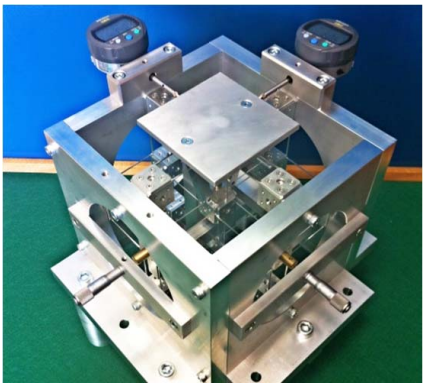

(B) X-Y-Z spatial positioning stage (Li, 2016)

FIGURE 1.6: Compliant positioning stages

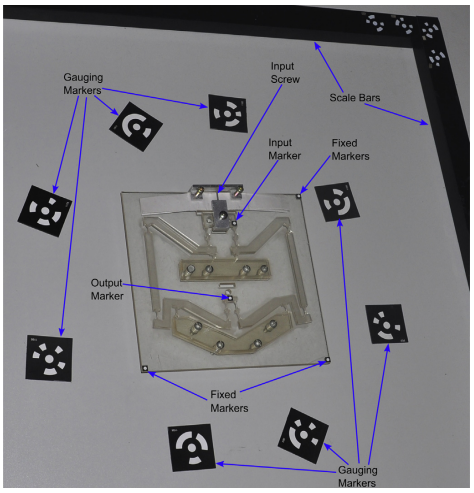

FIGURE 1.7: Displacement amplifier (Chen, Ma, and Li, 2016)

mechanisms graphically depicted in Fig. 1.9 present high load-bearing ability, which is a promising option for high payload. Besides, CMs can also use slender structure under tension to display loading bearing ability as well (Wu and Hao, 2020). The concept of CMs can be used in many other mechanical applications as well, such as parallel continuum manipulators (Fig. 1.12), cable-driven continuum manipulators (Thomas et al., 2021)(Kota et al., 2005) (Fig. 1.11a), concentric-tube robots (Thomas et al., 2021)(Kota et al., 2005) (Fig. 1.11b), microelectromechanical systems (MEMs) (Kota et al., 2001) (Fig. 1.13), aircraft structures (Kota et al., 2003), creative art and design (Megaro

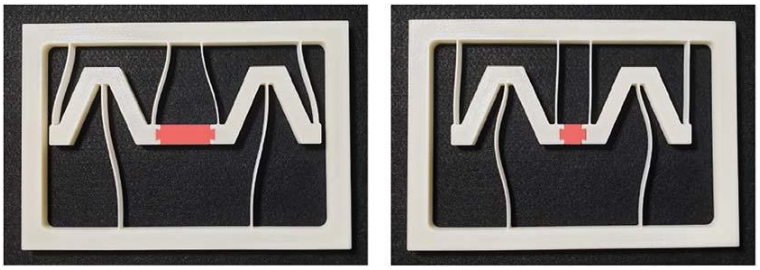

(A) Constant force mechanisms (CFMs)

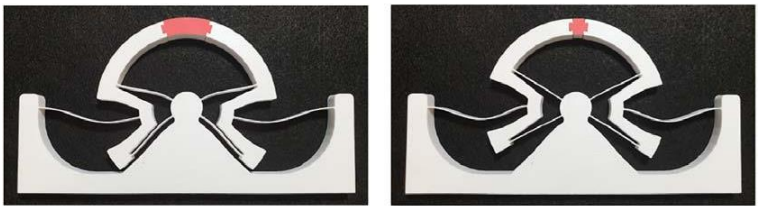

(B) Constant torque mechanisms (CTMs)

FIGURE 1.8: Compliant mechanisms for constant force and torque outputs (Kuppens et al., 2021)

(A) Rest state of a 3D-printed cellular contact-aided compliant mechanism

(B) Payload state of a 3D-printed cellular contact-aided compliant mechanism

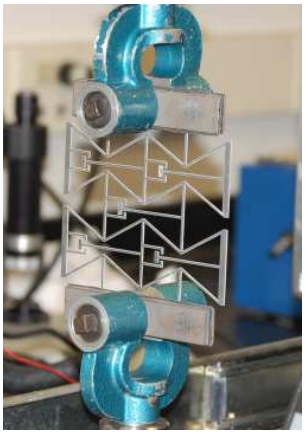

(C) Experimental testing of a fabricated cellular contact-aided compliant mechanism

FIGURE 1.9: Contact-aided compliant mechanisms (Mehta, 2010)

FIGURE 1.10: Creative compliant-mechanism-based design (Megaro et al., 2017)

et al., 2017) (Fig. 1.10), rigid-compliant mechanisms (Qin et al., 2013) and so on.

As reviewed above, it is clear that CMs have already presented desired characteristics in various engineering areas. Thanks to the current academic progress of applied mechanics and applied mathematics, we are able to analyze CMs via using these tools, for example, performance prediction and model-based design or optimization. However, there is a gap between the research community of CMs and the field of applied mechanics and applied mathematics since various rod (beam) theories and mathematical methods are already available but they are not widely used in modeling

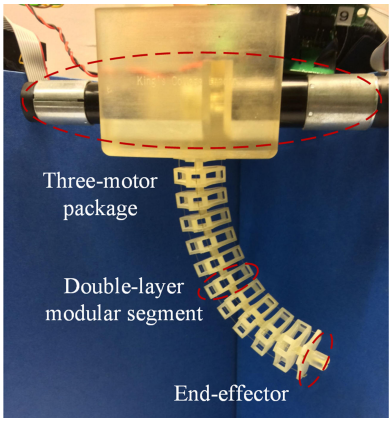

(A) Cable-driven continuum manipulator (Qi et al., 2015)

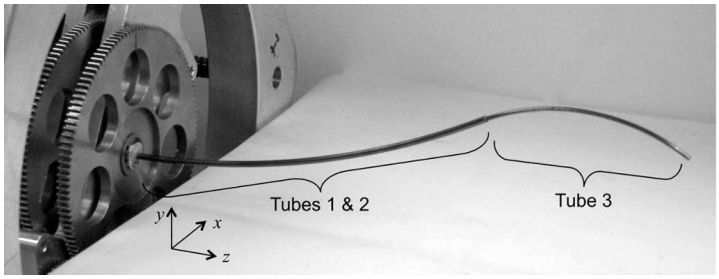

(B) Concentric-tube robots (Dupont et al., 2009)

FIGURE 1.11: Typical continuum manipulators

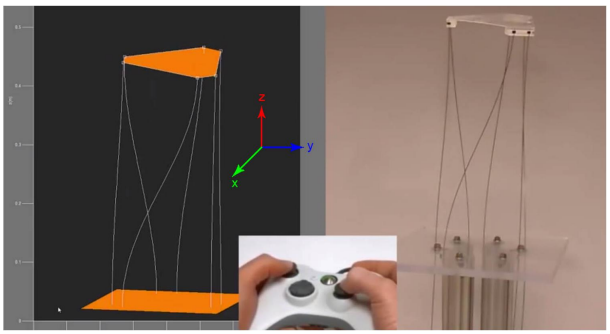

FIGURE 1.12: Parallel continuum manipulator (Till et al., 2015)

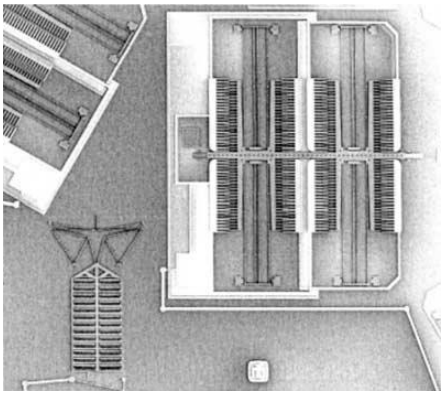

FIGURE 1.13: CM-based microelectromechanical systems (Ma et al., 2016)

CMs. For example, the commonly-used tools for large deflections of slender beams are chained algorithms that are not only coding-unfriendly but also computationally expensive. In the next section, the commonly used modeling tools will be discussed in detail where the limitations and the scope of application are presented.

1.2.2 Timoshenko beam theory and Euler Bernoulli beam theory

In CMs, the elementary built-in slender structures can be normally modeled via beam and rod theories. Therefore, we would like to first recall Timoshenko beam theory, the formulation of which is presented below with its corresponding

graphical demonstration shown in Fig. 1.14:

$$\begin{aligned}
&\frac{\mathrm{d}^3y}{\mathrm{d}x^3} = \frac{\mathrm{d}^2\theta}{\mathrm{d}x^2} = \frac{V(x)}{EI} = \frac{\frac{\mathrm{d}M(x)}{\mathrm{d}x}}{EI} \\
&\frac{\mathrm{d}^2y}{\mathrm{d}x^2} = \frac{\mathrm{d}\theta}{\mathrm{d}x} = \frac{M(x)}{EI} \\
&\frac{\mathrm{d}y}{\mathrm{d}x} = \theta(x) = \int_0^x \frac{M(x)}{EI}\mathrm{d}x - \frac{k_t V(x)}{GA} = \int_0^x \frac{M(x)}{EI}\mathrm{d}x - \frac{k_t \frac{\mathrm{d}M(x)}{\mathrm{d}x}}{GA}
\end{aligned} \tag{1.1}$$

with

$$M(x) = M_o + F_x y_\mathrm{A} + F_y(x_\mathrm{A} - x) \tag{1.2}$$

where E denotes the Young's modulus; I denotes the second moment of inertia of the rectangular cross section ($I = \frac{1}{12}h^3w$); A denotes the area of the cross section ($A = wh$); G denotes the shear modulus ($G = \frac{E}{2(1+\nu)}$ for isotropic materials); k_t denotes Timoshenko shear coefficient ($k_t = \frac{12+11\nu}{10+10\nu}$)(Cowper, 1966) and ν is the Poisson's ratio of the material; $\frac{\mathrm{d}^2y}{\mathrm{d}x^2}$ denotes the linearized curvature of the beam; $V(x)$ denotes the shear force at the cross section; $M(x)$ denotes the moment exerted at point x due to external forces and moments, which in this case is the beam-end loading: F_x, F_y and M_o (see Fig. 1.14); L, h and w denote the length, depth and width of the beam. Note that this linear theory is only applicable to small deflections, equivalently when $\frac{\mathrm{d}y}{\mathrm{d}x}$ is small, without considering geometric nonlinearity. Therefore, Eq. (1.2) can be simplified:

$$M(x) = M_o + F_y(L - x) \tag{1.3}$$

where $x_\mathrm{A} \approx L$ and $y_\mathrm{A} \approx 0$ in small deflections. Besides, M_o should be carefully handled since a relatively larger M_o

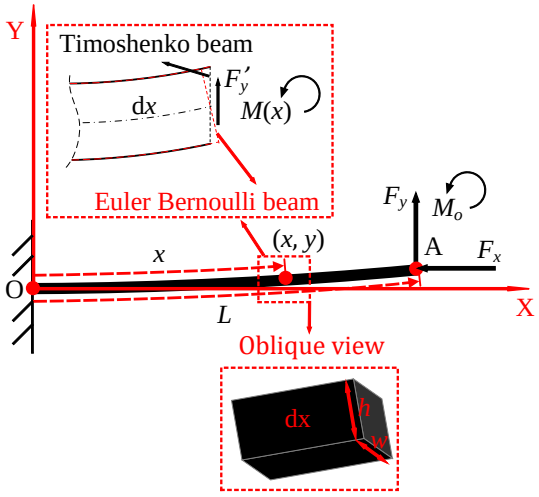

FIGURE 1.14: Small (linear) deflection of Timoshenko beam compared to Euler-Bernoulli beam subjected to beam-end loading

can easily break the assumption made for the linearized curvature as well as small deflections. Although the effect of axial force F_x in bending is ignored as presented in Eq. (1.3), it plays an important role in stress stiffening even in small deflections. Here, we proceed with $M_o = 0$, which results in a very common beam-deflection case, beam-end concentrated loading:

$$M(x) = F_y(L - x) \tag{1.4}$$

Rearranging Eq. (1.1) and Eq. (1.4), we will be able to arrive at the following:

$$\begin{aligned}
&\frac{\mathrm{d}y}{\mathrm{d}x} = \theta(x) = \frac{k_t F_y}{GA} + \frac{F_y L}{EI}x - \frac{F_y}{2EI}x^2 \\
&y(x) = \frac{k_t F_y}{GA}x + \frac{F_y L}{2EI}x^2 - \frac{F_y}{6EI}x^3
\end{aligned} \tag{1.5}$$

In Eq. (1.1), $\frac{M(x)}{EI}$ is the resulting curvature due to bending, which is also the major contribution to beam deflections. Different from Euler Bernoulli beam theory, it is assumed that the cross section of the beam is not normal to the beam axis any more since the shear strain of the cross section is considered. $\frac{k_t V(x)}{GA}$ denotes the extra rotation of the cross section due to the local shear force, which is taken into account by Timoshenko beam theory. Logically, ignoring the shear strain of the cross section, we can easily derive the governing equations of Euler Bernoulli beam theory:

$$\begin{aligned}
&\frac{\mathrm{d}^2 y}{\mathrm{d}x^2} = \frac{\mathrm{d}\theta}{\mathrm{d}x} = \frac{M(x)}{EI} = \frac{F_y(L-x)}{EI} \\
&\frac{\mathrm{d}y}{\mathrm{d}x} = \theta(x) = \int_0^x \frac{M(x)}{EI}\mathrm{d}x = \theta(x) = \frac{F_y L}{EI}x - \frac{F_y}{2EI}x^2 \\
&y(x) = \int_0^x \frac{F_y L}{EI}x - \frac{F_y}{2EI}x^2 \mathrm{d}x = \frac{F_y L}{2EI}x^2 - \frac{F_y}{6EI}x^3
\end{aligned} \tag{1.6}$$

As mentioned before, both the mentioned linear Timoshenko beam theory and Euler Bernoulli beam theory are valid only if analyzing small deflections. Precisely, since the curvature

$$\kappa(x) = \frac{\frac{\mathrm{d}^2 y}{\mathrm{d}x^2}}{[1 + (\frac{\mathrm{d}y}{\mathrm{d}x})^2]^{3/2}} \tag{1.7}$$

then by assuming the Y-axis deflection of the beam is small, i.e. $\frac{\mathrm{d}y}{\mathrm{d}x} \approx 0$, we have:

$$\kappa(x) = \frac{\mathrm{d}^2 y}{\mathrm{d}x^2} \tag{1.8}$$

Similarly, x is chosen as the independent variable due to the fact that the deformed beam axis still approximately coincides with X axis in small-deflection cases (see Fig. 1.14), yielding Eqs. (1.1)(1.5) for Timoshenko beam and Eq. (1.6) for Euler Bernoulli beam. Note that the classic Euler Bernoulli beam theory and Timoshenko beam theory **do not consider the axial (X-axis) displacement** of the studied beam because in small-deflection cases, the axial displacement is small enough to be neglected.

Remark 1 *It should be noticed that based on mentioned linear models, screw theory is commonly*

1.2.3 Linearized geometrically nonlinear beam models

In the literature, one of the most common applications based on CMs is compliant positioning stages (Awtar, Slocum, and Sevincer, 2007)(Howell, 2013a)(Howell, 2013b). These positioning stages provide accurate motions within small-to-intermediate ranges where the built-in flexible members (flexures) serve as the core functional elements. In this context, **the axial displacement of the flexures can not be neglected anymore** although it's still within a small-intermediate range (Awtar, Slocum, and Sevincer, 2007). This is because the deflection of every single flexible member is coupled with each other when considering the deformation of the whole studied CM. Obviously, the classic Timoshenko beam theory and Euler Bernoulli beam theory reviewed in the last section are not applicable to this case. Therefore, accurately modeling these flexures to consider not only the vertical deflection but also the axial displacement of every point along the flexible beam, would be beneficial to the performance prediction and optimization of the studied compliant mechanisms.

1.2.3.1 Beam constraint model (BCM)

To handle intermediate-range deflections as well as consider the axial displacement, Awtar also utilizes the linearization technique (Awtar, 2003) as shown in (1.8) to reformulate (1.1) and (1.2):

$$EI\frac{\mathrm{d}^2 y}{\mathrm{d}x^2} = F_x(y_\mathrm{A} - y) + F_y(x_\mathrm{A} - x) + M_o \tag{1.9}$$

where y in $F_x(y_A - y)$ can not be neglected since the assumption of small deflections is not valid anymore and most importantly the axial (X-axis) displacement of the beam-end is considered. Note that (1.9) is a linear ODE and obviously can be handled much easier than the nonlinear one, such the nonlinear curvature term in (1.7). Several nice and clear mathematical manipulations have been implemented starting from (1.9), and Awtar then derived a closed-form solution to intermediate-range-deflection problems of slender straight beams with constant rectangular cross sections in his PhD thesis (Awtar, 2003):

$$\begin{aligned}\begin{bmatrix} f_y \\ m_o \end{bmatrix} &= A_b \begin{bmatrix} \hat{y}(1) \\ \hat{\theta}(1) \end{bmatrix} - f_x B_b \begin{bmatrix} \hat{y}(1) \\ \hat{\theta}(1) \end{bmatrix} \\ \hat{x}(1) - 1 &= -\frac{h^2}{12} f_x + \begin{bmatrix} \hat{y}(1) \\ \hat{\theta}(1) \end{bmatrix}^\top C_b \begin{bmatrix} \hat{y}(1) \\ \hat{\theta}(1) \end{bmatrix} - f_x \begin{bmatrix} \hat{y}(1) \\ \hat{\theta}(1) \end{bmatrix}^\top D_b \begin{bmatrix} \hat{y}(1) \\ \hat{\theta}(1) \end{bmatrix}\end{aligned} \tag{1.10}$$

where

$$\begin{aligned} A_b &= \begin{bmatrix} 12 & -6 \\ -6 & 4 \end{bmatrix};\ B_b = \begin{bmatrix} 1.2 & -0.1 \\ -0.1 & 2/15 \end{bmatrix} \\ C_b &= \begin{bmatrix} -0.6 & 1/20 \\ 1/20 & -1/15 \end{bmatrix};\ D_b = \begin{bmatrix} 1/700 & -1/1400 \\ -1/1400 & 11/6300 \end{bmatrix}; \end{aligned} \tag{1.11}$$

and

$$f_x = \frac{F_x L^2}{EI};\ f_y = \frac{F_y L^2}{EI};\ m_o = \frac{M_o L}{EI};\ \hat{x}(1) = \frac{x(L)}{L};\ \hat{y}(1) = \frac{y(L)}{L};\ \hat{\theta}(1) = \frac{\theta(L)}{1} \tag{1.12}$$

Note that in (1.10) and (1.12), L denotes the beam length. $x(L), y(L), \theta(L)$ denote the beam-end coordinates whereas $\hat{x}(1), \hat{y}(1), \hat{\theta}(1)$ denote the nondimensionalized beam-end coordinates. Obviously, given any set of f_x, f_y and m_o, to obtain $\hat{x}(1)$, $\hat{y}(1)$ and $\hat{\theta}(1)$, the formulations (1.10) along with (1.11) of BCM are **closed-form**:

$$\begin{aligned}\begin{bmatrix} \hat{y}(1) \\ \hat{\theta}(1) \end{bmatrix} &= (A_b - f_x B_b)^{-1} \begin{bmatrix} f_y \\ m_o \end{bmatrix} \\ \hat{x}(1) &= -\frac{h^2}{12} f_x + \begin{bmatrix} \hat{y}(1) \\ \hat{\theta}(1) \end{bmatrix}^\top C_b \begin{bmatrix} \hat{y}(1) \\ \hat{\theta}(1) \end{bmatrix} - f_x \begin{bmatrix} \hat{y}(1) \\ \hat{\theta}(1) \end{bmatrix}^\top D_b \begin{bmatrix} \hat{y}(1) \\ \hat{\theta}(1) \end{bmatrix} + 1\end{aligned} \tag{1.13}$$

Similarly, **BCM also has a closed-form formulation** for the stored energy (Awtar and Sen, 2010):

$$\hat{E}_p = \frac{1}{2}\left(\frac{h^2}{12}\right) f_x^2 + \frac{1}{2} \begin{bmatrix} \hat{y}(1) \\ \hat{\theta}(1) \end{bmatrix}^\top A_b \begin{bmatrix} \hat{y}(1) \\ \hat{\theta}(1) \end{bmatrix} + \frac{1}{2} f_x^2 \begin{bmatrix} \hat{y}(1) \\ \hat{\theta}(1) \end{bmatrix}^\top D_b \begin{bmatrix} \hat{y}(1) \\ \hat{\theta}(1) \end{bmatrix} \tag{1.14}$$

Logically, we can obtain the dimensional formulations of (1.13) via (1.12). For the dimensional version of $\hat{E}_p$ for BCM, we have:

$$E_p = \frac{EI}{L} \hat{E}_p \tag{1.15}$$

Clearly, BCM offers a handy formulation to calculate the beam-end coordinates or displacements when the beam is subjected to beam-end loading within intermediate-range deflection. In particular, the axial stretch term in (1.13), $-\frac{h^2}{12} f_x$ must not be neglected in flexure-based CMs since it serves as a considerable part in modeling these CMs. Essentially, BCM takes care of bending strain and axial strain in intermediate-range deflections. Note that in (1.13), **the term $\hat{x}(1)$ that represents the axial displacement has been taken into account.** However, mathematically speaking, the model is a linearized model formulated in (1.9) for small-deflection problems so it's normal that it can not be used in large-deflection problems.

1.2.3.2 Timoshenko beam constraint model (TBCM)

Chen and his co-workers extended the work of BCM (Awtar, Slocum, and Sevincer, 2007) to consider the shear strain in intermediate-range deflection (Chen and Ma, 2015) which should be considered in analyzing the statics of stubby beams. TBCM shares the same formulation with BCM, Eq. (1.10) to Eq. (1.13) whereas the corresponding model

matrices A_t, B_t, C_t, D_t are modified via introducing Poisson's ratio ν to consider the shear strain (see details in Chen and Ma, 2015).

1.2.3.3 Chained algorithms for large-deflection problems

The reviewed BCM and TBCM above, as explained, only take care of small-to-intermediate deflections. To consider large deflections of slender beams, chained algorithms serve as an effective option. Here, we would like to recall the original definition of chained algorithms in Howell's classic work: "The chained algorithm requires discretization of the object being modeled into beam elements and each element is analyzed in succession, the chained algorithm is similar to Finite Element Analysis and lends itself well to CM analysis, the chained algorithm is so named because it requires discretization of the object being modeled into beam elements and analyzes each element in succession". This definition clearly implies that chained algorithm actually introduces the concept of Finite Element Method (FEM) (Rao, 2017) where the summation of relatively smaller deflection of all discretized elements results in feasible analysis of larger deflection, which is termed as geometric nonlinearity. A representative case of chained algorithms, called chained beam constraint model (CBCM), has been proved to be an effective choice for modeling large deformation of straight beams (Chen and Bai, 2016; Ma and Chen, 2016) as well as ICBs (Chen et al., 2019). **Note that chained-TBCM (CTBCM) could also be a good model for large-deflection problems where bending, shear and axial strains are all considered.**

From the author's point of view, chained algorithms not only provide an intuitive and straightforward concept to analyze large deflections, but also potentially present possibilities of modeling contact problems. This is because in each fundamental constitutive model, it is always possible to add potential disturbances at each discretized and adjacent points in between two elementary constitutive models, the idea of which also comes from FEM (Rao, 2017). Besides chained algorithms, geometrically nonlinear Euler Bernoulli beam theory is also a feasible option to handle large deflections of slender beam where the curvature expression is exactly defined and not linearized.

1.2.4 Geometrically nonlinear Euler Bernoulli beam theory

In the current literature, modeling large deflections has been one of the most fundamental problems in the research community of CMs (Ling et al., 2020). To analyze large deflections of slender beams, besides chained algorithms, we can move onto geometrically nonlinear Euler Bernoulli beam theory. Different from the classic Euler Bernoulli beam theory, geometrically nonlinear Euler Bernoulli beam equation is expressed in the local coordinate system as shown in Fig. 1.15. Basically, the constitutive equation of the geometrically nonlinear one is formulated as below:

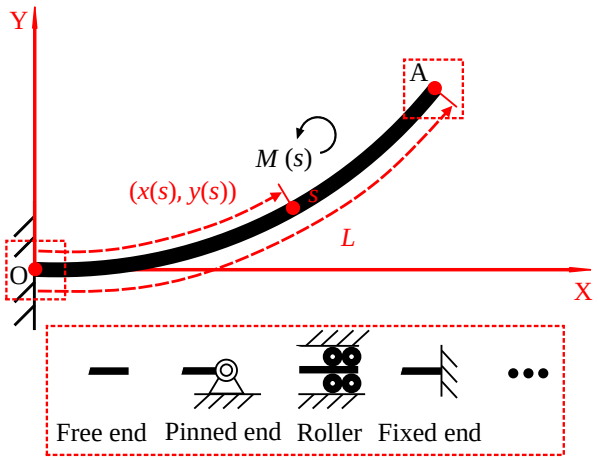

FIGURE 1.15: Geometrically nonlinear Euler Bernoulli beam theory

$$EI\kappa(s) = EI\frac{\mathrm{d}\theta}{\mathrm{d}s} = M(s) \tag{1.16}$$

which implies that the external moment $M(s)$ is proportional to the current curvature $\kappa(s) = \frac{\mathrm{d}\theta}{\mathrm{d}s}$ at point s. The existence of $M(s)$ distributed along the beam is due to different loading exerted on the beam, such as beam-end loading, pressure, distributed loading and so on (Wu and Zheng, 2022a).

Remark 2 *Similar to* (1.7)*, we also have the relationship expressed in body frame:*

$$\kappa(s) = \frac{\frac{\mathrm{d}^2 y}{\mathrm{d}x^2}}{[1 + (\frac{\mathrm{d}y}{\mathrm{d}x})^2]^{3/2}} \tag{1.17}$$

which explains that the classic Euler Bernoulli beam equation (1.6) *is actually linearized from the geometrically nonlinear one* (1.16)*. That means the latter drops the assumption for small deflections to directly deal with large-deflection problems.*

As shown in Fig. 1.15, physically and practically speaking, it's often easy to derive two boundary conditions (the beam base $s = 0$ and the beam end $s = L$) for the studied slender beam (Wu and Zheng, 2022a). Therefore, this physical insight drives us to differentiate (1.16), which ends up with the following BVP:

$$\begin{aligned} &\text{D.E. } EI\frac{\mathrm{d}^2\theta}{\mathrm{d}s^2} = \frac{\mathrm{d}M(s)}{\mathrm{d}s}, \quad s \in [0, L] \\ &\text{B.C. } g\left(\theta(0), \theta'(0), \theta(L), \theta'(L)\right) = 0 \end{aligned} \tag{1.18}$$

where $g \in \mathbb{R}^2$ represents different independent boundary conditions (see Fig. 1.15) defined at $s = 0$ and $s = L$. To solve (1.18), not only CM researchers, but also a large number of researchers from the fields of applied mechanics, beam theories and so on have been contributing to this topic (see a comprehensive review in Wu and Zheng, 2022a). So far, solving (1.18) under some simple boundary conditions, such as beam-end loading, has already been achieved in the field of CMs, and several noticeable contributions have been made by researchers: elliptic integral method, shooting method and pseudo rigid body models (PRBMs).

1.2.4.1 Elliptic integral method

To solve (1.18) under the boundary conditions of beam-end loading, Howell used elliptic integral method to derive the semi-analytical solution which is the most accurate solution (Howell, 2013a). However, this method still suffers from the following in terms of feasibility: some integrals still need to be numerically calculated so the analytical method is not completely closed-form; it's not handy if we conduct model-based optimization since we need to check some data in the database (Howell, 2013a).

1.2.4.2 Shooting method

From a mathematical point of view, (1.18) is a typical two-point BVP so shooting method can be used in this case since it's a universal method for this sort of problems (Osborne, 1969). This method is commonly used in the academic community of beam theories and mechanics (Song and Li, 2007) whereas in CM research community it's seldom used (Ling et al., 2020). Briefly speaking, the concept of shooting method is simple: we first transform the BVP into an initial value problem (IVP) via guessing the initial to shoot at the right boundary target at the other side, during which Newton's method is used to instruct the guessing. However, this method also suffers from some disadvantages due to its nature. For example, in each iteration, we actually solved an IVP via Euler's method or its relatives, which could be time-consuming after several iterations via Newton's method; the step size of Euler's method or its relatives is a tough problem, and also needs to be carefully chosen since the choice of its length is a trade-off result of accuracy and efficiency of shooting method.

1.2.4.3 Pseudo rigid body models

Some chained-PRBMs somehow can be regarded as a chained algorithm but we still pick the whole type of PRBMs up as an individual group of methods due to its unique concept. (Chained-)PRBMs artfully transforms the static beam deflection into a kinematic motion of a rigid mechanism where a limited number of rigid links associated with

stiffness joints to approximate the solution to (1.18). Basically, in the current literature, there are mainly two types of (Chained)-PRBMs: the first one is based on the learning from a large set of data whereas the second type is essentially a discretization strategy for (1.18).

1. **Learning strategy:** the first type is the classic one where a small number of rigid links are used always with the need of estimating model parameters. For example, (Howell, 2013a) provides a closed-form formulation for analyzing large deflection, which is significantly useful in the process of first-stage design. However, it suffers from the limitation of predicting larger end slope of flexible beams. The method proposed in (Venkiteswaran and Su, 2016) is also efficient since only one unknown needs to be solved (see Eq. (13) in Venkiteswaran and Su, 2016) using Newton's method or its relatives. However, it also needs to estimate the model parameters in advance. To us, this method is more like using a large number of cases (where the beam is subjected to different loading conditions) to train the best parameters for the model via optimization (see Eq. (15) in Venkiteswaran and Su, 2016). This type of 'learning' strategies is common in the field of machine learning. Only if the number of training cases approach infinite, the final model will always converge to the correct or accepted solutions under given convergence criteria (Carleo et al., 2019). Note that in this strategy, both prismatic and rotation joints may be used.

2. **Discretization strategy:** (Jin et al., 2020) is another typical one. If the number n of the rigid links is large enough or approaches infinite, this chained-PRBM can accurately approximate the solution to BVP (1.18) essentially since in their method the following relation has been adopted:

$$M(s) = K\delta\theta \tag{1.19}$$

where $K = \frac{EI}{l}$ and l is the length of each rigid link and $l = \frac{L}{n}$ with L being the beam length. If the number n approaches infinitely large, equivalently, l approaches infinitely small, we have

$$M(s) = K\delta\theta = EI \lim_{l\to 0} \frac{\delta\theta}{l} = EI\frac{\mathrm{d}\theta}{\mathrm{d}s} \tag{1.20}$$

with the boundary conditions available. Then, this method directly goes back to numerically solve ODE (1.16) with reliable accuracy. However, due to the large number of links discretized, it ends up with a large number of unknowns to be numerically solved. As a result, the group of equations derived from the principle of minimal potential energy or Euler equation (moment equilibrium) can be solved by Newton's method or its relatives. The high dimension of the Jacobian matrix will logically result in expensive computational cost when calculating its inverse (Kelley, 2003). Obviously, chained-PRBMs reduce the modeling complexity but it ends up with a time-consuming high-dimensional model, which is a typical trade-off option. Note that in this strategy, only rotation joints are used.

Besides the simpler static modeling process of PRBMs (especially the discretization strategy), a more representative advantage of PRBMs is that we can easily formulate the kinetic energy and elastic energy of the slender beam via the same method for rigid robots to derive dynamic model, which is much easier than directly deriving that of a flexible member (Yu et al., 2005)(Yu, Feng, and Xu, 2012)(Yu and Zhang, 2019). As reviewed from Section 1.2.2 to Section 1.2.4, several beam theories that are used for analysis of planar deflection have been discussed. In the next section, Cosserat rod theory that's used for spatial deflection will be introduced in detail. In CMs, these beam theories are more used since most classic designs are planar (Howell, 2013b). However, with the development of this research area, the needs for designing spatial CMs will gradually increase so does Cosserat rod theory.

1.2.5 Cosserat rod theory

Cosserat rod theory is an effective tool to model large spatial deflections of elastic rods (Rubin and Cardon, 2002), and it's now commonly used in robotics, especially soft robotics (Armanini et al., 2021). It should be noted that the complete (dynamic) Cosserat rod model was first introduced in robotics to model hyper-redundant swimming robots and to solve their inverse dynamics (Boyer, Porez, and Khalil, 2006). Then, this model has been later applied to the study of creeping snake like the robots in (Boyer, Ali, and Porez, 2011).

Recently, with the development of soft robotics, Cosserat rod theory has been gradually used in modeling continuum manipulators (Jones, Gray, and Turlapati, 2009)(Rucker and Webster III, 2011)(Chikhaoui et al., 2019)(Till,

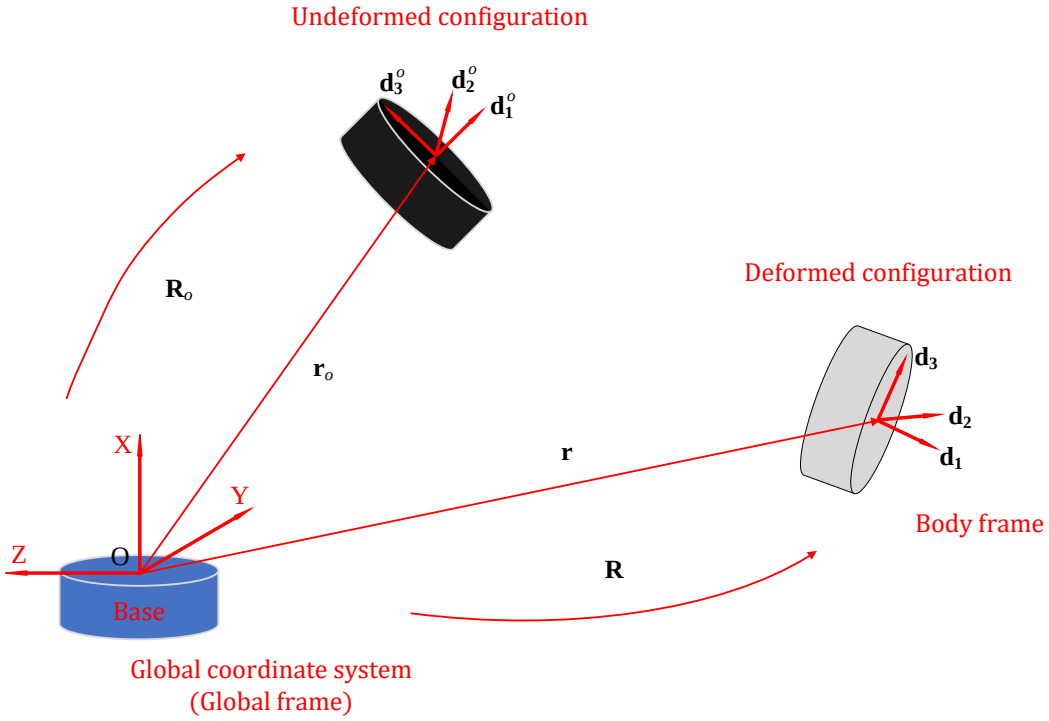

FIGURE 1.16: Geometrical representation of a Cosserat rod

Aloi, and Rucker, 2019), concentric-tube robots (Dupont et al., 2009)(Rucker, Jones, and Webster III, 2010) spatial compliant parallel platform (Orekhov, Aloi, and Rucker, 2017)(Till et al., 2015), soft robots with fluidic (Sadati et al., 2017) and cable (Renda et al., 2017) actuation in both kinematic and dynamic studies (Till, Aloi, and Rucker, 2019).

However, in the field of classic CMs, it has not been widely adopted (Ling et al., 2020). The statics in Cosserat rod theory is expressed by a set of ordinary differential equations (ODEs) constrained by two boundary conditions, which is mathematically termed as a two-point boundary value problem. Cosserat rod theory follows an important assumption: each cross section behaves as a rigid body (Antman, 2005), and it takes care of bending, torsion, elongation and shear in spatial deflection of rods under the framework of geometrical nonlinearity. Similar to the above, we review the statics of these studied slender structure under the framework of Cosserat rod theory. The governing equations of Cosserat rod theory will be explained in the following sections: geometrical representation, equilibrium equations, transformation between local frame and global frame and the fundamental classic constitutive relationships. Finally, some reduced models and commonly-used numerical methods are briefly discussed.

1.2.5.1 Geometrical representation

As shown in Fig. 1.16, any section along a Cosserat rod can be described by $\mathrm{r}(s)$ and $\mathbf{R}(s)$ where $\mathbf{R}(s) = [\mathbf{d_1}, \mathbf{d_2}, \mathbf{d_3}]$. Note that $\mathbf{d_i}$ is a unit vector where $i = 1, 2, 3$. The important assumption that each cross section behaves as a rigid body is reflected by the fact that in Cosserat rod, the angle between $\mathbf{d_2}$ and $\mathbf{d_3}$ remains constant. Normally, we set $\mathbf{d_2}$ and $\mathbf{d_3}$ orthogonal to each other, and then $\mathbf{d_1}$ is defined as another orthogonal vector to both d_2 and d_3 such that $\mathbf{d_1} = \mathbf{d_2} \times \mathbf{d_3}$. In the geometrical representation, all variables depend on a parameter s as the curvilinear coordinate along the rod axis of the undeformed configuration where

$$(\mathbf{r}_o(s), \mathbf{R}_o(s)),\ s \in [0, L] \tag{1.21}$$

denotes the undeformed/unconstrained configuration. logically, we have:

$$\frac{\partial \mathbf{r}_o}{\partial s} = \mathbf{v}_o(s);\ \frac{\partial \mathbf{R}_o(s)}{\partial s} = \hat{\mathbf{u}}_o(s)\mathbf{R}_o(s) \tag{1.22}$$

where $\mathbf{u}_o$ and $\mathbf{v}_o$ stand for the initial curvature and linear pre-strain of the rod respectively. $\hat{\mathbf{u}}_o(s)$ is the skew-symmetric matrix of $\mathbf{u}_o$. It represents the cross product in matrix notation such that $\mathbf{a} \times \mathbf{b} = \hat{\mathbf{a}}\mathbf{b}$; $\mathbf{a} \in \mathbb{R}^{3\times1}$, $\mathbf{b} \in \mathbb{R}^{3\times1}$.

Therefore, for any vector $\mathbf{a} = [a_1, a_2, a_3]^\top$, the skew-symmetric matrix of $\mathbf{a}$ is defined as:

$$\hat{\mathbf{a}} = \begin{bmatrix} 0 & -a_3 & a_2 \\ a_3 & 0 & -a_1 \\ -a_2 & a_1 & 0 \end{bmatrix} \tag{1.23}$$

Then, the unstretched length of the studied rod can be calculated via:

$$L = \int_0^L |\mathbf{v}_o(s)| \mathrm{d}s \tag{1.24}$$

For geometrical representation of the deformed rod, we logically have the following:

$$\frac{\partial \mathbf{r}(s)}{\partial s} = \mathbf{v}(s); \ \frac{\partial \mathbf{R}(s)}{\partial s} = \hat{\mathbf{u}}(s)\mathbf{R}(s) \tag{1.25}$$

1.2.5.2 Equilibrium equations

If we consider equilibrium of the rod at each cross section s, we have the following:

$$\frac{\partial \mathbf{n}(s)}{\partial s} = -\mathbf{f}(s); \ \frac{\partial \mathbf{m}(s)}{\partial s} = -\mathbf{l}(s) - \mathbf{v}(s) \times \mathbf{n}(s) \tag{1.26}$$

where $\mathbf{f}(s)$ and $\mathbf{l}(s)$ stand for the distributed forces and moments exerted on the rod expressed in global frame whereas $\mathbf{n}(s)$ and $\mathbf{m}(s)$ denote the respective internal forces and moments.

1.2.5.3 From global frame to local frame

Now, we have a set of ordinary differential equations (ODEs) that governs the spatial deflection of a rod, and they can be written in the global coordinate system (global frame):

$$\begin{aligned} &\frac{\partial \mathbf{r}(s)}{\partial s} = \mathbf{v}(s); \ \frac{\partial \mathbf{R}(s)}{\partial s} = \hat{\mathbf{u}}(s)\mathbf{R}(s) \\ &\frac{\partial \mathbf{n}(s)}{\partial s} = -\mathbf{f}(s); \ \frac{\partial \mathbf{m}(s)}{\partial s} = -\mathbf{l}(s) - \mathbf{v}(s) \times \mathbf{n}(s) \end{aligned} \tag{1.27}$$

which can be also written in body frame:

$$\begin{aligned} &\frac{\partial \mathbf{r}(s)}{\partial s} = \mathbf{R}(s)v(s); \ \frac{\partial \mathbf{R}(s)}{\partial s} = \mathbf{R}(s)\hat{u}(s) \\ &\frac{\partial n(s)}{\partial s} = -\mathbf{R}^\top(s)\mathbf{f}(s) - u(s) \times n(s); \ \frac{\partial m(s)}{\partial s} = -\mathbf{R}^\top(s)\mathbf{l}(s) - v(s) \times n(s) - u(s) \times m(s) \end{aligned} \tag{1.28}$$

with the boundary conditions:

$$\mathbf{R}(0) = \begin{bmatrix} 1 & 0 & 0 \\ 0 & 1 & 0 \\ 0 & 0 & 1 \end{bmatrix}; \ \mathbf{n}(L) = \begin{bmatrix} F_x \\ F_y \\ F_z \end{bmatrix}; \ \mathbf{m}(L) = \begin{bmatrix} M_x \\ M_y \\ M_z \end{bmatrix} \tag{1.29}$$

where the boundary conditions here refer the ones of beam-end loading scenario just for example. Obviously, the boundary conditions need to correspond to the physical constraints in reality. Note that the above variables defined in the global coordinate system are all in bold whereas the rest are defined in the local one. Essentially, this above is a Robin boundary value problem (BVP) of a system of ODEs where the state vector is defined at one end, and its derivative is defined at the other end (Gakhov, 2014).

1.2.5.4 Constitutive equations

Here, we proceed with a linear elasticity assumption for the constitutive relationships of the Cosserat rod:

$$n(s) = K^n(s)(v - v_o);\ m(s) = K^m(s)(u - u_o) \tag{1.30}$$

with the two stiffness matrices defined as:

$$K^n(s) = \begin{bmatrix} E(s)A(s) & 0 & 0 \\ 0 & G(s)A(s) & 0 \\ 0 & 0 & G(s)A(s) \end{bmatrix};\ K^m(s) = \begin{bmatrix} G(s)J_z(s) & 0 & 0 \\ 0 & E(s)I_2(s) & 0 \\ 0 & 0 & E(s)I_3(s) \end{bmatrix} \tag{1.31}$$

where $G(s)$, $E(s)$, $A(s)$, $I_i(s)$ (for $i = 2,3$) and $J_z(s)$ denote respectively Shear Modulus, Young's Modulus, the cross section area, the second moment of inertia of the cross section along $\mathbf{d_i}(s)$ and the polar moment of inertia at torsional cross section's center located at the neutral fiber.

1.2.5.5 Reduced, simplified models and commonly-used numerical methods

1. **Kirchhoff rod model:** in Cosserat rod theory, six types of strains (two directions of bending, axial twisting, two directions of shear and axial strains) are all considered. However, in practical applications, two directions of bending and axial twisting are the main contributors to spatial deflections. Therefore, neglecting shear and axial strains in Cosserat rod theory, we can end up with the governing equations of Kirchhoff rod model (Langer and Singer, 1996), which turns out to be an effective and trade-off choice of accuracy and modeling complexity in modeling continuum robots and related manipulators (Rucker, Jones, and Webster III, 2010). It should be highlighted that in the community of graphics Kirchhoff rod model has been widely used to model slender structures, such as hair (Bertails et al., 2006), super-helices (Bertails, 2009), super-clothoids (Bertails-Descoubes, 2012), elastic rods (Bergou et al., 2008), viscous threads (Bergou et al., 2010), elastic ribbons (Charrondière et al., 2020) and so on.

2. **Spatial PRBMs:** similarly, using the concept of PRBM, we can also simplify Cosserat rod model or Kirchhoff rod model via assuming that the rod is composed of a finite number of rigid links with a series of passive universal joints with stiffness. Then, we can easily write down the governing equations without touching the set of ordinary differential equations of rod theories, which hugely decreases the modeling complexity. Finally, what we end up with is called spatial PRBMs or 3D PRBMs (Ramirez and Lusk, 2011)(Chimento, Lusk, and Alqasimi, 2014)(Rasmussen et al., 2006).

3. **Commonly-used methods:** essentially speaking, the governing equations of Cosserat rod theory are a set of ordinary differential equations constrained by two-point boundary conditions. This type of BVPs can be typically solved via shooting method. It has been proved effective in modeling continuum manipulators for forward/inverse kinematics (Black, Till, and Rucker, 2017) and forward dynamics (Till, Aloi, and Rucker, 2019). However, the major drawback of shooting method lies in being computationally expensive due to the iterative forward integration involved. Several contributions addressed this issue for some continuum manipulators (Till et al., 2015)(Rucker and Webster, 2011) but the difficulty still remains for modeling frameworks where many Cosserat rods are coupled. Besides, (Orekhov and Simaan, 2020) introduced a strategy to solve Cosserat rod equations where collocation method and Magnus Expansion are used. Using this strategy, the strain vector are approximated via Chebyshev polynomials, and the rotation matrix is integrated using Magnus expansion to ensure that it always stays in the group of $SO3$ (Spatial Orthogonal Group in 3 dimensions) (Amehri, Zheng, and Kruszewski, 2022).

1.2.6 Finite element method

Generally speaking, finite element method (FEM) is a numerical technique for solving problems which are described by differential equations or can be formulated as functional minimization (Nikishkov, 2004)(Rao, 2017). The FEM we use in CMs refers to **solid-mechanics-based FEM** and **beam-theory-based FEM**. Therefore, in the field of CMs, these studied differential equations are derived via solid mechanics and beam theories respectively since we are

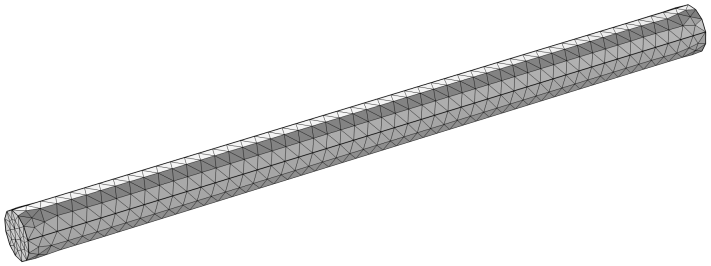

FIGURE 1.17: A slender flexible structure discretized by a set of fine mesh elements

always interested in the deformation of the built-in flexible members in the studied CMs. For a deformable body of irregular shapes or if we consider complex mechanical interference, it's nearly impossible to find the global governing equations to characterize the deformation so FEM is used to locally analyze the deformation of each discretized fine mesh element. Applying Lagrange-Euler method to handle the whole system of the discretized mesh elements (as shown in Fig. 1.17), we will be able to derive the dynamic or static governing equations, which is, mathematically speaking, functional minimization. FEM normally provides accurate solutions but it is computationally expensive, which is why FEM is normally used as a verification method instead of conducting model-based optimization and performance prediction (Wu and Zheng, 2022b).

1.2.7 Constant curvature and piecewise constant curvature

Different from the typical CMs, continuum manipulators can be considered as a special type of CMs normally driven by cables. Constant curvature (CC) and piecewise constant curvature (PCC) models are commonly used in kinematic modeling of continuum manipulators (Webster III and Jones, 2010). Basically, the CC and PCC models assume that the backbones of the continuum manipulators have constant curvature and piecewise constant curvature depending on the structure design of the manipulators. Here, we take planar continuum manipulators for example. As shown in Fig. 1.18a, the manipulator is composed of one segment, and the two cables are mounted along the constant-cross-section backbone parallelly. In this case, we can assume the backbone of the manipulator bends in a constant-curvature shape where the curvature κ is spatially constant along the backbone but changed by different inputs Δl_1 and Δl_2 (the change of cable lengths). In Fig. 1.18b, the manipulator is composed of two segments, and there are two cables attached to the end of each segment. The four cables are parallelly mounted along the constant-cross-section backbone. Likewise, the backbone of each segment can be assumed to bend in a spatially-constant-curvature shape (κ_1 and κ_2) so we can consider the curvature of the whole backbone is spatially-piece-wise-constant. Under the CC and PCC assumptions, we can easily develop the geometric or kinematic models for the continuum manipulators. Besides, in Ian Walker's work (Hannan and Walker, 2003)(Jones and Walker, 2006), Denavit-Hartenberg (D-H) convention is used to assist the modeling process, which connects the classic modeling procedure for rigid manipulators with that of continuum ones. This bridge also ensures the success and promotion of PCC and CC models in the field of continuum manipulators (Hannan and Walker, 2003)(Jones and Walker, 2006).

1.3 Contributions of the thesis

1.3.1 Contributions and layout of the manuscript

As stated in Section 1.2, it is clearly found out that in the field of CMs, there is no existing results on how to geometrically define random-shape initially curved beams and efficiently modeling large deflection of these slender structures under complex loading conditions. In particular, efficiently modeling nonlinear buckling and post-bucking to serve the design of CMs has not been achieved to the best of our knowledge. Besides, there is also few results for model-based design (optimization) and model-based control of CMs. If the mentioned problems are not solved, researchers may still suffer from the time-consuming trial-and-error design process and be stuck with global-enumeration-based design framework or purely empirical design methods. To handle the mentioned concerns, in this thesis, we investigate the problem in the following chapters of the thesis (See Fig. 1.19). In Chapter 2, we introduce various mathematical tools

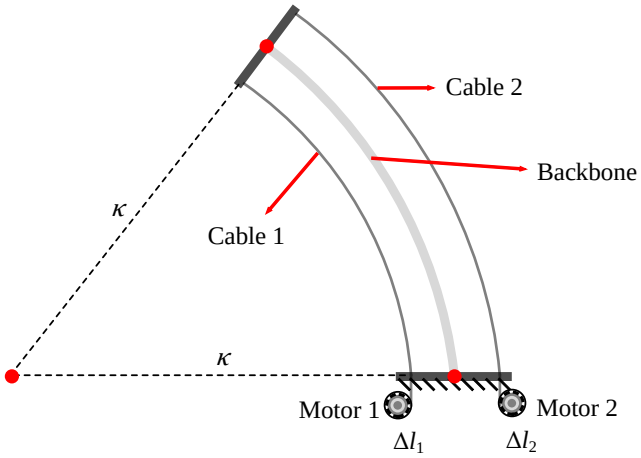

(A) Constant curvature model

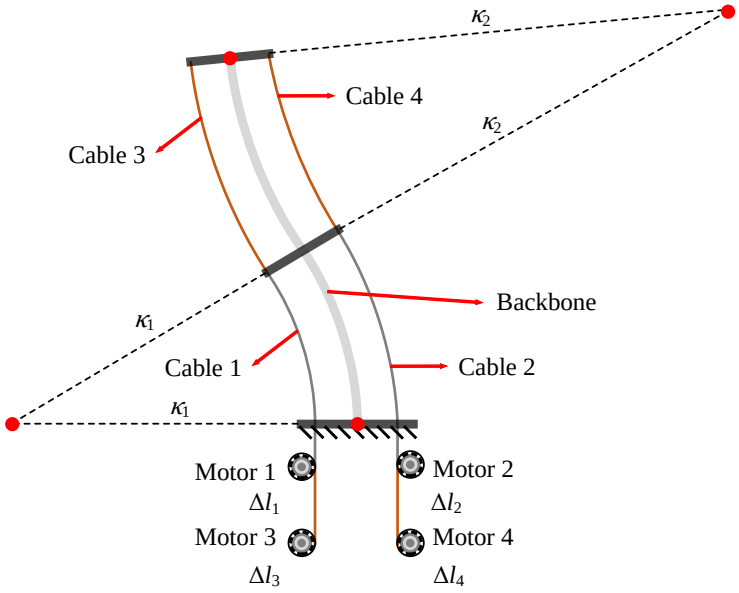

(B) Piecewise constant curvature model

FIGURE 1.18: Kinematic models for continuum manipulators

in detail that are used to solve BVPs of ODEs and optimization problems since the formulations of modeling large deflections are BVPs and optimization problems as stated in Chapter 3.

Chapter 3 is mainly composed of three aspects. First, we introduce the geometrical definition of arbitrary planar beams in different coordinate systems and the strategy of coordinate transformation to body frame. The pros and cons of designing planar beams are discussed followed by potential contributions to the geometric definition of spatial beams and coordinate transformation via the similar strategy. This problem is formulated as ODEs. Then, we present the modeling of large deflections under various boundary conditions via Newtonian mechanics where an arbitrary planar slender beam subjected to different loading conditions is studied. This can be formulated as a BVP of an ODE. In particular, the modeling of nonlinear buckling and post-buckling is presented as well. Finally, we introduce the modeling of large deflections under various boundary conditions via Lagrangian mechanics, and similarly different loading conditions are discussed as well. Note that in Lagrangian framework, the problem is formulated as functional minimization.

In Chapter 4, with the modeling strategies and mathematical tools available, we use these tools to efficiently solve different models developed in Chapter 3. In terms of coordinate transformation, we use collocation method to approximate the solution (to the ODE). Secondly, for models (BVPs) developed via Newtonian mechanics, we use various numerical methods, hybrid methods and semi-analytical methods to analyze large-deflection problems. Then, under Lagrangian framework, we transform the problem of functional minimization into an optimization problem, and use Lagrange multiplier to numerically solve the problem. Finally, a comprehensive case study is presented to

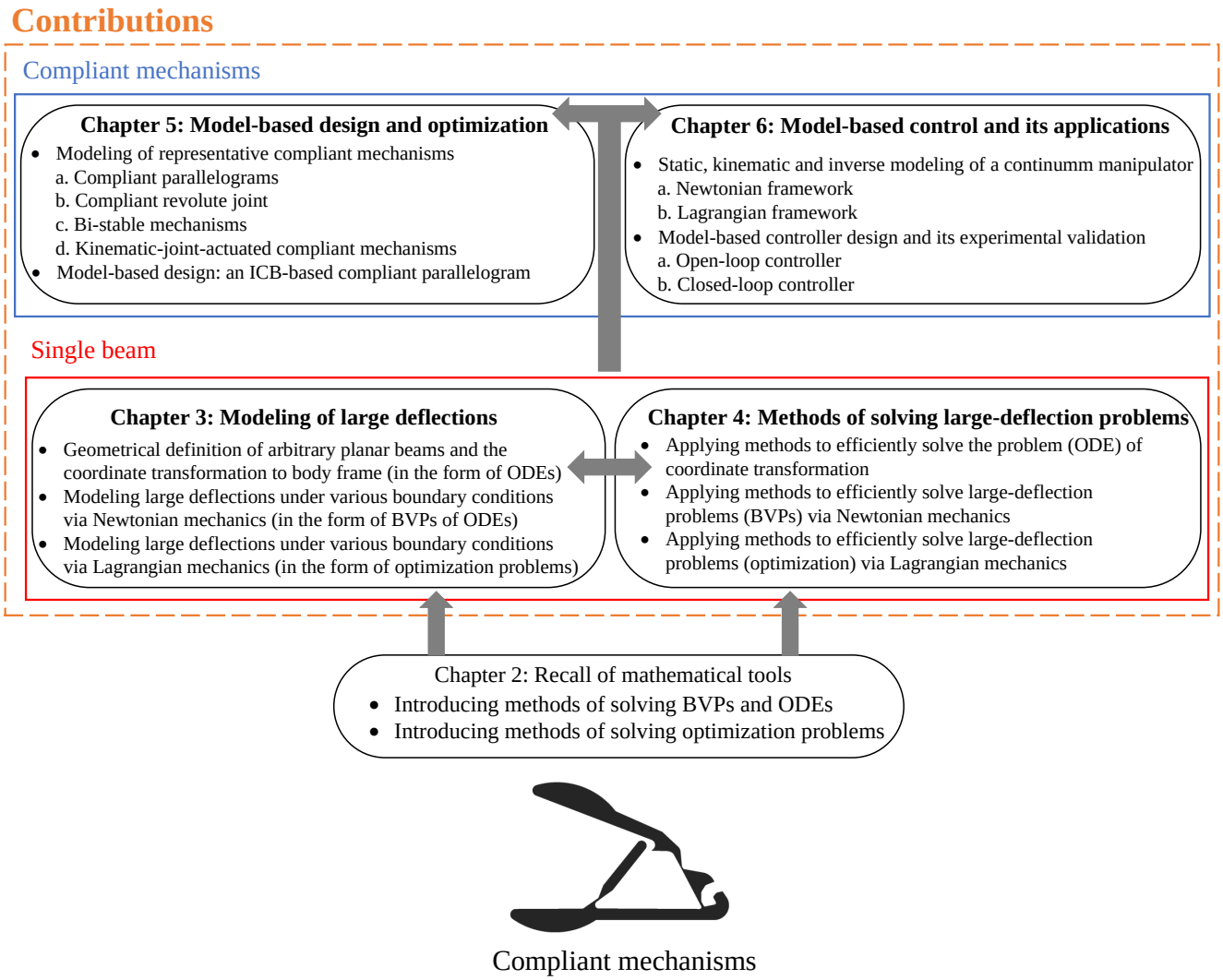

FIGURE 1.19: Layout of the present thesis

verify the proposed methodology.

Different from modeling a single slender structure stated in Chapter 4, Chapter 5 first clarifies the modeling of a compliant mechanism where four types of representative CMs are modeled. In these illustrative examples, the high efficiency and reliable accuracy of the mathematical tools for solving the constitutive models have been proved. Depending on the efficient and accurate modeling framework, a fast optimization-based design process of an ICB-based compliant parallelogram is carried out followed by the experimental validation.

In Chapter 6, we finally present an experimental implementation of controlling a continuum manipulator. The statics, kinematics and inverse modeling is first demonstrated through Newtonian framework and Lagrangian framework respectively. Then, the model-based controller design process is presented accordingly followed experimental validation where closed-loop and open-loop ones are both tested.

Chapter 7 provides the conclusions of the present thesis and presents the perspective of future work, including the geometric definition of 3D beams (along with the transformation into body frame), the analysis of multi-stable compliant mechanisms from Lagrangian point of view and efficient numerical methods for full-mode Cosserat rod theory.

1.3.2 Publications

The following lists my publications during my Ph.D. study.

1. Zhou X, Wang H, Wu K, Zheng G. Fixed-time neural network trajectory tracking control for the rigid-flexible coupled robotic mechanisms with large beam-deflections. Applied Mathematical Modelling. 2023 Feb 10.

2. Chen R, Wang W, Wu K, Zheng G, Xu X, Wang H, Luo J. Design and Optimization of a Novel Compliant Planar Parallelogram Mechanism Utilizing Initially Curved Beams. Mechanism and Machine Theory. 2023 Jan 1;179:105092.

3. Wu K, Zheng G, Chen G. Extending Timoshenko Beam Theory for Large Deflections in Compliant Mechanisms. Journal of Mechanisms and Robotics. 2022 Dec 19:1-2.

4. Wu K, Zheng G. Solutions to Large Beam-deflection Problems by Taylor Series and Padé Approximant for Compliant Mechanisms. Mechanism and Machine Theory. 2022 Nov 1;177:105033.

5. Wu K, Zheng G. Insight into Numerical Solutions of Static Large Deflection of General Planar Beams for Compliant Mechanisms. Mechanism and Machine Theory. 2022 Jun 1;172:104757.

6. Wu K, Zheng G. Theoretical Analysis on Nonlinear Buckling, Post-buckling of Slender Beams and Bi-stable Mechanisms. Journal of Mechanisms and Robotics. 2022 Jun 1;14(3).

7. Wu K, Zheng G, Zhang J. FEM-based Trajectory Tracking Control of a Soft Trunk Robot. Robotics and Autonomous Systems. 2022 Apr 1;150:103961.

8. Wu K, Zheng G. A Comprehensive Static Modeling Methodology via Beam Theory for Compliant Mechanisms. Mechanism and Machine Theory. 2022 Mar 1;169:104598.

9. Wu K, Zheng G. FEM-Based Nonlinear Controller for a Soft Trunk Robot. IEEE Robotics and Automation Letters. 2022 Mar 16;7(2):5735-40. (selected for demonstration in IROS)

10. Wu K, Zheng G, Hao G. Efficient Spatial Compliance Analysis of General Initially Curved Beams for Mechanism Synthesis and Optimization. Mechanism and Machine Theory. 2021 Aug 1;162:104343.

11. Wu K, Zheng G. FEM-based Gain-scheduling Control of a Soft Trunk Robot. IEEE Robotics and Automation Letters. 2021 Feb 23;6(2):3081-8. (selected for demonstration in ICRA)

Chapter 2

Mathematical Background

2.1 Introduction

In this chapter, some useful mathematical methods and theorems will be recalled, including approximation of continuous functions, numerical solutions to algebraic equations, numerical methods to approximate ODE with known initial conditions, numerical methods to solve BVPs, closed-form solutions to BVP and methods for optimization problems and so on. These methods will be used to solve the mathematical problems in Chapter 3 to Chapter 6 which are derived from modeling of flexible structures as well as compliant mechanisms.

2.2 Approximation of continuous functions

Note that in this thesis, we aim to find a continuous solution to several highly nonlinear ODEs and BVPs (such as the governing equations of geometrically nonlinear Euler–Bernoulli beam theory stated in Chapter 3), but its exact analytical solution is very hard to find. Therefore, we bypass the difficult task to approximate the exact analytical solution using polynomials as basis functions, which is based on Weierstrass's first theorem (Stone, 1948).

Theorem 1 (Weierstrass's first theorem) *If $f(x)$ is a given continuous function for $\underline{x} \leq x \leq \bar{x}$ where $\underline{x}$ and $\bar{x}$ represent the lower bound and upper bound of x, and if ϵ is an arbitrary positive quantity (or an infinitesimal), then there exists an approximating polynomial $P(x) = \sum_{i=0}^{n} c_i x^i$ with $c_i \in \mathbb{R}$ and $n \in \mathbb{Z}_0^+$ such that*

$$|f(x) - P(x)| < \varepsilon$$

for $\underline{x} \leq x \leq \bar{x}$.

This theorem implies that, instead of finding the exact solution to the studied BVPs, we can find some specific polynomials that can quite accurately approximate the exact solution.

2.3 Numerical methods of solving algebraic equations

To model slender structures or compliant mechanisms (stated in Chapter 4 and Chapter 5), we normally end up solving a group of nonlinear equations. In the literature, there are several methods to handle nonlinear equations or systems of equations. In this thesis, we would like to proceed with a commonly used method called Newton-Raphson method for these problems. Here, a brief recap is presented to solve a general nonlinear equation $f(x) = 0 \in \mathbb{R}^{N\times 1}$ with $x \in \mathbb{R}^{n\times 1}$ $(N \geq n)$, which can be realized by the following iterative equation:

$$x_i = x_{i-1} - \left[\frac{\partial f(x)}{\partial x}\right]^{-1}_{|x=x_{i-1}} f(x_{i-1})$$

where x_i represents the ith iterative solution with x_0 being a given initial guess value. Obviously, the major computation of this algorithm lies in calculating the pseudo inverse $(N > n)$ or the inverse $(N = n)$ of $\frac{\partial f(x)}{\partial x}$ (Yuan, 2010)(Courrieu, 2008). After the convergence (in practice the convergence criteria is set as $||x_{i+1} - x_i|| \leq \varepsilon$ where ε is a pre-defined threshold), we can finally obtain the solution x to $f(x) = 0$. The dimension of the Jacobian matrix

$\frac{\partial f(x)}{\partial x}$ is $\mathbb{R}^{N\times n}$. Therefore, the higher values of N and n of the studied matrix, which leads to higher dimension of the matrix, would result in more computational time for computing the pseudo inverse or the inverse of this matrix.

2.4 Numerical methods of approximating ODEs with known initial boundary conditions

As stated in Chapter 3, modeling of slender beams can yield BVPs. Somehow, to handle these BVPs, transforming them into initial value problems (IVPs) under a shooting framework is a feasible choice. In general, given a general nonlinear ODE

$$\frac{\mathrm{d}y}{\mathrm{d}x} = g(x,y)$$

for $x \in [x_0, x_n]$ with the known initial condition $y(x_0) = y_0$, and it is difficult or impossible to find out its analytical solution if $g(x,y)$ is highly nonlinear. Numerical methods are thus needed to approximate its solution. Euler method and Runge-Kutta method are two commonly used ones, which will be recalled hereafter. Consider $y = f(x)$ is the solution to the above ODE with $y(x_0) = y_0$ where x_0 is the known initial condition.

Explicit Euler's method: Denote Δh as the fixed sampling step of the space $[x_0, x_n]$ for x, i.e., $x_{i+1} = x_i + \Delta h$, and then we proceed with $y_{i+1} = y_i + g(x_i, y_i)\Delta h$ for $0 \le i \le n-1$. Finally, we will end up with $f(x_{i+1}) \approx y_{i+1}$.

Runge-Kutta method: Similarly, Runge-Kutta method is also a popular choice for numerically solving ODE with known initial conditions. The formula of the fourth Runge-Kutta method is presented below. Then, we proceed with the following formula:

$$k_1 = \Delta h g(x_i, y_i);\ k_2 = \Delta h g(x_i + \frac{\Delta h}{2};\ y_i + \frac{k_1}{2});\ k_3 = \Delta h g(x_i + \frac{\Delta h}{2}, y_i + \frac{k_2}{2});\ k_4 = \Delta h g(x_i + \Delta h, y_i + k_3)$$
$$y_{i+1} = y_i + \frac{1}{6}(k_1 + 2k_2 + 2k_3 + k_4)$$

which computes the approximate solution as $f(x_{i+1}) \approx y_{i+1}$.

2.5 Numerical methods of solving BVPs

As reviewed in Chapter 2, modeling slender beams via geometrical nonlinear Euler Bernoulli beam theory results in a general form, such as BVP (1.18). Generally speaking, BVPs have boundary conditions that are given at two points. Normally, it's very hard to find the analytical (closed-form) solution if the studied BVPs are nonlinear. Therefore, in this section, we are going present several numerical methods for solving BVPs. These numerical methods will be used in the following chapters. For the sake of simplicity, let's take an arbitrary second-order nonlinear BVP for example:

$$\begin{aligned} \text{D.E.}\quad & \frac{\mathrm{d}^2y}{\mathrm{d}x^2} = f(x,y) \\ \text{B.C.}\quad & y(0) = a \\ & \frac{\mathrm{d}y}{\mathrm{d}x}(1) = b \end{aligned} \tag{2.1}$$

for $0 \le x \le 1$. In the following, we are going to apply different methods to solving BVP (2.1) for demonstration.

2.5.1 Finite difference method

Finite difference method (FDM) defines n sampling points ($a = y(0) < y_1 < y_2 < y_3 < y_4 ... < y_{n-1} = y(1)$) as unknowns, which correspond to the evenly sampling points ($0 = x(0) < x_1 < x_2 < x_3 < x_4 ... < x_{n-1} = 1$). Then by using those points to approximate $\frac{\mathrm{d}^2y}{\mathrm{d}x^2} \approx \frac{y_{i+1}-2y_i+y_{i-1}}{[1/(n-1)]^2}$, BVP (2.1) can be written into the following discrete

manner:

$$\begin{aligned}
&\frac{y_2 - 2y_1 + y(0)}{[1/(n-1)]^2} - f(x_1, y_1) = 0 \\
&\frac{y_{i+1} - 2y_i + y_{i-1}}{[1/(n-1)]^2} - f(x_{i-1}, y_{i-1}) = 0, \text{ for } 2 \leq i \leq n-2 \\
&\frac{\frac{y_{n-1} - y_{n-2}}{1/(n-1)} - b}{1/(n-1)} - f(x_{n-1}, y_{n-1}) = 0
\end{aligned} \tag{2.2}$$

where the first and the last equation take into account the two boundary conditions presented in (2.1). Clearly, there are altogether $n-1$ equations available and $n-1$ unknowns to be solved. Then, we can numerically handle (2.2), which contains $n-1$ equations, using Newton-Raphson method presented in Section 2.3 to obtain the values of y_i for $0 \leq i \leq n-1$, equivalently to approximate the solution to BVP (2.1). Besides, we take one step further to add an iterative strategy for automatically choosing the number of sampling points n: if $|y_{n_k}(s) - y_{n_{k-1}}(s)| \leq \varepsilon$ where n_k is the kth option ($k = 1, 2, 3...$) for n and $y_{n_k}(s)$ is the approximation under n_k sampling points, then n is settled: $n = n_k$; if not, $n = n_{k+1} = n_k + 1$. This strategy enables the method adaptive to solve the studied system (2.2) without manually setting up n.

2.5.2 Shooting method

As the term implies, shooting method (SH) is essentially a trial method via mathematical methods to direct its guessing to reach the corrective answer. Here, we first need to transform BVP (2.1) into an IVP which can be directly solved using Euler's method or Runge-Kutta method presented in Section 2.4:

$$\begin{aligned}
\text{D.E.} \quad & \frac{\mathrm{d}^2 y}{\mathrm{d}x^2} = f(x, y) \\
\text{I.C.} \quad & y(0) = a \\
& \frac{\mathrm{d}y}{\mathrm{d}x}(0) = b_i
\end{aligned} \tag{2.3}$$

where b_i denotes the ith trial for $\frac{\mathrm{d}y}{\mathrm{d}x}(0)$ in the ith iteration. Then, we can define IVP (2.3) as a function $F(b_i)$ where obviously b_i is the input and $\frac{\mathrm{d}y}{\mathrm{d}x}(1)$ is the output of the function. Therefore, what we actually to solve is:

$$F^*(b_i) = F(b_i) - b = 0 \tag{2.4}$$

We can solve this type of nonlinear equations via utilizing the presented Newton-Raphson method in Section 2.3. After the convergence, we can then obtain the desired initial condition b_i for IVP (2.3). Therefore, the solution to IVP (2.3) can be approximated via Euler's method or Runge-Kutta method presented in Section 2.4.

2.5.3 Weighted residual methods

As reported in the literature, weighted residual methods (WRMs) (Hatami, 2017) are an approximation technique for solving differential equations. According to Theorem 1, we can then define a function $\tilde{y}(x)$, which is an nth-order polynomial, to approximate the solution to BVP (2.1), i.e.,

$$\tilde{y} = \sum_{i=0}^{n} c_i x^i \tag{2.5}$$

where there are $n+1$ unknown coefficients ($i = 0, 1, 2, 3...n$). With the above chosen polynomial solution $\tilde{y}$, an approximation residual can be defined as follows:

$$\mathcal{R}(x) = \frac{\mathrm{d}^2 \tilde{y}}{\mathrm{d}x^2} - f(\tilde{y}, x) \neq 0 \tag{2.6}$$

In terms of satisfying the boundary conditions defined in (2.1), we then have the corresponding constraints expressed via $\tilde{y}(x)$ as follows:

$$\begin{aligned} \text{B.C.} \quad & \tilde{y}(0) = a \\ & \frac{\mathrm{d}\tilde{y}}{\mathrm{d}x}(1) = b \end{aligned} \tag{2.7}$$

Therefore, we logically arrive at:

$$\begin{aligned} \tilde{y}(0) &= \sum_{i=0}^{n} c_i 0^i = a \\ \frac{\mathrm{d}\tilde{y}}{\mathrm{d}x}(1) &= \sum_{i=0}^{n} i c_i = b \end{aligned} \tag{2.8}$$

The essence of weighted residual method is to force the residual (2.6) to zero in some average sense over the domain:

$$\int_0^1 \mathcal{W}_j \mathcal{R}(x) \mathrm{d}x = 0, \quad (j = 1, 2, 3...n-1) \tag{2.9}$$

where $\mathcal{W}_j$ is the weight function; $n-1$ refers to the **least** number of weight functions, equivalently the **least** number of the equations derived from (2.9) (for instance, we could have $n+1$ equations derived from (2.9) in least square method in Section 2.5.3.3); logically, we can solve the $n+1$ unknown coefficients c_i defined in (2.5) via **at least** $n-1+2 = n+1$ equations from (2.8) and (2.9). Such a problem can be solved by applying Newton-Raphson method presented in Section 2.3. Note that in (2.8) and (2.9), there are at least 3 equations available so we have $n+1 \geq 3$, equivalently $n \geq 2$, which means 2th or higher-order polynomials should be used to approximate the solution to BVP (2.1).

In order to apply weighted residual methods, it is necessary to initialize a trial guess for (2.5) to start its iterative computation which might play an important role in the convergence and local minima. In this context, we can have two different ways to set the initial values of c_i:

1. **Direct way:** We randomly initialize the values of c_i, which yields a random shape of $\tilde{y}(x)$.
2. **Indirect way:** We choose a globally initial guess for $\tilde{y}(x)$, such as trigonometric functions, which yields the corresponding c_i for the $\tilde{y}(x)$.

The direct way is suitable for the scenario where the problem tends to have only one single solution, i.e., it contains only global minima. The indirect way goes for the scenario where we reasonably initialize the initial guess (possibly near the final solution) for the final solution via using the existing information. Similarly, we can also implement the iterative strategy for automatically choosing the order of pre-set polynomial n: if $|\tilde{y}_{n_k}(s) - \tilde{y}_{n_{k-1}}(s)| \leq \varepsilon$ where n_k is the kth option ($k = 1, 2, 3...$) for n and $\tilde{y}_{n_k}(s)$ is the approximation using a polynomial of n_kth order, then n is settled: $n = n_k$; if not, $n = n_{k+1} = n_k + 1$. This strategy enables the method adaptive to solve the studied system of equations (2.8) and (2.9) without manually setting up n.

Another important issue related to weighted residual methods is how to choose the weight function. Intuitively, different choices of those weight functions lead to different implementations of the weighted residual methods with different performances. The following explains some popularly used techniques to choose weight functions.

2.5.3.1 Collocation method

As a commonly-used type of weighted residual method, collocation method has already been a widely accepted option of solving two-point BVPs. This method essentially conducts collocation with several continuous polynomial functions to approximate the target unknown function under given boundary conditions (Russell and Shampine, 1972). In this method, the weight functions are taken from the family of Dirac δ function in the domain, i.e. $W_j(x) = \delta(x - x_j)$ where x_j is termed as a collocation point. Substituting (2.5) and (2.6) into (2.9) results in the forcing of the

residual to zero at the specific collocation points, i.e.,

$$\int_0^1 \mathcal{W}_j(x)\mathcal{R}(x)\mathrm{d}s = \mathcal{R}(x_j) = 0, \quad (j = 1,2,3...n-1). \tag{2.10}$$

where $x_j = \dfrac{j}{n}$ and (2.10) contains $n-1$ equations. Considering 2 extra boundary conditions, there are altogether $n+1$ equations to solve $n+1$ polynomial coefficients c_i $(i = 0,1,2,3...n)$.

2.5.3.2 Subdomain method

Subdomain method (SUM) can be regarded as a modification of the aforementioned collocation method. The idea of such a method is to force the weighted residual to zero not only at fixed collocation points in the domain but also over various subsections of the domain. To implement this method, the weight functions are set to the same integers, and the integral over the entire domain is broken into $(n-1)$ subdomains that are sufficient to evaluate all unknown coefficients defined in (2.5). Substituting (2.5) and (2.6) into (2.9), we will have:

$$\int_{\frac{(j-1)}{n-1}}^{\frac{j}{n-1}} \mathcal{R}(x)\mathrm{d}x = 0, \quad (j = 1,2,3...n-1). \tag{2.11}$$

where (2.11) contains $n-1$ equations. Considering 2 extra boundary conditions, there are altogether $n+1$ equations to solve $n+1$ polynomial coefficients c_i $(i = 0,1,2,3...n)$.

2.5.3.3 Least square method

In least square method (LSM), the continuous summation of all the squared residuals is minimized:

$$\begin{aligned} &\min_{c_0,c_1,c_2...c_n} \Upsilon(x), \text{ with } \Upsilon(x) = \int_0^1 \mathcal{R}^2(x)\mathrm{d}x \\ &\text{s.t. } \tilde{y}(0) = a \\ &\qquad \frac{\mathrm{d}\tilde{y}}{\mathrm{d}x}(1) = b \end{aligned} \tag{2.12}$$

where $c_0, c_1, c_2...c_n$ are the polynomial unknown coefficients defined in (2.5). In order to achieve a minimal of this scalar function, the derivatives of $\Upsilon(x)$ with respect to all the unknown parameters must be zero:

$$\frac{\partial \Upsilon(x)}{\partial c_i} = 2\int_0^1 \frac{\partial \mathcal{R}(x)}{\partial c_i}\mathcal{R}(x)\mathrm{d}x = 0 \quad (i = 0,1,2,3...n) \tag{2.13}$$

Comparing with (2.9), the weight functions in this method are chosen as:

$$\mathcal{W}_j(x) = \frac{\partial \mathcal{R}(x)}{\partial c_i}, \quad (j = i+1 = 1,2,3...n+1) \tag{2.14}$$

where (2.14) contains $n+1$ equations. Considering 2 extra boundary conditions, there are altogether $n+3$ equations to solve $n+1$ polynomial coefficients c_i $(i = 0,1,2,3...n)$.

2.5.3.4 Galerkin method

In Galerkin method (GM), instead of using the derivative of the residual with respect to the unknown c_i defined in (2.5), the derivative of the approximating function is used, and the weight functions are chosen as follows:

$$\mathcal{W}_j(x) = \frac{\partial \tilde{y}(x)}{\partial c_i}, \quad (j = i+1 = 1,2,3...n+1) \tag{2.15}$$

Hence (2.9) will yields

$$\int_0^1 \frac{\partial \tilde{y}(x)}{\partial c_i}\mathcal{R}(x)\mathrm{d}s = 0, \quad (j = 1,2,3...n+1) \tag{2.16}$$

where (2.16) contains $n+1$ equations. With 2 extra boundary conditions, there are altogether $n+3$ equations to solve $n+1$ polynomial coefficients c_i $(i = 0,1,2,3...n)$.

2.5.3.5 Method of moments

In method of moments (MOM), the weight functions are chosen from the family of polynomials:

$$\mathcal{W}_j(x) = x^j, \quad j = 1,2,3...n-1 \tag{2.17}$$

Rearranging (2.9) will yields

$$\int_0^1 x^j\mathcal{R}(x)\mathrm{d}x = 0, \quad (j = 1,2,3...n-1) \tag{2.18}$$

where (2.18) contains $n-1$ equations. With 2 extra boundary conditions, there are altogether $n+1$ equations to solve $n+1$ polynomial coefficients c_i $(i = 0,1,2,3...n)$.

2.5.3.6 Rayleigh Ritz method

In Rayleigh Ritz method (RRM), the principle of integration by parts is used:

$$\begin{aligned}\int_0^1 \mathcal{W}_j\mathcal{R}(x)\mathrm{d}s &= \int_0^1 \mathcal{W}_j[\frac{\mathrm{d}^2\tilde{y}}{\mathrm{d}x^2} - f(\tilde{y},x)]\mathrm{d}s \\ &= [\mathcal{W}_j\frac{\mathrm{d}\tilde{y}}{\mathrm{d}x}]_0^1 - \int_0^1 \frac{\mathrm{d}\mathcal{W}_j}{\mathrm{d}x}\frac{\mathrm{d}\tilde{y}}{\mathrm{d}x}\mathrm{d}x - \int_0^1 \mathcal{W}_j f(\tilde{y},x)\mathrm{d}x = 0\end{aligned} \tag{2.19}$$

for $1 \le j \le n+1$, where the weight functions are chosen in the following manner:

$$\mathcal{W}_j = \frac{\partial \tilde{y}}{\partial c_i}, \quad (j = i+1 = 1,2,3...n+1) \tag{2.20}$$

Note that (2.19) contains $n+1$ equations. With 2 extra boundary conditions, there are altogether $n+3$ equations to solve $n+1$ polynomial coefficients c_i $(i = 0,1,2,3...n)$.

2.5.3.7 Weighted residual methods from global to local

From Section 2.5.3.1 to Section 2.5.3.6, all the mentioned weighted residual methods are handled in a global manner. However, these methods can be all implemented in a local manner for higher accuracy and approximating complex solutions to more BVPs, such as BVPs' solutions of highly frequent vibration (where in the case of beam-deflection problems, it refers to high-order buckling phenomena). Unlike the procedure explained in Section 2.5.3.1 to Section 2.5.3.6 from a global perspective, the following explains how BVP (2.1) is handled using one of the mentioned weighted residual methods, i.e. collocation method in a local manner (Shampine, Kierzenka, Reichelt, et al., 2000).

Generally speaking, by dividing the interval $[0,1]$ into $j+1$ points $0 = x_0 < x_1 < \cdots < x_j = 1$, collocation method approximates the solution to the above BVP via linear combination of well-chosen basis functions by satisfying D.E. and B.C. at all collocation points. Precisely, denote by $\tilde{y}$ the approximate solution to BVP (2.1), and suppose that a cubic polynomial $p_k(x)$ is chosen to approximate the solution $\tilde{y}$ to BVP (2.1) on each sub-interval $[x_{k-1}, x_k]$, i.e., $\tilde{y} = \sum_{k=1}^{j} p_k(s)$ where

$$p_k(s) = \begin{cases} \sum_{i=0}^{3} c_{ki}s^i, & \forall s \in [s_{k-1}, s_k] \\ 0, & \text{otherwise} \end{cases} \tag{2.21}$$

with c_{ki} for $0 \le i \le 3$ being the 4 unknown polynomial coefficients on the kth interval. In total, we have $4j$ unknown parameters to be identified. Clearly, $\tilde{y}$ should satisfy the D.E. in BVP (2.1) for all collocations points, and this yields

the following $3j$ algebraic equations to be fulfilled:

$$\begin{aligned}
&\frac{\mathrm{d}^2\tilde{y}}{\mathrm{d}x^2}(x_{k-1}) - f(\tilde{y}(x_{k-1}), x_{k-1}) = 0 \\
&\frac{\mathrm{d}^2\tilde{y}}{\mathrm{d}x^2}(\bar{x}^k_{k-1}) - f(\tilde{y}(\bar{x}^k_{k-1}), \bar{x}^k_{k-1}) = 0 \\
&\frac{\mathrm{d}^2\tilde{y}}{\mathrm{d}x^2}(x_k) - f(\tilde{y}(x_k), x_k) = 0
\end{aligned} \tag{2.22}$$

where $\bar{x}^k_{k-1} = \frac{x_{k-1}+x_k}{2}$. Note that the approximated solution $\tilde{y}$ is a combination of a series of local cubic polynomials, therefore additional equation should be imposed to guarantee the continuity at all collocation points, i.e.,

$$p_{k-1}(x_{k-1}) = p_k(x_{k-1}), \forall k \in [2, j] \tag{2.23}$$

Hence we have the above $j-1$ algebraic equations due to the continuity conditions. Together with the 2-dimensional B.C. in (2.1), we finally obtain a set of algebraic equations with dimension $3j + j - 1 + 2 = 4j + 1$, which will be used to compute those $4j$ unknowns parameter c_{ki} defined in (2.21).

So far, we have demonstrated the collocation method performed in a local manner (Shampine, Kierzenka, Reichelt, et al., 2000). In common weighted residual methods (see Section 2.5.3.1 to Section 2.5.3.6), they are all implemented in a global manner, which means a single global polynomial $\tilde{y} \in C^1$ is used to approximate the solution to (2.1). However, the solution via the locally-performed collocation method only ensures the continuity of $\tilde{y}$, equivalently $\tilde{y} \in C^0$, which ends up with non-differentiable piecewise polylines for the solution $\tilde{y}$. Intuitively, this non-differentiability of $\tilde{y}$ may contradict the nature of material mechanics since the relevant physical variables are always continuous and differentiable, equivalently $y \in C^1$ (Boresi, Schmidt, Sidebottom, et al., 1985). To treat such a problem, we take one step further to modify the collocation method via ensuring the differentiability of $\tilde{y}$, i.e., $\tilde{y} \in C^0$. By imposing the following derivative continuity conditions at all collocation points:

$$\frac{\mathrm{d}p_{k-1}}{\mathrm{d}x}(x_{k-1}) = \frac{\mathrm{d}p_k}{\mathrm{d}x}(x_{k-1}), \forall k \in [2, j] \tag{2.24}$$

This extra added constraints of derivative continuity leads to a differentiable global approximation of the solution to the studied BVP (2.1), bypassing the need of conducting curve fitting process afterwards. It is clear that (2.24) yields another $j-1$ equations, ending up with altogether $4j + 1 + j - 1 = 5j$ algebraic equations available. In summary, the collocation method enables us to solve the $4j$ unknowns c_{ki} based on the $4j+1$ equations from (2.1), (2.22) and (2.23), or $5j$ equations from (2.1), (2.22) (2.23) and (2.24) which can be numerically solved via Newton-Raphson method presented in Section 2.3.

2.5.4 Taylor series method and Padé approximant

Taylor series method (TSM) and Padé approximant (PA) are typical methods for semi-analytically solving a two-point BVP of a nonlinear ODE. In this section, we briefly recap the details of these two methods. (Abbasbandy and Bervillier, 2011) is recommended for readers who need a more detailed explanation.

2.5.4.1 Taylor series method

Taylor series method is an old and well-known method for solving a BVP of an ODE, and we still take BVP (2.1) for example. Obviously, it would be easier to find a solution if the two boundary conditions are defined at only one point (Cauchy problem). For example,

$$\begin{aligned}
y(0) &= a \\
\frac{\mathrm{d}y}{\mathrm{d}x}(0) &= b_o
\end{aligned} \tag{2.25}$$

where b_o is the unknown to be solved. Similar to the scheme of shooting method as stated in Section 2.5.2, we are rather interested in semi-analytical methods based on Taylor series. In this context, we can expand the solution $y(x)$

to BVP (2.1) around $x = 0$ via Taylor series (Maclaurin series):

$$y(x) = \sum_{i=0}^{\infty} c_i x^i \tag{2.26}$$

According the ODE in (2.1), the coefficients c_i can be expressed by a and b_o in a recurrent manner:

$$y(x) = \sum_{i=0}^{\infty} c_i(a, b_o) x^i \tag{2.27}$$

If the series does converge to the solution, the method will only provide an approximate solution since only series of a limited number n are considered in practice:

$$\tilde{y}(x) = \sum_{i=0}^{n} c_i(a, b_o) x^i \tag{2.28}$$

Therefore, differentiating (2.28) results in:

$$\frac{\mathrm{d}y}{\mathrm{d}x}(x) = \sum_{i=1}^{n} i c_i(a, b_o) x^{i-1} \tag{2.29}$$

At this stage, we have two strategies to solve b_o:

1. **Explicit strategy**
   The second BC in (2.1) is explicitly imposed, namely:

$$\frac{\mathrm{d}y}{\mathrm{d}x}(1) = \sum_{i=1}^{n} i c_i(a, b_o) = b \tag{2.30}$$

2. **Minimal strategy**
   The auxiliary condition is obtained by imposing that the next term of the truncated Taylor series vanishes:

$$c_{n+1}(a, b_o) = b \tag{2.31}$$

Obviously, we can numerically solve (2.30) and (2.31) via Newton-Raphson method.

2.5.4.2 Padé approximant

Given the truncated series (2.28) of a finite order n, one can approximate its sum by a rational function:

$$\sum_{i=0}^{n} c_i(a, b_o) x^i = \frac{P(x)}{Q(x)} \tag{2.32}$$

where $P(x)$ and $Q(x)$ are polynomial functions of respective pth and qth order. Logically, the coefficients of $P(x)$ and $Q(x)$ are determined as functions of a and b_o so that:

$$\begin{aligned} &P(x) = Q(x) \sum_{i=0}^{n} c_i(a, b_o) x^i + o[x^{n+1}] \\ &Q(0) = 1 \\ &p + q = n \end{aligned} \tag{2.33}$$

Similar to Taylor series method, to satisfy a condition at $x = 1$, we will have the following relationship:

$$\frac{\mathrm{d}(\frac{P(x)}{Q(x)})}{\mathrm{d}x}(1) = b \tag{2.34}$$

Obviously, we can numerically solve (2.34) via Newton-Raphson method. The details can be found in (Wu and Zheng, 2022c).

2.6 Closed-form solution to BVPs: Adomian decomposition method

As mentioned above, it's always good to have analytical solutions to BVPs since they often provide physically intuitive, concise and closed-form formulations. Adomian decomposition method, which is a semi-analytical method for solving ordinary and partial nonlinear differential equations (Adomian, 2013), is introduced here to handle nonlinear BVPs. This method was developed from 1970s to 1990s by American mathematician, George Adomian (Adomian, 2013). Briefly speaking, the essence of this method is involving the famous "Adomian polynomials" which allow for solution convergence of the nonlinear portion of the differential equations via Maclaurin expansion, without simply linearizing the system to find the analytical solution (Wazwaz, 2010). In this section, we keep taking BVP (2.1) as an example.

Here, we illustrate the basic ideas of Adomian decomposition method (ADM) via the case of a nonlinear ordinary differential equation written in a general form:

$$\hat{L}_t[y(x)] + \hat{R}[y(x)] + \hat{N}[y(x)] = f(x) \tag{2.35}$$

where $\hat{L}_t[.] = \frac{\mathrm{d}^n}{\mathrm{d}x^n}[.]$ denotes the derivative operator with respect to x, while $\hat{R}[.]$ is the linear operator, generally containing derivatives with respect to x. Moreover, $\hat{N}[.]$ represents a nonlinear analytical operator, and $f(x)$ is a non-homogeneous arbitrary function, assumed to be independent of $y(x)$. Then, we assume that the operator $\hat{L}_t$ is invertible, and therefore we can apply $\hat{L}_t^{-1}$ to both sides of (2.35):

$$y(x) = \hat{L}_t^{-1}[f(x)] - \hat{L}_t^{-1}[\hat{R}[y(x)]] - \hat{L}_t^{-1}[\hat{N}[y(x)]] \tag{2.36}$$

where the boundary conditions are used in $\hat{L}_t^{-1}[f(x)]$ here. ADM decomposes the solution $y(x)$ and the nonlinearity $\hat{N}[y(x)]$ into series:

$$y(x) = \sum_{n=0}^{\infty} y_n(x), \ \hat{N}[y(x)] = \sum_{n=0}^{\infty} \mathcal{A}_n \tag{2.37}$$

where $\mathcal{A}_n$ are the Adomian polynomials.

To compute $\mathcal{A}_n$, we set $\hat{N}[y(x)] = f(y(x))$. As defined before, $\hat{N}[.]$ is a nonlinear analytical operator so $f(y)$ logically serves as a nonlinear function of y. Now, consider the Taylor series of $f(y)$ around y_0:

$$f(y) = f(y_0) + f'(y_0)(y-y_0) + \frac{1}{2!}f''(y_0)(y-y_0)^2 + \frac{1}{3!}f'''(y_0)(y-y_0)^3 + ... \tag{2.38}$$

where $y = y_0 + y_1 + y_2 + y_3 + y_4 + y_5 + y_6 + y_7 ....$ Then, (2.38) can be therefore reformulated:

$$\begin{aligned} f(y) =& f(y_0) + f'(y_0)(y_1 + y_2 + y_3 + y_4 + y_5 + y_6 + y_7 ...) \\ &+ \frac{1}{2!}f''(y_0)(y_1 + y_2 + y_3 + y_4 + y_5 + y_6 + y_7 ...)^2 \\ &+ \frac{1}{3!}f'''(y_0)(y_1 + y_2 + y_3 + y_4 + y_5 + y_6 + y_7 ...)^3 + ... \end{aligned} \tag{2.39}$$

By expanding all terms of (2.39), we will have:

$$\begin{aligned} f(y) =& f(y_0) + f'(y_0)y_1 + f'(y_0)y_2 + f'(y_0)y_3 + ... \\ &+ \frac{1}{2!}f''(y_0)y_1^2 + \frac{2}{2!}f''(y_0)y_1y_2 + \frac{1}{2!}f''(y_0)y_1y_3 + ... \\ &+ \frac{1}{3!}f'''(y_0)y_1^3 + \frac{3}{3!}f'''(y_0)y_1^2y_2 + \frac{1}{3!}f'''(y_0)y_1^2y_3 + ... \end{aligned} \tag{2.40}$$

Then, re-ordering all terms of series (2.40), we have

$$\begin{aligned}
\mathcal{A}_0 &= f(y_0) \\
\mathcal{A}_1 &= y_1 f'(y_0) \\
\mathcal{A}_2 &= y_2 f'(y_0) + \frac{1}{2!} y_1^2 f''(y_0) \\
\mathcal{A}_3 &= y_3 f'(y_0) + \frac{2}{2!} y_1 y_2 f''(y_0) + \frac{1}{3!} y_1^3 f''(y_0) \\
&\dots
\end{aligned} \tag{2.41}$$

Hence,

$$\mathcal{A}_n = \frac{1}{n!} \frac{\mathrm{d}^n}{\mathrm{d}\lambda^n} [\hat{N}[\sum_{n=0}^{\infty} \lambda^n y_n]]_{\lambda=0}, n \geq 0. \tag{2.42}$$

To find the $\mathcal{A}_n$ via Adomian general formulation, these polynomials can be computed as follows:

$$\begin{aligned}
\mathcal{A}_0 &= \hat{N}(y_0) \\
\mathcal{A}_1 &= \frac{\mathrm{d}}{\mathrm{d}\lambda} \hat{N}[y_0 + \lambda y_1] \Big|_{\lambda=0} \\
\mathcal{A}_2 &= \frac{1}{2!} \frac{\mathrm{d}^2}{\mathrm{d}\lambda^2} \hat{N}[y_0 + \lambda y_1 + \lambda^2 y_2] \Big|_{\lambda=0} \\
\mathcal{A}_3 &= \frac{1}{3!} \frac{\mathrm{d}^3}{\mathrm{d}\lambda^3} \hat{N}[y_0 + \lambda y_1 + \lambda^2 y_2 + \lambda^3 y_3] \Big|_{\lambda=0} \\
&\dots
\end{aligned} \tag{2.43}$$

where y_0 is the solution to $\hat{L}_t[y(x)] = f(x) - \hat{R}[y(x)]$. From (2.36), (2.37) and (2.43), we will easily have the recurrent relation:

$$y_n = -\hat{L}_t^{-1} \mathcal{A}_{n-1}, \; n \geq 1 \tag{2.44}$$

2.7 Methods of solving optimization problems

To model slender beams under energy framework, we normally end up facing a functional minimization problem stated in Chapter 4. However, if we bypass the functional variation process, we can alternatively transform the problem into a simple optimization problem. Generally speaking, optimization is the act of obtaining the best result under given conditions. In design, construction, and maintenance of any engineering system, engineers and researchers need to make many technological and managerial decisions at different stages. The final goal of all these mentioned decisions is either to minimize the effort required (such as human labor or computational expense) or to maximize the desired benefit (such as the performance of a mechanical application). Since the effort required or the benefit desired in any practical situation can be expressed as a function of certain decision variables, optimization can be defined as the process of finding the conditions that have the maximum or minimum value of a function (Rao, 2019). In the following, typical methods for two commonly-encountered optimization problems are presented.

2.7.1 Optimization problems with linear equality constraints

1. For the studied classic type of problems, we first write it into a general form below:

$$\begin{aligned}
&\min_{x \in \mathbb{R}^n} \; f(x) \\
&s.t. \quad Cx = b
\end{aligned} \tag{2.45}$$

where $C \in \mathbb{R}^{p\times n}$, $\text{rank}(C) = p < n$, $x \in \mathbb{R}^n$ and $b \in \mathbb{R}^p$. According to Karush–Kuhn–Tucker conditions Jahn, 2017, the necessary and sufficient conditions of x^* being the optimum solution is that there exist $\lambda^* \in \mathbb{R}^p$:

$$\begin{aligned} Cx^* &= b \\ \nabla f(x^*) + C^\top \lambda^* &= 0 \end{aligned} \tag{2.46}$$

Essentially, there are $n + p$ equations to solve $n + p$ unknowns ($x \in \mathbb{R}^n$ and $\lambda^* \in \mathbb{R}^p$). Normally, (2.46) is a group of nonlinear equations so we can use Newton Raphson method and its relative methods to find the numerical solution.

2. Alternatively, directly replacing some variables via the linear constraints stated in (2.45), we can end up with **a simple optimization without constraints**:

$$\min_{\bar{x}\in\mathbb{R}^{n-p}} \; f(\bar{x}) \tag{2.47}$$

where $\bar{x} \in \mathbb{R}^{n-p}$. Logically, we just need to find $\bar{x}^*$ that satisfy the following:

$$\nabla f(\bar{x}^*) = 0 \tag{2.48}$$

Clearly, there are $n - p$ equations to solve $n - p$ unknowns. Similarly, we can use Newton Raphson method and its relative methods to solve (2.48) as well.

2.7.2 Optimization problems with nonlinear equality constraints

First, we can write the problem into a general form below:

$$\begin{aligned} \min_{x} \;& f(x) \\ s.t. \;& g(x) = 0 \end{aligned} \tag{2.49}$$

where $g(x) = 0$ is a nonlinear constraint of $x \in \mathbb{R}^n$. We can solve this type of problems via Lagrange Multiplier(LM) (Bertsekas, 2014). Therefore, (2.49) can be equivalently transformed to

$$\min_{x,\lambda} \; f^*(x,\lambda) = f(x) + \lambda g(x) \tag{2.50}$$

which is a simple optimization problem without constraints. Then, we have:

$$\nabla f^*(x,\lambda) = 0 \tag{2.51}$$

Logically, (2.51) can be numerically solved via Newton-Raphson method.

Chapter 3

Static Modeling of Planar Large Deflections

3.1 Introduction

In the current literature, there have been several great contributions reviewed above in terms of modeling large deflections of slender beams. As stated above, modeling large deflections is not a new topic but in engineering fields like CMs, we focus on simpler and more straightforward methods that can be directly used to assist CM designers. Besides, we also seek for constitutive theories and methods to meet the needs of offering more design possibilities. For example, the current methods may more focus on straight beams, and they can not handle beams of complex geometries, such as varying cross sections or varying initial curvature. Using the most of the current methods is also difficult to formulate different boundary conditions like prismatic constraints or revolute joints in the modeling. Apart from beam-end loading, most of the current methods are not handy to take care of gravity, pressure in large deflections, blocking the way for more engineering scenarios. On the contrary, it's possible to use Cosserat rod theory or Kirchhoff rod theory to model the mentioned desired scenarios but its high modeling complexity prevents it from being widely used in the field of CMs. Here in this chapter, we first present the strategy of geometrical definition of arbitrary planar beams, and then offer a deep insight of geometrically nonlinear Euler Bernoulli beam theory as well as extend this theory to cover more engineering scenarios.

3.2 Geometrical definition of arbitrary planar beams

Before analyzing large deflections of slender beams, geometrical definition of these slender beams is essential since besides simple straight beams, designers may have uncountable options for the other initial geometry of a slender beam, such as initial curvature and varying cross sections. Therefore, characterizing the shapes of slender beams mainly includes two aspects: defining the axis curves and the cross sections. Obviously, it's easy to define the cross sections for some standard shapes like rectangle and round ones as shown in Fig. 3.1 (w and h denote the width and depth of the rectangular cross section respectively; d denotes the diameter of the round cross section; L denotes the beam length), and it's also handy to calculate the corresponding physical quantities, such as cross section area (rectangular cross sections: $A = wh$; round cross sections: $A = \frac{\pi d^2}{4}$) and second moment of inertia of the cross section area (rectangular cross sections: $I = \frac{1}{12}wh^3$; round cross sections: $I = \frac{1}{64}\pi d^4$). Besides, the cross sections can be defined varying from the beam base to the beam end just via using differentiable functions.

On the contrary, the axis curves could be more variable. We have three options of coordinate systems to define axis curves: Cartesian coordinate system, polar coordinate system and body frame. Each coordinate system benefits from pros and suffers from cons to some extent. In this section, the details will be provided to guide readers to choose the best tool to characterize axis curves. Note that in this thesis, we focus on planar axis curves.

3.2.1 Cartesian coordinate system

Cartesian coordinate system is the most commonly used coordinate system in many engineering areas. To define the axis curves, any differentiable function within an interval of the independent variable could be used to define a beam axis:

$$y = f(x);\ x \in [\underline{x}, \bar{x}] \tag{3.1}$$

Obviously, it's intuitively straightforward and handy to do so as graphically shown in Fig. 3.2a (for simplicity, $\underline{x} = 0$). However, it turns out to be impossible to define some specific axis curves just by one function. For example, in Fig.

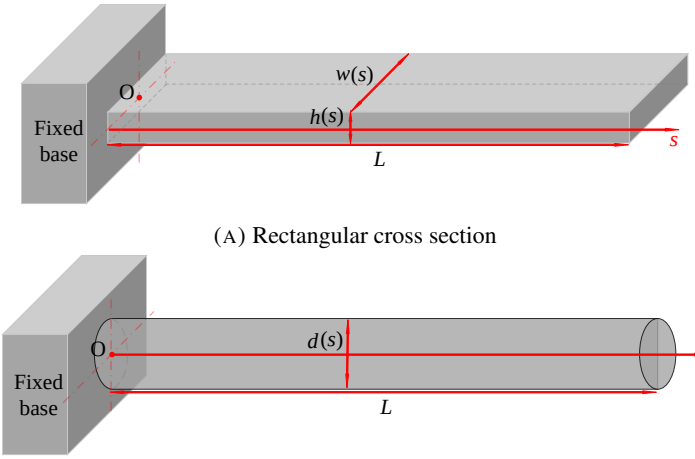

(A) Rectangular cross section

(B) Round cross section

FIGURE 3.1: Geometrical definition of cross sections of beams

3.2b, the curve is defined within $x \in [\underline{x}, \bar{x}]$ but we can clearly see that between $[x_A, \bar{x}]$, any x corresponds to two function values (such as points B and C). We could still stick to Cartesian coordinate system here and use more than one function to define the axis curves under a piecewise framework. Specifically, in Fig. 3.2b, we can use $f_1(x)$ defined within $x \in [\underline{x}, \bar{x}]$ and $f_2(x)$ (highlighted in blue) defined within $x \in [x_A, \bar{x}]$ as the whole axis curve. Honestly speaking, this is feasible but a little bit complex and user-unfriendly.

For other information of the curve defined in Cartesian coordinate system, we have the expression for the initial curvature:

$$\kappa_o(x) = \frac{1}{R(x)} = \frac{\frac{\mathrm{d}^2 y}{\mathrm{d}x^2}}{[1 + (\frac{\mathrm{d}y}{\mathrm{d}x})^2]^{3/2}} \tag{3.2}$$

where R denotes radius of curvature. For curve length, we have:

$$L = \int_{\underline{x}}^{\bar{x}} \sqrt{1 + (\frac{\mathrm{d}y}{\mathrm{d}x})^2}\mathrm{d}x \tag{3.3}$$

where L denotes the length of the axis curve, equivalently the beam length as well.

3.2.2 Polar coordinate system

For the cases shown in Fig. 3.2b, polar coordinate system can serve as a possible alternative. Also as a commonly-used coordinate system, it is very useful in cases where the relationship between two points is most easily expressed

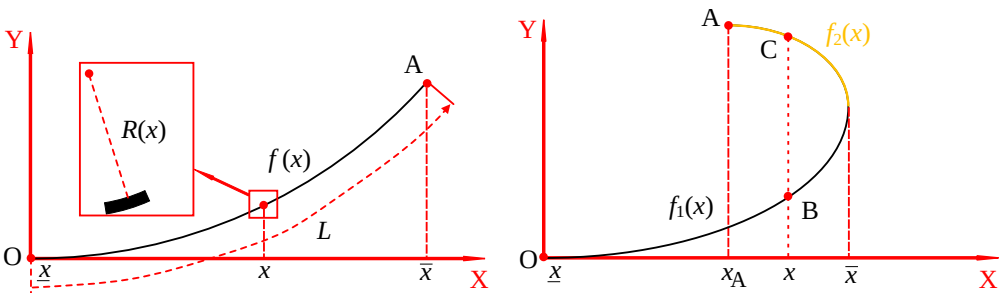

(A) Defining an axis curve by a function in Cartesian coordinate system

(B) The axis curve that needs to be defined by multiple functions in Cartesian coordinate system

FIGURE 3.2: Definition of axis curves in Cartesian coordinate system

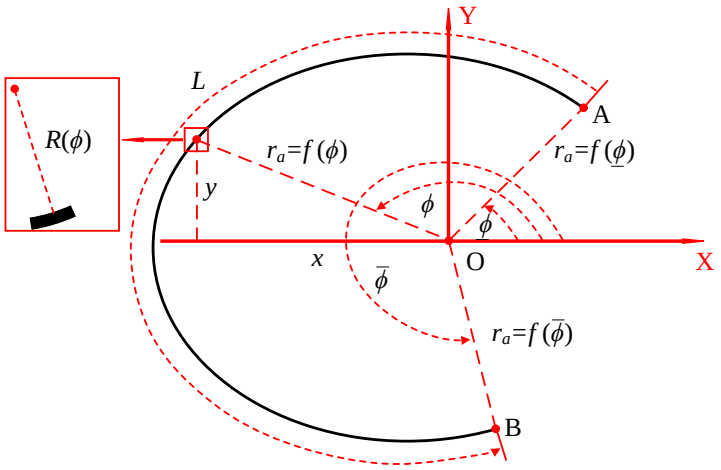

FIGURE 3.3: Definition of axis curves in polar coordinate system

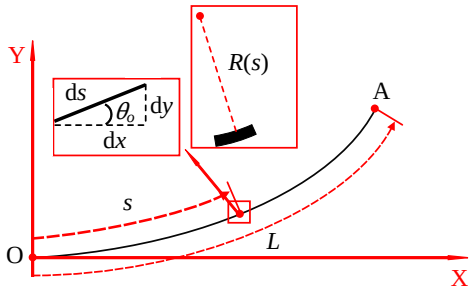

FIGURE 3.4: Definition of axis curves in body frame

in terms of angles and distance as shown in Fig. 3.3. The formulation can be expressed as:

$$r_a = f(\phi);\ \phi \in [\underline{\phi}, \bar{\phi}] \tag{3.4}$$

with

$$x(\phi) = r_a \cos\phi; \quad y(\phi) = r_a \sin\phi \tag{3.5}$$

Obviously, (3.4) and (3.5) can serve as a better tool than (3.1) to characterize the type of axis curves in Fig. 3.2b where the case of point B and point C can be perfectly expressed in Fig. 3.3. To characterize the initial curvature, we have:

$$\kappa_o(\phi) = \frac{1}{R(\phi)} = \frac{|r_a^2 + 2(\frac{\mathrm{d}r_a}{\mathrm{d}\phi})^2 - r_a\frac{\mathrm{d}^2 r_a}{\mathrm{d}\phi^2}|}{[r_a^2 + (\frac{\mathrm{d}r_a}{\mathrm{d}\phi})^2]^{\frac{3}{2}}} \tag{3.6}$$

Then, the curve length, equivalently the beam length as well L, can be formulated as:

$$L = \int_{\underline{\phi}}^{\bar{\phi}} \sqrt{r_a^2 + (\frac{\mathrm{d}r_a}{\mathrm{d}\phi})^2}\mathrm{d}\phi \tag{3.7}$$

3.2.3 Body frame

The last and the most important coordinate system is body frame, which is commonly used in soft robotics (Craig, 2005)(Renda et al., 2018). The reason why it's considered as the most important one is that the large-deflection analysis is directly based on this coordinate system (Wu and Zheng, 2022a)(Wu and Zheng, 2022b)(Wu and Zheng, 2022d). In body frame, we define the initial rotation angle θ_o as a function of s (see Fig. 3.4).

$$\theta_o(s) = f(s);\ s \in [0, L] \tag{3.8}$$

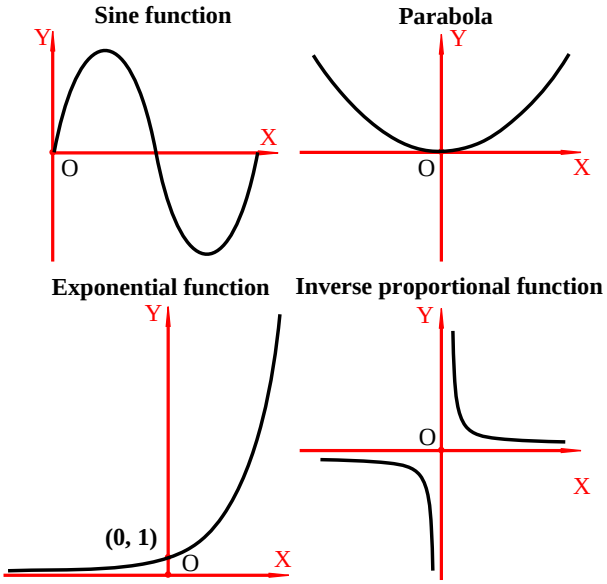

FIGURE 3.5: Curves defined in Cartesian coordinate system

with

$$\frac{\mathrm{d}x}{\mathrm{d}s}(s) = \cos\theta_o(s);\ \frac{\mathrm{d}y}{\mathrm{d}s}(s) = \sin\theta_o(s) \tag{3.9}$$

According to (3.9), the coordinates of the fabricated shape of the studied beam can be characterized via

$$x(s) = \int_0^s \cos\theta_o(\xi)\mathrm{d}\xi;\ y(s) = \int_0^s \sin\theta_o(\xi)\mathrm{d}\xi,\quad s \in [0, L] \tag{3.10}$$

According to the definition of curvature, we have the expression for the initial curvature κ_o:

$$\kappa_o(s) = \frac{1}{R(s)} = \frac{\mathrm{d}\theta_o}{\mathrm{d}s}(s) \tag{3.11}$$

where R denotes the initial radius of curvature as shown in Fig. 3.4. Logically, (3.10) and (3.11) can better deal with the case in Fig. 3.2b than (3.1) since the independent variable s is defined along the beam axis which avoids directly using the variables x and y.

3.2.4 Insights into the three coordinate systems regarding defining axis curves

As introduced above, the three different coordinate systems have pros and cons respectively. This section aims to clarify how to choose the the most proper coordinate system in terms of defining an axis curve in different practical cases. Generally speaking, designing the axis curves of flexible beams essentially lies in two scenarios: **designing axis curves without constraints** and **designing axis curves under constraints**.

3.2.4.1 Designing axis curves without constraints

In terms of freely designing an axis curve, we would like to state that it totally depends on the user habits. The one that meets users' tastes or needs would logically and sometimes intuitively improve the efficiency and creativity of design process. For example, the exact shapes of some curves can be directly expressed in Cartesian coordinate system by transcendental functions ($\sin(x)$, e^x, $\log(x)$ and so on) and algebraic functions (like polynomial functions of different order). Even if the designer wants to freestyle a bit by hand, one can just collect the Cartesian coordinates and use a polynomial to fit the curve as long as the drawn curve can be assumed continuous and differentiable (according to Weierstrass theorems (Stone, 1948)). **Note that** we don't normally consider axis curves that are not differentiable since it can easily cause stress concentration under deflection. If this is a must in some circumstances, we can use more than one polynomials to piecewise approximate and fit the curve. Some representative curves defined in Cartesian coordinate system are shown in Fig. 3.5.

In polar coordinate system, it's handy to define some classic curves like Cardioids, Lemniscates, rose curves and Archimedes' spirals (see Fig. 3.6) whereas they are difficult and not quite easy-to-implement to directly define in the other two coordinate systems. The expressions for the mentioned curves defined in polar coordinate system are as follows:

$$\begin{aligned}
\textbf{Cardioid} &: r_a = a \pm b\cos\phi;\ r = a \pm b\sin\phi \\
\textbf{Lemniscate} &: r_a^2 = a^2\cos 2\phi;\ r^2 = a^2\sin 2\phi \\
\textbf{Rose curve} &: r_a = a\cos n\phi;\ r = a\sin n\phi \\
\textbf{Archimedes' spiral} &: r_a = a + b\phi
\end{aligned} \tag{3.12}$$

where a, b and n are constant values. Under this framework, one of the key features of this coordinate system lies in the exact geometrical relationship between two points by using a physical length and a rotation angle. In body

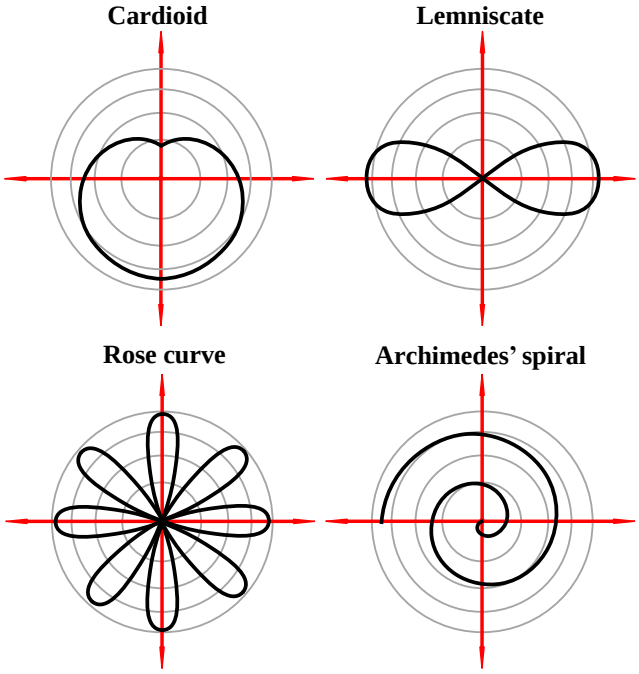

FIGURE 3.6: Classic curves defined in polar coordinate system

frame, we can directly focus on the curvature and the axis length to define a curve via (3.8) and (3.11). In terms of the curvature design, we have constant-curvature curves (which are circles) and varying-curvature curves (essentially defining the curvature as a function of s). For example, the initial curvature expressions of two representative curves shown in Fig. 3.7 are formulated below:

$$\begin{aligned}
\textbf{Constant-curvature curve} &: \kappa_o(s) = \frac{1}{R(s)} = a \\
\textbf{Varying-curvature curve} &: \kappa_o(s) = \frac{1}{R(s)} = \frac{1}{a + bs^2}
\end{aligned} \tag{3.13}$$

where a is constant. As shown in Fig .3.7, it's just easy to notice that the curvature of the left curve stays constant whereas that of the right one gradually decreases, which also corresponds to (3.13). Besides, we can also directly choose the axis length as a geometrical constraint via (3.8) as well in this coordinate system. As stated above, the curves defined in Cartesian and polar coordinate systems both utilize the exact geometrical information (like lengths and angles), which are physically intuitive and clear. Logically, the curvature and the curve length are passively generated due to the exact geometric definition of curves. Then, if we have some special needs for the axis curvature and the axis length, we can define the curves in body frame instead where the users can directly adjust these mentioned geometric properties. Therefore, depending on different design requirements, we can always choose the most suitable one among the aforementioned three options to define a curve.

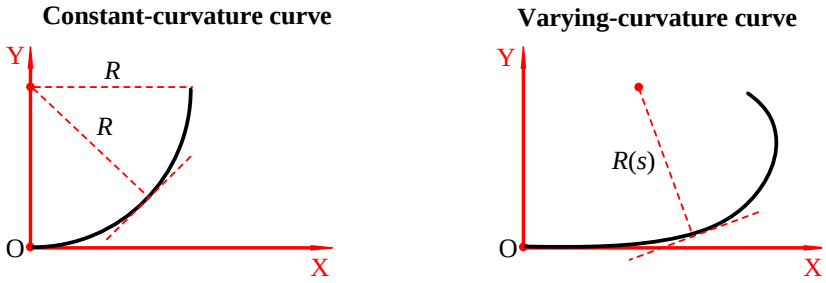

FIGURE 3.7: Curves defined in body frame

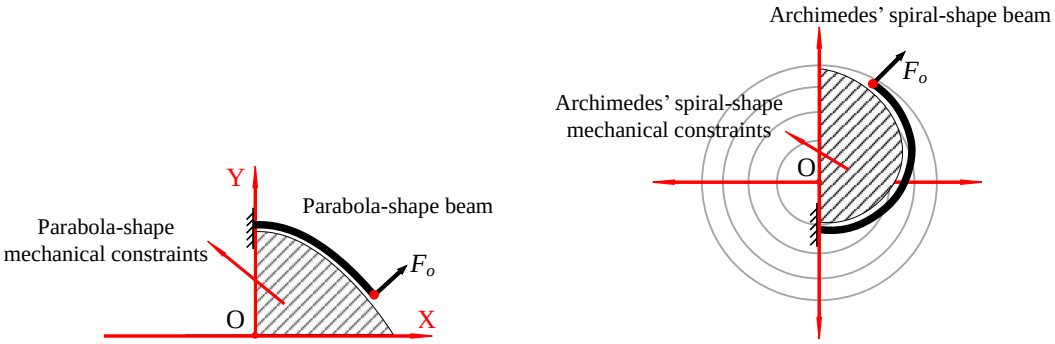

(A) Mechanical constraints defined in Cartesian coordinate system

(B) Mechanical constraints defined in polar coordinate system

FIGURE 3.8: Definition of axis curves under mechanical constraints

3.2.4.2 Designing axis curves under constraints

As discussed above, we have presented the scenario of defining an axis curve without constraints in different coordinate systems. However, in engineering, we always have **constraints** to consider. Specifically in CMs, no matter avoiding mechanical contact or utilizing mechanical interference, it's always essential to take care of these mechanical constraints.

In the mentioned two cases, mechanical constraints, normally defined in Cartesian coordinate system and polar coordinate system (since they are more geometrically intuitive and clear), play a major role in this design process (no matter by intuitiveness and creativity or under optimization framework). Logically, the problem of defining axis curves in different coordinate systems is somehow transformed into choosing a proper function for the axis curve in the respective coordinate systems to satisfy these constraints. Examples in Cartesian coordinate system and polar coordinate system are shown in Fig. 3.8. Obviously, for curves defined in body frame, we can not directly link them to the mechanical constraints expressed in Cartesian coordinate system and polar coordinate system. Therefore, we always need to transform and express the curves into Cartesian coordinate system via (3.10). In that sense, directly defining curves in Cartesian coordinate system and polar coordinate system to consider mechanical constraints expressed in the corresponding coordinate system may be more handy and straightforward.

Generally speaking, facing different needs, we can choose the most proper coordinate system to meet our design requirements. After the definition of beam shapes (the axis curve and the cross section), the next step is to analyze beam deflections. As is well-known in the state-of-the-art, many beam theories and rod theories are used to analyze the deflection of beams based on body frame (Renda et al., 2018)(Wu and Zheng, 2022a). Therefore, the transformation of curves from other coordinate systems to body frame turns out to be important, which is also one of the focuses in this section.

3.2.5 Transformation from other coordinate systems to body frame

As mentioned above, users may define the beam geometry (beam axis) in each of the aforementioned three coordinate systems. However, they all have to be transformed into body frame for large-deflection analysis. Here, we can still formulate the transformation process as looking for solutions to some specific ODEs. The details about solving the problem are presented in Section 4.2.

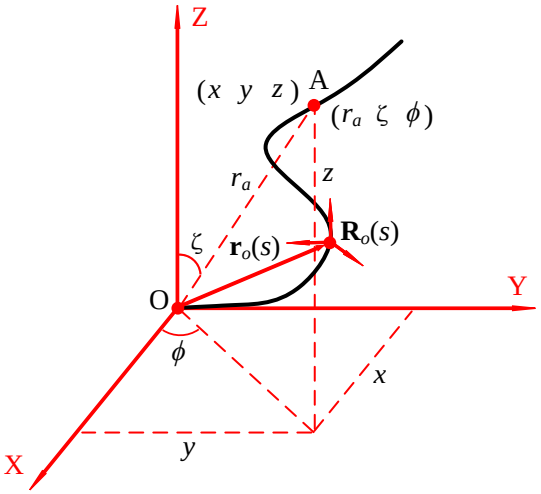

FIGURE 3.9: Spatial curves defined in 3D coordinate systems

3.2.5.1 From Cartesian coordinate system to body frame

Supposing we have designed a curve $y(x)$ in Cartesian coordinate system, we then transfer the exact shape into body frame where we look for a function $\theta_o(s)$ used to express the same shape. Obviously, the link is that they can both be expressed in Cartesian coordinate system so we have the following relationship:

$$\begin{bmatrix} \int_0^{\int_{\underline{x}}^{x} \sqrt{1+(\frac{\mathrm{d}y}{\mathrm{d}t}(t))^2}\mathrm{d}t} \sin\theta_o(s)\mathrm{d}s - y(x) \\ \int_0^{\int_{\underline{x}}^{x} \sqrt{1+(\frac{\mathrm{d}y}{\mathrm{d}t}(t))^2}\mathrm{d}t} \cos\theta_o(s)\mathrm{d}s - x \end{bmatrix} = \begin{bmatrix} 0 \\ 0 \end{bmatrix}, \quad x \in [\underline{x}, \bar{x}] \tag{3.14}$$

where $\theta_o(s)$ is the desired unknown function as well as the solution to (3.14).

3.2.5.2 From polar coordinate system to body frame

Likewise, the curve defined in polar coordinate system can be also transformed into body frame where the links is formulated as below:

$$\begin{bmatrix} \int_0^{\int_{\underline{\phi}}^{\phi} \sqrt{r_a(t)^2+(\frac{\mathrm{d}r_a}{\mathrm{d}t}(t))^2}\mathrm{d}t} \cos\theta_o(s)\mathrm{d}s - r_a(\phi)\cos\phi \\ \int_0^{\int_{\underline{\phi}}^{\phi} \sqrt{r_a(t)^2+(\frac{\mathrm{d}r_a}{\mathrm{d}t}(t))^2}\mathrm{d}t} \sin\theta_o(s)\mathrm{d}s - r_a(\phi)\sin\phi \end{bmatrix} = \begin{bmatrix} 0 \\ 0 \end{bmatrix}, \quad \phi \in [\underline{\phi}, \bar{\phi}] \tag{3.15}$$

where, similarly, $\theta_o(s)$ is the desired unknown function as well as the solution to (3.15).

3.2.6 From 2D to 3D: defining the geometry of 3D beams

In terms of defining the geometry of 3D beams, it is logical for us to consider using functions of two variables in the respective coordinate systems, such as

$$z = f(x, y) \tag{3.16}$$

defined a 3D Cartesian coordinate system (see Figure 3.9), and

$$r_a = f(\phi, \zeta) \tag{3.17}$$

defined in the spherical coordinate system (see Figure 3.9). Besides, to define the geometry of 3D slender rods in local coordinate system needs the geometrical representation (1.22) used in Cosserat rod theory (see Figure 3.9). Note that (3.16), (3.17) and (1.22) share the same link (where they can be expressed in 3D Cartesian coordinate system) as the 2D one so we can also formulate the 3D geometry transformation among different coordinate systems as problems of solving ODEs like (3.14) and (3.15).

3.3 Moment balance via Newtonian mechanics

With geometrical definition of slender beams ready, we can then move onto the analysis of large deflections. In this thesis, we present two ways to handle the problem: one is Newtonian mechanics, and the other is Lagrangian mechanics (will be discussed in Section 3.4). Newtonian mechanics is based on the application of Newton's Laws of motion where the exerted forces on the object and the motion of the object are studied in detail. For the analysis of statics, the equilibrium state of each particle in the studied system are analyzed accordingly. In this section, we first present geometrically nonlinear Euler Bernoulli Beam theory which clarifies that the moment balance along the beam along with the constitutive relationship serves as the core for modeling large deflections of slender beams. Via this beam theory, three major types of large-deflection problems are discussed followed by the nondimensionalization of the governing equation. Then, we present the detailed derivation of the reduced-mode Cosserat rod model for large-planar-deflection problems where bending, axial and shear strains are all considered. Finally, we move forward to propose two strategies to handle the full-mode Cosserat rod model.

3.3.1 Geometrically nonlinear Euler Bernoulli beam theory

Regarding modeling the deflection of a slender beam, we need to extend the geometrically nonlinear Euler-Bernoulli beam equation from (1.16):

$$EI(s)(\kappa(s)-\kappa_o(s))=M(s) \tag{3.18}$$

with

$$\kappa(s)=\frac{\mathrm{d}\theta}{\mathrm{d}s};\ \kappa_o(s)=\frac{\mathrm{d}\theta_o}{\mathrm{d}s}=\frac{1}{R(s)} \tag{3.19}$$

where $\theta(s)$, $\theta_o(s)$, E, $I(s)$, $\kappa(s)$, $\kappa_o(s)$, $R(s)$ and $M(s)$ denote the current rotation angle, the initial rotation angle, the Young's modulus, the second moment of inertia of cross sections, the current curvature, the initial curvature, the initial radius of curvature and the exerted moment along the beam axis. Note that $I(s)$ and $\kappa_o(s)$ could be functions of s due to the fabricated geometries of the studied beams. Clearly, (3.18) and (3.19) assume the linear relationship between the rotational strain $(\kappa(s)-\kappa_o(s))$ and the exerted moment $M(s)$ at s, which essentially is a typical formulation of Hooke's law. In the following, we focus on the three types of large deflection of slender beams: general large deflection, (post)-buckling and contact problems since they are very common during the operation of CMs (Howell, 2013a)(Wu and Zheng, 2022d). In the final part of Section 3.3.1, the nondimensionalization of the governing BVPs is presented to reveal its mathematical essence which lays the foundation for applying mathematical tools (stated in Chapter 4) for solving the developed models in the following.

3.3.1.1 General large deflection

Commonly speaking, in most cases, the studied beams subjected to different loading conditions normally only have one deflected shape, which means that the corresponding BVPs only have one solution for each case from a mathematical point of view. In Euler Bernoulli beam theory, we have the following geometrical relationships:

$$\frac{\mathrm{d}x}{\mathrm{d}s}(s)=\cos\theta(s);\ \frac{\mathrm{d}y}{\mathrm{d}s}(s)=\sin\theta(s) \tag{3.20}$$

Logically, according to (3.20), we can characterize the deflected beam shape via:

$$x(s)=\int_0^s\cos\theta(\xi)\mathrm{d}\xi;\ y(s)=\int_0^s\sin\theta(\xi)\mathrm{d}\xi,\quad s\in[0,L] \tag{3.21}$$

In the following, we present two most common cases of general large deflection: a slender straight beam and a slender beam of varying initial curvature subjected to beam-end loading conditions respectively. Besides, in Remark 3, we extend the case to a more general one where different loading conditions and different beam geometries are considered, which yields a relatively more complex BVP that defines this comprehensive scenario.

1. **A slender straight beam subjected to beam-end loading**
   Here, we start with the simplest case: a slender straight beam of constant cross sections subjected to pure

beam-end loading, as shown in Fig. 3.10. Obviously, we have

$$\kappa_o(s) = 0;\ \frac{\mathrm{d}I}{\mathrm{d}s}(s) = 0$$

Therefore,

$$EI\kappa(s) = EI\frac{\mathrm{d}\theta}{\mathrm{d}s} = M(s) = F_y(x(L) - x(s)) + F_x(y(L) - y(s)) + M_o \tag{3.22}$$

Differentiating (3.22), we will be able to arrive at:

$$\frac{\mathrm{d}^2\theta}{\mathrm{d}s^2} = -\frac{F_y}{EI}\cos\theta(s) - \frac{F_x}{EI}\sin\theta(s) \tag{3.23}$$

where the relationships in (3.20) are utilized. Besides, as shown in Fig. 3.10, the beam is horizontally fixed at the base, and we can derive one boundary condition from (3.22) when $s = L$, so we can reach:

$$\theta(0) = 0;\ \frac{\mathrm{d}\theta}{\mathrm{d}s}(L) = \frac{M_o}{EI} \tag{3.24}$$

Then, we will have the following BVP using (3.23) and (3.24):

$$\begin{aligned} &\text{D.E.} \quad \frac{\mathrm{d}^2\theta}{\mathrm{d}s^2} = -\frac{F_y}{EI}\cos\theta(s) - \frac{F_x}{EI}\sin\theta(s) \\ &\text{B.C.} \quad \theta(0) = 0 \\ &\qquad \frac{\mathrm{d}\theta}{\mathrm{d}s}(L) = \frac{M_o}{EI} \end{aligned} \tag{3.25}$$

which is the most commonly studied case in CM research community (Howell, 2013a).

2. **A slender beam of varying initial curvature subjected to beam-end loading**

Here in this section, we focus on another common case: a slender ICB of initial curvature (see Fig. 3.11) subjected to beam-end loading, which leads to the following constraints:

$$\frac{\mathrm{d}I}{\mathrm{d}s}(s) = 0;\ \frac{\mathrm{d}\kappa_o}{\mathrm{d}s} \in \mathrm{C}^1$$

with

$$\kappa_o(s) = \frac{1}{R(s)}$$

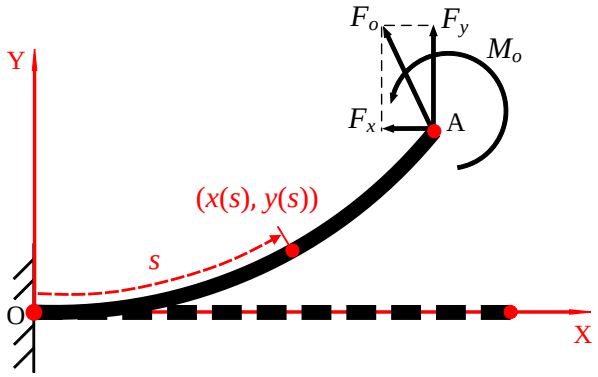

FIGURE 3.10: A slender straight beam subjected to beam-end loading

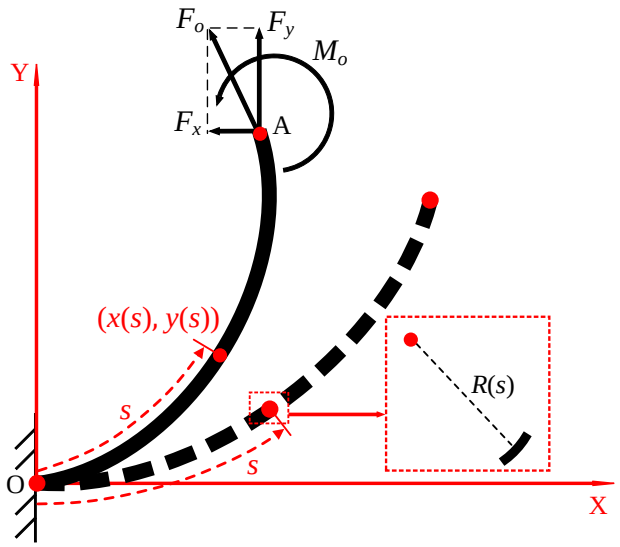

FIGURE 3.11: A slender beam of initial curvature subjected to beam-end loading

Obviously, the beam has an initial radius along the beam axis:

$$\frac{\mathrm{d}R}{\mathrm{d}s}(s) \in \mathbb{C}^1;\ R(s) \neq 0$$

Therefore,

$$EI(s)(\kappa(s) - \kappa_o(s)) = EI(s)(\frac{\mathrm{d}\theta}{\mathrm{d}s} - \kappa_o(s)) = M(s) = F_y(x(L) - x(s)) + F_x(y(L) - y(s)) + M_o \tag{3.26}$$

Arranging (3.26), we have:

$$EI\frac{\mathrm{d}\theta}{\mathrm{d}s} = F_y(x(L) - x(s)) + F_x(y(L) - y(s)) + M_o + EI\kappa_o(s) \tag{3.27}$$

Differentiating (3.27), we will be able to arrive at:

$$\frac{\mathrm{d}^2\theta}{\mathrm{d}s^2} = -\frac{F_y}{EI}\cos\theta(s) - \frac{F_x}{EI}\sin\theta(s) + \frac{\mathrm{d}\kappa_o}{\mathrm{d}s}(s) \tag{3.28}$$

According to Fig. 3.11, the corresponding boundary conditions are formulated as below:

$$\theta(0) = 0;\ \frac{\mathrm{d}\theta}{\mathrm{d}s}(L) = \frac{M_o}{EI} + \kappa_o(L) \tag{3.29}$$

Logically, we can obtain the following BVP rearranging (3.28) and (3.29):

$$\begin{aligned} &\text{D.E.} \quad \frac{\mathrm{d}^2\theta}{\mathrm{d}s^2} = -\frac{F_y}{EI}\cos\theta(s) - \frac{F_x}{EI}\sin\theta(s) + \frac{\mathrm{d}\kappa_o}{\mathrm{d}s}(s) \\ &\text{B.C.} \quad \theta(0) = 0 \\ &\qquad \frac{\mathrm{d}\theta}{\mathrm{d}s}(L) = \frac{M_o}{EI} + \kappa_o(L) \end{aligned} \tag{3.30}$$

Remark 3 *The above two cases are the most common ones in CMs. However, we can also consider pressure, distributed loading (gravity), distributed loading, varying cross sections and so on (see details in Wu and Zheng,*

2022a).

$$\begin{aligned} M(s) =& F_y(x(L)-x(s)) + F_x(y(L)-y(s)) + M_o + M^*(s) - \int_s^L q_y(s)[x(\gamma)-x(s)]\mathrm{d}\gamma \\ &+ \int_s^L q_x(s)[y(\gamma)-y(s)]\mathrm{d}\gamma + \int_s^L q_n(s)(x(\gamma)-x(s))\cos\theta(\gamma)\mathrm{d}\gamma \\ &+ \int_s^L q_n(s)(y(\gamma)-y(s))\sin\theta(\gamma)\mathrm{d}\gamma \end{aligned} \tag{3.31}$$

where q_x q_y, q_n and M^* denote distributed loading, pressure, distributed moment. Rearranging Eq. (3.18) and Eq. (3.31), we will end up with:

$$\begin{aligned} EI(s)\frac{\mathrm{d}\theta}{\mathrm{d}s} =& F_y(x(L)-x(s)) + F_x(y(L)-y(s)) + M_o + M^*(s) - \int_s^L q_y(s)[x(\gamma)-x(s)]\mathrm{d}\gamma \\ &+ \int_s^L q_x(s)[y(\gamma)-y(s)]\mathrm{d}\gamma + \int_s^L q_n(s)(x(\gamma)-x(s))\cos\theta(\gamma)\mathrm{d}\gamma \\ &+ \int_s^L q_n(s)(y(\gamma)-y(s))\sin\theta(\gamma)\mathrm{d}\gamma + EI(s)\kappa_o(s) \end{aligned} \tag{3.32}$$

Differentiating (3.32) results in:

$$\begin{aligned} E\frac{\mathrm{d}I}{\mathrm{d}s}\frac{\mathrm{d}\theta}{\mathrm{d}s} + EI(s)\frac{\mathrm{d}^2\theta}{\mathrm{d}s^2} =& -(F_y\cos\theta(s) + F_x\sin\theta(s)) + \frac{\mathrm{d}M^*(s)}{\mathrm{d}s} + q_y(s)\cos\theta(s)(L-s) \\ &+ \frac{\mathrm{d}q_y}{\mathrm{d}s}x(s)(L-s) + \frac{\mathrm{d}q_y}{\mathrm{d}s}\int_L^s\int_0^\gamma \cos\theta(\xi)\mathrm{d}\xi\mathrm{d}\gamma + q_x(s)\sin\theta(s)(s-L) \\ &+ \frac{\mathrm{d}q_x}{\mathrm{d}s}y(s)(s-L) + \frac{\mathrm{d}q_x}{\mathrm{d}s}\int_s^L\int_0^\gamma \sin(\theta(\xi))\mathrm{d}\xi\mathrm{d}\gamma + q_n(s)\cos\theta(s)\int_L^s\cos\theta(\xi)\mathrm{d}\xi \\ &+ \frac{\mathrm{d}q_n}{\mathrm{d}s}x(s)\int_L^s\cos\theta(\xi)\mathrm{d}\xi + \frac{\mathrm{d}q_n}{\mathrm{d}s}\int_s^L\int_0^\gamma \cos\theta(\xi)\mathrm{d}\xi\cos\theta(\gamma)\mathrm{d}\gamma \\ &+ q_n(s)\sin\theta(s)\int_L^s\sin\theta(\xi)\mathrm{d}\xi + \frac{\mathrm{d}q_n}{\mathrm{d}s}y(s)\int_L^s\sin\theta(\xi)\mathrm{d}\xi \\ &+ \frac{\mathrm{d}q_n}{\mathrm{d}s}\int_s^L\int_0^\gamma \sin\theta(\xi)\mathrm{d}\xi\sin\theta(\gamma)\mathrm{d}\gamma + E(\frac{\mathrm{d}I(s)}{\mathrm{d}s}\kappa_o(s) + \frac{\mathrm{d}\kappa_o(s)}{\mathrm{d}s}I(s)) \end{aligned} \tag{3.33}$$

subjected to the following two boundary conditions:

$$\begin{aligned} &B.C.\ \ \theta(0) = 0 \\ &\frac{\mathrm{d}\theta}{\mathrm{d}s}(L) = \frac{M_o}{EI(L)} + \frac{1}{R(L)} \end{aligned} \tag{3.34}$$

In summary, for a slender beam subjected to different loading conditions, we can describe its large deflection subjected to different loading conditions (as shown in Fig. 3.12) via (3.33) and (3.34), which is a highly nonlinear BVP. However, if the axial load, such as F_x, reaches the buckling limit, we can not directly handle the problem via (3.33) and (3.34) since multi solutions to the studied BVP exist. These special cases about buckling and post-buckling are studied in detail in the next section.

3.3.1.2 Buckling and post-buckling

However, in some circumstances, such as **buckling and post-buckling**, the flexible beams subjected to the same loading will yield more deflected shapes, which is totally different from the general deflection stated in Section 3.3.1.1. In other words, mathematically speaking, the corresponding governing BVPs will have multi-solutions when subjected to the same constraints. Now, we start with some insights into this special type of physical phenomena.

- **From an engineering perspective:**
  Flexible slender beams will present more diverse mechanical responses if buckling or post-buckling behavior

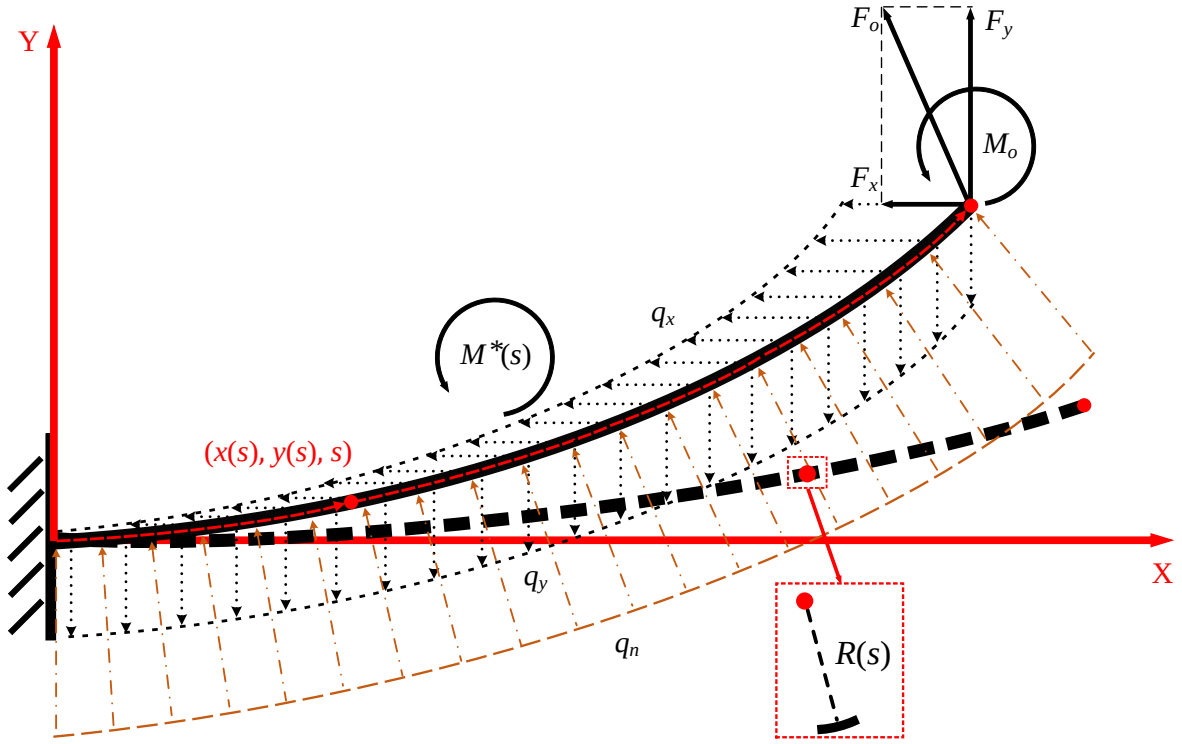

FIGURE 3.12: A slender beam subjected to external loading via Newtonian framework

occurs. Essentially, a slender beam tends to buckle into an unstable state if the axial loading reaches its critical value or equivalently its buckling limit, which is mainly due to imperfect geometry and off-axial loading or some external factors (Jones, 2006). In all the mentioned scenarios, the lateral deformation will immediately occur and then sharply increase if the axial force is beyond the buckling limit (Lacarbonara, 2008). From an engineering point of view, the 'instability' nature of buckling would lie in the following three aspects: the sharply decreasing axial stiffness, the rapidly increasing lateral displacement and the unpredictable situations after the axial load reaches the critical load as it normally has three potential choices: one buckled state, another buckled state with symmetric geometry and even the unbuckled equilibrium state (axially equilibrium state). For more theoretical details about buckling and post-buckling, the mentioned references here (Brush, Almroth, and Hutchinson, 1975) are recommended.

However, this 'instability' nature would also present benefits if dialectically treating and making most of it. For example, slender structures used in civil engineering, marine engineering and aircraft engineering have therefore drawn a huge concern regarding elastic instability that may cause structural failure (Timoshenko and Gere, 2009), which has to be avoided. On the other hand, the unique characteristics of buckling and post-buckling can also be masterly utilized in some mechanical applications, such as bi-stable or multi-stable compliant mechanisms (Chen and Ma, 2015). Here, we would like to characterize and **take advantages of these phenomena rather than simply avoid them** as the diverse mechanical response of buckling and post-buckling states would surely enrich some unexpectedly positive possibilities of current CMs.

- **The essence:**
  The buckling theory has been intensively investigated since linear buckling theory (Euler buckling) was derived by Euler in 1744 (Euler, 1744) and further refined for higher modes by Lagrange in 1770 (Lagrange, 1770). It's **worth noting** that the mentioned two authors both concluded their findings based on the famous beam equation by Bernoulli (Todhunter, 1893), which is (3.18). In this thesis, we only consider the buckling and post-buckling of slender straight beams, so we can simplify and differentiate (3.18):

$$E\frac{\mathrm{d}I}{\mathrm{d}s}(s)\frac{\mathrm{d}\theta}{\mathrm{d}s}(s) + EI(s)\frac{\mathrm{d}^2\theta}{\mathrm{d}s^2}(s) = \frac{\mathrm{d}M}{\mathrm{d}s}(s) \tag{3.35}$$

  Obviously, Eq. (3.35) is an ordinary differential equation (ODE) with respect to s to describe the change of θ

along s for $s \in [0, L]$. With different conditions defined at the point $s = 0$ and $s = L$, Eq. (3.35) becomes as a typical two-point boundary value problem (BVP). Mathematically, the existence of solution for a general BVP is a difficult problem. However, due to the fact that (3.35) arises from engineering applications, therefore it is well-posed with different but coherent boundary conditions (B.C.), which are determined by variant end-support cases of beams, as shown in Fig. 3.13: free end, pinned end, roller, fixed end, sliding end, etc. Summarizing what we have stated above, buckling problem is essentially to analyze a two-point BVP (3.35). To be more specific, we briefly present two representative cases for buckling and post-buckling problems respectively. First, as shown in Fig. 3.14a, the studied slender beam of constant cross sections is subjected to an axial load F_x and different B.C., which yields the following BVP:

$$\begin{aligned} &\text{D.E.} \quad \frac{\mathrm{d}^2\theta}{\mathrm{d}s^2} = -\frac{F_x}{EI}\sin\theta, \quad s \in [0, L] \\ &\text{B.C.} \quad g\left(\theta(0), \theta'(0), \theta(L), \theta'(L)\right) = 0 \end{aligned} \tag{3.36}$$

where $g \in \mathbb{R}^2$ represents different independent boundary conditions defined at $s = 0$ and $s = L$. Unlike buckling problem shown in Fig. 3.14a where only the axial force F_x exists, post-buckling problems might contain external F_y and M_o (see Fig. 3.14b), and this can be formulated as follows:

$$\begin{aligned} &\text{D.E.} \quad \frac{\mathrm{d}^2\theta}{\mathrm{d}s^2} = -\frac{F_y}{EI}\cos\theta - \frac{F_x}{EI}\sin\theta \\ &\text{B.C.} \quad g\left(\theta(0), \theta'(0), \theta(L), \theta'(L)\right) = 0 \end{aligned} \tag{3.37}$$

Note that both in Fig. 3.14a and Fig. 3.14b, the red dash line boxes suggest that different boundary conditions defined in BVPs (3.36) and (3.37). We would like to emphasize that BVPs (3.36) and (3.37) may have different solutions under the same boundary conditions, which in this case corresponds to the different geometries of the slender beam subjected to an axial load F_x above some buckling limit (see Fig. 3.14). Essentially speaking, this is because BVP (3.36) has gone through a *bifurcation phenomenon*, and we would like to briefly recall the definition of *bifurcation* (Chow and Hale, 2012) here:

Definition 1 *In dynamical system described by an ODE as* $\frac{dx}{dt} = f(x, p)$ *with* $x \in \mathbb{R}^{n_x}$ *and* $p \in \mathbb{R}^{n_p}$, *a bifurcation solution to* x *occurs when a small smooth change of* p *causes a sudden "qualitative" or topological change of* x *in its behavior.*

In our case, BVP (3.36) can be regarded as the *dynamical system* as we can always consider BVP (3.36) as a dynamical system with respect to s. In such an ODE, *bifurcation parameter* refer to the axial loading F_x which may trigger the *sudden "qualitative" or topological change of* θ. This definition theoretically explains the possible sudden and rapid geometry change of slender structures when the axial load reaches the critical limit, which is termed as *buckling*. Therefore, BVP (3.36) can describe the buckling phenomenon as shown in Fig. 3.14a: the buckled beam will always have two potential geometries (see Geometry 1 and Geometry 3) and more importantly it is also possible for the beam to stay axially equilibrium (Geometry 2). Note that we don't consider any imperfection of the studied beam here, but if we do (for instance, a small initial curvature of the beam), logically the beam will result in some buckled state, such as Geometry 1 and Geometry 3 in Fig. 3.14a.

Supposing the beam has buckled and presented the potential Geometry 1 or Geometry 3 as displayed in Fig. 3.14a, the beam will go through post-buckling phenomenon subjected to some extra beam-end loading conditions (F_y and M_o) and eventually reaches Geometry A or Geometry B respectively as shown in Fig. 3.14a. Obviously, BVP (3.37) can be utilized to describe this post-buckling behavior. A bifurcation diagram (Fig.

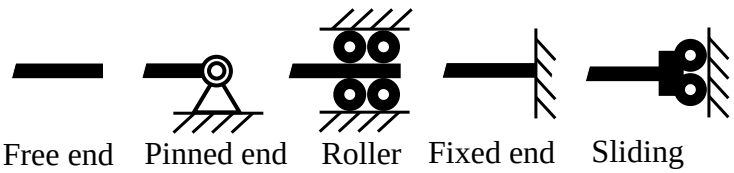

FIGURE 3.13: Different types of beam ends

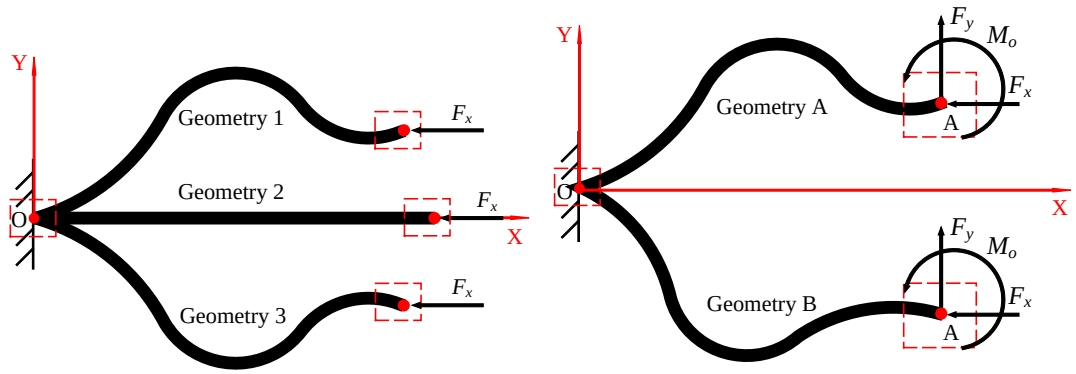

(A) Buckling geometry (B) Post-buckling geometry

FIGURE 3.14: Schematic geometry of (post)-buckling of a slender beam

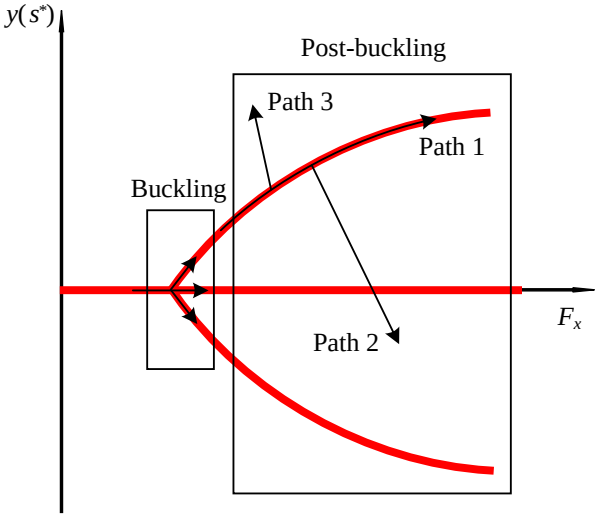

FIGURE 3.15: Schematic bifurcation diagram of (post)-buckling

3.15) is used to explain the process of buckling and post-buckling where in particular Path 1 is due to the continuous increase of F_x whereas Path 2 and Path 3 are possibly the results of the combined loading conditions F_x, F_y and M_o. Note that there always exists a point $s^* \in [0, L]$ such that the lateral displacement of this point $y(s^*)$ will go through a bifurcation phenomenon as shown in Fig. 3.14a and Fig. 3.14b.

1. **A slender straight beam subjected to an axial load**

   This case aims to study a slender beam with one end fixed to the base and the other end only subjected to an axial force F_x without any other constraints, which is graphically displayed in Fig. 3.16. Starting from Eq. (3.18), we can obtain:

$$EI(s)(\kappa(s) - \kappa_o(s)) = EI\frac{\mathrm{d}\theta}{\mathrm{d}s} = M(s) = F_x(y(L) - y(s)) \tag{3.38}$$

   with

$$\kappa_o(s) = 0;\ \frac{\mathrm{d}I}{\mathrm{d}s}(s) = 0$$

   Then, differentiating (3.38) leads to:

$$EI\frac{\mathrm{d}^2\theta}{\mathrm{d}s^2} = -F_x \sin\theta(s) \tag{3.39}$$

   Rearranging (3.39), we will have the following:

$$\frac{1}{2}EI(\frac{\mathrm{d}\theta}{\mathrm{d}s})^2 - F_x\cos\theta(s) = C \tag{3.40}$$

where C is an unknown constant which can be determined by the boundary conditions. Precisely,

$$C = \frac{1}{2}EI(\frac{\mathrm{d}\theta}{\mathrm{d}s}(L))^2 - F_x\cos\theta(L) = -F_x\cos\alpha \tag{3.41}$$

where $EI\frac{\mathrm{d}\theta}{\mathrm{d}s}(L) = 0$ and $\theta(L) = \alpha$, and α is an unknown parameter to be determined. Similarly,

$$C = \frac{1}{2}EI(\frac{\mathrm{d}\theta}{\mathrm{d}s}(0))^2 - F_x\cos\theta(0) = \frac{F_x^2}{2EI}y(L)^2 - F_x \tag{3.42}$$

where $EI\frac{\mathrm{d}\theta}{\mathrm{d}s}(0) = F_x y(L)$ and $\theta(0) = 0$. Rearranging (3.41) drives us to have:

$$\frac{\mathrm{d}\theta}{\mathrm{d}s} = \pm\sqrt{\frac{2F_x}{EI}(\cos\theta(s) - \cos\alpha)} \tag{3.43}$$

which actually results in three possibilities. If $\theta(s) = 0$, then we can easily obtain $\alpha = \theta(s) = 0$ and $\frac{\mathrm{d}\theta}{\mathrm{d}s}(s) = 0$, which leads to Scenario 2 as shown in Fig. 3.16. Otherwise, we will have:

$$\frac{\mathrm{d}\theta}{\mathrm{d}s} = +\sqrt{\frac{2F_x}{EI}(\cos\theta(s) - \cos\alpha)} \tag{3.44}$$

if $\alpha > 0$ and

$$\frac{\mathrm{d}\theta}{\mathrm{d}s} = -\sqrt{\frac{2F_x}{EI}(\cos\theta(s) - \cos\alpha)} \tag{3.45}$$

if $\alpha < 0$, which clearly corresponds to Scenarios 1 and 3 as shown in Fig. 3.16. Here, we only take (3.44) for example to finish the rest deduction and logically solving (3.45) follows the same procedure. Assume $f(\alpha)$ as:

$$f(\alpha) = \int_0^{\alpha^-} \frac{1}{\sqrt{\frac{2F_x}{EI}(\cos\theta(s) - \cos\alpha)}}\mathrm{d}\theta - \int_{0^+}^{L^-}\mathrm{d}s \tag{3.46}$$

then we can obtain the value of α by solving $f(\alpha) = 0$ via Newton-Raphson method (Ypma, 1995). If we consider (3.41) and (3.42) together, we can easily derive the expression for $y(L)$:

$$y(L) = \sqrt{(1-\cos\alpha)\frac{2EI}{F_x}} \tag{3.47}$$

So far, we have got all the information of the boundary conditions:

$$\text{B.C. } \theta(0) = 0;\ \frac{\mathrm{d}\theta}{\mathrm{d}s}(0) = \frac{F_x y(L)}{EI};\ \theta(L) = \alpha;\ \frac{\mathrm{d}\theta}{\mathrm{d}s}(L) = 0 \tag{3.48}$$

Differentiating (3.39) twice ends up with a fourth-order ODE:

$$EI\frac{\mathrm{d}^4\theta}{\mathrm{d}s^4} + F_x(-\sin\theta(s)(\frac{\mathrm{d}\theta}{\mathrm{d}s})^2 + \cos\theta(s)\frac{\mathrm{d}^2\theta}{\mathrm{d}s^2}) = 0 \tag{3.49}$$

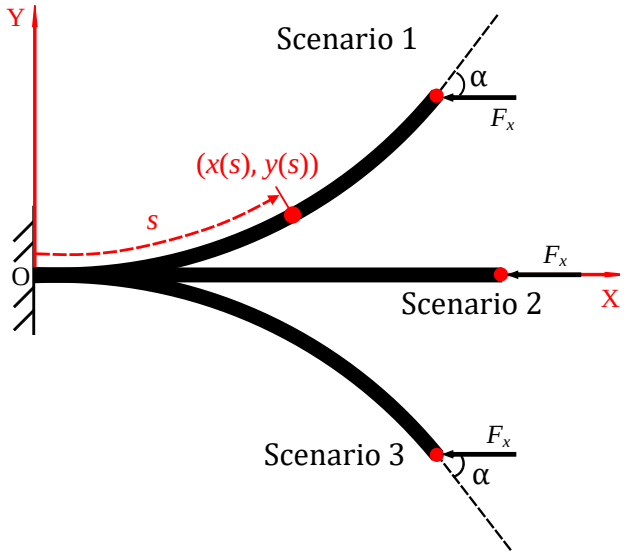

FIGURE 3.16: A slender beam subjected to an axial load

Logically, we can obtain the governing BVP via rearranging (3.48) and (3.49):

$$\begin{aligned}
&\text{D.E.} \quad EI\frac{\mathrm{d}^4\theta}{\mathrm{d}s^4} + F_x(-\sin\theta(s)(\frac{\mathrm{d}\theta}{\mathrm{d}s})^2 + \cos\theta(s)\frac{\mathrm{d}^2\theta}{\mathrm{d}s^2}) = 0 \\
&\text{B.C.} \quad \theta(0) = 0 \\
&\qquad \frac{\mathrm{d}\theta}{\mathrm{d}s}(0) = \frac{F_x y(L)}{EI} \\
&\qquad \theta(L) = \alpha \\
&\qquad \frac{\mathrm{d}\theta}{\mathrm{d}s}(L) = 0
\end{aligned} \tag{3.50}$$

2. **A slender straight beam subjected to an axial load and constraint by the sliding revolute joints at the both ends**
In this section, we study the beam buckling problem about a slender straight beam subjected to an axial load and constraint by the sliding revolute joints at the both ends, as shown in Fig. 3.17. Note that this case can be considered as a simple combined one of rigid and flexible mechanisms. We first start with its fundamental equation derived from Eq. (3.18):

$$EI(s)(\kappa(s) - \kappa_o(s)) = EI\frac{\mathrm{d}\theta}{\mathrm{d}s} = M(s) = F_x(y(L) - y(s)) \tag{3.51}$$

with

$$\kappa_o(s) = 0; \ \frac{\mathrm{d}I}{\mathrm{d}s}(s) = 0$$

Then, differentiating (3.51) results in:

$$EI\frac{\mathrm{d}^2\theta}{\mathrm{d}s^2} = -F_x\sin\theta(s) \tag{3.52}$$

Rearranging (3.52), we will obtain the following:

$$\frac{1}{2}EI(\frac{\mathrm{d}\theta}{\mathrm{d}s})^2 - F_x\cos\theta(s) = C \tag{3.53}$$

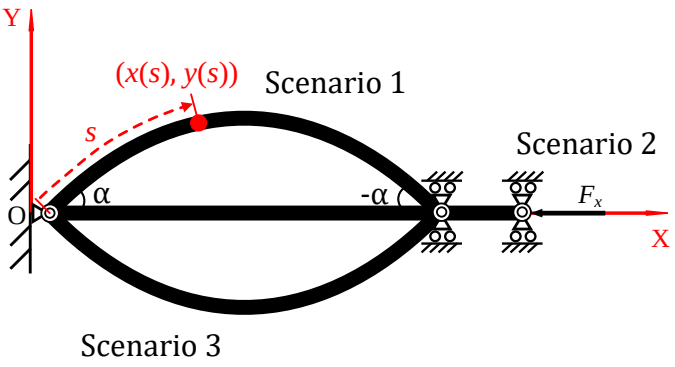

FIGURE 3.17: A slender straight beam subjected to an axial load and constraint by the sliding revolute joints at the both ends

where C is an unknown constant. C can be determined by the boundary conditions. Precisely,

$$C = \frac{1}{2}EI(\frac{\mathrm{d}\theta}{\mathrm{d}s}(0))^2 - F_x\cos\theta(0) = -F_x\cos\alpha \tag{3.54}$$

where $EI\dfrac{\mathrm{d}\theta}{\mathrm{d}s}(0) = 0$ and $\theta(0) = \alpha$, and α is an unknown parameter to be determined. Similarly,

$$C = \frac{1}{2}EI(\frac{\mathrm{d}\theta}{\mathrm{d}s}(L))^2 - F_x\cos\theta(L) = -F_x\cos\alpha \tag{3.55}$$

where $EI\dfrac{\mathrm{d}\theta}{\mathrm{d}s}(L) = 0$ and $\theta(L) = 0$. Rearranging (3.54) and (3.55) drives us to have:

$$\frac{\mathrm{d}\theta}{\mathrm{d}s} = \pm\sqrt{\frac{2F_x}{EI}(\cos\theta(s) - \cos\alpha)} \tag{3.56}$$

It is obvious that the differential system (3.56) has three solutions: if $\theta(s) = 0$, then we can easily obtain $\alpha = \theta(s) = 0$ and $\dfrac{\mathrm{d}\theta}{\mathrm{d}s}(s) = 0$, which leads to Scenario 2 as shown in Fig. 3.17. Otherwise, we will have:

$$\frac{\mathrm{d}\theta}{\mathrm{d}s} = -\sqrt{\frac{2F_x}{EI}(\cos\theta(s) - \cos\alpha)} \tag{3.57}$$

if $\alpha > 0$ and

$$\frac{\mathrm{d}\theta}{\mathrm{d}s} = +\sqrt{\frac{2F_x}{EI}(\cos\theta(s) - \cos\alpha)} \tag{3.58}$$

if $\alpha < 0$, which clearly corresponds to Scenarios 1 and 3 as shown in Fig. 3.17. For idea demonstration, we just take (3.57) for example, and solving (3.58) has the same procedure. Assuming $f(\alpha)$ as:

$$f(\alpha) = \int_{\alpha^-}^{-\alpha^+} -\frac{1}{\sqrt{\frac{2F_x}{EI}(\cos\theta(s) - \cos\alpha)}}\mathrm{d}\theta - \int_{0^+}^{L^-}\mathrm{d}s \tag{3.59}$$

Therefore, $f(\alpha) = 0$ can be logically solved via Newton-Raphson method to obtain the value of α. Then, we can start to handle the fourth-order system:

$$EI\frac{\mathrm{d}^4\theta}{\mathrm{d}s^4} + F_x(-\sin\theta(s)(\frac{\mathrm{d}\theta}{\mathrm{d}s})^2 + \cos\theta(s)\frac{\mathrm{d}^2\theta}{\mathrm{d}s^2}) = 0 \tag{3.60}$$

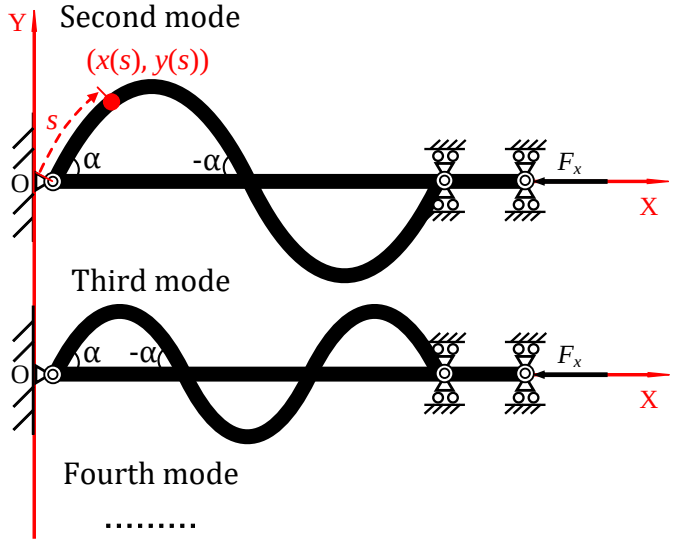

FIGURE 3.18: A slender straight beam subjected to an axial load and constraint by the moving revolute joints at the both ends (different modes of buckling)

as all the boundary conditions are known at this point:

$$\text{B.C. } \theta(0) = \alpha;\ \frac{\mathrm{d}\theta}{\mathrm{d}s}(0) = 0;\ \theta(L) = -\alpha;\ \frac{\mathrm{d}\theta}{\mathrm{d}s}(L) = 0 \tag{3.61}$$

Logically, we can obtain the governing BVP via rearranging (3.61) and (3.60):

$$\begin{aligned}
&\text{D.E. } \ EI\frac{\mathrm{d}^4\theta}{\mathrm{d}s^4} + F_x(-\sin\theta(s)(\frac{\mathrm{d}\theta}{\mathrm{d}s})^2 + \cos\theta(s)\frac{\mathrm{d}^2\theta}{\mathrm{d}s^2}) = 0\\
&\text{B.C. } \ \theta(0) = \alpha\\
&\qquad \frac{\mathrm{d}\theta}{\mathrm{d}s}(0) = 0\\
&\qquad \theta(L) = -\alpha\\
&\qquad \frac{\mathrm{d}\theta}{\mathrm{d}s}(L) = 0
\end{aligned} \tag{3.62}$$

Remark 4 *For the Nth ($N = 1, 2, 3...$) mode of the buckling behaviors (Euler, 1744)(Euler, 1759)(Oldfather, Ellis, and Brown, 1933) that is displayed in Fig. 3.18, we just need to follow the strategy below:*

$$f(\alpha) = \int_{\alpha^-}^{-\alpha^+} -\frac{1}{\sqrt{\frac{2F_x}{EI}(\cos\theta(s) - \cos\alpha)}}\mathrm{d}\theta - \int_{0^+}^{\frac{L}{N}^-} \mathrm{d}s \tag{3.63}$$

As long as α is obtained, revisiting (3.60)(3.61)(3.62) will provide the corresponding Nth-mode solution to $\theta(s)$.

3. **Post-buckling: a slender straight beam subjected to an axial load and a vertical load**
This section actually is a further study of the case shown in Fig. 3.16, which deals with its corresponding post-buckling behavior as shown in Fig. 3.19. Suppose the post-buckling behavior starts from point A through point B, and ends at point C. We first need to manipulate its governing equation (3.18) into the following handy state:

$$EI(s)(\kappa(s) - \kappa_o(s)) = EI\frac{\mathrm{d}\theta}{\mathrm{d}s} = M(s) = F_x(y(L) - y(s)) - F_y(x(L) - x(s)) \tag{3.64}$$

with

$$\kappa_o(s) = 0;\ \frac{\mathrm{d}I}{\mathrm{d}s}(s) = 0$$

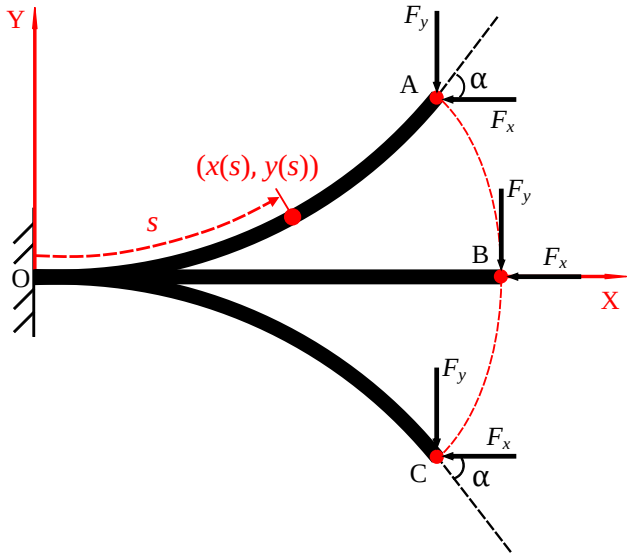

FIGURE 3.19: A slender straight beam subjected to an axial load and constraint by sliding pairs at the both ends

Differentiating (3.64) results in:

$$EI\frac{\mathrm{d}^2\theta}{\mathrm{d}s^2} = -F_x \sin\theta(s) + F_y \cos\theta(s) \tag{3.65}$$

Rearranging (3.65) leads to the following:

$$\frac{1}{2}EI(\frac{\mathrm{d}\theta}{\mathrm{d}s})^2 - F_x \cos\theta(s) - F_y \sin\theta(s) = C \tag{3.66}$$

where C is to be determined by the boundary conditions. Precisely, we have the following relation:

$$C = \frac{1}{2}EI(\frac{\mathrm{d}\theta}{\mathrm{d}s}(0))^2 - F_x \cos\theta(0) - F_y \sin\theta(0) = \frac{1}{2}EI(\frac{\mathrm{d}\theta}{\mathrm{d}s}(0))^2 - F_x \tag{3.67}$$

where $\theta(0) = 0$, and $\dfrac{\mathrm{d}\theta}{\mathrm{d}s}(L)$ stays unknown for the moment. Similarly we get:

$$C = \frac{1}{2}EI(\frac{\mathrm{d}\theta}{\mathrm{d}s}(L))^2 - F_x \cos\theta(L) - F_y \sin\theta(L) = -F_x \cos\alpha - F_y \sin\alpha \tag{3.68}$$

where $EI\dfrac{\mathrm{d}\theta}{\mathrm{d}s}(L) = 0$ and $\theta(L) = \alpha$, and α stays unknown for the moment. Substituting (3.68) into (3.66) yields:

$$\frac{\mathrm{d}\theta}{\mathrm{d}s} = \pm\sqrt{\frac{2F_x}{EI}(\cos\theta(s) - \cos\alpha) + \frac{2F_y}{EI}(\sin\theta(s) - \sin\alpha)} \tag{3.69}$$

Obviously, $\theta(s) = 0$ and $F_y = 0$ is one unique solution (that is point B in Fig. 3.19) of (3.69) as well as (3.65). If $\alpha > 0$, we will have:

$$f(\alpha, F_y) = \int_0^{\alpha^-} \frac{1}{\sqrt{\frac{2F_x}{EI}(\cos\theta(s) - \cos\alpha) + \frac{2F_y}{EI}(\sin\theta(s) - \sin\alpha)}}\mathrm{d}\theta - \int_0^{L^-} \mathrm{d}s = 0 \tag{3.70}$$

Given α or F_y, (3.70) can be directly solved using Newton-Raphson method. Similarly, if $\alpha < 0$, we will arrive at:

$$f(\alpha, F_y) = \int_0^{\alpha^+} \frac{-1}{\sqrt{\frac{2F_x}{EI}(\cos\theta(s) - \cos\alpha) + \frac{2F_y}{EI}(\sin\theta(s) - \sin\alpha)}}\mathrm{d}\theta - \int_0^{L^-} \mathrm{d}s = 0 \tag{3.71}$$

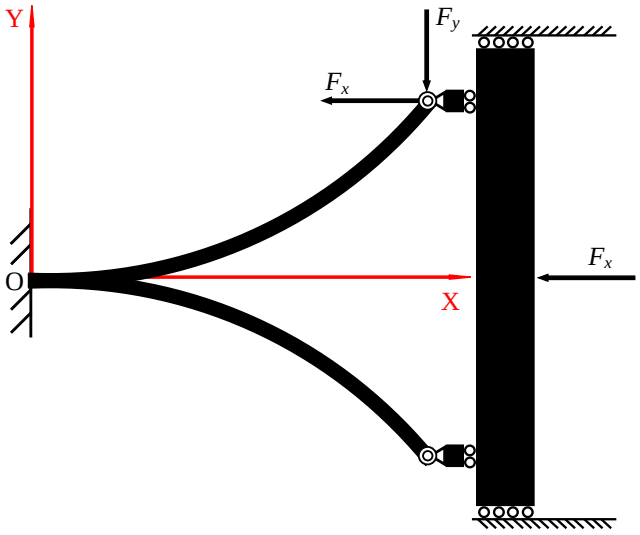

FIGURE 3.20: Conceptual design of Fig. 3.19

Obviously, (3.71) can be solved in the same manner using Newton-Raphson method. As long as α and F_y are known, we can logically find out the expression and its value of $\frac{d\theta}{ds}(0)$ by rearranging (3.67) and (3.68):

$$\frac{d\theta}{ds}(0) = \pm\sqrt{\frac{2}{EI}(F_x - F_x\cos\alpha - F_y\sin\alpha)} \tag{3.72}$$

So far, the essential information of the boundary conditions can be summarized as:

$$\text{B.C. } \theta(0) = 0;\ \frac{d\theta}{ds}(0) = \pm\sqrt{\frac{2}{EI}(F_x - F_x\cos\alpha - F_y\sin\alpha)};\ \theta(L) = \alpha;\ \frac{d\theta}{ds}(L) = 0 \tag{3.73}$$

Differentiating (3.65) twice ends up with the fourth-order ODE:

$$EI\frac{d^4\theta}{ds^4} + F_x(-\sin\theta(s)(\frac{d\theta}{ds})^2 + \cos\theta(s)\frac{d^2\theta}{ds^2}) + F_y(\cos\theta(s)(\frac{d\theta}{ds})^2 + \sin\theta(s)\frac{d^2\theta}{ds^2}) = 0 \tag{3.74}$$

Finally, we can obtain the governing BVP via rearranging (3.73) and (3.74):

$$\begin{aligned}
&\text{D.E. } EI\frac{d^4\theta}{ds^4} + F_x(-\sin\theta(s)(\frac{d\theta}{ds})^2 + \cos\theta(s)\frac{d^2\theta}{ds^2}) + F_y(\cos\theta(s)(\frac{d\theta}{ds})^2 + \sin\theta(s)\frac{d^2\theta}{ds^2}) = 0\\
&\text{B.C. } \theta(0) = 0\\
&\quad \frac{d\theta}{ds}(0) \pm \sqrt{\frac{2}{EI}(F_x - F_x\cos\alpha - F_y\sin\alpha)}\\
&\quad \theta(L) = \alpha\\
&\quad \frac{d\theta}{ds}(L) = 0
\end{aligned} \tag{3.75}$$

Remark 5 *If we consider the practical design that involves this post-buckling behavior, the mechanism would follow the layout as shown in Fig. 3.20.*

4. **Post-buckling problem: a slender straight beam subjected to an axial load and a vertical load constraint by the sliding revolute joints at the both ends**
This section is the further study of the case shown in Fig. 3.17. Likewise, we would like to analyze the post-buckling behavior from point A through B finally to point C (see Fig. 3.21). The governing equation is first

derived from (3.18) and needs to be arranged in a clear way:

$$EI(s)(\kappa(s)-\kappa_o(s)) = EI\frac{\mathrm{d}\theta}{\mathrm{d}s} = M(s) = -F_x y(s) + \frac{F_y}{2}x(s) \tag{3.76}$$

with

$$\kappa_o(s) = 0;\ \frac{\mathrm{d}I}{\mathrm{d}s}(s) = 0$$

Differentiating (3.76), we will obtain:

$$EI\frac{\mathrm{d}^2\theta}{\mathrm{d}s^2} = -F_x\sin\theta(s) + \frac{F_y}{2}\cos\theta(s) \tag{3.77}$$

Slightly manipulating (3.77), we then can reach:

$$\frac{1}{2}EI(\frac{\mathrm{d}\theta}{\mathrm{d}s})^2 - F_x\cos\theta(s) - \frac{F_y}{2}\sin\theta(s) = C \tag{3.78}$$

Substituting the boundary conditions $\theta(0) = \alpha$ and $\frac{\mathrm{d}\theta}{\mathrm{d}s}(0) = 0$ into (3.78) gives us:

$$C = -(F_x\cos\alpha + \frac{F_y}{2}\sin\alpha) \tag{3.79}$$

Similarly, substituting the boundary conditions $\theta(\frac{L}{2}) = 0$ and $\frac{\mathrm{d}\theta}{\mathrm{d}s}(\frac{L}{2})$ into (3.78) gives us:

$$C = \frac{1}{2}EI(\frac{\mathrm{d}\theta}{\mathrm{d}s}(\frac{L}{2}))^2 - F_x \tag{3.80}$$

Then, rearranging (3.78) and (3.79) yields:

$$\frac{\mathrm{d}\theta}{\mathrm{d}s} = \pm\sqrt{\frac{2F_x}{EI}(\cos\theta(s)-\cos\alpha) + \frac{F_y}{EI}(\sin\theta(s)-\sin\alpha)} \tag{3.81}$$

Clearly, we will have one unique solution ($\theta(s) = 0$ and $F_y = 0$) to (3.81) and (3.77). Besides, if $\alpha > 0$, we will have:

$$f(\alpha, F_y) = \int_{\alpha^-}^{0}\frac{-1}{\sqrt{\frac{2F_x}{EI}(\cos\theta(s)-\cos\alpha) + \frac{F_y}{EI}(\sin\theta(s)-\sin\alpha)}}\mathrm{d}\theta - \int_{0^+}^{\frac{L}{2}}\mathrm{d}s \tag{3.82}$$

If α or F_y is known, (3.82) can be solved using Newton-Raphson method. Similarly, if $\alpha < 0$, we will arrive at:

$$f(\alpha, F_y) = \int_{\alpha^+}^{0}\frac{1}{\sqrt{\frac{2F_x}{EI}(\cos\theta(s)-\cos\alpha) + \frac{F_y}{EI}(\sin\theta(s)-\sin\alpha)}}\mathrm{d}\theta - \int_{0^+}^{\frac{L}{2}}\mathrm{d}s \tag{3.83}$$

Similarly, if α or F_y is known, (3.83) can be solved using Newton-Raphson method as well. Then, we will be able to obtain the value of $\frac{\mathrm{d}\theta}{\mathrm{d}s}(\frac{L}{2})$ via dealing with (3.79) and (3.80) together:

$$\frac{\mathrm{d}\theta}{\mathrm{d}s}(\frac{L}{2}) = \mp\sqrt{\frac{1}{EI}(2F_x - 2F_x\cos\alpha - F_y\sin\alpha)} \tag{3.84}$$

Logically, the boundary conditions are all available:

$$\text{B.C. } \theta(0) = \alpha;\ \frac{\mathrm{d}\theta}{\mathrm{d}s}(0) = 0;\ \theta(\frac{L}{2}) = 0;\ \frac{\mathrm{d}\theta}{\mathrm{d}s}(\frac{L}{2}) = \mp\sqrt{\frac{1}{EI}(2F_x - 2F_x\cos\alpha - F_y\sin\alpha)} \tag{3.85}$$

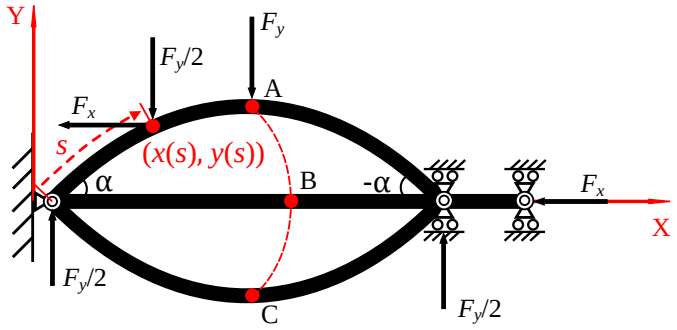

FIGURE 3.21: A slender straight beam subjected to an axial load and a vertical load constraint by the sliding revolute joints at the both ends

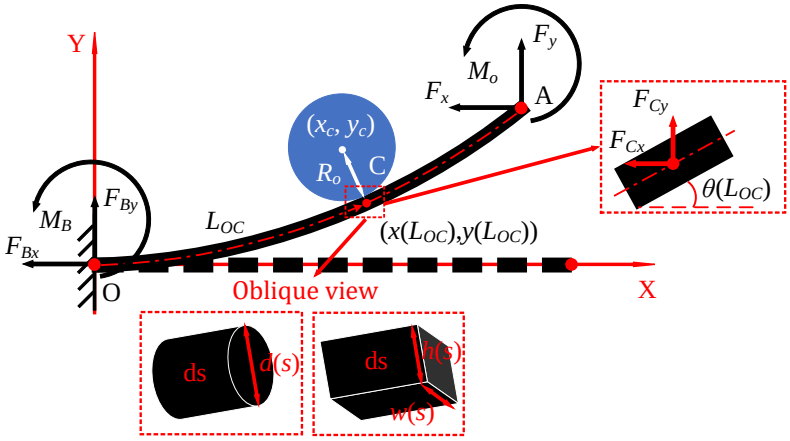

FIGURE 3.22: A slender straight beam subjected to beam-end loading and constraint by a rigid cylinder

Then, differentiating (3.77) twice gives us the final governing fourth-order ODE:

$$EI\frac{\mathrm{d}^4\theta}{\mathrm{d}s^4} + F_x(-\sin\theta(s)(\frac{\mathrm{d}\theta}{\mathrm{d}s})^2 + \cos\theta(s)\frac{\mathrm{d}^2\theta}{\mathrm{d}s^2}) + \frac{F_y}{2}(\cos\theta(s)(\frac{\mathrm{d}\theta}{\mathrm{d}s})^2 + \sin\theta(s)\frac{\mathrm{d}^2\theta}{\mathrm{d}s^2}) = 0 \tag{3.86}$$

Rearranging (3.85) and (3.86), we can reach the following BVP:

$$\begin{aligned}
&\text{D.E.} \quad EI\frac{\mathrm{d}^4\theta}{\mathrm{d}s^4} + F_x(-\sin\theta(s)(\frac{\mathrm{d}\theta}{\mathrm{d}s})^2 + \cos\theta(s)\frac{\mathrm{d}^2\theta}{\mathrm{d}s^2}) + \frac{F_y}{2}(\cos\theta(s)(\frac{\mathrm{d}\theta}{\mathrm{d}s})^2 + \sin\theta(s)\frac{\mathrm{d}^2\theta}{\mathrm{d}s^2}) = 0 \\
&\text{B.C.} \quad \theta(0) = \alpha \\
&\qquad \frac{\mathrm{d}\theta}{\mathrm{d}s}(0) = 0 \\
&\qquad \theta(\frac{L}{2}) = 0 \\
&\qquad \frac{\mathrm{d}\theta}{\mathrm{d}s}(\frac{L}{2}) = \mp\sqrt{\frac{1}{EI}(2F_x - 2F_x\cos\alpha - F_y\sin\alpha)}
\end{aligned} \tag{3.87}$$

3.3.1.3 Contact problem

Besides general large deflections and (post-)buckling, contact problems are also a common problem in CMs. Contact-aided CMs has been a popular area in this academic field, and the diverse designs provide many unexpectedly desired possibilities for current mechanical applications (Mankame and Ananthasuresh, 2002). Here, we focus on a simple contact problem in CMs to demonstrate the idea. Similarly, we also have the following pre-conditions for a slender

straight beam of constant cross sections:

$$\kappa_o(s) = 0;\ \frac{\mathrm{d}I}{\mathrm{d}s}(s) = 0$$

In Fig. 3.22, a slender straight beam is subjected to beam-end loading conditions and physically constraint by a rigid cylinder where the contact happens between the deflected beam and the cylinder. For this studied case, we need to consider the beam as two sub-parts: beam #OC and beam #CA as shown in Fig. 3.22. We define the length of #OC part as L_{OC} so that of the rest beam (#CA part) is logically equal to $L - L_{OC}$. Then, we will have two governing BVPs for the two respective sub-parts. For beam #OC,

$$EI(s)(\kappa(s) - \kappa_o(s)) = EI\frac{\mathrm{d}\theta}{\mathrm{d}s} = M(s) = F_{Cx}(y(L_{OC}) - y(s)) + F_{Cx}(x(L_{OC}) - x(s));\ s \in [0, L_{OC}] \tag{3.88}$$

Differentiating (3.88), we will have:

$$\frac{\mathrm{d}^2\theta}{\mathrm{d}s^2} = -\frac{F_{Cx}}{EI}\sin\theta - \frac{F_{Cy}}{EI}\cos\theta \tag{3.89}$$

subjected to

$$\text{B.C. } \theta(0) = 0;\ \frac{\mathrm{d}\theta}{\mathrm{d}s}(L_{OC}) = \frac{M_o}{EI} + F_x(y(L) - y(L_{OC})) + F_y(x(L) - x(L_{OC})) \tag{3.90}$$

Rearranging (3.89) and (3.90), we can reach the following BVP for beam #OC:

$$\begin{aligned}
&\text{D.E. } EI\frac{\mathrm{d}^2\theta}{\mathrm{d}s^2} = -\frac{F_{Cx}}{EI}\sin\theta - \frac{F_{Cy}}{EI}\cos\theta;\ s \in [0, L_{OC}]\\
&\text{B.C. } \theta(0) = 0\\
&\qquad \frac{\mathrm{d}\theta}{\mathrm{d}s}(L_{OC}) = \frac{M_o}{EI} + F_x(y(L) - y(L_{OC})) + F_y(x(L) - x(L_{OC}))
\end{aligned} \tag{3.91}$$

Similarly, we can derive the corresponding BVP for Beam #CA accordingly:

$$\begin{aligned}
&\text{D.E. } EI\frac{\mathrm{d}^2\theta}{\mathrm{d}s^2} = -\frac{F_x}{EI}\sin\theta - \frac{F_y}{EI}\cos\theta;\ s \in [L_{OC}, L]\\
&\text{B.C. } \frac{\mathrm{d}\theta}{\mathrm{d}s}(L) = \frac{M_o}{EI}
\end{aligned} \tag{3.92}$$

Besides, the force equilibrium relationships are as follows:

$$\begin{aligned}
&F_x + F_{Bx} + F_{Cx} = 0;\ \ F_y + F_{By} + F_{Cy} = 0\\
&M_B + M_o + F_x y(L) + F_y x(L) + F_{Cx} y(L_{OC}) + F_{Cy} x(L_{OC}) = 0
\end{aligned} \tag{3.93}$$

Finally, we have the geometrical relationships as well:

$$\left|\frac{F_{Cx}}{F_{Cy}}\right| = \tan\theta(L_{OC}) \tag{3.94}$$

with

$$\begin{aligned}
x_c + (R_o + \frac{h}{2})\sin\theta(L_{OC}) = x(L_{OC}) = \int_0^{L_{OC}} \cos\theta(s)\mathrm{d}s\\
y_c - (R_o + \frac{h}{2})\cos\theta(L_{OC}) = y(L_{OC}) = \int_0^{L_{OC}} \sin\theta(s)\mathrm{d}s
\end{aligned} \tag{3.95}$$

if the studied beam has rectangular cross sections, and

$$\begin{aligned}
x_c + (R_o + \frac{d}{2})\sin\theta(L_{OC}) = x(L_{OC}) = \int_0^{L_{OC}} \cos\theta(s)\mathrm{d}s\\
y_c - (R_o + \frac{d}{2})\cos\theta(L_{OC}) = y(L_{OC}) = \int_0^{L_{OC}} \sin\theta(s)\mathrm{d}s
\end{aligned} \tag{3.96}$$

if the studied beam has round cross sections.

3.3.1.4 Nondimensionalization of the governing BVPs

As stated above, different scenarios stated in Sections 3.3.1.1 to 3.3.1.3 are based on the governing BVPs subjected to different boundary conditions. In this section, we aim to dig into the mathematical essence of these governing BVPs. Normally, we can nondimensionalize any ODE derived from physical modeling to reveal its mathematical nature. Here, we take BVP (3.30) for example. First, the dependent variable θ and the independent variable s are nondimensionalized via:

$$\begin{aligned} \hat{\theta} &= \frac{\theta}{1};\ \theta = 1\hat{\theta} \\ \hat{s} &= \frac{s}{L};\ s = L\hat{s} \end{aligned} \tag{3.97}$$

Then, we can nondimensionalize (3.28) using (3.97) accordingly:

$$\frac{\mathrm{d}^2\hat{\theta}}{\mathrm{d}\hat{s}^2} = -\frac{F_y L^2}{EI}\cos\hat{\theta}(\hat{s}) - \frac{F_x L^2}{EI}\sin\hat{\theta}(\hat{s}) + \frac{\mathrm{d}\kappa_o}{\mathrm{d}\hat{s}}L \tag{3.98}$$

with the corresponding nondimensionalized boundary conditions from (3.29):

$$\begin{aligned} &\hat{\theta}(0) = 0 \\ &\frac{\mathrm{d}\hat{\theta}}{\mathrm{d}\hat{s}}(1) = \frac{M_o L}{EI} + L\kappa_o(L) = \frac{M_o L}{EI} + \frac{L}{R(L)} \end{aligned} \tag{3.99}$$

Reformulating (3.98) and (3.99), we can arrive at:

$$\begin{aligned} \text{D.E.}\quad & \frac{\mathrm{d}^2\hat{\theta}}{\mathrm{d}\hat{s}^2} = -f_y\cos\hat{\theta}(\hat{s}) - f_x\sin\hat{\theta}(\hat{s}) + \frac{\mathrm{d}\hat{\kappa}_o}{\mathrm{d}\hat{s}}(\hat{s}) \\ \text{B.C.}\quad & \hat{\theta}(0) = 0 \\ & \frac{\mathrm{d}\hat{\theta}}{\mathrm{d}\hat{s}}(1) = m_o + \hat{\kappa}_o(1) = m_o + \frac{1}{r(1)} \end{aligned} \tag{3.100}$$

where

$$f_x = \frac{F_x L^2}{EI};\ f_y = \frac{F_y L^2}{EI};\ m_o = \frac{M_o L}{EI};\ \hat{\kappa}_o(\hat{s}) = L\kappa_o(s);\ r(\hat{s}) = \frac{R(s)}{L};\ \hat{s}\in[0,1];\ s\in[0,L] \tag{3.101}$$

Logically, we will have the following to characterize the nondimensionalized beam shape:

$$\hat{x}(\hat{s}) = \int_0^{\hat{s}}\cos(\hat{\theta}(\xi))\mathrm{d}\xi;\ \hat{y}(\hat{s}) = \int_0^{\hat{s}}\sin(\hat{\theta}(\xi))\mathrm{d}\xi \tag{3.102}$$

where $\hat{x}(\hat{s})$ and $\hat{y}(\hat{s})$ are the nondimensionalized coordinates along the beam axis. In essence, ODE (3.100) governs all large-deflection scenarios of slender beams with initial curvature under beam-end loading conditions via this nondimensionalization framework. All the physical parameters can be represented by nondimensionalized values, see (3.101) and (3.102). This strategy provides both feasible and logical prerequisites for further discussions and manipulations of Euler Bernoulli beam equation.

3.3.2 Reduced-mode Cosserat rod model

Different from geometrically nonlinear Euler Bernoulli beam theory that only considers planar bending, Cosserat rod theory takes care of all linear strains (two shear strains, two bending strains, one twisting strain and one axial strain) along the rod for the analysis of spatial deflections. However, in compliant mechanisms, planar beam (or flexure)-deflections are very common during their operations so if we still stick to the original governing ODEs (1.27)(1.28), it is too theoretically complex and computationally expensive compared to former. Note that in some cases like flexure-based positioning stages where the axial strains of the beams of flexures can not be neglected (Awtar, 2003), Euler Bernoulli beam theory is logically not valid any more here.

Therefore, in this section, we aim to derive a more concise and simpler representation of a reduced-mode Cosserat rod model from (1.27)(1.28) for planar deflections to get rid of the modeling complexity of the full-mode one especially the formality of the rotation matrix $\mathbf{R}$. Before the detailed derivation (Section 3.3.2.3), we need to transform the local variables to global ones (Section 3.3.2.1) and introduce a new definition of rotation matrix (Section 3.3.2.2). Then, we present a mode-selection strategy for the reduced-mode Cosserat rod model in Section 3.3.2.4 where a clear relationship between geometrically nonlinear Euler Bernoulli beam theory and Cosserat rod theory is revealed. In the end, the nondimensionalization of the reduced-mode Cosserat rod model is presented.

3.3.2.1 Variable transformation from local to global

First, we manipulate the governing equations of Cosserat rod (1.28) by replacing all variables defined in body frame with the ones defined in the global frame via:

$$v(s) = K^n(s)^{-1}\mathbf{R}^\top(s)\mathbf{n}(s) + v_o; \;\; u(s) = K^m(s)^{-1}\mathbf{R}^\top(s)\mathbf{m}(s) + u_o \tag{3.103}$$

which logically yields the formulations in (3.104) to (3.107):

$$\frac{\partial \mathbf{r}(s)}{\partial s} = \mathbf{v}(s) = \mathbf{R}(s)[K^n(s)^{-1}\mathbf{R}^\top(s)\mathbf{n}(s) + v_o] \tag{3.104}$$

$$\frac{\partial \mathbf{R}(s)}{\partial s} = \mathbf{R}(s)\hat{u}(s) = \mathbf{R}(s)[K^m(s)^{-1}\hat{m}(s) + u_o] = \mathbf{R}(s)[K^m(s)^{-1}\mathbf{R}^\top\hat{(}s)\mathbf{m}(s) + u_o] \tag{3.105}$$

$$\frac{\partial n(s)}{\partial s} = \frac{\partial \mathbf{R}^\top(s)\mathbf{n}(s)}{\partial s} = -\mathbf{R}^\top(s)\mathbf{f}(s) - [K^m(s)^{-1}\mathbf{R}^\top(s)\mathbf{m}(s) + u_o] \times \mathbf{R}^\top(s)\mathbf{n}(s) \tag{3.106}$$

$$\begin{aligned}\frac{\partial m(s)}{\partial s} = \frac{\partial \mathbf{R}^\top(s)\mathbf{m}(s)}{\partial s} = &- \mathbf{R}^\top(s)\mathbf{l}(s) - [K^n(s)^{-1}R^\top(s)\mathbf{n}(s) + v_o] \times \mathbf{R}^\top(s)\mathbf{n}(s) \\ &- [K^m(s)^{-1}\mathbf{R}^\top(s)\mathbf{m}(s) + u_o] \times \mathbf{R}^\top(s)\mathbf{m}(s)\end{aligned} \tag{3.107}$$

Note that we have the following relationships for beam-end loading:

$$\mathbf{n}(s) = \mathbf{n}(L) \tag{3.108}$$

and

$$\mathbf{m}(s) = \mathbf{m}(L) + (\mathbf{r}(L) - \mathbf{r}(s)) \times \mathbf{n}(L) \tag{3.109}$$

where

$$\mathbf{r}(s) = \begin{bmatrix} x(s) \\ y(s) \\ z(s) \end{bmatrix} \tag{3.110}$$

3.3.2.2 Definition of rotation matrix

In particular, as noticed in (3.104) to (3.107), the only unknown variable is the rotation matrix, which means the unknowns have been transformed from the strains $v(s)$ and $u(s)$ to $\mathbf{R}(s)$. Therefore, according to Weierstrass's first theorem, we can proceed to define $\mathbf{R}(s)$ through the following decomposition:

$$\mathbf{R}(s) = \mathbf{R}_z(\theta(s))\mathbf{R}_y(\beta(s))\mathbf{R}_x(\alpha(s)) \tag{3.111}$$

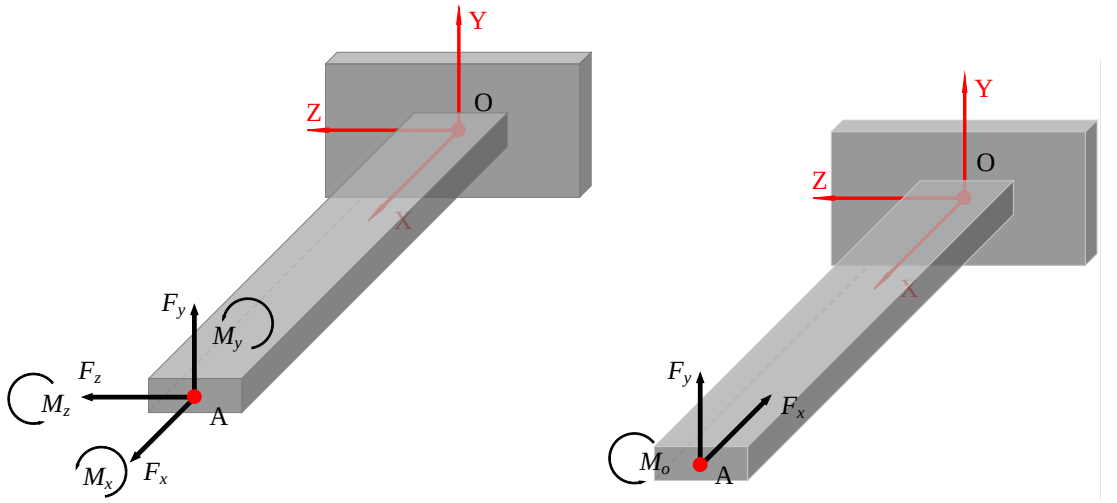

(A) A slender rod subjected to 3-D beam-end loading (B) A slender rod subjected to planar beam-end loading

FIGURE 3.23: Model reduction of Cosserat rod theory

where $\mathbf{R}_x(\alpha(s))$, $\mathbf{R}_y(\beta(s))$ and $\mathbf{R}_z(\theta(s))$ are defined as the rotation matrices around X, Y and Z axes respectively:

$$\begin{aligned}
\mathbf{R}_x(\alpha(s)) &= \begin{bmatrix} 1 & 0 & 0 \\ 0 & \cos\alpha(s) & -\sin\alpha(s) \\ 0 & \sin\alpha(s) & \cos\alpha(s) \end{bmatrix} \\
\mathbf{R}_y(\beta(s)) &= \begin{bmatrix} \cos\beta(s) & 0 & \sin\beta(s) \\ 0 & 1 & 0 \\ -\sin\beta(s) & 0 & \cos\beta(s) \end{bmatrix} \\
\mathbf{R}_z(\theta(s)) &= \begin{bmatrix} \cos\theta(s) & -\sin\theta(s) & 0 \\ \sin\theta(s) & \cos\theta(s) & 0 \\ 0 & 0 & 1 \end{bmatrix}
\end{aligned} \tag{3.112}$$

Under this framework, $\mathbf{R}(s) \in SO3$ is always satisfied due to the formality defined.

3.3.2.3 Derivations

As mentioned above, Cosserat rod theory can serve as an effective tool to model spatial deflections of rods taking care of bending, shear and stretch along the studied rod so planar deflections of beams can be modeled as well. However, the modeling process of planar beams would be a bit complex if we still stick to the original Cosserat rod theory. In this case, we have to directly deal with a set of ODEs like (1.27) and (1.28), which is however not necessary, because logically and also intuitively, the ODEs and vectors can be simplified into lower-dimensional ones when analyzing planar deflections. Therefore, we conduct model reduction on Cosserat rod equations from 3D to 2D deflection to consider bending, shear and stretch in planar deflections as demonstrated in Fig. 3.23. In Fig. 3.23a, the rod is subjected to spatial beam-end loading, and logically we can simplify the beam-end loading into the one that only results in planar deflections (see Fig. 3.23b). Supposing the studied beam is only deflected within X-O-Y plane, we can define:

$$\mathbf{r}(s) = \begin{bmatrix} x(s) \\ y(s) \\ 0 \end{bmatrix} \tag{3.113}$$

Logically, the boundary condition of the beam-end loading (1.29) can be simplified:

$$\mathbf{n}(L) = \begin{bmatrix} -F_x \\ F_y \\ 0 \end{bmatrix} \tag{3.114}$$

and

$$\mathbf{m}(L) = \begin{bmatrix} 0 \\ 0 \\ M_o \end{bmatrix} \tag{3.115}$$

where the minus sign in $-F_x$ is added here for coinciding with the coordinate system of Euler Bernoulli beam theory (see Fig. 1.15 and Fig. 3.23b). Similarly, the bending of the studied beam only happens around Z axis so the rotation matrix can be formulated as:

$$\mathbf{R}(s) = \mathbf{R}_z(\theta(s))\mathbf{R}_y(\beta(s))\mathbf{R}_x(\alpha(s)) = \mathbf{R}_z(\theta(s)) \begin{bmatrix} 1 & 0 & 0 \\ 0 & 1 & 0 \\ 0 & 0 & 1 \end{bmatrix} \begin{bmatrix} 1 & 0 & 0 \\ 0 & 1 & 0 \\ 0 & 0 & 1 \end{bmatrix} = \mathbf{R}_z(\theta(s)) \tag{3.116}$$

Therefore, the other boundary condition (1.29) at the fixed end yields:

$$\mathbf{R}_z(\theta(0)) = \begin{bmatrix} \cos\theta(0) & -\sin\theta(0) & 0 \\ \sin\theta(0) & \cos\theta(0) & 0 \\ 0 & 0 & 1 \end{bmatrix} = \begin{bmatrix} 1 & 0 & 0 \\ 0 & 1 & 0 \\ 0 & 0 & 1 \end{bmatrix} \tag{3.117}$$

Obviously, the constraint at the fixed can be simplified as:

$$\theta(0) = 0 \tag{3.118}$$

Note that the initial strain and curvature set for straight beams are as follows:

$$v_0 = \begin{bmatrix} 1 \\ 0 \\ 0 \end{bmatrix};\ u_0 = \begin{bmatrix} 0 \\ 0 \\ \kappa_o(s) \end{bmatrix} \tag{3.119}$$

so we can obtain the following via (3.103) and (3.119):

$$\begin{aligned} v(s) &= \begin{bmatrix} \frac{\sin\theta(s)F_y - \cos\theta(s)F_x}{A(s)E(s)} + 1 \\ \frac{\cos\theta(s)F_y + \sin\theta(s)F_x}{A(s)G(s)} \\ 0 \end{bmatrix} \\ u(s) &= \begin{bmatrix} 0 \\ 0 \\ \frac{M_z + (x(L)-x(s))F_y + (x(L)-x(s))F_x}{E(s)I(s)} + \kappa_o(s) \end{bmatrix} = \begin{bmatrix} 0 \\ 0 \\ \frac{\mathrm{d}\theta}{\mathrm{d}s}(s) \end{bmatrix} \end{aligned} \tag{3.120}$$

Then, we can formulate strain vector for planar deflections:

$$\epsilon(s) = \begin{bmatrix} \epsilon_a(s) \\ \epsilon_s(s) \\ \epsilon_b(s) \end{bmatrix} = \begin{bmatrix} 0 \\ 0 \\ \frac{\mathrm{d}\theta}{\mathrm{d}s}(s) - \kappa_o(s) \end{bmatrix} \tag{3.121}$$

Here, only beam-end loading is considered so we have

$$\mathbf{f}(s) = \begin{bmatrix} 0 \\ 0 \\ 0 \end{bmatrix};\ \mathbf{l}(s) = \begin{bmatrix} 0 \\ 0 \\ 0 \end{bmatrix} \tag{3.122}$$

Note that any arbitrary $\mathbf{f}(s)$ and $\mathbf{l}(s)$ can be considered as well but here we proceed with the beam-end loading conditions. Arranging (3.104) to (3.107) respectively via (3.113) to (3.122), we will be able to arrive at (3.123) to (3.126):

$$\begin{bmatrix} \frac{dx}{ds}(s) \\ \frac{dy}{ds}(s) \\ \frac{dz}{ds}(s) \end{bmatrix} = \begin{bmatrix} \cos\theta(s)(\epsilon_a(s)+1) - \sin\theta(s)\epsilon_s(s) \\ \sin\theta(s)(\epsilon_a(s)+1) + \cos\theta(s)\epsilon_s(s) \\ 0 \end{bmatrix} \tag{3.123}$$

$$\begin{bmatrix} -\frac{\sin\theta(s)f_m(s)}{E(s)I(s)} & -\frac{\cos\theta(s)f_m(s)}{E(s)I(s)} & 0 \\ \frac{\cos\theta(s)f_m(s)}{E(s)I(s)} & -\frac{\sin\theta(s)f_m(s)}{E(s)I(s)} & 0 \\ 0 & 0 & 0 \end{bmatrix} = \begin{bmatrix} 0 & 0 & 0 \\ 0 & 0 & 0 \\ 0 & 0 & 0 \end{bmatrix} \tag{3.124}$$

$$\begin{bmatrix} \frac{[\sin\theta(s)F_x + \cos\theta(s)F_y]f_m(s)}{E(s)I(s)} \\ \frac{[\cos\theta(s)F_x - \sin\theta(s)F_y]f_m(s)}{E(s)I(s)} \\ 0 \end{bmatrix} = \begin{bmatrix} 0 \\ 0 \\ 0 \end{bmatrix} \tag{3.125}$$

$$(\cos\theta(s)(\epsilon_a(s)+1) - \sin\theta(s)\epsilon_s(s) - \frac{dx}{ds}(s))F_y + (\sin\theta(s)(\epsilon_a(s)+1) + \cos\theta(s)\epsilon_s(s) - \frac{dy}{ds}(s))F_x = 0 \tag{3.126}$$

where

$$f_m(s) = (\frac{d\theta}{ds}(s) - \kappa_o(s))E(s)I(s) + F_x y(s) - F_x y(L) + F_y x(s) - F_y x(L) - M_o \tag{3.127}$$

Concluded from (3.123) to (3.127), we can reach the following relationships

$$f_m(s) = 0 \tag{3.128}$$

and

$$\frac{dx}{ds}(s) = \cos\theta(s)(\epsilon_a(s)+1) - \sin\theta(s)\epsilon_s(s); \quad \frac{dy}{ds}(s) = \sin\theta(s)(\epsilon_a(s)+1) + \cos\theta(s)\epsilon_s(s) \tag{3.129}$$

Here, we redefine the notation of Eq. (3.129) for more clarity:

$$\begin{aligned} (\frac{dx}{ds})_{\epsilon_{as}}(s) &= \cos\theta(s)(\epsilon_a(s)+1) - \sin\theta(s)\epsilon_s(s) \\ (\frac{dy}{ds})_{\epsilon_{as}}(s) &= \sin\theta(s)(\epsilon_a(s)+1) + \cos\theta(s)\epsilon_s(s) \end{aligned} \tag{3.130}$$

where ϵ_{as} implies that the formulations take care of the axial strain ϵ_a and shear strain ϵ_s. Differentiating (3.128) to eliminate the unknown constants as well as assuming the studied beam is of constant cross sections and made of isotropic material ($E(s)$, $A(s)$, $G(s)$, $J_z(s)$ and $I(s)$ are all constant within $s \in [0, L]$), we will have following ODE:

$$EI\frac{d^2\theta}{ds^2}(s) = -F_x(\frac{dy}{ds})_{\epsilon_{as}}(s) - F_y(\frac{dx}{ds})_{\epsilon_{as}}(s) + \frac{d\kappa_o}{ds}(s) \tag{3.131}$$

In (3.127), we can easily simplify the boundary condition of the beam-end loading by adding $s = L$:

$$\frac{d\theta}{ds}(L) = \frac{M_o}{EI} + \kappa_o(L) \tag{3.132}$$

Finally, together with the simplified boundary conditions (3.118) and (3.132), we will arrive the following governing BVP:

$$\begin{aligned} &\text{D.E.} \quad EI\frac{d^2\theta}{ds^2}(s) = -F_x(\frac{dy}{ds})_{\epsilon_{as}}(s) - F_y(\frac{dx}{ds})_{\epsilon_{as}}(s) + \frac{d\kappa_o}{ds}(s) \\ &\text{B.C.} \quad \theta(0) = 0 \\ &\qquad \frac{d\theta}{ds}(L) = \frac{M_o}{EI} + \kappa_o(L) \end{aligned} \tag{3.133}$$

To characterize the deformed beam shape, we can proceed with:

$$x(s) = \int_0^s (\frac{\mathrm{d}x}{\mathrm{d}\xi})_{\epsilon_{as}}(\xi)\mathrm{d}\xi;\ y(s) = \int_0^s (\frac{\mathrm{d}y}{\mathrm{d}\xi})_{\epsilon_{as}}(\xi)\mathrm{d}\xi \tag{3.134}$$

Via (3.121), the stored elastic energy in the beam can be calculated through:

$$E_p = \int_0^L \frac{1}{2}EA\epsilon_a^2 + \frac{1}{2}GA\epsilon_s^2 + \frac{1}{2}EI\epsilon_b^2\mathrm{d}s \tag{3.135}$$

3.3.2.4 Mode selection for the reduced-mode Cosserat rod model

In the reduced-mode Cosserat rod model (3.133) to (3.135) derived in Section 3.3.2.3, we can easily notice that in (3.121) the reduced model still considers bending, shear and stretch in planar deflections of beams. However, we don't always need to take care of all strains in the deflected beam since in some applications, some of them can be neglected but some need to be considered. For instance, shear strain for stubby beams (Hutchinson, 2001) and axial stretch in compliant parallelograms (Awtar, 2003) are both important factors in modeling them. Therefore, we utilize a mode-selection strategy to switch between different modes. First, we need to add a correction term into the strain vectors to take into account or drop some specific strains.

$$v(s) = H_1[K^n(s)^{-1}\mathbf{R}^\top(s)\mathbf{n}(s)] + v_o;\ \ u(s) = H_2[K^m(s)^{-1}\mathbf{R}^\top(s)\mathbf{m}(s)] + u_o \tag{3.136}$$

where H_1 and H_2 are defined as matrices for choosing the desired mode. In all planar beam theories, bending serves as the main contribution in planar deflections of beams so H_2 is fixed as:

$$H_2 = \begin{bmatrix} 0 & 0 & 0 \\ 0 & 0 & 0 \\ 0 & 0 & 1 \end{bmatrix} \tag{3.137}$$

Besides, to consider the axial stretch, we have:

$$H_1 = \begin{bmatrix} 1 & 0 & 0 \\ 0 & 0 & 0 \\ 0 & 0 & 0 \end{bmatrix} \tag{3.138}$$

To only take care of the shear of the cross sections, we have:

$$H_1 = \begin{bmatrix} 0 & 0 & 0 \\ 0 & 1 & 0 \\ 0 & 0 & 0 \end{bmatrix} \tag{3.139}$$

Logically, to consider both of them, H_1 yields

$$H_1 = \begin{bmatrix} 1 & 0 & 0 \\ 0 & 1 & 0 \\ 0 & 0 & 0 \end{bmatrix} \tag{3.140}$$

Instead of using (3.103), we use (3.136) to select the strains that need to be considered for different modeling purposes. Logically, we will be able to end up with a different version of (3.123) to (3.126) and (3.131) to (3.135).

In this case, we do a simple example for the mode-selection strategy stated above. We set $H_1 = \begin{bmatrix} 0 & 0 & 0 \\ 0 & 0 & 0 \\ 0 & 0 & 0 \end{bmatrix}$ and $H_2 = \begin{bmatrix} 0 & 0 & 0 \\ 0 & 0 & 0 \\ 0 & 0 & 1 \end{bmatrix}$ to only consider the bending of deflected beams. Then, we will be able to end up with similar

relationships as (3.123) to (3.126), which can be summarized as:

$$\begin{bmatrix} \frac{\mathrm{d}x}{\mathrm{d}s}(s) \\ \frac{\mathrm{d}y}{\mathrm{d}s}(s) \\ \frac{\mathrm{d}z}{\mathrm{d}s}(s) \end{bmatrix} = \begin{bmatrix} \cos\theta(s) \\ \sin\theta(s) \\ 0 \end{bmatrix} \tag{3.141}$$

$$(\frac{\mathrm{d}\theta}{\mathrm{d}s}(s) - \kappa_o)(s)I(s) + F_x y(s) - F_x y(L) + F_y x(s) - F_y x(L) - M_o = 0 \tag{3.142}$$

Similarly, assuming the studied beam is with constant cross sections and made of isotropic material ($E(s)$, $A(s)$, $G(s)$, $C(s)$, and $I(s)$ are all constant within $s \in [0, L]$), we can finally arrive at the following:

$$\begin{aligned} &\text{D.E. } EI(s)\frac{\mathrm{d}^2\theta}{\mathrm{d}s^2}(s) = -F_x\sin\theta(s) - F_y\cos\theta(s) + \frac{\mathrm{d}\kappa_o}{\mathrm{d}s} \\ &\text{B.C. } \theta(0) = 0 \\ &\qquad \frac{\mathrm{d}\theta}{\mathrm{d}s}(L) = \frac{M_o}{EI} + \kappa_o(L) \end{aligned} \tag{3.143}$$

with the characterization of beam shapes:

$$x(s) = \int_0^s \cos\theta(\xi)\mathrm{d}\xi;\ \ y(s) = \int_0^s \sin\theta(\xi)\mathrm{d}\xi \tag{3.144}$$

and the elastic energy can be formulated as:

$$E_p = \frac{1}{2}EI\epsilon_b^2\mathrm{d}s = \frac{1}{2}EI(\frac{\mathrm{d}\theta}{\mathrm{d}s})^2\mathrm{d}s \tag{3.145}$$

It is obvious that (3.143) to (3.145) essentially correspond to the governing equations (3.18)(3.20)(3.21) of Euler Bernoulli beam theory where only bending strain is considered. Therefore, it can be logically concluded that Euler Bernoulli beam theory is one reduced mode of Cosserat rod theory where planar bending serves as the only contribution to beam deflections.

3.3.2.5 Nondimensionalization of the reduced-mode Cosserat rod model

Similar to Section 3.3.1.4, the governing equations of the reduced-mode Cosserat rod theory can be nondimensionalized for better understanding of how different types of strains contribute to the final deflection as well. Therefore, the dependent variable θ and the independent variable s are nondimensionalized via:

$$\hat{\theta} = \frac{\theta}{1};\ \theta = 1\hat{\theta};\ \hat{s} = \frac{s}{L};\ s = L\hat{s} \tag{3.146}$$

where $\hat{\theta}$ and $\hat{s}$ denote the nondimensionalized θ and s respectively. Similarly, we go through the same procedure for $\epsilon_a(s)$ and $\epsilon_s(s)$ in Eq. (3.121) and Eq. (3.130):

$$\begin{aligned} (\frac{\mathrm{d}\hat{x}}{\mathrm{d}\hat{s}})_{\epsilon_{as}}(\hat{s}) &= \cos\hat{\theta}(\hat{s})(\hat{\epsilon}_a(\hat{s}) + 1) - \sin\hat{\theta}(\hat{s})\hat{\epsilon}_s(\hat{s}) \\ (\frac{\mathrm{d}\hat{y}}{\mathrm{d}\hat{s}})_{\epsilon_{as}}(\hat{s}) &= \sin\hat{\theta}(\hat{s})(\hat{\epsilon}_a(\hat{s}) + 1) + \cos\hat{\theta}(\hat{s})\hat{\epsilon}_s(\hat{s}) \end{aligned} \tag{3.147}$$

where

$$\hat{\epsilon}_a(\hat{s}) = \frac{f_y\sin\hat{\theta}(\hat{s}) - f_x\cos\hat{\theta}(\hat{s})}{12}\eta^2;\ \hat{\epsilon}_s(\hat{s}) = \frac{(1+\nu)(\sin\hat{\theta}(\hat{s})f_x) + \cos\hat{\theta}(\hat{s})f_y}{6}\eta^2 \tag{3.148}$$

η is the slenderness ratio of the studied beam defined as $\eta = \frac{h}{L}$. Then, we can nondimensionalize (3.133) using (3.146) accordingly:

$$\begin{aligned} \text{D.E.} \quad & \frac{\mathrm{d}^2\hat{\theta}}{\mathrm{d}\hat{s}^2} = -f_y(\frac{\mathrm{d}\hat{x}}{\mathrm{d}\hat{s}})_{\epsilon_{as}} - f_x(\frac{\mathrm{d}\hat{y}}{\mathrm{d}\hat{s}})_{\epsilon_{as}} + \frac{\mathrm{d}\hat{\kappa}_o}{\mathrm{d}\hat{s}} \\ \text{B.C.} \quad & \hat{\theta}(0) = 0 \\ & \frac{\mathrm{d}\hat{\theta}}{\mathrm{d}\hat{s}}(1) = m_o + \hat{\kappa}_o(1) = m_o + \frac{1}{r(1)} \end{aligned} \tag{3.149}$$

where

$$f_x = \frac{F_x L^2}{EI};\ f_y = \frac{F_y L^2}{EI};\ m_o = \frac{M_o L}{EI};\ \hat{\kappa}_o(\hat{s}) = L\kappa_o(s);\ r(\hat{s}) = \frac{R(s)}{L};\ \hat{s} \in [0,1];\ s \in [0,L] \tag{3.150}$$

To characterize the nondimensionalized beam shape, we can use the following nondimensionalized formulation via Eq. (3.147):

$$\hat{x}(\hat{s}) = \int_0^{\hat{s}} (\frac{\mathrm{d}\hat{x}}{\mathrm{d}\hat{\xi}})_{\epsilon_{as}} \mathrm{d}\hat{\xi};\ \hat{y}(\hat{s}) = \int_0^{\hat{s}} (\frac{\mathrm{d}\hat{y}}{\mathrm{d}\hat{\xi}})_{\epsilon_{as}} \mathrm{d}\hat{\xi} \tag{3.151}$$

where $\hat{x}(\hat{s})$ and $\hat{y}(\hat{s})$ are the nondimensionalized coordinates along the beam axis. Essentially, the nondimensionalized BVP (3.149) governs all large deflection scenarios where different materials, different beam geometries and different loading conditions are all considered. Under this framework of nondimensionalization, all physical parameters can be represented by nondimensionalized values (such as Eq. (3.150) and Eq. (3.151)).

Again, let's take a look at the effect of η in BVP (3.149). As long as the used isotropic material is settled, BVP (3.149) gradually converges to the following if $\eta \to 0$:

$$\begin{aligned} \text{D.E.} \quad & \frac{\mathrm{d}^2\hat{\theta}}{\mathrm{d}\hat{s}^2} = -(f_y \cos\hat{\theta}(\hat{s}) + f_x \sin\hat{\theta}(\hat{s})) + \frac{\mathrm{d}\hat{\kappa}_o}{\mathrm{d}\hat{s}} \\ \text{B.C.} \quad & \hat{\theta}(0) = 0 \\ & \frac{\mathrm{d}\hat{\theta}}{\mathrm{d}\hat{s}}(1) = m_o + \hat{\kappa}_o(1) = m_o + \frac{1}{r(1)} \end{aligned}$$

with the nondimensionalized formulation of characterizing the beam shape:

$$\hat{x}(\hat{s}) = \int_0^{\hat{s}} \cos\hat{\theta}(\xi)\mathrm{d}\xi;\ \hat{y}(\hat{s}) = \int_0^{\hat{s}} \sin\hat{\theta}(\xi)\mathrm{d}\xi$$

The above equations are exactly the nondimensionalized governing equations of Euler Bernoulli beam theory (see Eqs. (3.100)(3.101) in Section 3.3.1.4 and Wu and Zheng, 2022c). In other words, a slender beam ($\eta \to 0$) can be accurately modeled via Euler Bernoulli beam theory where the axial and shear strains could be neglected.

3.3.3 From 2D to 3D: full-mode Cosserat Rod theory

Previously, we focus on the planar modeling of slender beams. However, in CMs, spatial deflections of the elementary slender beams are of great importance so is the corresponding modeling. In the current literature, as reviewed in Section 1.2.5.5, the commonly-used methods for solving the governing equations of Cosserat rod are not user-friendly, also computationally expensive and complex. Here in this section, we propose a new numerical scheme to handle the problem via the framework of weighted residual methods. In the static model of Cosserat rod theory, the ODEs are defined in the group of $SO3$ due to the existence of rotation matrix. In the current literature, most studies deal with the model in the space of $SO3$, which is a bit complex from the engineering point of view. In this thesis, we propose to transform this variable defined in $SO3$ into vector space $\mathbb{R}^3$. It should be noted that, to solve Cosserat rod models, Finite Elements Method has been used in the transformation from $\mathbb{R}^3$ to Lie group SO(3), by J. C. Simo and his successors in the framework of the "geometrically exact FEM" (Simo and Vu-Quoc, 1988; Cardona and Geradin, 1988; Ibrahimbegović and Mikdad, 1998; Boyer and Primault, 2004; Sonneville, Cardona, and Brüls, 2014).

Here, we proceed with the spatial deflection of a slender rod subjected to beam-end loading conditions (see Fig 3.23a). First of all, we still need to use the formulations of (3.112) to define the rotation matrix. Due to the definition

of $\mathbf{R}(s)$ in (3.112), $\mathbf{R}(s)$ will always stay in the group of $SO3$. It should be noted that a similar definition of $\mathbf{R}(s)$ was proposed in (Isbister, Bailey, and Georgilas, 2021) but the authors use finite difference method to handle the ODEs, which is computationally expensive. Here, we consider the most common case: a slender rod subjected to beam-end loading. Then, we will have the following two representations of the governing ODEs respectively.

3.3.3.1 Global representation

In the global frame, (1.27) can be simplified:

$$\frac{\partial \mathbf{R}(s)}{\partial s} = \hat{\mathbf{u}}(s)\mathbf{R}(s); \quad \frac{\partial \mathbf{m}(s)}{\partial s} = -\mathbf{v}(s) \times \mathbf{n}(s) \tag{3.152}$$

subjected to the boundary conditions (1.29) and with the following rearranged constitutive equations:

$$\mathbf{n}(s) = \mathbf{R}(s)n(s) = \mathbf{R}(s)K^n(s)(\mathbf{R}(s)^\top \mathbf{v} - v_o); \quad \mathbf{m}(s) = \mathbf{R}(s)m(s) = \mathbf{R}(s)K^m(s)(\mathbf{R}(s)^\top \mathbf{u} - u_o) \tag{3.153}$$

Now, (3.152) and (3.153) are just a common set of ODEs with five unknown dependent variables: $\mathbf{u}$, $\mathbf{v}$, α, β and θ that are functions of s.

3.3.3.2 Local representation

Obviously, we have the same logic for the local-frame ODEs. (1.28) can be rearranged as follows:

$$\begin{aligned} \frac{\partial \mathbf{R}(s)}{\partial s} &= \mathbf{R}(s)\hat{u}(s) \\ \frac{\partial n(s)}{\partial s} &= -u(s) \times n(s) \\ \frac{\partial m(s)}{\partial s} &= -v(s) \times n(s) - u(s) \times m(s) \end{aligned} \tag{3.154}$$

which is subjected to the boundary conditions (1.29) with the constitutive equations (1.30). Similarly, Now, (3.154) and (1.30) are just a common set of ODEs with five unknown dependent variables: u, v, α, β and θ that are functions of s.

3.4 Energy framework via Lagrangian mechanics

In physics, different from Newtonian mechanics, Lagrangian mechanics is a formulation of classical mechanics founded on the stationary-action principle (also known as the principle of least action). The stationary action principle requires that the action functional of the system (that normally includes the kinematic energy and energy potential energy) must remain at a stationary point (a maximum, minimum, or saddle) throughout the time evolution of the system (Lagrange, 1853). This constraint allows the calculation of the equations of motion of the system using Lagrange's equations (Lagrange, 1853). Therefore, in this section, we aim to analyze large deflection of slender beams from the energy point of view. For static modeling, the stationary action principle, specifically, the principle of minimum total potential energy is used as the key to govern the mentioned physical process. Essentially, this is a problem of functional minimization since we are looking for a function (which determines the final deflected beam shape) to satisfy the minimum condition.

Similarly, we first formulate the problem via geometrically nonlinear Euler Bernoulli beam theory where the general deflection and the contact problem are discussed. Then, we utilize the reduced-mode Cosserat rod model to formulate the problem as well. In the end, we also apply this framework to full-mode Cosserat rod theory.

3.4.1 Geometrically nonlinear Euler Bernoulli beam theory

Here, we use geometrically nonlinear Euler Bernoulli beam theory to formulate the functional minimization problem. Then, the formulations of different loading scenarios (general large deflection and contact problem) of a slender beam are presented. In particular, we also demonstrate the theoretical validation of transforming the studied governing

equations from the energy framework to the moment-equilibrium framework (essentially, from Lagrangian mechanics to Newtonian mechanics) in Section 3.4.1.1.

- **Parameterization and functional minimization:**
  Parameterization is the prerequisite for this energy framework due to the involved optimization process. According to (3.19), the corresponding initial angle θ_o at an arbitrary point s along the beam axis yields:

$$\theta_o(s) = \int_0^s \kappa_o(\xi)\mathrm{d}\xi \tag{3.155}$$

  Similar to (3.21), the whole fabricated beam axis can be characterized through:

$$x_o(s) = \int_0^s \cos\theta_o(\xi)\mathrm{d}\xi;\ y_o(s) = \int_0^s \sin\theta_o(\xi)\mathrm{d}\xi; \tag{3.156}$$

  Considering $\frac{\mathrm{d}\theta}{\mathrm{d}s}(s)$ denotes the current curvature caused by bending at s and $\kappa_o(s)$ denotes the initial curvature, we can formulate the stored elastic energy E_p via:

$$E_p = \int_0^L \frac{1}{2}EI(s)(\frac{\mathrm{d}\theta}{\mathrm{d}s} - \kappa_o(s))^2\mathrm{d}s \tag{3.157}$$

  Logically, we can formulate the displacements of the conservative forces and moments exerted on the beam via (3.156) and (3.21). Then, we can write down the potential energy of the mentioned loading of the elastic system:

$$W_p = f_{W_p}(F(s), \theta(s), \kappa_o(s)) \tag{3.158}$$

  where $F(s)$ denotes the external loading exerted on the beam in a general form. Therefore, we can arrive at the formulation of the total potential energy via (3.157) and (3.158):

$$\begin{aligned}\Pi = E_p - W_p &= \int_0^L \frac{1}{2}EI(s)(\frac{\mathrm{d}\theta}{\mathrm{d}s} - \kappa_o(s))^2\mathrm{d}s - f_{W_p}(F(s), \theta(s), \kappa_o(s)) \\ &= f(\theta(s), \frac{\mathrm{d}\theta}{\mathrm{d}s}(s), I(s), E, F(s), \kappa_o(s))\end{aligned} \tag{3.159}$$

  where we should notice that the $\theta(s)$ is the only function. Besides, (3.159) is subjected to:

$$\theta(0) = 0;\ \frac{\mathrm{d}\theta}{\mathrm{d}s}(L) = \frac{M_o}{EI(L)} + \kappa_o(L) \tag{3.160}$$

  Therefore, according to the principle of minimum potential energy, what we need to do here is look for a proper function $\theta(s)$ that minimizes Π where $\theta(s)$ needs to satisfy the constraints (3.160) as well.

The following engineering scenarios are common and representative in CM-based applications as stated earlier in Section 3.3.1, also serving as a comparison to Newtonian framework. Here, we just pick up some representative cases in Section 3.3.1 for clarification.

3.4.1.1 General large deflection

Similarly, the cases of a slender straight beam and a slender beam of varying initial curvature subjected to beam-end loading conditions respectively are presented here. In Remark 8, a comprehensive scenario where different loading conditions and different beam geometries are considered is formulated as a BVP as well.

1. **A slender straight beam subjected to beam-end loading**
   As shown in Fig. 3.24, it's the simplest scenario where only beam-end loading is considered. Therefore, the

potential energy Π of the elastic system can be formulated via (3.159):

$$\begin{aligned}\Pi = f(\theta(s), \frac{\mathrm{d}\theta}{\mathrm{d}s}(s), s) &= \int_0^L \frac{1}{2} EI(s)(\frac{\mathrm{d}\theta}{\mathrm{d}s})^2 \mathrm{d}s - F_x(x_o(L) - \int_0^L \cos\theta(s)\mathrm{d}s) \\ &- F_y(\int_0^L \sin\theta(s)\mathrm{d}s - y_o(L)) - M_o(\theta(L) - \theta_o(L)) \\ &= \int_0^L \mathcal{L}(\theta(s), \frac{\mathrm{d}\theta}{\mathrm{d}s}(s), s)\mathrm{d}s\end{aligned} \tag{3.161}$$

where $\kappa_o(s) = 0$, $x_o(L) = L$, $y_o(L) = 0$, $\theta_o(L) = 0$ and I is constant since the straight beam is assumed to have constant cross sections here. Then, (3.161) is subjected to the following:

$$\theta(0) = 0; \ \frac{\mathrm{d}\theta}{\mathrm{d}s}(L) = \frac{M_o}{EI} \tag{3.162}$$

Remark 6 *Applying Lagrange Euler method to* (3.161)*, we will reach*

$$\frac{\partial \mathcal{L}}{\partial \theta} - \frac{\mathrm{d}}{\mathrm{d}s}(\frac{\partial \mathcal{L}}{\partial \theta'}) = -F_x \sin\theta(s) - F_y \cos\theta(s) - EI\frac{\mathrm{d}^2\theta}{\mathrm{d}s^2} = 0 \tag{3.163}$$

Reformulating (3.163) *and the constraints* (3.160)*, we will be able to arrive at:*

$$\begin{aligned} &\textit{D.E.} \quad \frac{\mathrm{d}^2\theta}{\mathrm{d}s^2} = -\frac{F_y}{EI}(\cos\theta(s) + \frac{F_x}{F_y}\sin\theta(s)) \\ &\textit{B.C.} \quad \theta(0) = 0 \\ &\qquad \frac{\mathrm{d}\theta}{\mathrm{d}s}(L) = \frac{M_o}{EI} \end{aligned}$$

which turns out to be BVP (3.25)*.*

2. **A slender beam of initial curvature subjected to beam-end loading**
   Here in this section, we move onto a different loading scenario: a slender beam of initial curvature subjected to beam-end loading (see BVP (3.30)). The total potential energy of the elastic system (see Fig. 3.25) can be

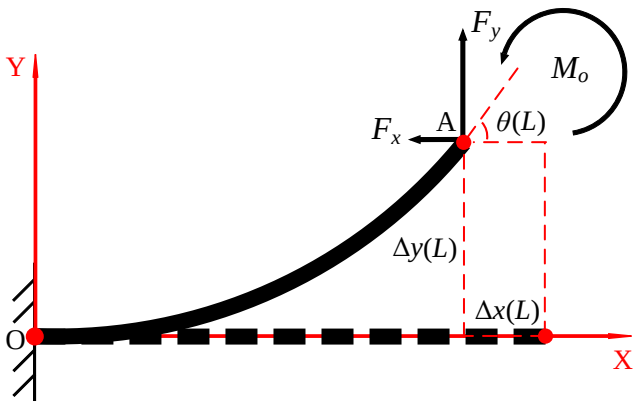

FIGURE 3.24: A slender straight beam subjected to beam-end loading demonstrated from Lagrange point of view

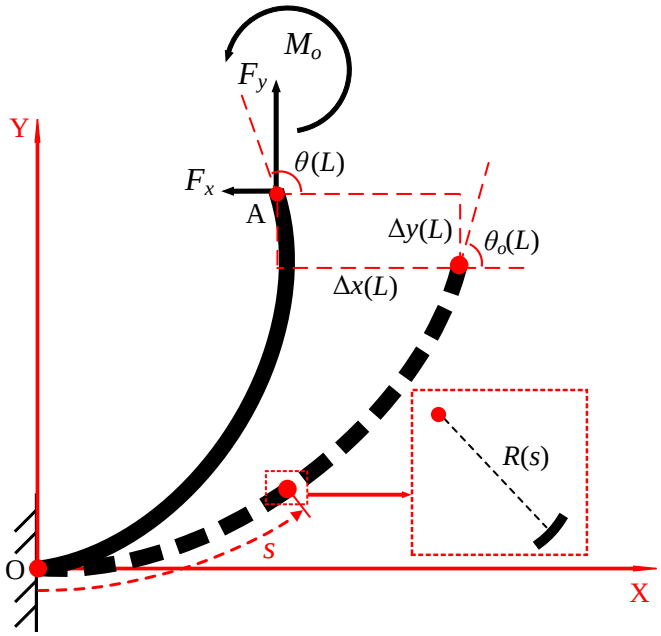

FIGURE 3.25: A slender beam of initial curvature subjected to beam-end loading demonstrated from Lagrangian point of view

formulated:

$$\begin{aligned}\Pi = f(\theta(s), \frac{\mathrm{d}\theta}{\mathrm{d}s}(s), s) &= \int_0^L \frac{1}{2} EI(s)(\frac{\mathrm{d}\theta}{\mathrm{d}s} - \kappa_o(s))^2 \mathrm{d}s - F_x(x_o(L) - \int_0^L \cos\theta(s)\mathrm{d}s) \\ &- F_y(\int_0^L \sin\theta(s)\mathrm{d}s - y_o(L)) - M_o(\theta(L) - \theta_o(L)) \\ &= \int_0^L \mathcal{L}(\theta(s), \frac{\mathrm{d}\theta}{\mathrm{d}s}(s), s)\mathrm{d}s\end{aligned} \tag{3.164}$$

where I is constant and $\kappa_o(s)$ is defined as a continuous and differentiable function of s since the ICB is assumed to have constant cross sections and uniformly varying curvature. Then, (3.164) is subjected to the following:

$$\theta(0) = 0;\ \frac{\mathrm{d}\theta}{\mathrm{d}s}(L) = \frac{M_o}{EI} + \kappa_o(L) \tag{3.165}$$

Remark 7 *Applying Lagrange Euler method to* (3.164)*, we will reach:*

$$\frac{\partial \mathcal{L}}{\partial \theta} - \frac{\mathrm{d}}{\mathrm{d}}(\frac{\partial \mathcal{L}}{\partial \theta'}) = -F_x \sin\theta(s) - F_y \cos\theta(s) + EI\frac{\mathrm{d}\kappa_o}{\mathrm{d}s} - EI\frac{\mathrm{d}^2\theta}{\mathrm{d}s^2} = 0 \tag{3.166}$$

Reformulating (3.166) *and the constraints* (3.160)*, we will be able to arrive at:*

$$\begin{aligned} &\textit{D.E.} \quad \frac{\mathrm{d}^2\theta}{\mathrm{d}s^2} = -\frac{F_y}{EI}(\cos\theta(s) + \frac{F_x}{F_y}\sin\theta(s)) + \frac{\mathrm{d}\kappa_o}{\mathrm{d}s} \\ &\textit{B.C.} \quad \theta(0) = 0 \\ &\qquad \frac{\mathrm{d}\theta}{\mathrm{d}s}(L) = \frac{M_o}{EI} + \kappa_o(L) \end{aligned}$$

which is actually BVP (3.30)*.*

Remark 8 *For simple loading scenarios stated above, it's both handy and straightforward to solve via moment equilibrium (Newtonian mechanics) or the energy framework (Lagrangian mechanics). In addition, it's also easy to prove*

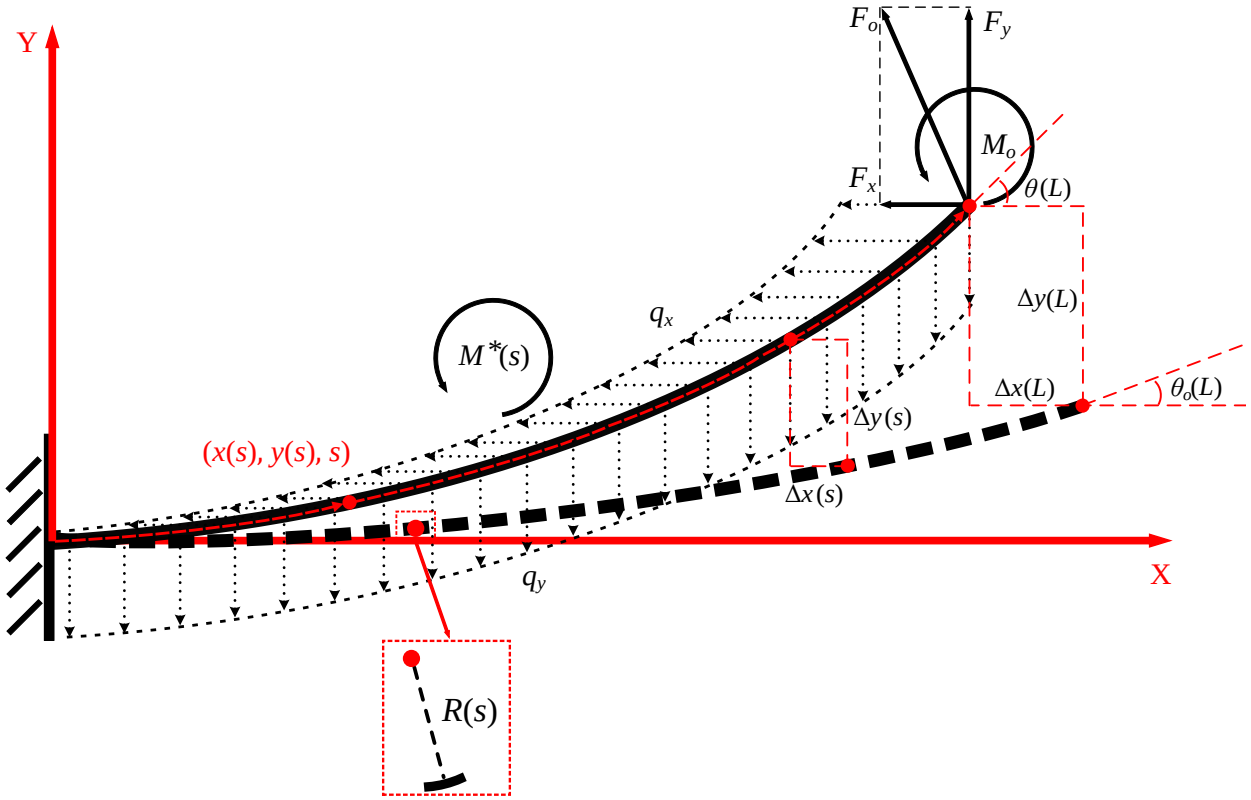

FIGURE 3.26: A slender beam subjected to external loading via Lagrangian framework

their equivalence in theory (see Remarks 6 and 7). However, it tends to be complex in some cases like gravity if we stick to Newtonian framework (Wu and Zheng, 2022a). Similar to Remark 3, we can also consider several more loading conditions as long as the these external loading conditions are conservative loading, such as varying cross-sections, gravity, beam-end loading conditions (see Fig. 3.24) and so on (see details in Fig. 3.26). Note that pressure can not be considered here since it is not conservative, which means the work done by pressure depends on the path not the displacement. To consider more possible scenarios, we write down the general formulation of the potential energy of the studied elastic system:

$$\begin{aligned}\Pi = f(\theta(s), \frac{\mathrm{d}\theta}{\mathrm{d}s}(s), s...) = &\int_0^L \frac{1}{2} EI(s)[\frac{\mathrm{d}\theta}{\mathrm{d}s} - \kappa_o(s)]^2 \mathrm{d}s - F_x[\int_0^L \cos\theta_o(s)\mathrm{d}s - \int_0^L \cos\theta(s)\mathrm{d}s] \\ &- F_y[\int_0^L \sin\theta(s)\mathrm{d}s - \int_0^L \sin\theta_o(s)\mathrm{d}s] - M_o[\theta(L) - \theta_o(L)] - \int_0^L q_x(s)[x_o(s) \\ &- \int_0^s \cos\theta(\xi)\mathrm{d}\xi]\mathrm{d}s - \int_0^L q_y(s)[\int_0^s \sin\theta(\xi)\mathrm{d}\xi - y_o(s)]\mathrm{d}s \\ &= \int_0^L \mathcal{L}(\theta(s), \frac{\mathrm{d}\theta}{\mathrm{d}s}(s), s...)\mathrm{d}s\end{aligned} \tag{3.167}$$

subjected to (3.160).

3.4.1.2 Contact problem

Utilizing physical contact in CMs gradually becomes important since some contact-aided CMs present better and diverse mechanical responses than the contact-free ones (Jin et al., 2020)(Mankame and Ananthasuresh, 2002) (previously discussed in Section 3.3.1.3). Besides the constraints stated in (3.160), we also have some external geometrical

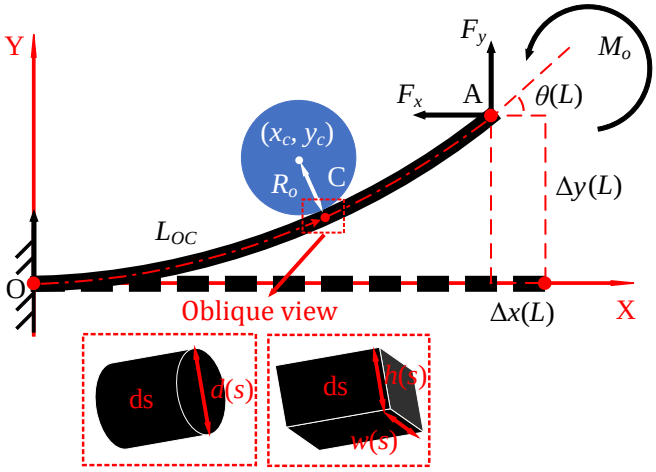

FIGURE 3.27: A slender straight beam subjected to beam-end loading and constraint by a rigid cylinder demonstrated from Lagrangian point of view

constraints for this studied scenario:

$$\begin{aligned}&\int_0^{L_{OC}} \cos\theta(s)\mathrm{d}s = x_c + (R_o + \frac{h}{2})\sin\theta(L_{OC});\ \int_0^{L_{OC}} \sin\theta(s)\mathrm{d}s = y_c - (R_o + \frac{h}{2})\cos\theta(L_{OC});\\ &[(\int_0^s \cos\theta(\xi)\mathrm{d}\xi - x_c)^2 + (\int_0^s \sin\theta(\xi)\mathrm{d}\xi - y_c)^2]^{0.5} \geq R_o + \frac{h}{2}\end{aligned} \tag{3.168}$$

or

$$\begin{aligned}&\int_0^{L_{OC}} \cos\theta(s)\mathrm{d}s = x_c + (R_o + \frac{d}{2})\sin\theta(L_{OC});\ \int_0^{L_{OC}} \sin\theta(s)\mathrm{d}s = y_c - (R_o + \frac{d}{2})\cos\theta(L_{OC});\\ &[(\int_0^s \cos\theta(\xi)\mathrm{d}\xi - x_c)^2 + (\int_0^s \sin\theta(\xi)\mathrm{d}\xi - y_c)^2]^{0.5} \geq R_o + \frac{d}{2}\end{aligned} \tag{3.169}$$

for rectangular cross sections and round cross sections respectively and L_{OC} is an unknown variable. Here, we assume the contact between the beam and the rigid cylinder is simply a straight line normal to the page (as shown in Fig 3.27). Then, we can formulate the total potential energy as follows:

$$\begin{aligned}\Pi = f(\theta(s), \frac{\mathrm{d}\theta}{\mathrm{d}s}(s), s) &= \int_0^L \frac{1}{2}EI(s)(\frac{\mathrm{d}\theta}{\mathrm{d}s})^2\mathrm{d}s - F_x(x_o(L) - \int_0^L \cos\theta(s)\mathrm{d}s)\\ &- F_y(\int_0^L \sin\theta(s)\mathrm{d}s - y_o(L)) - M_o(\theta(L) - \theta_o(L))\\ &= \int_0^L \mathcal{L}(\theta(s), \frac{\mathrm{d}\theta}{\mathrm{d}s}(s), s)\mathrm{d}s\end{aligned} \tag{3.170}$$

where $\kappa_o(s) = 0$, $x_o(L) = L$, $y_o(L) = 0$, $\theta_o(L) = 0$ and I is constant. In this case, it is clear that we need to look for a proper function $\theta(s)$ to minimize Π as well as to satisfy the constraints (3.160)(3.168)(3.169).

3.4.2 Reduced-mode Cosserat rod model

Similar to Section 3.4.1, we need to first formulate the total potential energy Π as a function of $\theta(s)$. According to (3.121)(3.135)(3.158), we can formulate the total potential energy as follows:

$$\begin{aligned}\Pi = E_p - W_p &= \int_0^L \frac{1}{2}EA(s)\epsilon_a^2 + \frac{1}{2}GA(s)\epsilon_s^2 + \frac{1}{2}EI(s)\epsilon_b^2 \mathrm{d}s - f_{W_p}(F(s),\theta(s),\kappa_o(s)) \\ &= \int_0^L \frac{1}{2}EA(s)(\frac{\sin\theta(s)F_y - \cos\theta(s)F_x}{EA(s)})^2 + \frac{1}{2}GA(s)(\frac{\cos\theta(s)F_y + \sin\theta(s)F_x}{GA(s)})^2 \\ &+ \frac{1}{2}EI(s)(\frac{\mathrm{d}\theta}{\mathrm{d}s}(s) - \kappa_o(s))^2 \mathrm{d}s - f_{W_p}(F(s),\theta(s),\kappa_o(s))\end{aligned} \tag{3.171}$$

where we should notice that $\theta(s)$ is the only unknown function. Besides, (3.171) is subjected to (3.160). For this functional minimization problem, we are looking for the proper function $\theta(s)$ and other associated functions or variables that minimize the value of Π.

3.4.3 From 2D to 3D: full-mode Cosserat Rod theory

Similar to the idea in Section 3.4.1 and Section 3.4.2, we have the same strategy for solving Cosserat rod theory. The elastic energy can be formulated as:

$$E_p = f_{E_p}(u(s), v(s)) \tag{3.172}$$

and the external potential energy is defined as:

$$W_p = f_{W_p}(F(s), \mathbf{R}(s), v_o(s)) \tag{3.173}$$

Logically, we will have the total potential energy:

$$\Pi = E_p - W_p = f_{E_p}(u(s), v(s)) - f_{W_p}(F(s), \mathbf{R}(s), \mathbf{r}(s), v_o(s)) \tag{3.174}$$

constrained by some boundary conditions, such as (1.29). Note that in (3.174), the unknown variables are $u(s)$, $v(s)$ and $\mathbf{R}(s)$. Essentially, we aim to find the proper functions $u(s)$, $v(s)$ and $\mathbf{R}(s)$ and other associated functions or variables that minimize the value of Π.

3.5 Conclusions

In this chapter, we first present the methodology for geometrical definition of planar slender structures in three different coordinate systems and the transformation to body frame (where geometrical nonlinear Euler Bernoulli beam equation is written). Secondly, we have mainly stated the modeling of large deflection of slender beams under different loading conditions via moment balance (Newtonian mechanics) and the energy framework (Lagrangian mechanics) respectively. We have also proved the equivalence of moment balance and the energy framework (see Remarks 6 and 7) in some simple cases. However, in some more complex scenarios such as varying distributed loading and varying initial curvature, studying the systems under the energy framework turns out more efficient and straightforward since the governing ODE (3.33) under Newtonian framework turns complicated with some tough double integration in it. On the contrary, formulating the problem via the energy framework results in a much simpler and more straightforward manner that is well-explained by the classic functional minimization problem. However, under the energy framework, we can not directly consider external forces that are not conservative, such as pressure. Besides, the analysis of spatial deflections using full-mode Cosserat rod theory are briefly discussed from the perspectives of moment balance and the energy framework respectively where new approximation strategies are proposed.

Chapter 4

Various Methods of Solving Large-deflection Problems Governed by Beam Theory

4.1 Introduction

As stated in Chapter 3, two modeling frameworks for large-deflection problems are explained in detail whereas, in this chapter, some standard methods introduced from applied mathematics are proposed to solve these models. First of all, a collocation scheme is used to handle the coordinate transformation problem, which aims to prepare for large-deflection analysis of slender beams. Secondly, approximate closed-form solutions, hybrid methods and numerical methods for solving large-deflection problems governed by beam theory are presented accordingly. Finally, a comprehensive study on geometrical definition to large-deflection analysis is presented to validate the proposed methodology. The aforementioned methods are all presented along with illustrative examples for validation.

4.2 Transformation from other coordinate systems into body frame

As mentioned above, users may define the beam geometry (beam axis) in each of the aforementioned three coordinate systems . However, these user-defined curves all have to be transformed into body frame for large deflection analysis. Here, we can formulate the transformation process as looking for solutions to some specific ODEs. According to Weierstrass theorem, we define a function $\vartheta_o(s)$ to approximate the curves defined in other coordinate systems, which is an nth-order polynomial:

$$\vartheta_o(s) = \sum_{i=0}^{n} c_i s^i \tag{4.1}$$

where there are $n+1$ unknown coefficients ($i = 0, 1, 2, 3...n$). If the curves defined in other coordinate systems have continuous and differentiable curvature (see (3.2) and (3.6)), (4.1) can be used straightforward since polynomials are continuous and differentiable. If the curves defined are not differentiable, we need to use piecewise functions to characterize the axis curve of the studied beam instead. In the following sections, we proceed with the differentiable ones.

4.2.1 Numerical strategy via weighted residual methods

Taking a look at (3.14), basically, we need to find a function $\vartheta(s)$ to satisfy (3.14), which equivalently can be considered as finding a solution to this 0th-order ODE. Therefore, according to the concept of weighted residual methods in Section 2.5.3, we need to define the residual function, and force it into 0 within a domain:

$$\mathcal{R}(x) = \begin{bmatrix} \int_0^{\int_{\underline{x}}^{x} \sqrt{1+(\frac{\mathrm{d}y}{\mathrm{d}t}(t))^2}\mathrm{d}t} \sin\vartheta_o(s)\mathrm{d}s - y(x) \\ \int_0^{\int_{\underline{x}}^{x} \sqrt{1+(\frac{\mathrm{d}y}{\mathrm{d}t}(t))^2}\mathrm{d}t} \cos\vartheta_o(s)\mathrm{d}s - x \end{bmatrix} \neq \begin{bmatrix} 0 \\ 0 \end{bmatrix}, \quad x \in [\underline{x}, \bar{x}] \tag{4.2}$$

and

$$\int_{\underline{x}}^{\bar{x}} \mathcal{W}_j \mathcal{R}(x)\mathrm{d}x = 0 \tag{4.3}$$

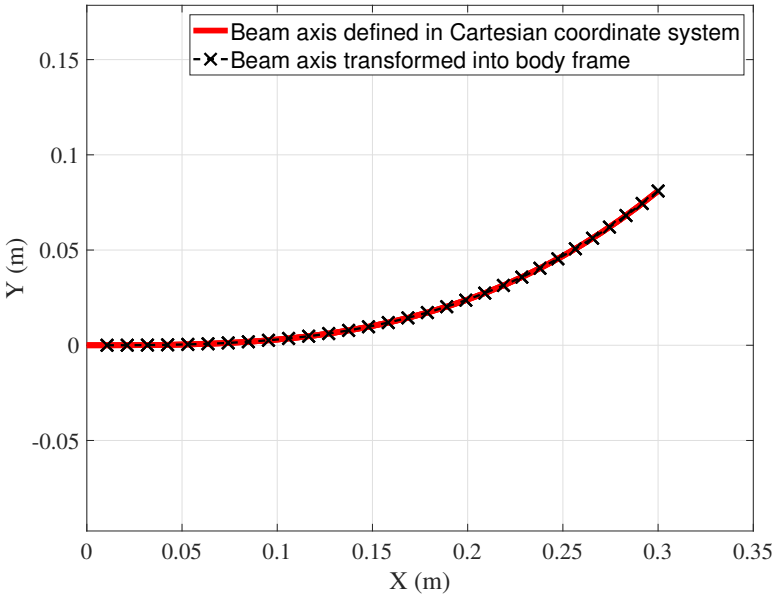

FIGURE 4.1: Cubic-function-shape beam axis transformed from Cartesian coordinate system to body frame

Obviously, if we use methods like Galerkin method to satisfy the weak form over the whole domain ($[\underline{x}, \bar{x}]$ in this case), we have to face numerical integration twice as shown in (4.3). Therefore, to bypass this difficulty, collocation method could be a handy option since we only need to satisfy (4.3) at some specific collocation points. We then define the weight functions as:

$$\mathcal{W}_j(x) = \delta(x - x_j) \tag{4.4}$$

where x_j is the chosen collocation point. Substituting (4.4) into (4.3), we have:

$$\int_{\underline{x}}^{\bar{x}} \mathcal{W}_j(x)\mathcal{R}(x)\mathrm{d}x = \mathcal{R}(x_j) = \begin{bmatrix} \int_0^{\int_{\underline{x}}^{x_j} \sqrt{1+(\frac{\mathrm{d}y}{\mathrm{d}x}(x))^2}\mathrm{d}x} \sin\vartheta_o(s)\mathrm{d}s - y(x_j) \\ \int_0^{\int_{\underline{x}}^{x_j} \sqrt{1+(\frac{\mathrm{d}y}{\mathrm{d}x}(x))^2}\mathrm{d}x} \cos\vartheta_o(s)\mathrm{d}s - x_j \end{bmatrix} = \begin{bmatrix} 0 \\ 0 \end{bmatrix},\ x_j = \underline{x} + \frac{(j-1)}{n}(\bar{x} - \underline{x}) \tag{4.5}$$

which contains $2n+2$ equations. Obviously, $\int_{\underline{x}}^{x_j} \sqrt{1 + (\frac{\mathrm{d}y}{\mathrm{d}x})^2}\mathrm{d}x$ can be explicitly calculated as long as x_j is given. In (4.5), there are altogether $2n+2$ equations to solve $2n+2$ unknown polynomial coefficients c_i.

Likewise, we have same strategy for (3.15) as well:

$$\begin{aligned} &\int_{\underline{\phi}}^{\bar{\phi}} \mathcal{W}_j(\phi)\mathcal{R}(\phi)\mathrm{d}\phi = \mathcal{R}(\phi_j) \\ &= \begin{bmatrix} \int_0^{\int_{\underline{\phi}}^{\phi_j} \sqrt{r_a(\phi)^2+(\frac{\mathrm{d}r_a}{\mathrm{d}\phi}(\phi))^2}\mathrm{d}\phi} \cos\vartheta(s)\mathrm{d}s - r(\phi_j)\cos\phi_j \\ \int_0^{\int_{\underline{\phi}}^{\phi_j} \sqrt{r_a(\phi)^2+(\frac{\mathrm{d}r_a}{\mathrm{d}\phi}(\alpha))^2}\mathrm{d}\phi} \sin\vartheta(s)\mathrm{d}s - r(\phi_j)\sin\phi_j \end{bmatrix} = \begin{bmatrix} 0 \\ 0 \end{bmatrix};\ \phi_j = \underline{\phi} + \frac{(j-1)}{n}(\bar{\phi} - \underline{\phi}) \end{aligned} \tag{4.6}$$

which contains $2n+2$ equations. Obviously, the $2n+2$ unknown coefficients can be also solved via (4.6). Logically, we can solve the above equations in (4.5)(4.6) via Newton Raphson method.

4.2.2 Illustrative examples

Here, we present typical cases for each of the following two scenarios. First of all, we define a cubic function in Cartesian coordinate system:

$$y = 10x^3,\ x \in [0, 0.3] \tag{4.7}$$

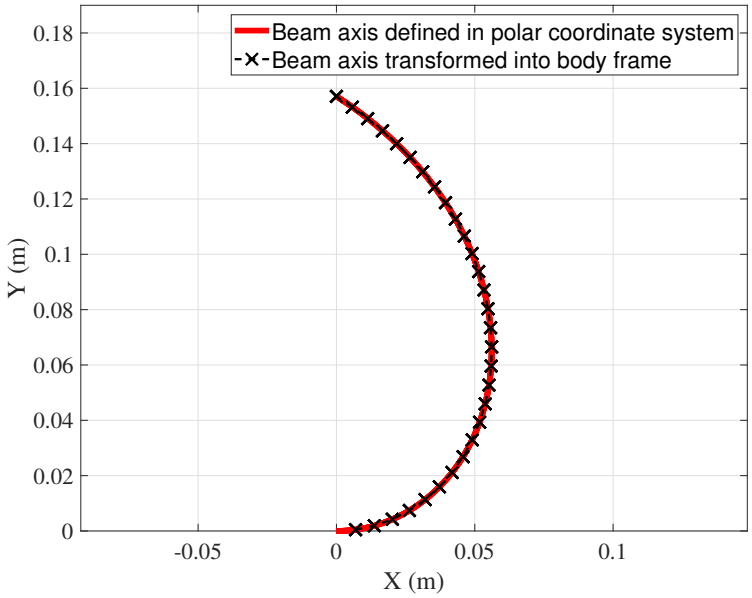

FIGURE 4.2: Archimedean-spiral-shape beam axis transformed from Cartesian coordinate system to body frame

Following (4.5), we can obtain the corresponding numerical solution ϑ_o. We can characterize the beam shape via (3.10). The axis curve defined in Cartesian coordinate system is compared to the one transformed in body frame as shown in Fig. 4.1. Similarly, if we define the beam axis using Archimedean spiral in polar coordinate system:

$$r_a = 0.1\phi,\ \phi \in [0, \pi] \tag{4.8}$$

Following (4.6), we can similarly have the graphical results as shown in Fig. 4.2 where the axis curve defined in polar coordinate system is compared to the one transformed in body frame.

4.3 Approximate closed-form solutions to BVPs

It's normally difficult to find analytical solutions to nonlinear ODEs. but we can instead try to find the closed-form approximate solutions to these ODEs using Adomian decomposition method (see Section 2.6). In this section, we apply Adomian decomposition method to Euler Bernoulli beam theory to seek for closed-form solutions. Here, we use the nondimensionalized one (3.100) as an example.

4.3.1 Detailed deduction

First of all, we can reformulate (3.100) into:

$$\hat{L}_t[\hat{\theta}(\hat{s})] + \hat{N}[\hat{\theta}(\hat{s})] = 0 \tag{4.9}$$

where $\hat{L}_t[.]$ here denotes the second derivative operator $\frac{\mathrm{d}^2}{\mathrm{d}\hat{s}^2}[.]$ and $\hat{N}[.]$ denotes the nonlinear operator: $\hat{N}[\hat{\theta}(\hat{s})] = f(\hat{\theta}) = f_y \cos\hat{\theta} + f_x \sin\hat{\theta}$. Integrating (4.9) twice (equivalently, $\hat{L}_t[.]^{-1}$), we have

$$\hat{\theta}(\hat{s}) = -\hat{L}_t^{-1}[\hat{N}[\hat{\theta}(\hat{s})]] \tag{4.10}$$

Precisely,

$$\hat{\theta}(\hat{s}) = \hat{\theta}(0) + \frac{\mathrm{d}\hat{\theta}}{\mathrm{d}\hat{s}}(1)\hat{s} - \int_0^{\hat{s}} \int_1^{\gamma} \hat{N}[\hat{\theta}]\mathrm{d}\hat{s}\mathrm{d}\gamma \tag{4.11}$$

where

$$\begin{aligned}\hat{\theta}(\hat{s}) &= \sum_{n=0}^{\infty} \hat{\theta}_n(\hat{s});\ \hat{N}[\hat{\theta}] = \sum_{n=0}^{\infty} \mathcal{A}_n; \\ \hat{\theta}_0(\hat{s}) &= \hat{\theta}(0) + \frac{\mathrm{d}\hat{\theta}}{\mathrm{d}\hat{s}}(1)\hat{s} = (m_o + \frac{1}{r})\hat{s}\end{aligned} \tag{4.12}$$

Obviously, we have

$$\sum_{n=1}^{\infty} \hat{\theta}_n(\hat{s}) = -\int_0^{\hat{s}} \int_1^t \sum_{n=0}^{\infty} \mathcal{A}_n \mathrm{d}\hat{s}\mathrm{d}t; \tag{4.13}$$

Now, we obtain the formulation for each decomposed $\hat{\theta}_n(\hat{s})$:

$$\hat{\theta}_n(\hat{s}) = -\int_0^{\hat{s}} \int_1^t \mathcal{A}_{n-1} \mathrm{d}\hat{s}\mathrm{d}t;\ n \geq 1 \tag{4.14}$$

Following (2.41), (2.42) and (4.14), we will be able to find the series $\sum_0^{\infty} \hat{\theta}_n$ by the recurrent relation. Here, we briefly present the recurrent process step by step:

$$\begin{aligned}&\text{Step 1: } \hat{\theta}_0 = (m_o + \frac{1}{r})\hat{s} \\ &\text{Step 2: } \mathcal{A}_0 = \hat{N}(\hat{\theta}_0) = f(\hat{\theta}_0) \\ &\text{Step 3: } \hat{\theta}_1 = -\int_0^{\hat{s}} \int_1^t \mathcal{A}_0 \mathrm{d}\hat{s}\mathrm{d}t \\ &\text{Step 4: } \mathcal{A}_1 = \frac{\mathrm{d}}{\mathrm{d}\lambda} \hat{N}[\hat{\theta}_0 + \lambda\hat{\theta}_1]\Big|_{\lambda=0} = \hat{\theta}_1 f'(\hat{\theta}_0) \\ &\text{Step 5: } \hat{\theta}_2 = -\int_0^{\hat{s}} \int_1^t \mathcal{A}_1 \mathrm{d}\hat{s}\mathrm{d}t \\ &\text{Step 6: } \mathcal{A}_2 = \frac{\mathrm{d}}{\mathrm{d}\lambda} \hat{N}[\hat{\theta}_0 + \lambda\hat{\theta}_1 + \lambda^2\hat{\theta}_2]\Big|_{\lambda=0} = \hat{\theta}_2 f'(\hat{\theta}_0) + \frac{1}{2!}\hat{\theta}_1^2 f''(\hat{\theta}_0) \\ &\text{Step 7: } ...\end{aligned} \tag{4.15}$$

Finally, we will be able to find the semi-analytical (closed-form and symbolic) solution to (3.100) via

$$\hat{\theta} = \sum_{n=0}^{\infty} \hat{\theta}_n \tag{4.16}$$

However, practically, instead of using the infinite series (4.16), we normally use the following truncated series for the studied problem:

$$\hat{\theta} = \sum_{n=0}^{m} \hat{\theta}_n \tag{4.17}$$

where we set normally $m \geq 7$ for large-deflection problems.

Remark 9 *As ADM is a method for solving general ODEs, the ODEs derived from several different engineering scenarios in CMs (Wu and Zheng, 2022a)(Wu and Zheng, 2022d) can be therefore solved in a semi-analytical manner. In the literature, (Banerjee, Bhattacharya, and Mallik, 2008) has stated a similar strategy without nondimensionalizing the governing ODE, and only straight beams are considered (see Section 4.1.1 in Banerjee, Bhattacharya, and Mallik, 2008).*

TABLE 4.1: Beam-end coordinates solved by Adomian decomposition method (ADM)

	Case	Case 1	Case 2	Case 3	Case 4
Loading	f_x	1	0.5	−0.5	−1
	f_y	0.6	0.3	−0.3	−0.6
	m_o	0.8	0.4	−0.4	−0.8
ADM	$\hat{x}(1)$	0.6606	0.9194	0.9615	0.8932
	$\hat{y}(1)$	0.6448	0.3464	−0.2408	−0.3899
	$\hat{\theta}(1)$	1.3601	0.6442	−0.4629	−0.7987
	NOS	8	8	8	8
FEM	$\hat{x}(1)$	0.6620	0.9194	0.9615	0.8932
	$\hat{y}(1)$	0.6441	0.3463	−0.2408	−0.3899
	$\hat{\theta}(1)$	1.3575	0.6441	−0.4629	−0.7988
	NOE	20	20	20	20
ER	$\hat{x}(1)$	0.21%	0.00%	0.00%	0.00%
	$\hat{y}(1)$	0.11%	0.02%	0.00%	0.00%
	$\hat{\theta}(1)$	0.19%	0.02%	0.00%	0.01%
CE (s)	ADM	0.22	0.21	0.25	0.22
	FEM	14	9	10	18

4.3.2 Improved Adomian decomposition method

According to (4.16) and (4.17), we have

$$\hat{\theta}_1 = \frac{f_x(\sin((m_o+\frac{1}{r})\hat{s}) - \cos((m_o+\frac{1}{r}))\hat{s}(m_o+\frac{1}{r}))}{(m_o+\frac{1}{r})^2} + \frac{f_y(\cos((m_o+\frac{1}{r})\hat{s}) + \hat{s}(m_o+\frac{1}{r})\sin((m_o+\frac{1}{r})) - 1)}{(m_o+\frac{1}{r})^2} \tag{4.18}$$

we can notice that the denominators in (4.18) will be equal to 0 if the beam is a straight beam ($\frac{1}{r}=0$) only subjected to beam-end forces ($m_o = 0$). In this case, we will have troubles in numerical calculation about dealing with the 0 in the denominators, usually ending up with huge values. Besides, in $\hat{\theta}_n$, such as (4.18), there are many transcendental functions, which are difficult to handle in numerical calculation. Therefore, to solve the mentioned two numerical problems as well as optimize the algorithm, we here utilize Taylor series to bypass these numerical traps.

Obviously, the mentioned two numerical problems originally come from the nonlinear operator $\hat{N}[\hat{\theta}(\hat{s})] = f(\hat{\theta}) = f_y\cos\hat{\theta} + f_x\sin\hat{\theta}$ which has highly nonlinear terms. Here, we use truncated polynomial functions to approximate $f(\hat{\theta})$:

$$\begin{aligned} f(\hat{\theta}) &= f_y\cos\hat{\theta} + f_x\sin\hat{\theta} \\ &= f_y(1 - \frac{\hat{\theta}^2}{2!} + \frac{\hat{\theta}^4}{4!} + ...) + f_x(\hat{\theta} - \frac{\hat{\theta}^3}{3!} + \frac{\hat{\theta}^5}{5!} + ...) \end{aligned} \tag{4.19}$$

Proceeding with (4.19) to follow the steps in (4.15), we will be able to reach the corresponding formulations for $\hat{\theta}$ in (4.16) and (4.17). In this way, we will be able to bypass the numerical traps of the denominators being 0 as well as sustain the acceptable accuracy.

4.3.3 Illustrative examples

To validate the proposed method (improved ADM), four cases are studied, and the nondimensionalized beam-end loading along with the initial curvature is given below:

$$\text{Case 1: } f_x = 1;\ f_y = 0.6;\ m_o = 0.8;\ \frac{1}{r} = 0;$$

$$\text{Case 2: } f_x = 0.5;\ f_y = 0.3;\ m_o = 0.4;\ \frac{1}{r} = 0;$$

$$\text{Case 3: } f_x = -0.5;\ f_y = -0.3;\ m_o = -0.4;\ \frac{1}{r} = 0;$$

$$\text{Case 4: } f_x = -1;\ f_y = -0.6;\ m_o = -0.8;\ \frac{1}{r} = 0;$$

The beam-end coordinates and deflected beam shapes solved via ADM are presented in Table 4.1 and Fig. 4.3 where FEM is used as verification as well.

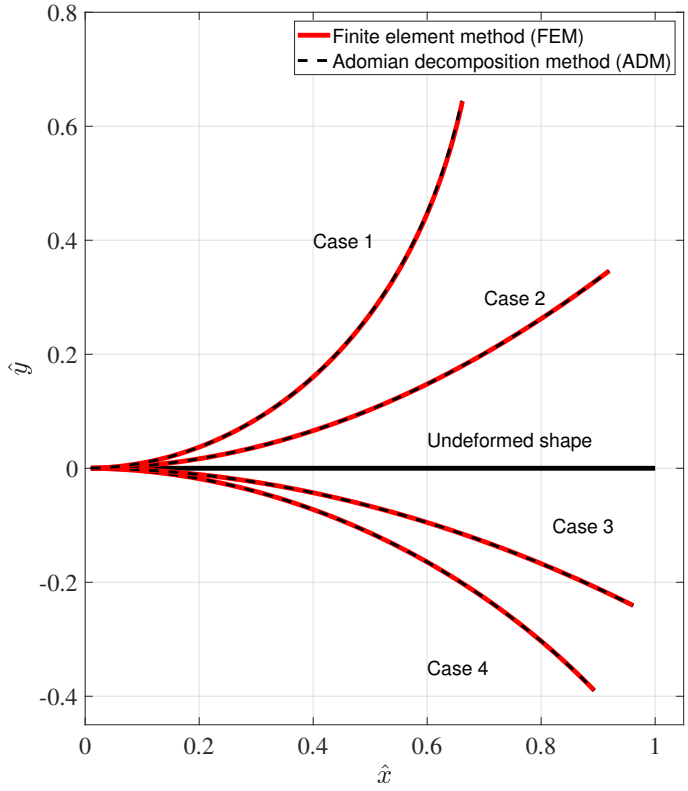

FIGURE 4.3: Graphical results solved via Adomian decomposition method (ADM)

4.4 Hybrid methods of solving BVPs

Besides the closed-form solutions, we have also proposed a hybrid method to solve the governing BVPs. As stated in BVP (3.100) in Section 3.3.1.4, the governing ODE is highly nonlinear. Obviously, we can linearize the nonlinear BVP so we can find the analytical solution to the linearized BVP that describes the intermediate-range deflection. Besides, the linearized model can be further chained for analyzing large deflections and contact problems where we have always analytical solutions in each elementary model. Therefore, in this context, we term this chained-model strategy as hybrid methods. In the first part of this section, we first introduce the linearization strategy for the original BVP (Section 4.4.1.1), and demonstrate the application of the linearized model to buckling problems (Section 4.4.1.2) and intermediate-range deflection (Section 4.4.1.3). Then, we present the chained algorithm for solving large-deflection problems, and clarify its potential applications to contact problems.

4.4.1 Linearized model for intermediate-range deflection

As reviewed in Section 1.2.3.1, in Chapter 3 of Awtar's PhD thesis (Awtar, 2003), he derived a simple, clear and also analytical formulation via assuming that the curvature of the deflected beam is small enough to avoid the body-frame coordinate system and instead use the global coordinate system, which is mathematically simpler and user-friendly. This methodology is termed as beam constraint model (BCM), serving as a good tool of modeling intermediate-range deflections in high-precision flexure-based motion stages. It has been successful and widely used in this field since its clear and precise formulation offers a sharp insight into flexure deflection and handy implementation.

4.4.1.1 Formulation of body-frame beam constraint model

Compared to the the beam constraint model (BCM) (Awtar, Slocum, and Sevincer, 2007) expressed in the global coordinate system, however, in this section, we formulate the proposed beam model via body frame, **namely body-frame beam constrain model (BBCM).** To reveal the mathematical essence of the governing equation, we proceed with the nondimensionalized BVP (3.100). Since we here deal with the most fundamental case (the intermediate-range deflection of a slender straight beam due to beam-end loading), BVP (3.100) needs to be modified a bit with the condition ($\kappa_o = 0$) as well as the boundary conditions:

$$\begin{aligned} &\text{D.E.} \quad \frac{\mathrm{d}^2\hat{\theta}}{\mathrm{d}\hat{s}^2} = -f_y \cos\hat{\theta}(\hat{s}) - f_x \sin\hat{\theta}(\hat{s}) \\ &\text{B.C.} \quad g\left(\hat{\theta}(0), \hat{\theta}'(0), \hat{\theta}(1), \hat{\theta}'(1)\right) = 0 \end{aligned} \tag{4.20}$$

where

$$f_x = \frac{F_x L^2}{EI};\ f_y = \frac{F_y L^2}{EI};\ m_o = \frac{M_o L}{EI};\ \hat{s} \in [0,1] \tag{4.21}$$

Note that the B.C. are rewritten into a more general manner instead of just representing beam-end loading, denoting different boundary conditions at the beam-end (see Fig. 4.4). Then, we can approximate the right hand side of the ODE (4.20) via the Maclaurin series of $\sin\hat{\theta}$ and $\cos\hat{\theta}$:

$$\begin{aligned} \sin\hat{\theta} &= \hat{\theta} - \frac{\hat{\theta}^3}{3!} + \frac{\hat{\theta}^5}{5!} - \frac{\hat{\theta}^7}{7!} + \frac{\hat{\theta}^9}{9!} - \ldots \\ \cos\hat{\theta} &= 1 - \frac{\hat{\theta}^2}{2!} + \frac{\hat{\theta}^4}{4!} - \frac{\hat{\theta}^6}{6!} + \frac{\hat{\theta}^8}{8!} - \ldots \end{aligned} \tag{4.22}$$

Under the assumption that $\hat{\theta}$ is small, then if we just use the first terms of these series:

$$\begin{aligned} \sin\hat{\theta} &\approx \hat{\theta} \\ \cos\hat{\theta} &\approx 1 \end{aligned} \tag{4.23}$$

we will end up with:

$$\begin{aligned} &\text{D.E.} \quad \frac{\mathrm{d}^2\hat{\theta}}{\mathrm{d}\hat{s}^2} + f_x\hat{\theta}(\hat{s}) = -f_y \\ &\text{B.C.} \quad g\left(\hat{\theta}(0), \hat{\theta}'(0), \hat{\theta}(1), \hat{\theta}'(1)\right) = 0 \end{aligned} \tag{4.24}$$

Obviously, the ODE of (4.24) is a typical **non-homogeneous second-order linear ODE** with constant coefficients. **Therefore, its analytical solution always exists given the available boundary conditions.**

Remark 10 *Note (4.24) is linearized from the original BVP (4.20) so it's able to locally work in the interval near the point of expansion where the linearized function (the truncated Maclaurin series) can relatively accurately approximate the original function. In other words, the value of $\hat{\theta}$ should better be within or at least not be too far away from its radius of convergence around $\hat{\theta} = 0$, which implies that this ODE only governs small-to-intermediate-range deflection of slender beams from the physical perspective.*

Logically, we will have the following:

$$\hat{x}(\hat{s}) = \int_0^{\hat{s}} \cos(\hat{\theta}(\xi)) - f_x\beta \mathrm{d}\xi;\ \hat{y}(\hat{s}) = \int_0^{\hat{s}} \sin(\hat{\theta}(\xi))\mathrm{d}\xi \tag{4.25}$$

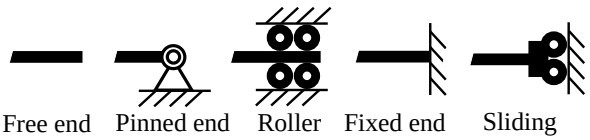

FIGURE 4.4: Different boundary conditions at beam ends

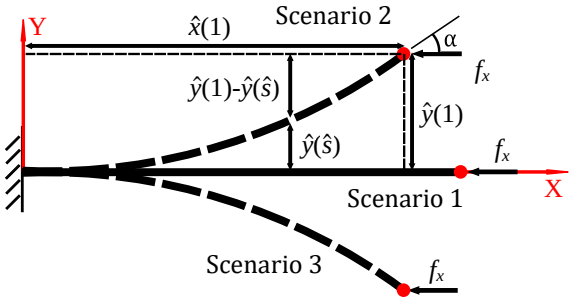

(A) Schematic diagram of a slender straight beam fixed at one end and exerted by an axial load

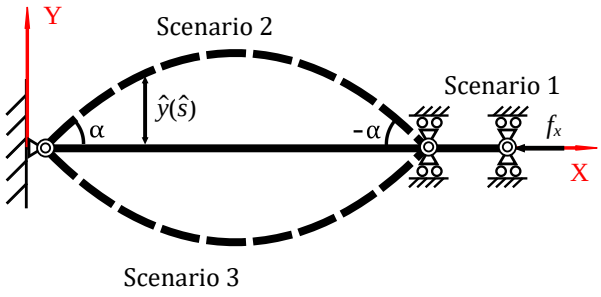

(B) Schematic diagram of a slender straight beam constrained by moving passive kinematic joints at both ends

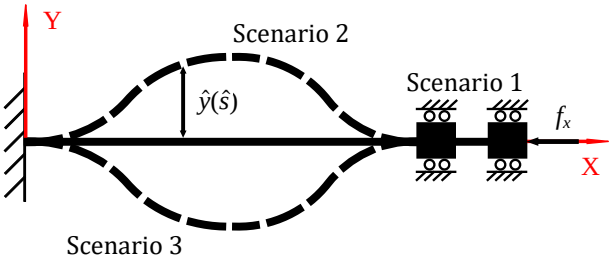

(C) Schematic diagram of a slender straight beam subjected by moving clamped constraints at the both ends

FIGURE 4.5: 3 typical types of buckling of a slender beam

where $\hat{x}(\hat{s})$ and $\hat{y}(\hat{s})$ are the nondimensionalized coordinates along the beam axis; $f_x\beta$ refers to the axial elastic stretch with $\beta = \frac{h^2}{12L^2}$ for rectangular cross sections and $\beta = \frac{r^2}{4L^2}$ for round cross sections.

Remark 11 *In (4.25), we add a correction term (regarding the elastic stretch of the slender beam) along the global X axis by logically assuming that in small-to-intermediate-range deflections, the axial stretch has an insignificant but essential contribution to the deformation in global X axis. Note BCM also incorporates elastic stretching (see Eqs. 3.11 and 3.12 in Chapter 3, Awtar, 2003)*

In the above stated, we term (4.24) along with (4.25) as **Body-frame Beam Constraint Model (BBCM)**. In the following, we aim to handle two commonly-encountered types of beam deflections (buckling and deflection due to beam-end loading) in CMs via BBCM.

4.4.1.2 Case 1: Buckling of a slender straight beam

The buckling initiation is studied here under different boundary conditions where a slender straight beam is only subjected by an axial load. Essentially, they all share the same governing equation derived from (4.24) with $f_y = 0$:

$$\frac{\mathrm{d}^2\hat{\theta}}{\mathrm{d}\hat{s}^2} + f_x\hat{\theta}(\hat{s}) = 0 \tag{4.26}$$

which is essentially the corresponding homogeneous ODE of the one in (4.24). Then, we can directly write down the general solution $\hat{\theta}_h(\hat{s})$ to (4.26):

$$\hat{\theta}_h(\hat{s}) = C_1\cos(\sqrt{f_x}\hat{s}) + C_2\sin(\sqrt{f_x}\hat{s}) \tag{4.27}$$

Logically, with boundary conditions available, we will be able to find the exact analytical solution to (4.26). Mathematically speaking, the essence of buckling is all about bifurcation of differential equations no matter derived from solid mechanics or beam theories. Here, three types of buckling subjected to three groups of boundary conditions are studied (see Fig. 4.5). Note the linearized ODE (4.26) is used here to characterize the buckling initiation (bifurcation of ODE (4.26)) since it's straightforward to analyze the buckling limits of different modes using (4.25) and (4.27). As stated in Remark 10, BBCM can only deal with intermediate-range deflections due to the linearization manipulation used so BBCM is only valid around the initiation areas.

- **Subcase 1: a slender straight beam fixed at one end and exerted by an axial load**
  As shown in Fig. 4.5a, the boundary conditions are

$$\text{B.C. } \hat{\theta}_h(0) = 0;\ \frac{\mathrm{d}\hat{\theta}_h(1)}{\mathrm{d}\hat{s}} = 0 \tag{4.28}$$

which yields the analytical solution:

$$\begin{aligned} \hat{\theta}_h(s) &= C_2 \sin(\sqrt{f_x}\hat{s}) \\ f_x^* &= [\frac{\pi}{2} + (n-1)\pi]^2;\ \ n = 1, 2, 3... \end{aligned} \tag{4.29}$$

To characterize the intermediate-range buckling shape, we need to follow the procedure below. Rearranging (4.20), we will have the following:

$$\frac{1}{2}(\frac{\mathrm{d}\hat{\theta}}{\mathrm{d}\hat{s}})^2 - f_x \cos\hat{\theta}(\hat{s}) = C \tag{4.30}$$

where C is an unknown constant which can be determined by the boundary conditions. Precisely,

$$C = \frac{1}{2}(\frac{\mathrm{d}\hat{\theta}}{\mathrm{d}\hat{s}}(1))^2 - f_x \cos\hat{\theta}(1) = -f_x \cos\alpha \tag{4.31}$$

where $\frac{\mathrm{d}\hat{\theta}}{\mathrm{d}\hat{s}}(1) = 0$ and $\hat{\theta}(1) = \alpha$, and α is an unknown parameter to be determined. Then, we can reach

$$\frac{1}{2}(\frac{\mathrm{d}\hat{\theta}}{\mathrm{d}\hat{s}})^2 - f_x \cos\hat{\theta}(\hat{s}) = -f_x \cos\alpha \tag{4.32}$$

Obviously, it's not hard to find that $\hat{\theta} = 0$ ($\alpha = \hat{\theta}(1) = 0$) is the solution to (4.32) (Scenario 1 in Fig. 4.5a). Besides, manipulating (4.32) drives us to obtain:

$$\frac{\mathrm{d}\hat{\theta}}{\mathrm{d}\hat{s}} = +\sqrt{2f_x(\cos\hat{\theta} - \cos\alpha)} \tag{4.33}$$

if $\alpha > 0$ (Scenario 2 in Fig. 4.5a) and

$$\frac{\mathrm{d}\hat{\theta}}{\mathrm{d}\hat{s}} = -\sqrt{2f_x(\cos\hat{\theta} - \cos\alpha)} \tag{4.34}$$

if $\alpha < 0$ (Scenario 3 in Fig. 4.5a). Taking Scenario 2 for example, we will have

$$f(\alpha) = \int_0^{\alpha^-} \frac{1}{\sqrt{2f_x(\cos\hat{\theta} - \cos\alpha)}}\mathrm{d}\hat{\theta} - \int_0^{1^-} \mathrm{d}\hat{s} \tag{4.35}$$

Obviously, we can therefore obtain the value of α via Newton-Raphson method. As long as α is available, the boundary conditions yield:

$$\text{B.C. } \hat{\theta}(0) = 0;\ \hat{\theta}(1) = \alpha;\ \frac{\mathrm{d}\hat{\theta}}{\mathrm{d}\hat{s}}(1) = 0 \tag{4.36}$$

Then, we will be able to arrive at

$$\hat{\theta}(\hat{s}) = \frac{\alpha}{\sin\sqrt{fx}} \sin(\sqrt{f_x}\hat{s}) \tag{4.37}$$

where $f_x > \frac{\pi^2}{4}$ and this is only the formulation for the first order buckling of a slender straight beam. Then, using (4.25) yields the exact characterization of the deflected beam shapes.

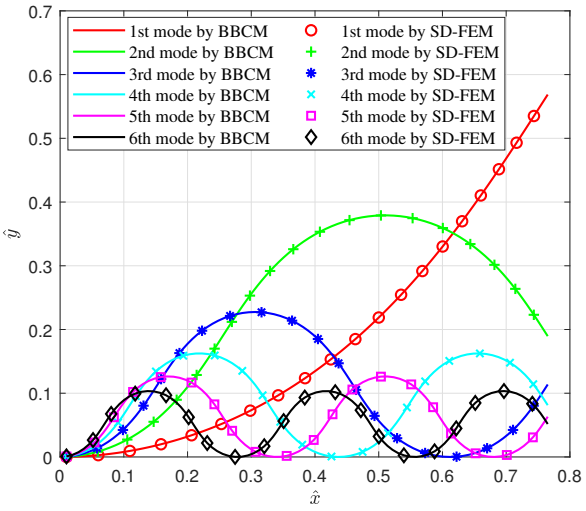

FIGURE 4.6: Diagram of different buckling modes for Subcase 1

TABLE 4.2: Buckling limits of different modes in Subcase 1

		1st	2nd	3rd	4th	5th	6th
f_x^*	BBCM	$(\frac{\pi}{2})^2$	$(\frac{3\pi}{2})^2$	$(\frac{5\pi}{2})^2$	$(\frac{7\pi}{2})^2$	$(\frac{9\pi}{2})^2$	$(\frac{11\pi}{2})^2$
	SD-FEM	2.4816	22.3370	62.0620	121.68	201.19	300.59
	ER	0.57%	0.58%	0.61%	0.63%	0.66%	0.68%

- **Subcase 2: a slender straight beam constrained by moving passive kinematic joints at both ends**
  The boundary conditions demonstrated in Fig. 4.5b are

$$\text{B.C.} \quad \frac{\mathrm{d}\hat{\theta}_h(0)}{\mathrm{d}\hat{s}} = 0; \ \frac{\mathrm{d}\hat{\theta}_h(1)}{\mathrm{d}\hat{s}} = 0 \tag{4.38}$$

which yields the analytical solution:

$$\begin{aligned} \hat{\theta}_h(s) &= C_1 \cos(\sqrt{f_x} s) \\ f_x^* &= (n\pi)^2; \ \ n = 1, 2, 3... \end{aligned} \tag{4.39}$$

Similarly, following the procedure like (4.30) to (4.35), we will be able to obtain the value of α. Rearranging (4.20), we will have the following:

$$\frac{1}{2}(\frac{\mathrm{d}\hat{\theta}}{\mathrm{d}\hat{s}})^2 - f_x \cos\hat{\theta}(\hat{s}) = C \tag{4.40}$$

where C is an unknown constant which can be determined by the boundary conditions. Precisely,

$$C = \frac{1}{2}(\frac{\mathrm{d}\hat{\theta}}{\mathrm{d}\hat{s}}(0))^2 - f_x \cos\hat{\theta}(0) = -f_x \cos\alpha \tag{4.41}$$

where $\frac{\mathrm{d}\hat{\theta}}{\mathrm{d}\hat{s}}(0) = 0$ and $\hat{\theta}(0) = \alpha$, and α is an unknown parameter to be determined. Then, we can reach

$$\frac{1}{2}(\frac{\mathrm{d}\hat{\theta}}{\mathrm{d}\hat{s}})^2 - f_x \cos\hat{\theta}(\hat{s}) = -f_x \cos\alpha \tag{4.42}$$

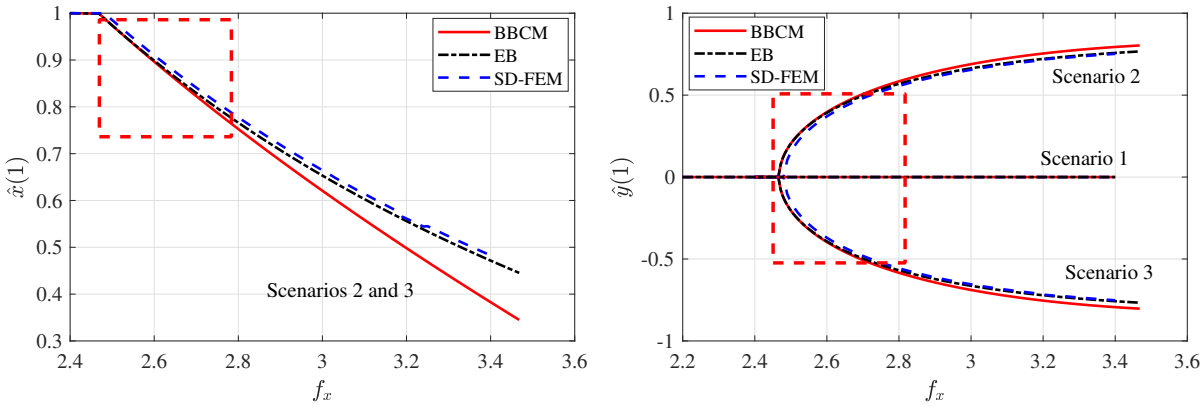

(A) f_x-$\hat{x}(1)$ (B) f_x-$\hat{y}(1)$

FIGURE 4.7: Bifurcation diagrams of Subcase 1

Obviously, it's not hard to find that $\hat{\theta} = 0$ ($\alpha = \hat{\theta}(1) = 0$) is the solution to (4.42) (Scenario 1 in Fig. 4.5b). Besides, manipulating (4.42) drives us to obtain:

$$\frac{\mathrm{d}\hat{\theta}}{\mathrm{d}\hat{s}} = -\sqrt{2f_x(\cos\hat{\theta} - \cos\alpha)} \tag{4.43}$$

if $\alpha > 0$ (Scenario 2 in Fig. 4.5b) and

$$\frac{\mathrm{d}\hat{\theta}}{\mathrm{d}\hat{s}} = +\sqrt{2f_x(\cos\hat{\theta} - \cos\alpha)} \tag{4.44}$$

if $\alpha < 0$ (Scenario 3 in Fig. 4.5b). Taking Scenario 2 for example, we will have

$$f(\alpha) = \int_{\alpha^1}^{-\alpha^+} \frac{-1}{\sqrt{2f_x(\cos\hat{\theta} - \cos\alpha)}} \mathrm{d}\hat{\theta} - \int_{0^+}^{1^-} \mathrm{d}\hat{s} \tag{4.45}$$

Logically, we can therefore obtain the value of α via Newton-Raphson method. As long as α is available, the boundary conditions yields:

$$\text{B.C. } \hat{\theta}(0) = \alpha;\ \hat{\theta}(1) = -\alpha;\ \hat{\theta}'(0) = 0;\ \hat{\theta}'(1) = 0 \tag{4.46}$$

we will have:

$$\hat{\theta}(\hat{s}) = \alpha\cos(\sqrt{f_x}s) \tag{4.47}$$

where $f_x > \pi^2$ and this is only the formulation for the first order buckling of a slender straight beam. Similarly, using (4.25) yields the exact characterization of the deflected beam shapes.

TABLE 4.3: Buckling limits of different modes in Subcase 2

		1st	2nd	3rd	4th	5th	6th
	BBCM	π^2	$4\pi^2$	$9\pi^2$	$16\pi^2$	$25\pi^2$	$36\pi^2$
f_x^*	SD-FEM	9.8205	39.2950	88.4610	157.36	246.02	354.43
	ER	0.50%	0.47%	0.41%	0.35%	0.29%	0.24%

- **Subcase 3: a slender straight beam subjected by moving clamped constraints at the both ends**
  In this subcase, the boundary conditions as shown in Fig. 4.5c are

$$\text{B.C. } \hat{\theta}_h(0) = 0;\ \hat{\theta}_h(\frac{1}{2}) = 0;\ \hat{\theta}_h(1) = 0 \tag{4.48}$$

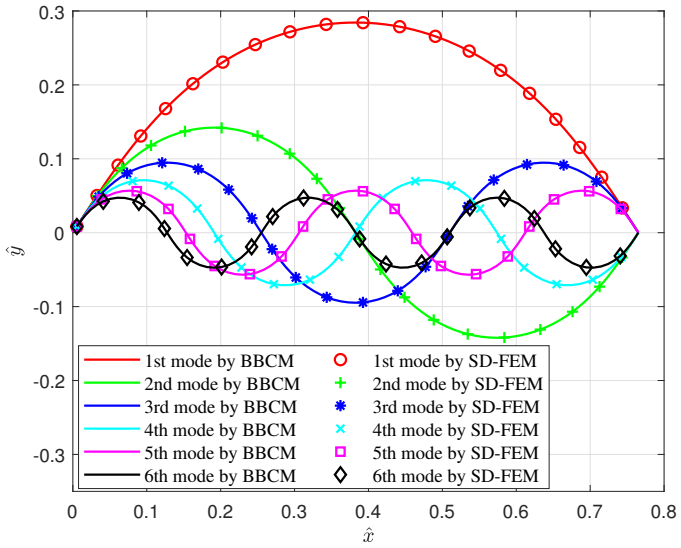

FIGURE 4.8: Diagram of different buckling modes for Subcase 2

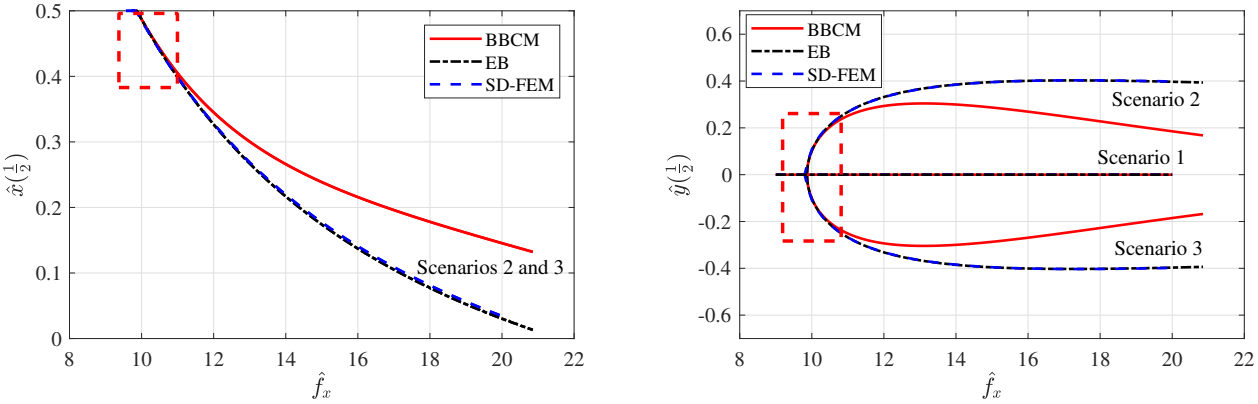

(A) $\hat{f}_x$-$\hat{x}(1)$ (B) $\hat{f}_x$-$\hat{y}(1)$

FIGURE 4.9: Bifurcation diagrams of Subcase 2

which yields the analytical solution:

$$\begin{aligned} \hat{\theta}_h(s) &= C_1 \sin(\sqrt{f_x} s) \\ f_x^* &= (2n\pi)^2; \;\; n = 1, 2, 3... \end{aligned} \tag{4.49}$$

In this subcase, since we can not get enough information from the boundary conditions, it could be complex if still being stuck using the analytical formulation (4.49). Therefore, we recommend going to back to Section 3.3.1.2 for details.

- **Results analysis and discussions**
  In (4.29), (4.39) and (4.49), f_x^* refers to the buckling limit and n stands for the nth-order buckling mode. In (4.29), (4.39) and (4.49), the amplitudes C_1 and C_2 of the trigonometric functions are not defined so any value would satisfy the conditions, and they could be positive and negative, yielding Scenario 2 and Scenario 3 in Fig. 4.5a, Fig. 4.5b and Fig. 4.5c. Here, C_1 and C_2 are chosen as 1 for simplicity. However, we can still use (4.29), (4.39) and (4.49) along with (4.25) to characterize the buckling mode shapes of different orders, as shown in Fig. 4.6, Fig. 4.8 and Fig. 4.10. Note that BBCM and SD-FEM denote the results of the proposed body-frame beam constraint model and solid-mechanics-based finite element method.

  Similarly, the corresponding buckling limits of different orders (modes) are also available in (4.29), (4.39) and

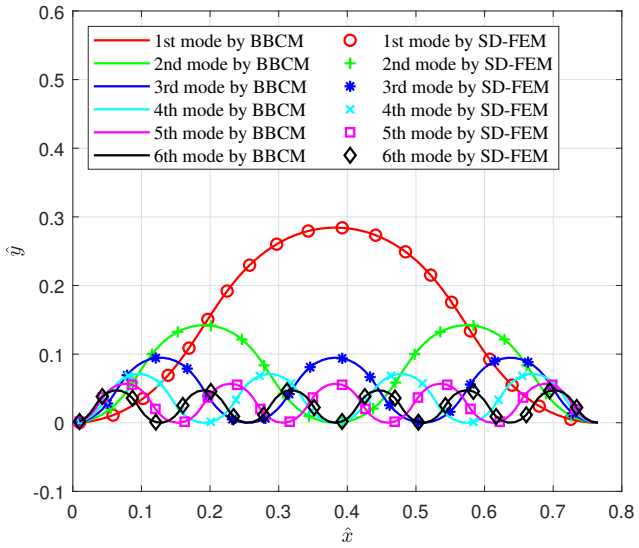

FIGURE 4.10: Diagram of different buckling modes for Subcase 3

TABLE 4.4: Buckling limits of different modes in Subcase 3

		1st	2nd	3rd	4th	5th	6th
	BBCM	$4\pi^2$	$16\pi^2$	$36\pi^2$	$64\pi^2$	$100\pi^2$	$144\pi^2$
f_x^*	SD-FEM	39.94	159.82	359.61	638.74	995.7	1428
	ER	1.15%	1.19%	1.20%	1.11%	0.88%	0.47%

(4.49), which are verified by solid-mechanics-based finite element method (See Tables. 4.2, 4.3 and 4.4). Note that BBCM, SD-FEM and ER denote the results of the proposed body-frame beam constraint model, solid-mechanics-based finite element method, and the errors with respect to SD-FEM.

Note that (4.37) and (4.47) should be regarded as semi-closed-form formulations since they also need a numerical process to get the value of α beforehand. However, the analytic formulations of (4.37) and (4.47) offer an intuitive understanding of deflected beam shape at least at small-to-intermediate-range deflections (see Figs. 4.7 and 4.9 where the numerical results are provided and compared to that of solid-mechanics-based finite element method (FEM) and Euler Bernoulli beam theory).

Taking a look at the two dash-line boxes in Fig. 4.7a and Fig. 4.7b, it can be concluded that from small to intermediate deflection range ($\hat{y}(1)$ is up to 0.4), BBCM can still capture relatively accurate results compared to that of solid mechanics. This is logical since BBCM is the linearized outcome of (4.20) with limited accuracy outside the radius of convergence. We can notice the same story in Subcase 2, specifically in the dash-line boxes in Fig. 4.9a and Fig. 4.9b. However, it's still promising since the closed-form formulations have provided a reliable prediction within intermediate range of deflection, and they can serve as the initial guesses for the original nonlinear governing equations stated in Section 3.3.1.2.

Overall speaking, BBCM can be used together with the methodology proposed in Chapter 3: first, we can analytically obtain the buckling limits and mode shapes as well as exact characterization of intermediate-range buckling via BBCM. Then, we can start from the pre-results of BBCM, such as buckling limits and mode shapes, to numerically handle the nonlinear buckling and post-buckling behaviors, which significantly speeds up the modeling process without both numerically and empirically guessing the buckling limits and mode shapes.

4.4.1.3 Case 2: a slender beam subjected to beam-end loading

This is the most common case in CMs, especially in compliant positioning mechanisms that require high-accuracy

motions (Howell, 2013a). In the previous work, the BCM has been proved remarkably effective in terms of modeling up to **intermediate-range deflections** of slender straight beams (see Fig. 4.11). Here, in this section, we deal with the intermediate-range deflection via the body-frame beam constraint model (BBCM).

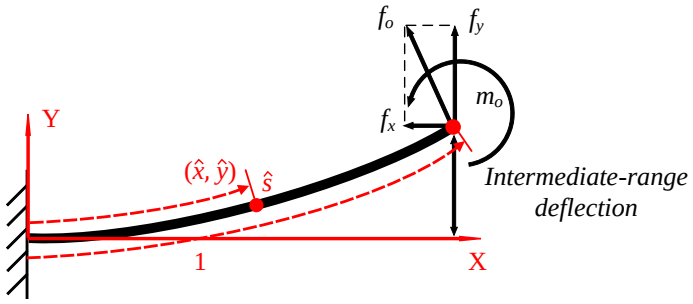

FIGURE 4.11: A slender straight beam fixed at one end and subjected to beam-end loading

- **Derivation**

$$\text{B.C. } \hat{\theta}(0) = 0;\ \hat{\theta}'(1) = m_o \tag{4.50}$$

Taking a look at (4.24), a typical non-homogeneous second-order linear ODE with constant coefficients, we normally seek the analytical solution through the following procedure. We assume the solution $\hat{\theta}(\hat{s}) = \hat{\theta}_h(\hat{s}) + \hat{\theta}_p(\hat{s})$ where $\hat{\theta}_h(\hat{s})$ is the analytical solution to the corresponding homogeneous second-order linear ODE and $\hat{\theta}_p(\hat{s})$ is the extra linear independent solution to the non-homogeneous part $-f_y$. First, $\theta_p(s)$ can be directly solved:

$$\hat{\theta}_p(\hat{s}) = -\frac{f_y}{f_x} \tag{4.51}$$

Then, in terms of the corresponding homogeneous second-order linear ODE, we have

$$\frac{\mathrm{d}^2\hat{\theta}}{\mathrm{d}\hat{s}^2} + f_x\hat{\theta}(\hat{s}) = 0 \tag{4.52}$$

For this homogeneous second-order linear ODE (4.52), there are three scenarios depending on the sign of f_x. If $f_x > 0$, obviously, we can directly write down the general solution $\hat{\theta}_h(\hat{s})$ to (4.52):

$$\hat{\theta}_h(\hat{s}) = C_1\cos(\sqrt{f_x}\hat{s}) + C_2\sin(\sqrt{f_x}\hat{s}) \tag{4.53}$$

Therefore, the general solution can be then formulated as:

$$\hat{\theta}(\hat{s}) = C_1\cos(\sqrt{f_x}\hat{s}) + C_2\sin(\sqrt{f_x}\hat{s}) - \frac{f_y}{f_x} \tag{4.54}$$

Logically, we can determine the two constant coefficients and find the final exact solution by satisfying (4.50):

$$\hat{\theta}(\hat{s}) = \frac{\sin(\sqrt{f_x}\hat{s})}{\cos(\sqrt{f_x})}\left(\frac{\sin(\sqrt{f_x})f_y}{f_x} + \frac{m_o}{\sqrt{f_x}}\right) + \frac{\cos(\sqrt{f_x}\hat{s})f_y}{f_x} - \frac{f_y}{f_x} \tag{4.55}$$

Then, if $f_x = 0$, rearranging (4.24), we will end up with the following:

$$\frac{\mathrm{d}^2\hat{\theta}}{\mathrm{d}\hat{s}^2} = -f_y \tag{4.56}$$

Satisfying (4.50), we will be able to find the analytical solution:

$$\hat{\theta}(\hat{s}) = -\frac{1}{2}f_y\hat{s}^2 + (m_o + f_y)\hat{s} \tag{4.57}$$

Finally, if $f_x < 0$, the general solution $\hat{\theta}_h(s)$ to (4.52) is:

$$\hat{\theta}_h(\hat{s}) = C_1 e^{\sqrt{-f_x}s} + C_2 e^{-\sqrt{-f_x}s} \tag{4.58}$$

Logically, the general solution can be then formulated as:

$$\hat{\theta}(\hat{s}) = C_1 e^{\sqrt{-f_x}s} + C_2 e^{-\sqrt{-f_x}s} - \frac{f_y}{f_x} \tag{4.59}$$

Then, we can determine the two constant coefficients by satisfying (4.50), and find the final exact solution:

$$\hat{\theta}(\hat{s}) = \frac{(f_y\sqrt{-f_x}e^{-\sqrt{-f_x}} + f_x m_o)e^{\sqrt{-f_x}\hat{s}} + (f_y\sqrt{-f_x}e^{\sqrt{-f_x}} - f_x m_o)e^{-\sqrt{-f_x}\hat{s}}}{\sqrt{-f_x}(e^{\sqrt{-f_x}} + e^{-\sqrt{-f_x}})f_x} - \frac{f_y}{f_x} \tag{4.60}$$

Now, we have the final analytical solution to (4.24) for **intermediate-range deflections** of slender straight beams:

$$\hat{\Gamma}(\hat{s}, f_x, f_y, m_o) = \begin{cases} \dfrac{\sin(\sqrt{f_x}\hat{s})}{\cos(\sqrt{f_x})}\left(\dfrac{\sin(\sqrt{f_x})f_y}{f_x} + \dfrac{m_o}{\sqrt{f_x}}\right) + \dfrac{\cos(\sqrt{f_x}\hat{s})f_y}{f_x} - \dfrac{f_y}{f_x}; (f_x > 0) \\ -\dfrac{1}{2}f_y\hat{s}^2 + (m_o + f_y)\hat{s}; (f_x = 0) \\ \dfrac{(f_y\sqrt{-f_x}e^{-\sqrt{-f_x}} + f_x m_o)e^{\sqrt{-f_x}\hat{s}} + (f_y\sqrt{-f_x}e^{\sqrt{-f_x}} - f_x m_o)e^{-\sqrt{-f_x}\hat{s}}}{\sqrt{-f_x}(e^{\sqrt{-f_x}} + e^{-\sqrt{-f_x}})f_x} - \dfrac{f_y}{f_x}; (f_x < 0) \end{cases} \tag{4.61}$$

where the analytical solution is formulated in a piecewise form depending on the sign of f_x.

Remark 12 *However, we are still interested in the continuity of the function $\hat{\Gamma}(\hat{s}, f_x, f_y, m_o)$ at $f_x = 0$. Therefore, we need to find out the limit of (4.61) while $f_x \to 0$ via L'Hôpital's rule. For $f_x \to 0^+$, we have*

$$\begin{aligned} \lim_{f_x\to 0^+}\hat{\Gamma}(\hat{s}, f_x, f_y, m_o) &= \lim_{f_x\to 0^+}\frac{\sin(\sqrt{f_x}\hat{s})\sin(\sqrt{f_x})f_y}{\cos(\sqrt{f_x})f_x} + \lim_{f_x\to 0^+}\frac{\sin(\sqrt{f_x}\hat{s})m_o}{\cos(\sqrt{f_x})\sqrt{f_x}} + \lim_{f_x\to 0^+}\frac{\cos(\sqrt{f_x}\hat{s})f_y}{f_x} - \frac{f_y}{f_x} \\ &= f_y\hat{s} + m_o\hat{s} - \frac{1}{2}f_y\hat{s}^2 \\ &= -\frac{1}{2}f_y\hat{s}^2 + (m_o + f_y)\hat{s} \end{aligned} \tag{4.62}$$

In terms of $f_x \to 0^-$, we have

$$\begin{aligned} \lim_{f_x\to 0^-}\hat{\Gamma}(\hat{s}, f_x, f_y, m_o) &= \lim_{f_x\to 0^-}\frac{(f_y\sqrt{-f_x}e^{-\sqrt{-f_x}} + f_x m_o)e^{\sqrt{-f_x}\hat{s}} + (f_y\sqrt{-f_x}e^{\sqrt{-f_x}} - f_x m_o)e^{-\sqrt{-f_x}\hat{s}}}{\sqrt{-f_x}(e^{\sqrt{-f_x}} + e^{-\sqrt{-f_x}})f_x} - \frac{f_y}{f_x} \\ &= -\frac{1}{2}f_y\hat{s}^2 + (m_o + f_y)\hat{s} \end{aligned} \tag{4.63}$$

Clearly, (4.62) and (4.63) proves the continuity of $\hat{\Gamma}(\hat{s}, f_x, f_y, m_o)$ at $f_x = 0$.

For nondimensional energy calculation, we have:

$$\hat{E}_p = \int_0^1 \frac{1}{2}\left(\frac{\partial\hat{\Gamma}}{\partial\hat{s}}\right)^2 d\hat{s} + \frac{1}{2}\left(\frac{h^2}{12}\right)f_x^2 \tag{4.64}$$

Here, we also present the dimensional formulation of BBCM for practical engineering purposes:

$\Gamma(s, F_x, F_y, M_o, E, I, L) =$

$$\begin{cases} \frac{\sin(\sqrt{\frac{F_x}{EI}}s)}{\cos(\sqrt{\frac{F_xL^2}{EI}})}(\frac{\sin(\sqrt{\frac{F_xL^2}{EI}})F_y}{F_x}+\frac{\frac{M_o}{EI}}{\sqrt{\frac{F_x}{EI}}})+\frac{\cos(\sqrt{\frac{F_x}{EI}}s)F_y}{F_x}-\frac{F_y}{F_x};(F_x>0) \\ -\frac{1}{2}\frac{F_yL}{EI}s^2+(\frac{M_o+F_yL}{EI})s;(F_x=0) \\ \frac{(\frac{F_yL^2}{EI}\sqrt{-\frac{F_xL^2}{EI}}e^{-\sqrt{-\frac{F_xL^2}{EI}}}+\frac{F_xM_oL^3}{EI})e^{\sqrt{-\frac{F_x}{EI}}s}+(\frac{F_yL^2}{EI}\sqrt{-\frac{F_xL^2}{EI}}e^{\sqrt{-\frac{F_xL^2}{EI}}}-\frac{F_xM_oL^3}{EI})e^{-\sqrt{-\frac{F_x}{EI}}s}}{\sqrt{-\frac{F_xL^2}{EI}}(e^{\sqrt{-\frac{F_xL^2}{EI}}}+e^{-\sqrt{-\frac{F_xL^2}{EI}}})\frac{F_xL^2}{EI}}-\frac{F_y}{F_x};(F_x<0) \end{cases} \tag{4.65}$$

$$x(s)=\int_0^s\cos(\Gamma(\xi,F_x,F_y,M_o,E,I,L))-\frac{F_x}{EA}\mathrm{d}\xi;\ \ y(s)=\int_0^s\sin(\Gamma(\xi,F_x,F_y,M_o,E,I,L))\mathrm{d}\xi;\ s\in[0,L]$$

where $A=wh$ which denotes the area of the constant cross-section. Besides, we can also calculate the stored elastic energy in the deflected beam via:

$$E_p=\frac{EI}{L}\hat{E}_p=\int_0^L\frac{1}{2}EI(\frac{\partial\Gamma}{\partial s})^2\mathrm{d}s+\frac{F_x^2L}{2EA} \tag{4.66}$$

Note that BCM also has a similar formulation for calculating the energy (Awtar and Sen, 2010), and we have demonstrated the formulation of BCM in Section 1.2.3.1 of this thesis.

Remark 13 *As we have stated earlier, one of the key differences is about the different coordinate systems used by BBCM and BCM. Being expressed in body frame makes BBCM consistent with the fruitful contributions in rod (Rubin and Cardon, 2002) and beam (Wu and Zheng, 2022a)(Wu and Zheng, 2022d) theories, specifically in the area of* ***geometrical nonlinearity****. This is essentially why BBCM offers standard formulations (or solutions) for the deflected beam shape, energy calculation and buckling problems. Besides, we can easily explore more based on the previous contributions in rod and beam theories. For example, considering different loading scenarios stated in ODE (3.33), we can reformulate and nondimensionalize the corresponding ODEs. Then, we will be able to have the following general formulation:*

$$\frac{\mathrm{d}^2\hat{\theta}}{\mathrm{d}\hat{s}^2}=f(\frac{\mathrm{d}\hat{\theta}}{\mathrm{d}\hat{s}},\hat{\theta},\hat{s},f_x,f_y...) \tag{4.67}$$

After that, we can linearize (4.67) using the similar manipulations, such as (4.22), (4.23) and (4.24) to obtain a linear ODE as well as to derive the analytical solution to this ODE. This also theoretically shows that BBCM can be a more practical and universal strategy to handle intermediate-range deflection, thanks to the previous contributions in academic literature on beam and rod theories.

- **Feasibility analysis of BBCM**

  In this section, we aim to analyze the scope of feasibility of the proposed BBCM via a straightforward enumeration strategy. Under the same boundary conditions (4.50), we use the original governing equation of Euler Bernoulli beam theory (4.20) as the standard to compare the results from BBCM, equivalently (4.24). In flexure-based CMs, the beam-end motions of the built-in flexures are the main contributors to the motions of these mechanisms. Therefore, we here use the following formulation to form the expression of the evaluated errors:

$$e_r=\sqrt{e_{r_x}^2+e_{r_y}^2+e_{r_\theta}^2} \tag{4.68}$$

  with

$$\begin{aligned} e_{r_x}^2&=(\int_0^1\cos(\hat{\Gamma}(\hat{s}))\mathrm{d}\hat{s}-\int_0^1\cos(\hat{\theta}_{NEB}(\hat{s}))\mathrm{d}\hat{s})^2 \\ e_{r_y}^2&=(\int_0^1\sin(\hat{\Gamma}(\hat{s}))\mathrm{d}\hat{s}-\int_0^1\sin(\hat{\theta}_{NEB}(\hat{s}))\mathrm{d}\hat{s})^2 \\ e_{r_\theta}^2&=(\hat{\Gamma}(1)-\hat{\theta}_{NEB}(1))^2 \end{aligned} \tag{4.69}$$

  where $\hat{\Gamma}(\hat{s})$ and $\hat{\theta}_{NEB}(\hat{s})$ denote the solutions to (4.24) and (4.20) under the boundary conditions (4.50).

TABLE 4.5: Accuracy evaluation results by BBCM and BCM

BBCM	$\hat{y}(1) < 0.1$; 95.66% $e_r < 5.5 \times 10^{-3}$;	$e_{r_{max}} = 1.53 \times 10^{-2}$
	$\hat{y}(1) < 0.2$;95.48% $e_r < 1.55 \times 10^{-2}$;	$e_{r_{max}} = 4.20 \times 10^{-2}$
	$\hat{y}(1) < 0.3$; 95.33% $e_r < 3.0 \times 10^{-2}$;	$e_{r_{max}} = 8.47 \times 10^{-2}$
BCM	$\hat{y}(1) < 0.1$; 96.05% $e_r < 5.5 \times 10^{-3}$;	$e_{r_{max}} = 1.49 \times 10^{-2}$
	$\hat{y}(1) < 0.2$;95.80% $e_r < 1.55 \times 10^{-2}$;	$e_{r_{max}} = 4.10 \times 10^{-2}$
	$\hat{y}(1) < 0.3$; 94.66% $e_r < 3.0 \times 10^{-2}$;	$e_{r_{max}} = 8.52 \times 10^{-2}$

Here, we consider f_x, f_y and m_o as the inputs of the model (4.24) and (4.20) where $f_x \in U_{f_x} = [\underline{f_x}, \overline{f_x}]$, $f_y \in U_{f_y} = [\underline{f_y}, \overline{f_y}]$ and $m_o \in U_{m_o} = [\underline{m_o}, \overline{m_o}]$, and e_r as the corresponding output. We can then formulate the whole admissible input space: $U = U_{f_x} \times U_{f_y} \times U_{m_o}$ with $U_{f_x}, U_{f_y}, U_{m_o} \in \mathbb{R}$. Then, we sample U_{f_x}, U_{f_y} and U_{m_o} via a set of N points, noted as $U^s_{f_x}$, $U^s_{f_y}$ and $U^s_{m_o}$ with fixed sampling lengths: $\frac{\overline{f_x}-\underline{f_x}}{N-1}$, $\frac{\overline{f_y}-\underline{f_y}}{N-1}$ and $\frac{\overline{m_o}-\underline{m_o}}{N-1}$, i.e., $U_{f_x} \approx U^s_{f_x}$, $U_{f_y} \approx U^s_{f_y}$ and $U_{m_o} \approx U^s_{m_o}$:

$$\begin{aligned} U^s_{f_x} &= \{\underline{f_x}, \underline{f_x} + \frac{\overline{f_x} - \underline{f_x}}{N-1}, ..., \underline{f_x} - \frac{\overline{f_x} - \underline{f_x}}{N-1}, \overline{f_x}\} \\ U^s_{f_y} &= \{\underline{f_y}, \underline{f_y} + \frac{\overline{f_y} - \underline{f_y}}{N-1}, ..., \underline{f_y} - \frac{\overline{f_y} - \underline{f_y}}{N-1}, \overline{f_y}\} \\ U^s_{f_x} &= \{\underline{m_o}, \underline{m_o} + \frac{\overline{m_o} - \underline{m_o}}{N-1}, ..., \underline{m_o} - \frac{\overline{m_o} - \underline{m_o}}{N-1}, \overline{m_o}\} \end{aligned} \tag{4.70}$$

and the input space can therefore be approximated by

$$U \approx U^s = U^s_{f_x} \times U^s_{f_y} \times U^s_{m_o} \tag{4.71}$$

From an engineering point of view, the following values are assigned to the corresponding parameters in (4.70) to evaluate the error (4.68) distribution through the sampling strategy (or the enumeration framework):

$$\begin{aligned} &\underline{f_x} = -1;\ \overline{f_x} = 1;\ \underline{f_y} = -1;\ \overline{f_y} = 1; \\ &\underline{m_o} = -1;\ \overline{m_o} = 1;\ N = 0.025 \end{aligned} \tag{4.72}$$

Then, we can obtain the following numerical results below in Table 4.5 where the results from BCM are compared. Note that the results from BCM follow the same evaluation framework as stated in (4.68) to (4.72). Obviously, in Table 4.5, under the same evaluation policy, BBCM maintains the same accuracy level as BCM in term of deflections within small-to-intermediate range.

4.4.1.4 Discussions

In this section, two major cases: buckling (Section 4.4.1.2) and beam deflections under beam-end loading (Section 4.4.1.3), are studied to verify the feasibility as well as the effectiveness of BBCM. Overall speaking, as stated above, BBCM and BCM are expressed in different coordinate systems. Being expressed in body frame makes BBCM more practical and consistent with those previously extensive studies on beam and rod theories, such as the standard formulations for beam shapes, energy calculation, varying and constant initial curvature, different types of loading (see Wu and Zheng, 2022a) and so on.

4.4.2 Chained algorithm utilizing the linearized model

As stated in Chapter 3, we have already stated the standard modeling of large deflection of slender beams via geometrically nonlinear Euler Bernoulli beam theory. Here, we have derived BBCM for intermediate-range deflections

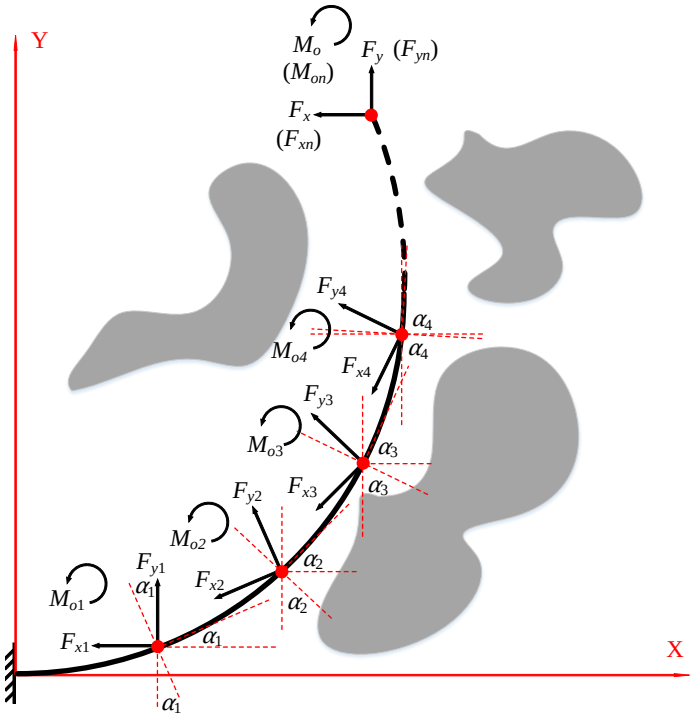

FIGURE 4.12: Schematic diagram of chained body-frame beam constraint model (CBBCM)

of slender beams. Under the concept of FEM, several linear beam elements can be chained together to analyze large deflection of slender beams, so is the case for BBCM as well. Although is it computationally expensive, it is easier to understand the essence of analysis. Besides, this proposed chained model can be used to consider contact problems.

4.4.2.1 Derivation for large-deflection problems via chained BBCM

Inspired from CBCM (Ma and Chen, 2016) and other similar chained algorithms, our proposed strategy also requires discretization of the whole beam being modeled into beam elements and analyzes each element in succession. In other words, the summation of small deflection of all discretized elements results in feasible analysis of larger deflection (geometric nonlinearity). Therefore, we can also do the same trick for BBCM to analyze large deflection. Supposing the whole beam is divided into n beam elements, and the length of each beam element $l = \frac{L}{n}$. The deflection of each beam element is governed by BBCM. Now, if we consider the whole beam as an elastic system as shown in Fig. 4.12, we need to develop three standard groups of equations.

1) **Constitutive equations**
According to (4.65), we have the following formulation for each beam element:

$$\Gamma_i(s, F_{xi}, F_{yi}, M_{oi}, E, I, l);\ x_i(s) = \int_0^s \cos\Gamma_i(\xi) - \frac{F_{xi}}{EA}\mathrm{d}\xi;\ y_i(s) = \int_0^s \sin\Gamma_i(\xi)\mathrm{d}\xi;\ s \in [0, l] \tag{4.73}$$

2) **Force equilibrium**

$$\begin{aligned}
&F_{y(i+1)}\sin\alpha_i + F_{x(i+1)}\cos\alpha_i = F_{xn}\\
&F_{y(i+1)}\cos\alpha_i - F_{x(i+1)}\sin\alpha_i = F_{yn}\\
&M_{on} + F_{xn}\{\sum_{i=1}^{n}[\sin\alpha_i x_{i+1}(l) + \cos\alpha_i y_{i+1}(l)]\} + F_{yn}\{\sum_{i=1}^{n}[\cos\alpha_i x_{i+1}(l) - \sin\alpha_i y_{i+1}(l)]\} = M_{oi}\\
&F_x = F_{xn};\ F_y = F_{yn};\ M_o = M_{on}
\end{aligned} \tag{4.74}$$

3) **Geometrical compatibility equations**

$$\alpha_0 = 0;\ \alpha_i = \sum_{j=1}^{i} \Gamma_i(l) \tag{4.75}$$

where i denotes the ith beam element ($i = 1, 2, 3...n$).

There are altogether $7n + 4$ equations from (4.73) to (4.75) to solve $7n$ unknowns, $\theta_i(l)$, $x_i(l)$, $y_i(l)$ and α_i ($i = 1, 2, 3...n$). It's obvious that Newton-Raphson method and its relatives can be used to obtain the numerical solutions. In terms of describing the deflected beam shape, we can just use the following formulations:

$$\begin{aligned} x(s) &= \sum_{i=0}^{j}[\cos\alpha_i x_{i+1}(l) - \sin\alpha_i y_{i+1}(l)] + \cos\alpha_j x_{j+1}(s) - \sin\alpha_j y_{j+1}(s);\ s \in [jl, (j+1)l] \\ y(s) &= \sum_{i=0}^{j}[\sin\alpha_i x_{i+1}(l) + \cos\alpha_i y_{i+1}(l)] + \sin\alpha_j x_{j+1}(s) + \cos\alpha_j y_{j+1}(s);\ s \in [jl, (j+1)l] \end{aligned} \tag{4.76}$$

where $j = 0, 1, 2, 3...n-1$. To calculate the stored elastic energy in the studied beam, we have

$$E_p = \sum_{i=1}^{n} E_{pi} = \sum_{i=1}^{n}[\int_0^l \frac{1}{2} EI(\frac{\partial\Gamma_i}{\partial s})^2 \mathrm{d}s + \frac{F_{xi}^2 l}{2EA}] \tag{4.77}$$

4.4.2.2 Potential applications to contact problems

Similar to FEM, this above chained algorithm takes into account the forces exerted at every node, which means this algorithm can be used to detect physical interaction with the external environment. It's logical the methodology in FEM (Rao, 2017) can be directly applied to this chained algorithm, and most possibly the computational expense would be reduced due to its existence of the corresponding analytic solution to each elementary beam model and the simplicity of the beam model.

4.5 Numerical methods of solving BVPs

In this section, we propose to use several useful numerical methods (stated in Chapter 2) to handle the BVPs derived from geometrically nonlinear Euler Bernoulli beam theory. Here, the governing BVP (3.25) that describes a straight beam subjected to beam-end loading stated is taken for example:

$$\begin{aligned} &\text{D.E.} \quad \frac{\mathrm{d}^2\theta}{\mathrm{d}s^2} = -\frac{F_y}{EI}\cos\theta(s) - \frac{F_x}{EI}\sin\theta(s) = f(\theta(s), s, F_x, F_y, E, I) \\ &\text{B.C.} \quad \theta(0) = 0 \\ &\qquad \frac{\mathrm{d}\theta}{\mathrm{d}s}(L) = \frac{M_o}{EI} \end{aligned} \tag{4.78}$$

where F_x, F_y, M_o, E, I are known. To start with, the geometric and material parameters chosen for the studied straight beam is shown in the following:

$$E = 200 \times 10^9 \text{ Pa};\ \nu = 0.3;\ w = 0.01 \text{ m};\ h = 0.004 \text{ m};\ L = 0.2 \text{ m};\ I = \frac{wh^3}{12}$$

In terms of the exerted beam-end loading, it is shown as follows:

$$\begin{aligned} &\text{Loading case 1: } F_x = 1000 \text{ N};\ F_y = 1000 \text{ N};\ M_o = 60 \text{ N.m}; \\ &\text{Loading case 2: } F_x = 500 \text{ N};\ F_y = 500 \text{ N};\ M_o = 30 \text{ N.m}; \\ &\text{Loading case 3: } F_x = -500 \text{ N};\ F_y = -500 \text{ N};\ M_o = -30 \text{ N.m}; \\ &\text{Loading case 4: } F_x = -1000 \text{ N};\ F_y = 1000 \text{ N};\ M_o = -60 \text{ N.m}; \end{aligned}$$

Since the shear strain is not considered in Euler-Bernoulli beam model, ν is logically not involved in our numerical algorithms. Besides, in this section, FEM via Euler Bernoulli beam element is used to verify the results respectively, such as beam-end coordinates and the exact deflected beam shapes. The computational expense (CE) and the corresponding error (ER) with respect to FEM are presented in the following respect results.

4.5.1 Finite difference method

According to Section 2.5.1, we can use finite difference method to handle (4.78) where it is discretized following the manner of (2.2). The beam-end coordinates and deflected beam shapes are presented in Table 4.6 and Fig. 4.13.

4.5.2 Shooting method

According to Section 2.5.2, we can reformulate (4.78) using the classic shooting strategy (2.3) and (2.4). The beam-end coordinates and the deflected beam shapes are presented in Table 4.7 and Fig. 4.14.

4.5.3 Weighted residual methods

Here, several weighted residual methods are used to solve BVP (4.78). According to Weierstrass theorem, we define a function $\vartheta_o(s)$ to approximate the solution to (4.78), which is an nth-order polynomial:

$$\vartheta(s) = \sum_{i=0}^{n} c_i s^i \tag{4.79}$$

Then, the residual function is defined below:

$$\mathcal{R}(s) = \frac{\mathrm{d}^2\vartheta}{\mathrm{d}s^2} - f(\vartheta(s), s, F_x, F_y, E, I) \neq 0 \tag{4.80}$$

Therefore, we can force the residual into zero over the domain $s \in [0, L]$.

$$\int_0^L \mathcal{W}_j \mathcal{R}(s)\mathrm{d}s = 0, \quad (j = 1, 2, 3...n+1) \tag{4.81}$$

In the meantime, the boundary conditions in (4.78) also need to be satisfied:

$$\begin{aligned} &\text{B.C. } \vartheta(0) = 0 \\ &\frac{\mathrm{d}\vartheta}{\mathrm{d}s}(L) = \frac{M_o}{EI} \end{aligned} \tag{4.82}$$

(4.80) and (4.81) contain $n+3$ equations altogether, and it is logically feasible to solve the $n+1$ unknown polynomial coefficients via Newton-Raphson method.

4.5.3.1 Collocation method

In collocation method, the weight function $\mathcal{W}_j$ is chosen as:

$$\mathcal{W}_j(s) = \delta(s - s_j) \tag{4.83}$$

The beam-end coordinates and deflected beam shapes are presented in Table 4.8 and Fig. 4.15.

4.5.3.2 Subdomain method

In subdomain method, the weight function $\mathcal{W}_j$ is chosen as any integer but (4.81) is satisfied within several subdomains:

$$\int_{\frac{(j-1)}{n+1}}^{\frac{j}{n+1}} \mathcal{R}(s)\mathrm{d}s = 0 \tag{4.84}$$

The beam-end coordinates and deflected beam shapes are presented in Table 4.9 and Fig. 4.16.

4.5.3.3 Least square method

In least square method, the weight function $\mathcal{W}_j$ is chosen as:

$$\mathcal{W}_j(s) = \frac{\partial \mathcal{R}(s)}{\partial c_{j-1}} \tag{4.85}$$

The beam-end coordinates and deflected beam shapes are presented in Table 4.10 and Fig. 4.17.

4.5.3.4 Galerkin method

In Galerkin method, the weight function $\mathcal{W}_j$ is chosen as:

$$\mathcal{W}_j(s) = \frac{\partial \vartheta(s)}{\partial c_{j-i}} \tag{4.86}$$

The beam-end coordinates and deflected beam shapes are presented in Table 4.11 and Fig. 4.18.

4.5.3.5 Method of moment

In collocation method, the weight function $\mathcal{W}_j$ is chosen as:

$$\mathcal{W}_j(s) = s^j \tag{4.87}$$

The beam-end coordinates and deflected beam shapes are presented in Table 4.12 and Fig. 4.19.

4.5.3.6 Rayleigh Ritz method

In Rayleigh Ritz method, the principle of integration by parts is used following manner of (2.19):

$$\int_0^L \mathcal{W}_j \mathcal{R}(s)\mathrm{d}s = \int_0^L \mathcal{W}_j[\frac{\mathrm{d}^2\vartheta}{\mathrm{d}s^2} - f(\vartheta, s)]\mathrm{d}s = [\mathcal{W}_j \frac{\mathrm{d}\vartheta}{\mathrm{d}s}]_0^L - \int_0^L \frac{\mathrm{d}\mathcal{W}_j}{\mathrm{d}s}\frac{\mathrm{d}\vartheta}{\mathrm{d}s}\mathrm{d}s - \int_0^L \mathcal{W}_j f(\vartheta, s)\mathrm{d}s = 0 \tag{4.88}$$

where the weight functions are chosen in the following manner:

$$\mathcal{W}_j = \frac{\partial \vartheta}{\partial c_{j-1}} \tag{4.89}$$

The beam-end coordinates and deflected beam shapes are presented in Table 4.13 and Fig. 4.20.

4.5.3.7 Weighted residual methods from global to local

In this method, instead of approximating the solution to (4.78) via collocation method in a global manner, we locally approximate the solution via collocation method (see details in Section 2.5.3.7). The beam-end coordinates and deflected beam shapes are presented in Table 4.14 and Fig. 4.21.

TABLE 4.6: Beam-end coordinates solved by finite difference method (FDM)

	Case	Case 1	Case 2	Case 3	Case 4
Loading	F_x (N)	1000	500	−500	−1000
	F_y (N)	1000	500	−500	−1000
	M_o (N.m)	60	30	−30	−60
FDM	$x(L)$ (m)	0.01493	0.09137	0.1739	0.1554
	$y(L)$ (m)	0.1598	0.1526	−0.08811	−0.1114
	$\theta(L)$ (rad)	2.3173	1.6466	−0.8062	−1.1113
FEM	$x(L)$ (m)	0.01492	0.09105	0.1739	0.1556
	$y(L)$ (m)	0.1599	0.1527	−0.8817	−0.1114
	$\theta(L)$ (rad)	2.3185	1.6512	−0.8066	−1.1092
ER	$x(L)$	0.07%	0.35%	0.00%	0.13%
	$y(L)$	0.06%	0.07%	0.07%	0.00%
	$\theta(L)$	0.05%	0.27%	0.05%	0.19%
CE (s)	FDM	1.00	0.89	0.88	0.89
	FEM	13.00	12.00	7.00	8.00

Note that 640 sampling points are used.

TABLE 4.7: Beam-end coordinates solved by shooting method (SH)

	Case	Case 1	Case 2	Case 3	Case 4
Loading	F_x (N)	1000	500	−500	−1000
	F_y (N)	1000	500	−500	−1000
	M_o (N.m)	60	30	−30	−60
SH	$x(L)$ (m)	0.01491	0.09098	0.1739	0.1556
	$y(L)$ (m)	0.1598	0.1527	−0.08810	−0.1113
	$\theta(L)$ (rad)	2.3171	1.6512	−0.8061	−1.1085
FEM	$x(L)$ (m)	0.01492	0.09105	0.1739	0.1556
	$y(L)$ (m)	0.1599	0.1527	−0.8817	−0.1114
	$\theta(L)$ (rad)	2.3185	1.6512	−0.8066	−1.1092
ER	$x(L)$	0.07%	0.08%	0.00%	0.00%
	$y(L)$	0.06%	0.00%	0.08%	0.09%
	$\theta(L)$	0.06%	0.00%	0.06%	0.06%
CE (s)	SH	0.91	0.78	0.86	0.81
	FEM	13.00	12.00	7.00	8.00

Note that Runge-Kutta method is used, and the predefined threshold for convergence is set as 1^{-20}.

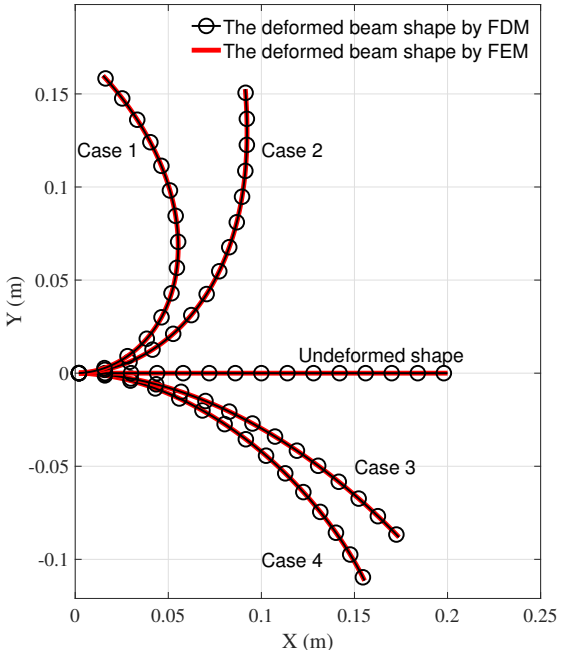

FIGURE 4.13: Graphical results solved via finite difference method (FDM)

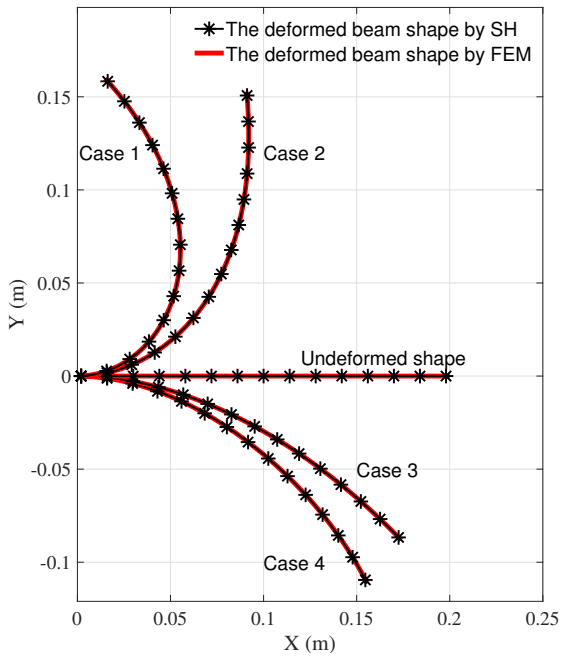

FIGURE 4.14: Graphical results solved via shooting method (SH)

TABLE 4.8: Beam-end coordinates solved by globally-implemented collocation method (CMG)

	Case	Case 1	Case 2	Case 3	Case 4
Loading	F_x (N)	1000	500	-500	-1000
	F_y (N)	1000	500	-500	-1000
	M_o (N.m)	60	30	-30	-60
CMG	$x(L)$ (m)	0.01532	0.09100	0.1739	0.1556
	$y(L)$ (m)	0.1599	0.1527	-0.08810	-0.1113
	$\theta(L)$ (rad)	2.3120	1.6511	-0.8060	-1.1081
FEM	$x(L)$ (m)	0.01492	0.09105	0.1739	0.1556
	$y(L)$ (m)	0.1599	0.1527	-0.8817	-0.1114
	$\theta(L)$ (rad)	2.3185	1.6512	-0.8066	-1.1092
ER	$x(L)$	2.68%	0.05%	0.00%	0.00%
	$y(L)$	0.00%	0.00%	0.08%	0.09%
	$\theta(L)$	0.28%	0.00%	0.07%	0.10%
CE (s)	CMG	0.11	0.08	0.12	0.22
	FEM	13.00	12.00	7.00	8.00

Note that 6th-order polynomials are used to approximate the solution.

TABLE 4.9: Beam-end coordinates solved by subdomain method (SUM)

	Case	Case 1	Case 2	Case 3	Case 4
Loading	F_x (N)	1000	500	-500	-1000
	F_y (N)	1000	500	-500	-1000
	M_o (N.m)	60	30	-30	-60
SUM	$x(L)$ (m)	0.01491	0.09098	0.1739	0.1556
	$y(L)$ (m)	0.1598	0.1527	-0.08810	-0.1113
	$\theta(L)$ (rad)	2.3175	1.6513	-0.8061	-1.1084
FEM	$x(L)$ (m)	0.01492	0.09105	0.1739	0.1556
	$y(L)$ (m)	0.1599	0.1527	-0.8817	-0.1114
	$\theta(L)$ (rad)	2.3185	1.6512	-0.8066	-1.1092
ER	$x(L)$	0.07%	0.08%	0.00%	0.00%
	$y(L)$	0.06%	0.00%	0.08%	0.09%
	$\theta(L)$	0.04%	0.00%	0.06%	0.07%
CE (s)	SUM	0.30	0.25	0.24	0.37
	FEM	13.00	12.00	7.00	8.00

Note that 6th-order polynomials are used to approximate the solution.

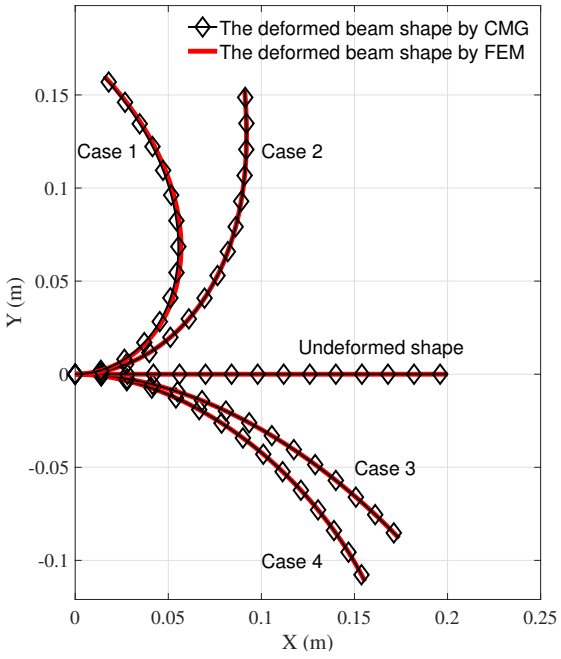

FIGURE 4.15: Graphical results solved via globally-implemented collocation method (CMG)

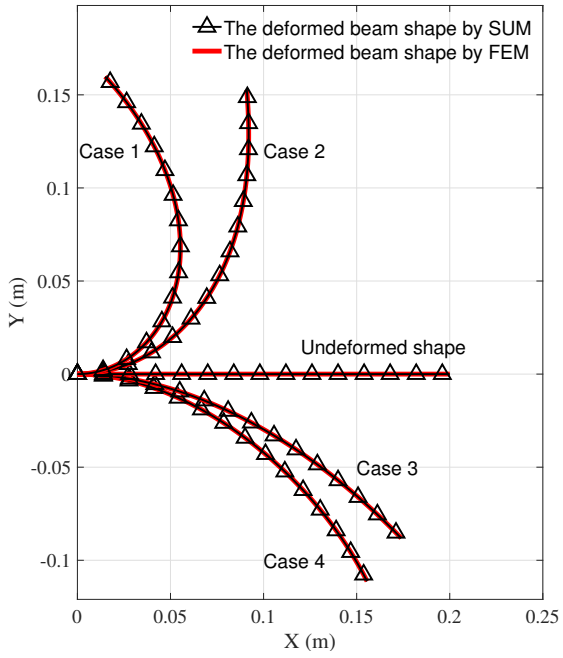

FIGURE 4.16: Graphical results solved via subdomain method (SUM)

TABLE 4.10: Beam-end coordinates solved by least square method (LSM)

	Case	Case 1	Case 2	Case 3	Case 4
Loading	F_x (N)	1000	500	-500	-1000
	F_y (N)	1000	500	-500	-1000
	M_o (N.m)	60	30	-30	-60
LSM	$x(L)$ (m)	0.01491	0.09098	0.1739	0.1556
	$y(L)$ (m)	0.1598	0.1527	-0.08810	-0.1113
	$\theta(L)$ (rad)	2.3177	1.6512	-0.8061	-1.1085
FEM	$x(L)$ (m)	0.01492	0.09105	0.1739	0.1556
	$y(L)$ (m)	0.1599	0.1527	-0.8817	-0.1114
	$\theta(L)$ (rad)	2.3185	1.6512	-0.8066	-1.1092
ER	$x(L)$	0.07%	0.08%	0.00%	0.00%
	$y(L)$	0.06%	0.00%	0.08%	0.09%
	$\theta(L)$	0.03%	0.00%	0.06%	0.06%
CE (s)	LSM	0.46	0.40	0.39	0.50
	FEM	13.00	12.00	7.00	8.00

Note that 6th-order polynomials are used to approximate the solution.

TABLE 4.11: Beam-end coordinates solved by Galerkin method (GM)

	Case	Case 1	Case 2	Case 3	Case 4
Loading	F_x (N)	1000	500	-500	-1000
	F_y (N)	1000	500	-500	-1000
	M_o (N.m)	60	30	-30	-60
GM	$x(L)$ (m)	0.01495	0.09099	0.1739	0.1556
	$y(L)$ (m)	0.1598	0.1527	-0.08810	-0.1113
	$\theta(L)$ (rad)	2.3148	1.6502	-0.8062	-1.1092
FEM	$x(L)$ (m)	0.01492	0.09105	0.1739	0.1556
	$y(L)$ (m)	0.1599	0.1527	-0.8817	-0.1114
	$\theta(L)$ (rad)	2.3185	1.6512	-0.8066	-1.1092
ER	$x(L)$	0.20%	0.07%	0.00%	0.00%
	$y(L)$	0.06%	0.00%	0.08%	0.09%
	$\theta(L)$	0.16%	0.06%	0.05%	0.00%
CE (s)	GM	0.22	0.19	0.19	0.31
	FEM	13.00	12.00	7.00	8.00

Note that 6th-order polynomials are used to approximate the solutions.

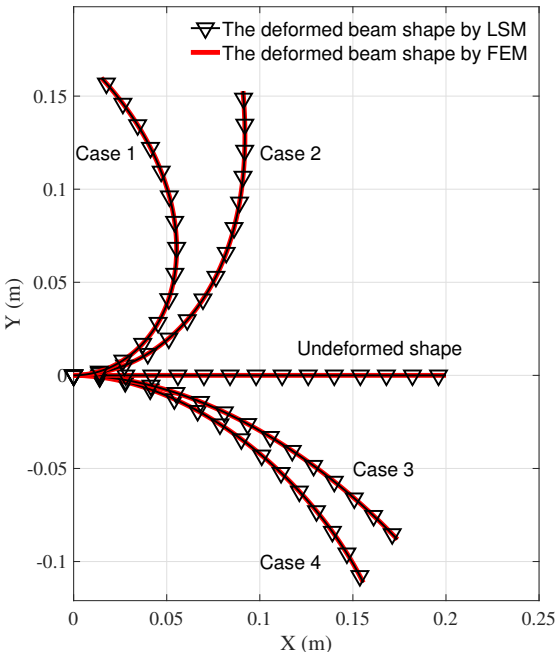

FIGURE 4.17: Graphical results solved via least square method (LSM)

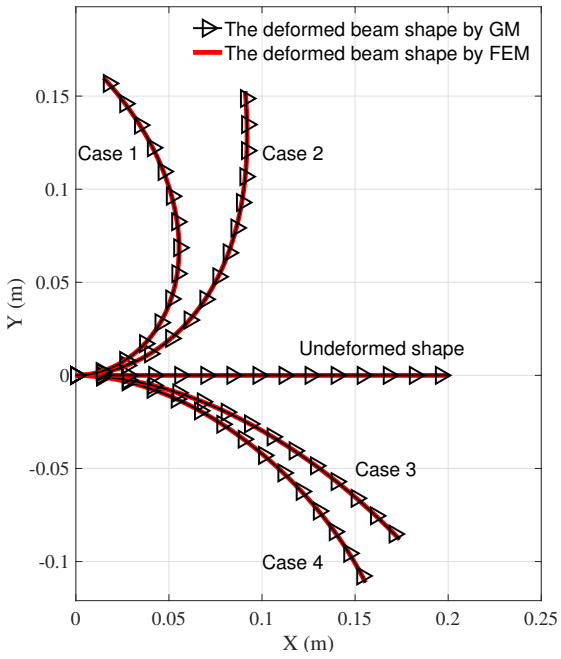

FIGURE 4.18: Graphical results solved via Galerkin method (GM)

TABLE 4.12: Beam-end coordinates solved by method of moment (MOM)

	Case	Case 1	Case 2	Case 3	Case 4
Loading	F_x (N)	1000	500	-500	-1000
	F_y (N)	1000	500	-500	-1000
	M_o (N.m)	60	30	-30	-60
MOM	$x(L)$ (m)	0.01497	0.09100	0.1739	0.1556
	$y(L)$ (m)	0.1598	0.1527	-0.08810	-0.1113
	$\theta(L)$ (rad)	2.3174	1.6512	-0.8061	-1.1085
FEM	$x(L)$ (m)	0.01492	0.09105	0.1739	0.1556
	$y(L)$ (m)	0.1599	0.1527	-0.8817	-0.1114
	$\theta(L)$ (rad)	2.3185	1.6512	-0.8066	-1.1092
ER	$x(L)$	0.34%	0.05%	0.00%	0.00%
	$y(L)$	0.06%	0.00%	0.08%	0.09%
	$\theta(L)$	0.05%	0.00%	0.06%	0.06%
CE (s)	MOM	0.21	0.17	0.20	0.30
	FEM	13.00	12.00	7.00	8.00

Note that 4th-order polynomials are used to approximate the solutions.

TABLE 4.13: Beam-end coordinates solved by Rayleigh Ritz method (RRM)

	Case	Case 1	Case 2	Case 3	Case 4
Loading	F_x (N)	1000	500	-500	-1000
	F_y (N)	1000	500	-500	-1000
	M_o (N.m)	60	30	-30	-60
RRM	$x(L)$ (m)	0.01495	0.09099	0.1739	0.1556
	$y(L)$ (m)	0.1598	0.1527	-0.08810	-0.1113
	$\theta(L)$ (rad)	2.3148	1.6502	-0.8062	-1.1092
FEM	$x(L)$ (m)	0.01492	0.09105	0.1739	0.1556
	$y(L)$ (m)	0.1599	0.1527	-0.8817	-0.1114
	$\theta(L)$ (rad)	2.3185	1.6512	-0.8066	-1.1092
ER	$x(L)$	0.20%	0.07%	0.00%	0.00%
	$y(L)$	0.06%	0.00%	0.08%	0.09%
	$\theta(L)$	0.16%	0.06%	0.05%	0.00%
CE (s)	RRM	0.41	0.31	0.30	0.31
	FEM	13.00	12.00	7.00	8.00

Note that 4th-order polynomials are used to approximate the solutions.

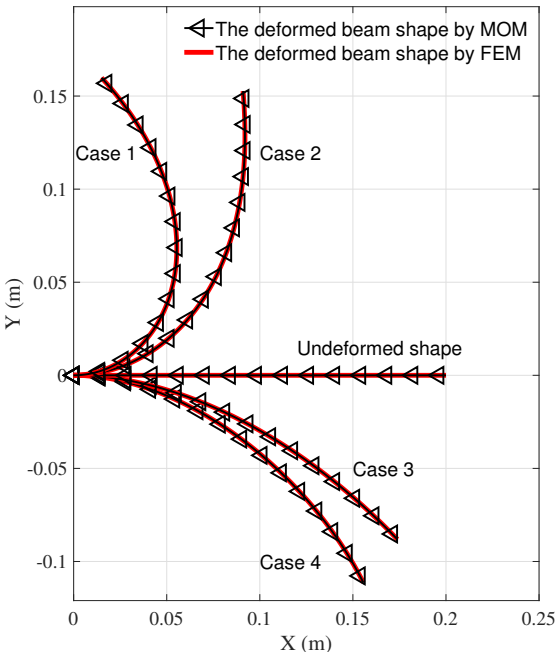

FIGURE 4.19: Graphical results solved via method of moment (MOM)

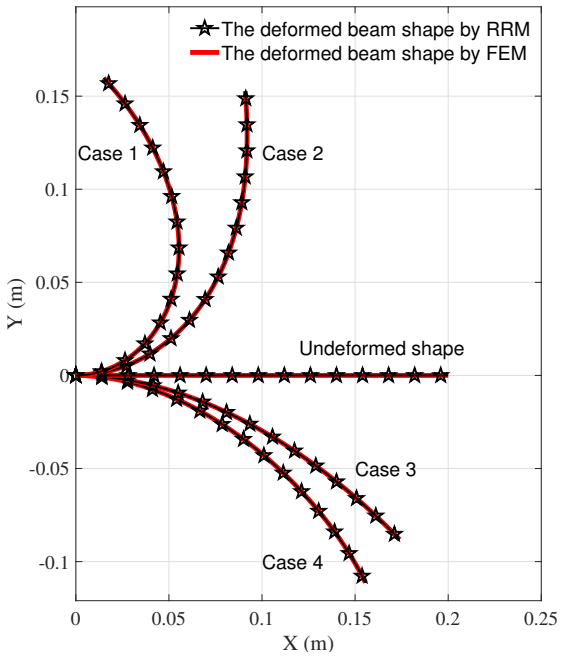

FIGURE 4.20: Graphical results solved via Rayleigh Ritz method (RRM)

TABLE 4.14: Beam-end coordinates solved by locally-implemented collocation method (CML)

	Case	Case 1	Case 2	Case 3	Case 4
Loading	F_x (N)	1000	500	-500	-1000
	F_y (N)	1000	500	-500	-1000
	M_o (N.m)	60	30	-30	-60
CML	$x(L)$ (m)	0.01491	0.09099	0.1739	0.1556
	$y(L)$ (m)	0.1598	0.1527	-0.08808	-0.1113
	$\theta(L)$ (rad)	2.3196	1.6512	-0.8061	-1.1085
FEM	$x(L)$ (m)	0.01492	0.09105	0.1739	0.1556
	$y(L)$ (m)	0.1599	0.1527	-0.8817	-0.1114
	$\theta(L)$ (rad)	2.3185	1.6512	-0.8066	-1.1092
ER	$x(L)$	0.07%	0.07%	0.00%	0.00%
	$y(L)$	0.06%	0.00%	0.10%	0.09%
	$\theta(L)$	0.04%	0.00%	0.06%	0.06%
CE (s)	CML	0.41	0.31	0.30	0.31
	FEM	13.00	12.00	7.00	8.00

Note that 3 collocation points and 2 sub-intervals are defined.

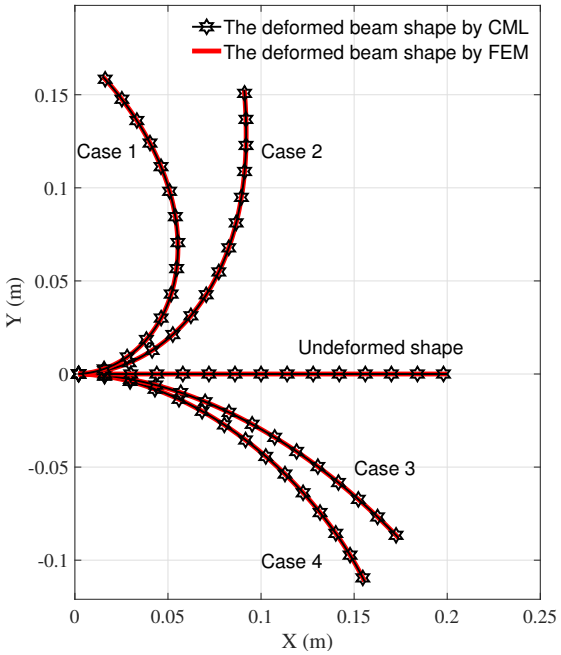

FIGURE 4.21: Graphical results solved via locally-implemented collocation method (CML)

4.5.4 Taylor series method and Padé approximant

4.5.4.1 Taylor series method

Taylor series is a simple and effective option to approximate a given analytic function within its radius of convergence (Spiegel, 1991). Noticing the form of BVP (4.78), it's handy and straightforward to calculate derivatives at $s = 0$ considering the existence of trigonometric functions in the ODE along with one of the boundary conditions: $\theta(0) = 0$. Therefore, we construct a Maclaurin series to approximate the solution to BVP (4.78):

$$\vartheta(s) = \sum_{i=0}^{n} \frac{\frac{\mathrm{d}^i\theta}{\mathrm{d}s^i}(0)}{i!} s^i \tag{4.90}$$

where $\vartheta(s)$ is noted as the approximate solution to (4.78) with order n and all $\frac{\mathrm{d}^i\theta}{\mathrm{d}s^i}(0)$ derivatives are obtained via using chain rule on the governing differential equation of (4.78) in an iterative manner (see Appendix A for the detailed deduction). As it has been shown in the appendix that any ith-order of $\frac{\mathrm{d}^i\theta}{\mathrm{d}s^i}(0)$ can be expressed as a function of one unknown variable $\frac{\mathrm{d}\theta}{\mathrm{d}s}(0)$, so for the sake of simplicity we note it as:

$$\frac{\mathrm{d}^i\theta}{\mathrm{d}s^i}(0) = f_i(\frac{\mathrm{d}\theta}{\mathrm{d}s}(0)) \tag{4.91}$$

where the functions f_i are given in the appendix. Consequently, we can arrive at the approximation of $\frac{\mathrm{d}\theta}{\mathrm{d}s}(s)$ expressed as a function of the unknown variable $\frac{\mathrm{d}\theta}{\mathrm{d}s}(0)$, i.e.,

$$\frac{\mathrm{d}\vartheta}{\mathrm{d}s}(s) = \frac{\mathrm{d}(\sum_{i=0}^{n} \frac{\frac{\mathrm{d}^i\theta}{\mathrm{d}s^i}(0)}{i!} s^i)}{\mathrm{d}s} = \sum_{i=1}^{n} \frac{f_i(\frac{\mathrm{d}\theta}{\mathrm{d}s}(0))}{(i-1)!} s^{(i-1)} \tag{4.92}$$

According to the "Explicit" strategy stated in Section 2.5.4.1, the second boundary condition provided in (4.78): $\frac{\mathrm{d}\theta}{\mathrm{d}s}(L) = \frac{M_o}{EI}$ is explicitly imposed, i.e.,

$$\frac{\mathrm{d}\vartheta}{\mathrm{d}s}(L) = \sum_{i=1}^{n} \frac{f_i(\frac{\mathrm{d}\theta}{\mathrm{d}s}(0))}{(i-1)!} L^{(i-1)} = \frac{M_o}{EI} \tag{4.93}$$

which assumes that the series converges within $[0, L]$ if $n \to +\infty$. Logically, (4.92) will be a sufficient condition to numerically determine $\frac{\mathrm{d}\theta}{\mathrm{d}s}(0)$ when n is large enough. Besides, in (4.93) there is only one unknown: $\frac{\mathrm{d}\theta}{\mathrm{d}s}(0)$, and equivalently it is a low-dimensional model. Therefore, we can use Newton-Raphson method or other related methods to both directly and efficiently solve (4.93). As long as the value of $\frac{\mathrm{d}\theta}{\mathrm{d}s}(0)$ is obtained, we can logically approximate $\theta(s)$ via (4.90).

4.5.4.2 Padé approximant

A Taylor series can often be accelerated quite dramatically (or turned from divergent to convergent) by being rearranged into a ratio of two such series. Supposing we have approximated the solution to BVP (4.78) using Maclaurin series shown in (4.90), we can then construct a rational function via:

$$\vartheta(s) = \sum_{i=0}^{n} \frac{\frac{\mathrm{d}^i\theta}{\mathrm{d}s^i}(0)}{i!} s^i = \sum_{i=0}^{n} c_i s^i = \frac{P(s)}{Q(s)} = \frac{\sum_{i=0}^{p} a_i s^i}{\sum_{i=0}^{q} b_i s^i} \tag{4.94}$$

where $c_i = \frac{1}{i!}\frac{\mathrm{d}^i\theta}{\mathrm{d}s^i}(0)$, $P(s)$ and $Q(s)$ are polynomial functions of respective order p and q. (4.94) is called the Padé approximant $[p,q]$ of $\vartheta(s)$. The unknown coefficients a_i and b_i of $P(s)$ and $Q(s)$ are determined by (4.90):

$$\begin{aligned} &P(s) = Q(s)\vartheta(s) + o[s^{n+1}] \\ &Q(0) = 1 \\ &p + q = n \end{aligned} \tag{4.95}$$

equivalently,

$$c_0 + c_1 s + c_2 s^2 + ... = \frac{a_0 + a_1 s + a_2 s^2 + ...}{1 + b_1 s + b_2 s^2 + ...} \tag{4.96}$$

Multiplying up the denominator gives the following equivalent set of relations:

$$\begin{aligned} a_0 &= c_0 \\ a_1 &= c_1 + c_0 b_1 \\ a_2 &= c_2 + c_1 b_1 + c_0 b_2 \\ a_3 &= c_3 + c_2 b_1 + c_1 b_2 + c_0 b_3 \\ &... \end{aligned} \tag{4.97}$$

With c_i given (derived in Section 4.5.4.1), each new line introduces 2 new unknowns, a_i and b_i. However, due to the constraint $p + q = n$, then there will be as many equations as unknowns (ignoring all terms $O(s^{p+q+1})$). For instance, if $n = 2$ and $p = q = 1$, then we have $a_0 = c_0$, $a_1 = c_1 + c_0 b_1$ and $0 = c_2 + c_1 b_1$
, i.e., 3 unknowns with 3 equations. Consequently, we can solve all these unknown coefficients a_i and b_i as functions of c_i, equivalently functions of $\frac{\mathrm{d}^i\theta}{\mathrm{d}s^i}(0)$. Next, differentiating $\frac{P(s)}{Q(s)}$:

$$\frac{\mathrm{d}}{\mathrm{d}s}\left(\frac{P(s)}{Q(s)}\right) = \frac{P'(s)Q(s) - P(s)Q'(s)}{Q^2(s)} \tag{4.98}$$

and explicitly satisfying the second boundary condition $s = L$:

$$\frac{P'(L)Q(L) - P(L)Q'(L)}{Q^2(L)} = \frac{M_o}{EI} \tag{4.99}$$

where there is only one unknown $\frac{\mathrm{d}\theta}{\mathrm{d}s}(0)$, it can be therefore easily solved via Newton-Raphson method. Then, we can finalize the formulation of the rational function (4.94) to approximate the solution to BVP (4.78):

$$\vartheta(s) = \frac{\sum_{i=0}^{p} a_i s^i}{\sum_{i=0}^{q} b_i s^i} \tag{4.100}$$

Remark 14 *Considering the characteristics of rational functions, (4.100) may present the following* 2 *undesired properties in terms of characterizing or approximating* $\theta(s)$*:*

1. *if* $\sum_{i=0}^{q} b_i \tilde{s}^i = 0$ *and* $\sum_{i=0}^{p} a_i \tilde{s}^i = 0$*, (4.100) will have a hole at* $s = \tilde{s}$*.*
2. *if* $\sum_{i=0}^{q} b_i \tilde{s}^i = 0$ *and* $\sum_{i=0}^{p} a_i \tilde{s}^i \neq 0$*, (4.100) will have a vertical asymptote at* $s = \tilde{s}$*.*

Note that either of the above scenarios contracts the continuum hypothesis stated in solid mechanics. We can ignore the hole when numerically approximating $\theta(s)$ *in terms of the first. For the latter scenario, we need to change* p *and* q *(normally increase them) to avoid the vertical asymptote.*

In terms of the preset order of the Taylor series and Padé approximant for analyzing large deflection of slender beams, (Wu and Zheng, 2022c) is recommended for readers (see Section 3.2 in (Wu and Zheng, 2022c)).

TABLE 4.15: Beam-end coordinates solved by Taylor series method (TSM) and Padé approximant (PA)

	Case	Case 1	Case 2	Case 3	Case 4
Loading	f_x	1.3	0.65	−0.65	−2.6
	f_y	0.9	0.45	−0.45	−1.8
	m_o	0.4	0.2	−0.2	−0.8
TSM	$\hat{x}(1)$	0.7157	0.9379	0.9767	0.8769
	$\hat{y}(1)$	0.6130	0.3098	−0.1916	−0.4247
	$\hat{\theta}(1)$	1.1633	0.5324	−0.3357	−0.8255
	Order	16	8	4	16
PA	$\hat{x}(1)$	0.7145	0.9379	0.9767	0.8757
	$\hat{y}(1)$	0.6140	0.3098	−0.1918	−0.4264
	$\hat{\theta}(1)$	1.1663	0.5324	−0.3360	−0.8304
	Order	10	8	4	10
WRM	$\hat{x}(1)$	0.7146	0.9377	0.9765	0.8756
	$\hat{y}(1)$	0.6139	0.3104	−0.1924	−0.4266
	$\hat{\theta}(1)$	1.1658	0.5336	−0.3371	−0.8311
CBCM	$\hat{x}(1)$	0.7146	0.9376	0.9765	0.8756
	$\hat{y}(1)$	0.6139	0.3104	−0.1925	−0.4267
	$\hat{\theta}(1)$	1.1659	0.5336	−0.3372	−0.8311
	NOE	16	16	16	16
FEM	$\hat{x}(1)$	0.7149	0.9377	0.9766	0.8756
	$\hat{y}(1)$	0.6139	0.3104	−0.1925	−0.4269
	$\hat{\theta}(1)$	1.1657	0.5335	−0.3372	−0.8315
	NOE	15	15	15	15
ER_{TSM}	$\hat{x}(1)$	0.11%	0.02%	0.01%	0.15%
	$\hat{y}(1)$	0.15%	0.19%	0.47%	0.52%
	$\hat{\theta}(1)$	0.21%	0.21%	0.44%	0.08%
ER_{PA}	$\hat{x}(1)$	0.06%	0.02%	0.01%	0.01%
	$\hat{y}(1)$	0.02%	0.19%	0.36%	0.12%
	$\hat{\theta}(1)$	0.05%	0.21%	0.36%	0.08%
CE (s)	TSM	0.008	0.009	0.009	0.011
	PA	0.010	0.009	0.010	0.010
	WRM	0.020	0.027	0.012	0.017
	CBCM	0.20	0.30	0.25	0.35
	FEM	11	5	4	8

4.5.4.3 Numerical validation

In this section, the numerical validation is carried out via the nondimensionalization framework for more straightforward comparisons. According to (3.100), we derive the nondimensionalized one of BVP (4.78), equivalently (3.25):

$$\begin{aligned} \text{D.E.}\quad & \frac{\mathrm{d}^2\hat{\theta}}{\mathrm{d}\hat{s}^2} = -f_y\cos\hat{\theta}(\hat{s}) - f_x\sin\hat{\theta}(\hat{s}) \\ \text{B.C.}\quad & \hat{\theta}(0) = 0 \\ & \frac{\mathrm{d}\hat{\theta}}{\mathrm{d}\hat{s}}(1) = m_o \end{aligned} \tag{4.101}$$

The nondimensionalized beam-end loading is given below:

$$\begin{aligned} &\text{Case 1: } f_x = 1.3;\ f_y = 0.9;\ m_o = 0.4; \\ &\text{Case 2: } f_x = 0.65;\ f_y = 0.45;\ m_o = 0.2; \\ &\text{Case 3: } f_x = -0.65;\ f_y = -0.45;\ m_o = -0.2; \\ &\text{Case 4: } f_x = -2.6;\ f_y = -1.8;\ m_o = -0.8; \end{aligned}$$

The beam-end coordinates and deflected beam shapes are presented in Table 4.15 and Fig. 4.22 where CBCM and weighted residual methods are used as verification as well.

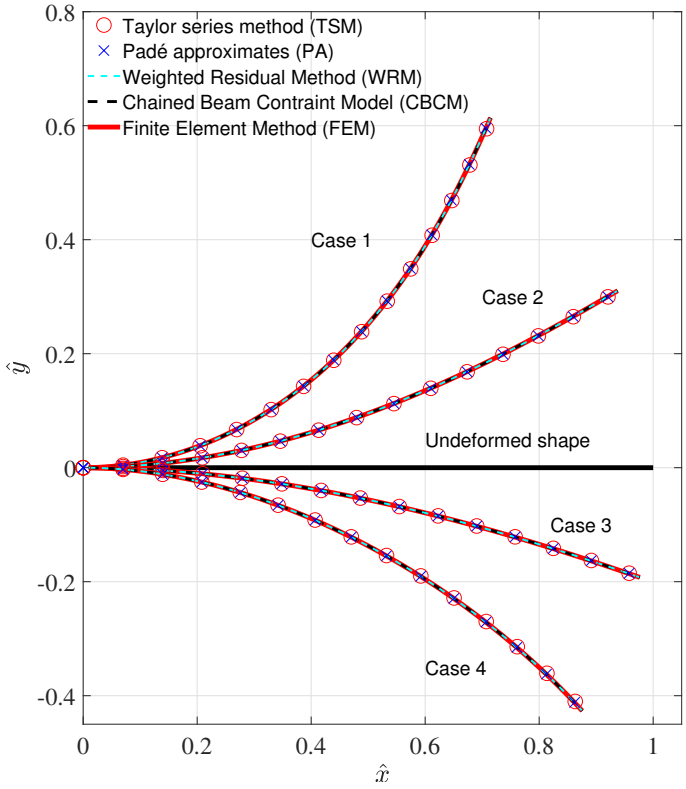

FIGURE 4.22: Graphical results solved via Taylor series method (TSM) and Padé approximant (PA)

4.6 Numerical method of solving optimization problems

Different from Section 4.3 to Section 4.5, we work on the ODEs that are derived via Newtonian mechanics. As stated earlier, if we study the topic of large deflections, we need to face functional minimization problems. As stated in (3.159), the functional Π is a function of function $\theta(s)$. According to the principle of minimum total potential energy, we aim to search for a proper function $\theta(s)$ that minimizes the given functional Π, which is a classic problem in functional analysis. Mathematically speaking, it's always better to find the exact analytical function of $\theta(s)$ but this is always hard to achieve. Instead, from the perspective of engineering, we can bypass the difficulties of deriving the analytical one via using polynomials to approximate the desired function. Similarly, according to Weierstrass's first theorem, we can then define an nth-order polynomial function to approximate the desired function, i.e.,

$$\vartheta(s) = \sum_{i=0}^{n} c_i s^i \tag{4.102}$$

where there are $n+1$ unknown coefficients ($i = 0, 1, 2, 3...n$). Then, the functional minimization problem stated in (3.159) can be transformed into a function of c where $c = [c_0, c_1, ..., c_n]^\top$.

$$\Pi = f(\theta(s), \frac{\mathrm{d}\theta}{\mathrm{d}s}(s), I(s), E, F(s), \kappa_o(s)) \approx \bar{\Pi} = f(\vartheta(s), \frac{\mathrm{d}\vartheta}{\mathrm{d}s}(s), I(s), E, F(s), \kappa_o(s)) = f(c) \tag{4.103}$$

where $\bar{\Pi}$ denotes the approximate potential energy, and $I(s)$, E, $F(s)$ and $\kappa_o(s)$ are known given an elastic system subjected to a given loading condition. Besides, we have two constraints: $\vartheta(0) = 0$ and $\frac{\mathrm{d}\vartheta}{\mathrm{d}s}(L) - \frac{M_o}{EI(L)} = 0$ when seeking for the minimum of $\bar{\Pi}$, which yields:

$$\begin{aligned} &c_0 = 0 \\ &c_1 + 2Lc_2 + cL^2c_3 + 4L^3c_4 + ...(n-1)L^{n-2}c_{n-1} + nL^{n-1}c_n - \frac{M_o}{EI(L)} = 0 \end{aligned} \tag{4.104}$$

TABLE 4.16: Beam-end coordinates solved by Lagrange multiplier (LM)

	Case	Case 1	Case 2	Case 3	Case 4
Loading	F_x (N)	1000	500	−500	−1000
	F_y (N)	1000	500	−500	−1000
	M_o (N.m)	60	30	−30	−60
LM	$x(L)$ (m)	0.01491	0.09098	0.1739	0.1556
	$y(L)$ (m)	0.1598	0.1527	−0.08810	−0.1113
	$\theta(L)$ (rad)	2.3176	1.6512	−0.8061	−1.1085
FEM	$x(L)$ (m)	0.01492	0.09105	0.1739	0.1556
	$y(L)$ (m)	0.1599	0.1527	−0.8817	−0.1114
	$\theta(L)$ (rad)	2.3185	1.6512	−0.8066	−1.1092
ER	$x(L)$	0.061%	0.07%	0.00%	0.00%
	$y(L)$	0.06%	0.00%	0.08%	0.09%
	$\theta(L)$	0.04%	0.00%	0.06%	0.06%
CE (s)	LM	0.33	0.27	0.29	0.57
	FEM	13.00	12.00	7.00	8.00

Note that 6th-order polynomials are used to approximate the solutions.

Here, we still take the simplest scenario where only beam-end loading is considered (shown in Fig. 3.24), and we need to write down its approximate potential energy $\bar{\Pi}$ instead of the governing BVP:

$$\begin{aligned}\bar{\Pi} = f(c) &= \int_0^L \frac{1}{2} EI(s)(\frac{\mathrm{d}\vartheta}{\mathrm{d}s} - \kappa_o(s))^2 \mathrm{d}s - F_x \Delta x(L) - F_y \Delta y(L) - M_o \Delta\vartheta(L) \\ &= \int_0^L \frac{1}{2} EI(s)(\frac{\mathrm{d}\vartheta}{\mathrm{d}s} - \kappa_o(s))^2 \mathrm{d}s - F_x(x_o(L) - \int_0^L \cos\vartheta(s)\mathrm{d}s) - F_y(\int_0^L \sin\vartheta(s)\mathrm{d}s - y_o(L)) \\ &- M_o(\vartheta(L) - \theta_o(L)) \\ &= \int_0^L \frac{1}{2} EI(\sum_{i=1}^n i c_i s^{i-1})^2 \mathrm{d}s - F_x(L - \int_0^L \cos(\sum_{i=0}^n c_i s^i)\mathrm{d}s) - F_y \int_0^L \sin(\sum_{i=0}^n c_i s^i)\mathrm{d}s - M_o \sum_{i=0}^n c_i L^i\end{aligned} \tag{4.105}$$

where $\kappa_o(s) = 0$, $x_o(L) = L$, $y_o(L) = 0$, $\theta_o(L) = 0$ and I is constant since the straight beam is assumed to have constant cross sections here. Therefore, this functional minimization problem finally yields a constrained optimization subjected to (4.104). According to Lagrange Multiplier (LM) stated in Section 2.7, we can rewrite down the objective function:

$$f^*(c, \lambda_1, \lambda_2) = f(c) + \lambda_1(c_0 - 0) + \lambda_2(c_1 + 2Lc_2 + ...(n-1)L^{n-2}c_{n-1} + nL^{n-1}c_n - \frac{M_o}{EI(L)}) \tag{4.106}$$

To minimize $f^*(c, \lambda_1, \lambda_2)$, following (2.51) yields

$$\nabla f^*(c, \lambda_1, \lambda_2) = 0 \tag{4.107}$$

Logically, we can solve (4.107) via Newton Raphson method. For numerical validation, the geometric and material parameters chosen for the studied straight beam is shown in the following:

$$E = 200 \times 10^9 \text{ Pa};\ \nu = 0.3;\ w = 0.01 \text{ m};\ h = 0.004 \text{ m};\ L = 0.2 \text{ m};\ I = \frac{wh^3}{12}$$

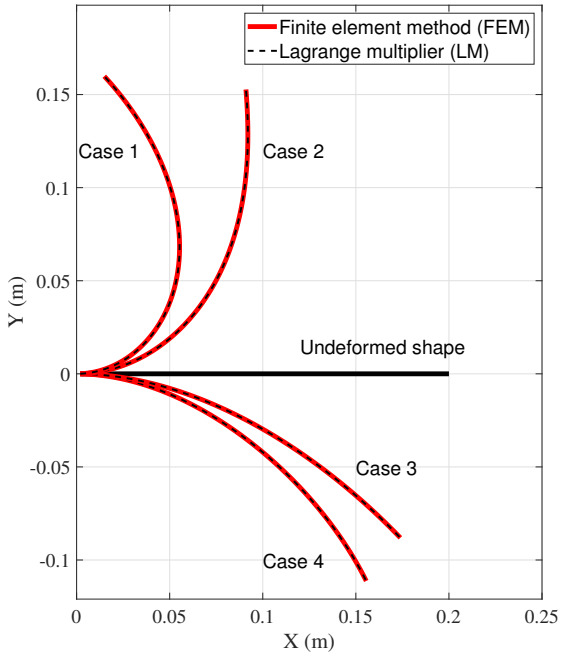

FIGURE 4.23: Graphical results solved via Lagrange multiplier

In terms of the exerted beam-end loading, it is shown as follows:

$$\begin{aligned}
&\text{Loading case 1: } F_x = 1000\ \text{N};\ F_y = 1000\ \text{N};\ M_o = 60\ \text{N.m};\\
&\text{Loading case 2: } F_x = 500\ \text{N};\ F_y = 500\ \text{N};\ M_o = 30\ \text{N.m};\\
&\text{Loading case 3: } F_x = -500\ \text{N};\ F_y = -500\ \text{N};\ M_o = -30\ \text{N.m};\\
&\text{Loading case 4: } F_x = -1000\ \text{N};\ F_y = 1000\ \text{N};\ M_o = -60\ \text{N.m};
\end{aligned}$$

Since the shear strain is not considered in Euler-Bernoulli beam model, ν is logically not involved in our numerical algorithms. The beam-end coordinates and deflected beam shapes solved via LM are presented in Table 4.16 and Fig. 4.23 where FEM is used as verification as well. The computational expense (CE) and the corresponding error (ER) with respect to FEM are presented in the following respect results.

4.7 A comprehensive case study

This section can be regarded as a comprehensive case study where several aforementioned topics in Chapter 4 are involved here. Therefore, we demonstrate the whole process of designing a planar beam to the analysis of its large deflection subjected to some certain loading conditions.

4.7.1 Geometrical definition of a planar beam

In terms of the geometrical definition of a planar beam, we need to define the properties of the cross sections and the beam axis as well. For the properties of the cross sections, we have:

$$w = 0.01\ \text{m};\ h = 0.004\ \text{m};\ I = \frac{wh^3}{12}\ \text{m}^4$$

Then, we can define the beam axis in Cartesian coordinate system:

$$y = \frac{\sin(10\pi x)}{100},\ x \in [0, 0.2] \tag{4.108}$$

TABLE 4.17: Polynomial coefficients of $\vartheta_o(s)$

c_0	c_1	c_2	c_3	c_4	c_5	c_6	c_7
0.2936	2.1368	−220.6939	870.9514	1.2342×10^4	-8.5224×10^4	1.4259×10^5	-7.7151×10^3

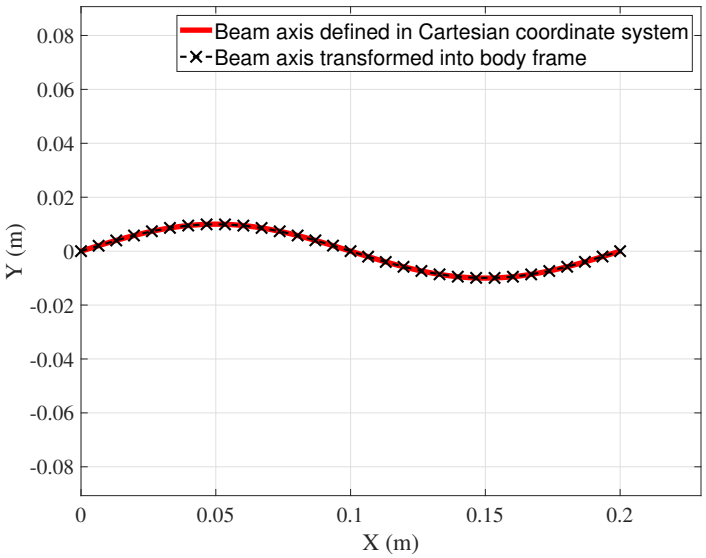

FIGURE 4.24: Sine-shape beam axis transformed from Cartesian coordinate system to body frame

Following (4.5) and (3.10), we can finally characterize the exact beam shape in body frame as shown in Fig. 4.24 where 7th-order polynomial expressed in body frame is used:

$$\vartheta_o = \sum_{i=0}^{7} c_i s^i \tag{4.109}$$

where the polynomial coefficients of $\vartheta_o(s)$ are presented in Table 4.17. According to (3.11), the initial curvature can be calculated:

$$\kappa_o = \frac{\mathrm{d}\vartheta_o}{\mathrm{d}s} \tag{4.110}$$

Logically, following (3.3), the beam length can be calculated:

$$L = \int_0^{0.2} \sqrt{1 + (\frac{\mathrm{d}y}{\mathrm{d}x})^2}\mathrm{d}x = 0.2048 \text{ m} \tag{4.111}$$

4.7.2 Material and loading conditions

Here, we choose structural steel as the material of the studied beam:

$$E = 200 \times 10^9 \text{ Pa};\ \rho = 7850 \text{ kg/m}^3$$

Supposing the beam is in a space where the gravity there is 500 times of the one on the earth, to consider this hypergravity, we have

$$q_y = 500 \times \frac{Lwh\rho g}{L} = 500 \times wh\rho g = 1.5386 \times 10^3 \text{ N/m}$$

Therefore, four cases of beam-end loading conditions are presented below:

$$\begin{aligned}
&\text{Loading case 1: } F_x = 1000\ \text{N};\ F_y = 1000\ \text{N};\ M_o = 60\ \text{N.m}\\
&\text{Loading case 2: } F_x = 500\ \text{N};\ F_y = 500\ \text{N};\ M_o = 30\ \text{N.m}\\
&\text{Loading case 3: } F_x = 0\ \text{N};\ F_y = 0\ \text{N};\ M_o = 0\ \text{N.m}\\
&\text{Loading case 4: } F_x = -500\ \text{N};\ F_y = 500\ \text{N};\ M_o = -30\ \text{N.m}
\end{aligned}$$

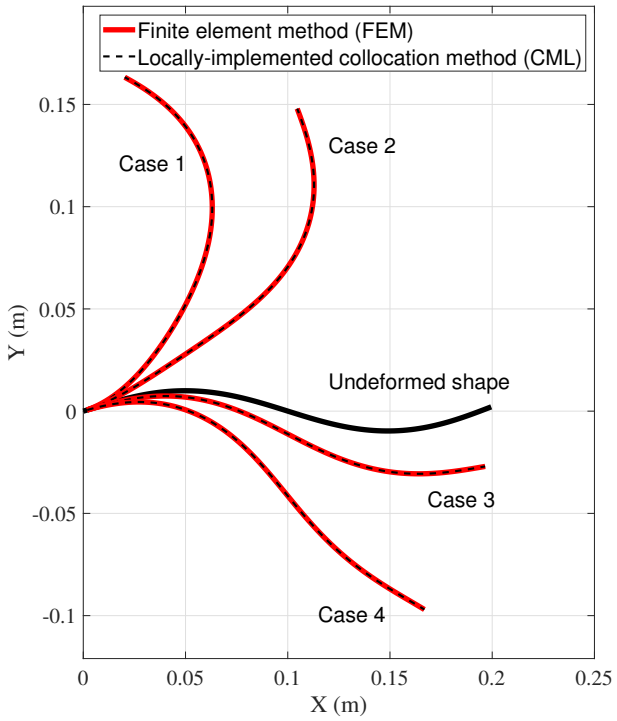

FIGURE 4.25: Graphical results of the studied comprehensive case

4.7.3 Governing BVP and the results

According to (3.33) and (3.34), we can write down the governing BVP for this studied problem:

$$\begin{aligned}
&\text{D.E.} \quad \frac{\mathrm{d}^2\theta}{\mathrm{d}s^2} = -\frac{F_y\cos\theta(s) + F_x\sin\theta(s)}{EI} + \frac{\mathrm{d}\kappa_o}{\mathrm{d}s} + \frac{q_y(s)\cos\theta(s)(L-s)}{EI}\\
&\text{B.C.} \quad \theta(0) = 0\\
&\qquad \frac{\mathrm{d}\theta}{\mathrm{d}s}(L) = \frac{M_o}{EI} + \kappa_o(L)
\end{aligned} \tag{4.112}$$

Logically, we can numerically solve BVP (4.112) via any of the numerical methods mentioned in Section 4.5. Here, the deflected shape of the studied beam due to the mentioned loading conditions is complex so we use locally-implemented collocation method (CML) stated in Section 2.5.3.7 to locally approximate the solution to BVP (4.112). The beam-end coordinates and deflected beam shapes solved via CML are presented in Table 4.18 and Fig. 4.25 where FEM is used as verification as well. The computational expense (CE) and the corresponding error (ER) with respect to FEM are presented in Table 4.18.

TABLE 4.18: Beam-end coordinates of the deflected beam in the studied comprehensive case

	Case	Case 1	Case 2	Case 3	Case 4
Loading	F_x (N)	1000	500	0	-500
	F_y (N)	1000	500	0	-500
	M_o (N.m)	60	30	0	-30
	q_y (N/m)	1.5386×10^3			
CML	$x(L)$ (m)	0.02026	0.1046	0.1966	0.1668
	$y(L)$ (m)	0.1633	0.1480	-0.02703	-0.09701
	$\theta(L)$ (rad)	2.6463	1.9318	0.1719	-0.5432
FEM	$x(L)$ (m)	0.02087	0.1050	0.1966	0.1671
	$y(L)$ (m)	0.1630	0.1475	-0.02683	-0.09661
	$\theta(L)$ (rad)	2.6416	1.9286	-0.1730	-0.5396
ER	$x(L)$	2.92%	0.38%	0.18%	0.18%
	$y(L)$	0.18%	0.34%	0.75%	0.41%
	$\theta(L)$	0.184%	0.17%	0.64%	0.67%
CE (s)	CML	1.52	0.66	0.60	0.50
	FEM	28.00	25.00	4.00	5.00

Note that 7th-order polynomials are used to approximate the solutions.

4.8 Conclusions

In this chapter, we have stated different mathematical tools for modeling large deflection of slender beams. For the governing BVP derived under Newtonian framework, we have presented closed-form solutions, hybrid methods and numerical methods. From the perspective of energy framework, we transform the functional minimization problem (where we look for a proper function to minimize the functional) into a typical optimization problem (where we look for some unknown polynomial coefficients that can approximate the desired function). The major difference between the two strategies is essentially the difference between dealing with BVPs and optimization problems respectively. As long as conservative forces are not involved in the studied system, Lagrangian formulation is relatively easier than Newtonian formulation in the framework of numerical optimization. On the contrary, if we are interested in the details of the system (such as the internal force), Newtonian framework would be a nicer option in this case. No matter which strategy is used to model the system, we need to find the most suitable one for the faced situation.

Chapter 5

Model-based Design and Optimization

5.1 Introduction

In the last chapter, we have stated how to model the flexible structures via beam theories and the corresponding mathematical tools. In this chapter, we are going to use the developed modeling and approximation techniques to design different CMs and to optimize the design of CMs. From the design point of view, the proposed methods can be used to precisely and more efficiently to predict the performance of CMs (compared to FEM). In terms of optimization, the proposed modeling methods can be used to efficiently optimize the geometric parameters of the CMs to fulfill a given task. Therefore, we start from demonstrating the feasibility of modeling some typical CMs to presenting the model-based optimization via an ICB-based compliant parallelogram.

5.2 Modeling of representative compliant mechanisms

To model compliant mechanisms, we have to develop the following three standard groups of equations according to solid mechanics (Dym, Shames, et al., 1973):

a) **Constitutive equations**: describing the deformation of flexible members subjected to external loading.

b) **Force equilibrium equations**: describing the force and moment equilibrium of the deformable system.

c) **Geometrical compatibility equations**: describing the geometrical relationships of the deformable system.

The static modeling of CMs are based on the above three principles, and we are normally interested in the force-displacement relationships of a reference point of the studied mechanisms. In this section, four types of mechanisms are studied, which are compliant parallelograms, compliant revolute joints, bi-stable mechanisms, and kinematic-control-based compliant mechanisms. In particular, the last one is a novel type of CMs where they are actuated by the displacement of kinematic joints instead of actual forces. In this case, these new CMs could be more accurately controlled since the measurement of forces can be a tough one while sensing the displacements in kinematic joints could be easier, for example, the rotation of the revolute joints can be actuated and measured by servo motors. All the mentioned cases have illustrated examples presented accordingly.

5.2.1 Compliant parallelograms

In this section, a typical CM, **a straight-beam-based compliant parallelogram** is studied. As shown in Fig. 5.1, the mechanism is composed of a rigid motion stage and two compliant beams (Beam #1 and Beam #2). K is the reference point. Other geometric information and loading conditions are also provided in Fig. 5.1. Normally, compliant parallelograms serve as positioning stages where the built-in flexible beams are deflected within intermediate range. Therefore, in terms of the constitutive models for each flexible beams, BBCM are used along with BCM and SD-FEM for verification. The static model is composed of three parts: constitutive equations, force equilibrium equations and geometric compatibility equations.

- **Static modeling**

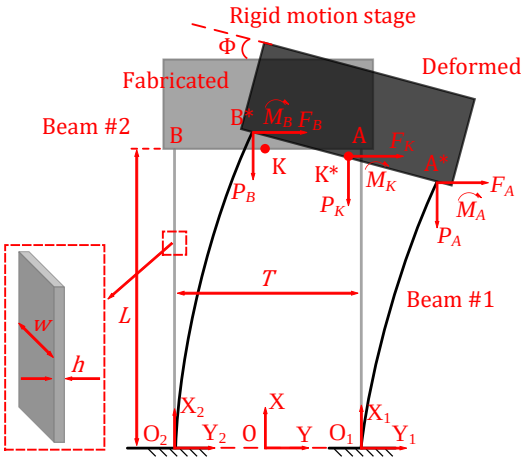

FIGURE 5.1: Schematic diagram of a straight-beam-based compliant parallelogram

1) **Constitutive equations**
For Beam #1, according to (4.65), we have

$$\Gamma_1(s, P_A, F_A, M_A, E, I, L);\ x_1(s) = \int_0^s \cos(\Gamma_1(\xi)) - \frac{P_A}{EA}\mathrm{d}\xi;\ y_1(s) = \int_0^s \sin(\Gamma_1(\xi))\mathrm{d}\xi;\ s \in [0, L] \tag{5.1}$$

For Beam #2, according to (4.65), we have

$$\Gamma_2(s, P_B, F_B, M_B, E, I, L);\ x_2(s) = \int_0^s \cos(\Gamma_2(\xi)) - \frac{P_B}{EA}\mathrm{d}\xi;\ y_2(s) = \int_0^s \sin(\Gamma_2(\xi))\mathrm{d}\xi;\ s \in [0, L] \tag{5.2}$$

2) **Force equilibrium equations**

$$\begin{aligned} &F_K - F_A - F_B = 0;\ P_K - P_A - P_B = 0 \\ &M_K - M_A - M_B + F_K T/2 \sin\Phi - P_K T/2 \cos\Phi - F_B T \sin(\Phi) + P_B T \cos(\Phi) = 0 \end{aligned} \tag{5.3}$$

3) **Geometric compatibility equations**

$$\begin{aligned} &\begin{bmatrix} x_A \\ y_A \end{bmatrix} = \begin{bmatrix} L \\ T/2 \end{bmatrix};\ \begin{bmatrix} x_{A^*} \\ y_{A^*} \end{bmatrix} = \begin{bmatrix} \int_0^L \cos\Gamma_1(s)\mathrm{d}s \\ \int_0^L \sin\Gamma_1(s)\mathrm{d}s \end{bmatrix} + \begin{bmatrix} 0 \\ T/2 \end{bmatrix}; \\ &\begin{bmatrix} x_B \\ y_B \end{bmatrix} = \begin{bmatrix} L \\ -T/2 \end{bmatrix};\ \begin{bmatrix} x_{B^*} \\ y_{B^*} \end{bmatrix} = \begin{bmatrix} \int_0^L \cos\Gamma_2(s)\mathrm{d}s \\ \int_0^L \sin\Gamma_2(s)\mathrm{d}s \end{bmatrix} - \begin{bmatrix} 0 \\ T/2 \end{bmatrix}; \\ &\mathrm{AB} = [(x_A - x_B)^2 + (y_A - y_B)^2]^{0.5} = T;\ \mathrm{A^*B^*} = [(x_{A^*} - x_{B^*})^2 + (y_{A^*} - y_{B^*})^2]^{0.5} = T; \\ &|x_{A^*} - x_{B^*}| = T\sin\Phi;\ |y_{A^*} - y_{B^*}| = T\cos\Phi;\ \Gamma_1(L) = \Gamma_2(L) = \Phi; \\ &\begin{bmatrix} x_K \\ y_K \end{bmatrix} = \frac{1}{2}\begin{bmatrix} x_A \\ y_A \end{bmatrix} + \frac{1}{2}\begin{bmatrix} x_B \\ y_B \end{bmatrix};\ \begin{bmatrix} x_{K^*} \\ y_{K^*} \end{bmatrix} = \frac{1}{2}\begin{bmatrix} x_{A^*} \\ y_{A^*} \end{bmatrix} + \frac{1}{2}\begin{bmatrix} x_{B^*} \\ y_{B^*} \end{bmatrix};\ \begin{bmatrix} \Delta x \\ \Delta y \end{bmatrix} = \begin{bmatrix} x_{K^*} \\ y_{K^*} \end{bmatrix} - \begin{bmatrix} x_K \\ y_K \end{bmatrix} \end{aligned} \tag{5.4}$$

where $\begin{bmatrix} x_A & y_A \end{bmatrix}^\top$, $\begin{bmatrix} x_{A^*} & y_{A^*} \end{bmatrix}^\top$, $\begin{bmatrix} x_B & y_B \end{bmatrix}^\top$, $\begin{bmatrix} x_{B^*} & y_{B^*} \end{bmatrix}^\top$, $\begin{bmatrix} x_K & y_K \end{bmatrix}^\top$ and $\begin{bmatrix} x_{K^*} & y_{K^*} \end{bmatrix}^\top$ are the coordinates of A, A*, B, B*, K and K* in the global coordinate system X-O-Y (see Fig. 5.1). Then, we can numerically solve Eq. (5.1) to (5.4) using Newton-Raphson method. Besides, $\begin{bmatrix} \Delta x & \Delta y & \Phi \end{bmatrix}^T$ refers to the translational and rotational displacements of K, the reference point of the modeled mechanism.

- **Numerical results**
We are interested in the relationships between applied loads $\begin{bmatrix} F_K & P_K & M_K \end{bmatrix}^T$ and the corresponding displacements $\begin{bmatrix} \Delta x & \Delta y & \Phi \end{bmatrix}^T$ both at the reference point K. The material properties and geometry information are

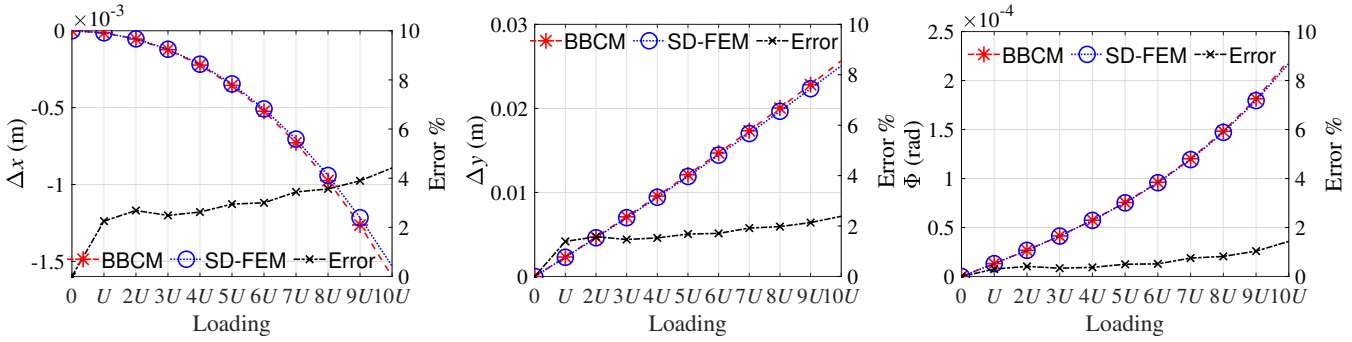

(A) Δx-iU (B) Δy-iU (C) Φ-iU

FIGURE 5.2: Numerical results of the studied compliant parallelogram by BBCM

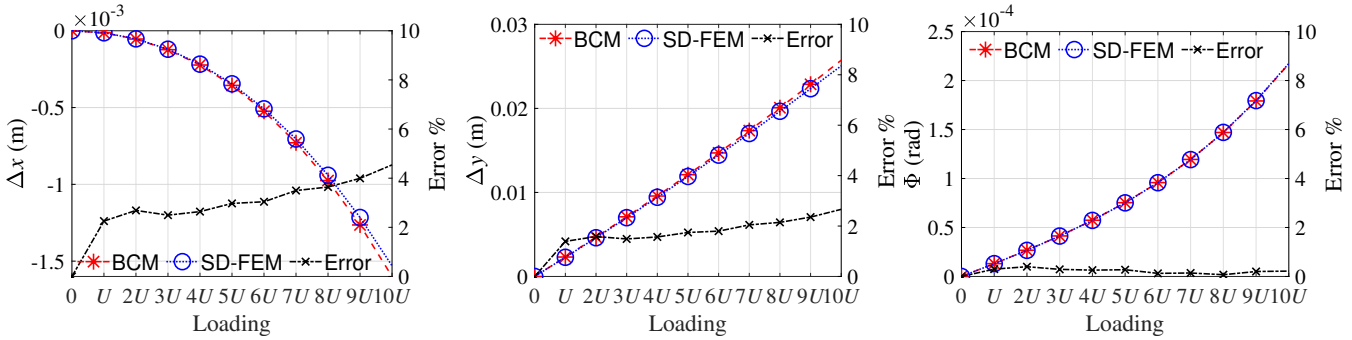

(A) Δx-iU (B) Δy-iU (C) Φ-iU

FIGURE 5.3: Numerical results of the studied compliant parallelogram by BCM

provided in the following:

$$E = 200 \times 10^9 \text{ Pa};\ w = 0.015 \text{ m};\ h = 0.0045 \text{ m};\ L = 0.25 \text{ m};\ I = \frac{wh^3}{12};\ T = 0.2 \text{ m};\ A = hw$$

The applied loads are set up as:

$$\begin{bmatrix} F_K \\ P_K \\ M_K \end{bmatrix} = iU = i \begin{bmatrix} 80 \text{ N} \\ 80 \text{ N} \\ 4 \text{ N.m} \end{bmatrix} \quad (i = 1, 2, 3, 4..10)$$

The numerical results are provided in Fig. 5.2 and Fig. 5.3. In both modeling process, the next-step initial guess is set up as the last-step answer for faster convergence (Rao, 2017). It can be easily noticed that results from BBCM achieve the same accuracy level as BCM does where the maximum transverse deflection of the built-in flexible beams goes up to 10% of the beam length L. Then, we can characterize the deflected beam shapes via (5.1) and (5.2) (see the maximum deflected configuration of the studied CM under $10U$ in Fig. 5.4), which serves as a handy tool to analyze the potential mechanical interference during the motion of the CM. Besides, we can also calculate the stored elastic energy in the studied CM via BBCM:

$$E_p = E_{p1} + E_{p2} = \int_0^L \frac{1}{2} EI(\frac{\partial \Gamma_1}{\partial s})^2 \mathrm{d}s + \frac{P_A^2 L}{2EA} + \int_0^L \frac{1}{2} EI(\frac{\partial \Gamma_2}{\partial s})^2 \mathrm{d}s + \frac{P_B^2 L}{2EA} \tag{5.5}$$

The results via BBCM and BCM are plotted in Fig. 5.5 where the errors of both are all below 4% along the motion of the studied CM.

5.2.2 Compliant revolute joint

In this section, **a straight-beam-based cross-axis compliant revolute joint** is modeled where the presented 9 numerical methods stated in Section 4.5 are used to handle the constitutive equation, BVP (3.25). As shown in Fig. 5.6, the

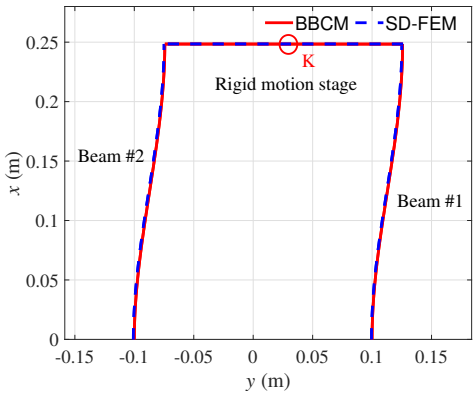

FIGURE 5.4: The maximum deflected graphical results of the studied CM obtained by BBCM and SD-FEM

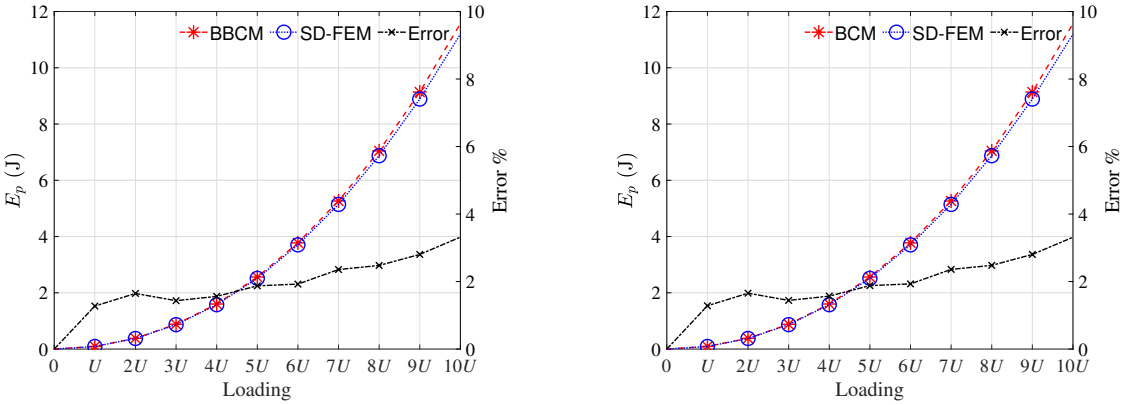

(A) E_p-iU via BBCM (B) E_p-iU via BCM

FIGURE 5.5: The stored elastic energy stored in the studied CM

revolute joint is composed of two slender straight beams (beam #1 and beam #2) and a rigid link. Each of the beams is fixed at one end respectively (O_1 and O_2) and attached to a rigid link AB on the other end. Similarly, L, w, and h refer to the length, width, and thickness of the 2 involved elementary beams respectively. The global coordinate frame X-O-Y is established at the mid-point of O_1 and O_2. A combined load composed of F_K, P_K and M_K is applied at the reference point K (the mid-point of AB), resulting in a deformed shape of the studied revolute mechanism shown in Fig. 5.6. F_A, P_A and M_A are the forces and moment exerted at the tip A of beam #1 by the rigid link. F_B, P_B and M_B are the forces and moment exerted at the tip B of beam #2 by the rigid link. Besides, A^*, B^* and K^* refer to the points after deformation accordingly. Φ is the rotational angle of the revolute joint. 2 local coordinate systems are set up for each flexible beam (see X_1-O_1-Y_1 and X_2-O_2-Y_2 in Fig. 5.6). Note that we assume $O_1O_2 = AB = T$ for this revolute joint and $\angle Y_1O_1O = \pi - \angle Y_2O_2O = \alpha$. Similarly, the static model is also composed of three parts: constitutive equations, force equilibrium equations and geometric compatibility equations.

- **Static modeling**

1) **Constitutive relationships**

$$\textbf{Beam \#1:}\quad \text{D.E.}\quad \frac{\mathrm{d}^2\theta_1}{\mathrm{d}s^2} = -\frac{F_A}{EI}\left(\cos\theta_1(s) + \frac{P_A}{F_A}\sin\theta_1(s)\right)$$
$$\text{B.C.}\quad \theta_1(0) = 0 \qquad (5.6)$$
$$\frac{\mathrm{d}\theta_1}{\mathrm{d}s}(L) = \frac{M_A}{EI}$$

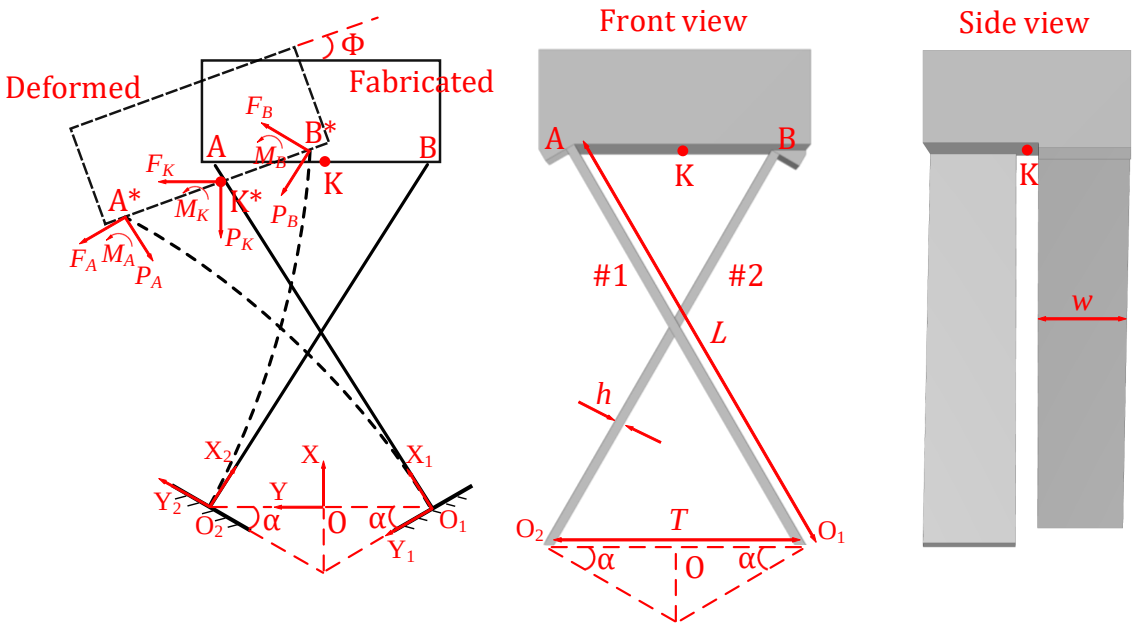

FIGURE 5.6: Constitutive, force equilibrium and compatibility relationships of a straight-beam-based cross-axis compliant revolute joint and its schematic geometry

$$\textbf{Beam \#2:}\quad \text{D.E.}\quad \frac{\mathrm{d}^2\theta_2}{\mathrm{d}s^2} = -\frac{F_B}{EI}\left(\cos\theta_2(s) + \frac{P_B}{F_B}\sin\theta_2(s)\right)$$
$$\text{B.C.}\quad \theta_2(0) = 0 \qquad (5.7)$$
$$\frac{\mathrm{d}\theta_2}{\mathrm{d}s}(L) = \frac{M_B}{EI}$$

2) **Force equilibrium**

$$\begin{aligned} &F_K - F_A\cos\alpha - F_B\cos\alpha - P_B\sin\alpha + P_A\sin\alpha = 0\\ &P_K - P_A\cos\alpha - P_B\cos\alpha - F_A\sin\alpha + F_B\sin\alpha = 0\\ &M_K - M_A - M_B + F_K T/2\sin\Phi - P_K T/2\cos\Phi - F_B T\sin(\alpha+\Phi) + P_B T\cos(\alpha+\Phi) = 0 \end{aligned} \qquad (5.8)$$

3) **Geometric compatibility relationships**

$$\begin{aligned} &\begin{bmatrix} x_A \\ y_A \end{bmatrix} = \begin{bmatrix} L\cos\alpha \\ L/2\sin\alpha \end{bmatrix},\ \begin{bmatrix} x_{A^*} \\ y_{A^*} \end{bmatrix} = \begin{bmatrix} \cos\alpha & -\sin\alpha \\ \sin\alpha & \cos\alpha \end{bmatrix}\begin{bmatrix} \int_0^L \cos\theta_1(s)\mathrm{d}s \\ \int_0^L \sin\theta_1(s)\mathrm{d}s \end{bmatrix} + \begin{bmatrix} 0 \\ -T/2 \end{bmatrix}\\ &\begin{bmatrix} x_B \\ y_B \end{bmatrix} = \begin{bmatrix} L\cos\alpha \\ -L/2\sin\alpha \end{bmatrix},\ \begin{bmatrix} x_{B^*} \\ y_{B^*} \end{bmatrix} = \begin{bmatrix} \cos\alpha & \sin\alpha \\ -\sin\alpha & \cos\alpha \end{bmatrix}\begin{bmatrix} \int_0^L \cos\theta_2(s)\mathrm{d}s \\ \int_0^L \sin\theta_2(s)\mathrm{d}s \end{bmatrix} + \begin{bmatrix} 0 \\ T/2 \end{bmatrix}\\ &\mathrm{AB} = [(x_A - x_B)^2 + (y_A - y_B)^2]^{0.5} = \mathrm{A^*B^*} = [(x_{A^*} - x_{B^*})^2 + (y_{A^*} - y_{B^*})^2]^{0.5} = T\\ &|x_{A^*} - x_{B^*}| = T\sin\Phi,\ |y_{A^*} - y_{B^*}| = T\cos\Phi,\ \theta_1(L) = \theta_2(L) = \Phi\\ &\begin{bmatrix} x_K \\ y_K \end{bmatrix} = \frac{1}{2}\begin{bmatrix} x_A \\ y_A \end{bmatrix} + \frac{1}{2}\begin{bmatrix} x_B \\ y_B \end{bmatrix},\ \begin{bmatrix} x_{K^*} \\ y_{K^*} \end{bmatrix} = \frac{1}{2}\begin{bmatrix} x_{A^*} \\ y_{A^*} \end{bmatrix} + \frac{1}{2}\begin{bmatrix} x_{B^*} \\ y_{B^*} \end{bmatrix},\ \begin{bmatrix} \Delta x \\ \Delta y \end{bmatrix} = \begin{bmatrix} x_{K^*} \\ y_{K^*} \end{bmatrix} - \begin{bmatrix} x_K \\ y_K \end{bmatrix} \end{aligned} \qquad (5.9)$$

where $\begin{bmatrix} x_A & y_A \end{bmatrix}^T$, $\begin{bmatrix} x_{A^*} & y_{A^*} \end{bmatrix}^T$, $\begin{bmatrix} x_B & y_B \end{bmatrix}^T$, $\begin{bmatrix} x_{B^*} & y_{B^*} \end{bmatrix}^T$, $\begin{bmatrix} x_K & y_K \end{bmatrix}^T$ and $\begin{bmatrix} x_{K^*} & y_{K^*} \end{bmatrix}^T$ are the coordinates of A, A*, B, B*, K and K* in the global coordinate system X-O-Y (see Fig. 5.6).. Then, we can numerically solve Eq. (5.6) to (5.9) using Newton-Raphson method. Besides, $\begin{bmatrix} \Delta x & \Delta y & \Phi \end{bmatrix}^T$ refers to the translational and rotational displacements of K, the reference point of the modeled revolute mechanism. Particularly, the 9 proposed methods in Section 4.5 are used respectively to handle the constitutive equations (5.6) and (5.7).

- **Numerical results**

  Modeling the studied revolute mechanism is all about finding out the relationships between applied loads

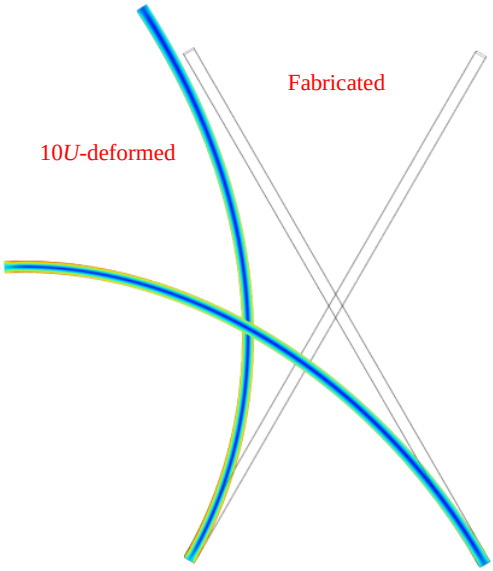

FIGURE 5.7: he deflection of straight-beam-based cross-axis compliant revolute joint via FEM

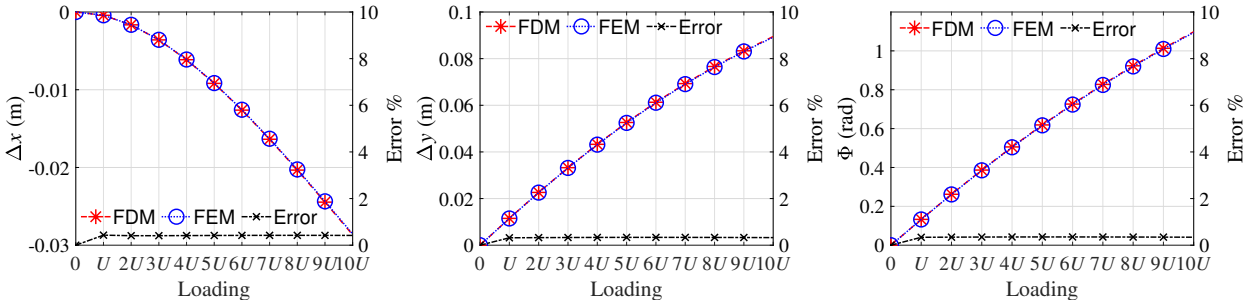

(A) $iU - \Delta x$ (B) $iU - \Delta y$ (C) $iU - \Phi$

FIGURE 5.8: Numerical results by finite difference method (FDM)

$\begin{bmatrix} F_K & P_K & M_K \end{bmatrix}^T$ and the corresponding displacements $\begin{bmatrix} \Delta x & \Delta y & \Phi \end{bmatrix}^T$ both at the reference point K. The material properties and geometry information are provided in the following:

$$E = 200 \times 10^{10} \text{ Pa};\ w = 0.01 \text{ m};\ h = 0.004 \text{ m};\ L = 0.2 \text{ m};\ I = \frac{wh^3}{12};\ T = \frac{L}{2};\ \alpha = \frac{\pi}{6};$$

The applied loads are set up as:

$$\begin{bmatrix} F_K \\ P_K \\ M_K \end{bmatrix} = iU = i \begin{bmatrix} 50 \text{ N} \\ -20 \text{ N} \\ 10 \text{ N.m} \end{bmatrix} \quad (i = 1, 2, 3, 4..10)$$

The results of iU and $\begin{bmatrix} \Delta x & \Delta y & \Phi \end{bmatrix}^T$ are provided via using the proposed methods in Section 4.5 respectively, followed by FEM verification (see Fig. 5.8 to Fig. 5.16). Obviously, every method proposed in Section 4.5 presents high accuracy compared to solid-mechanics-based FEM with errors all below 0.5%. In all these numerical methods, the next-step initial guess is set up as the last-step answer for faster convergence (Rao, 2017). The graphical results of the deflected beams solved by FEM are shown in Fig. 5.7 where the fabricated and the $10U-$deformed mechanisms are presented respectively.

5.2.3 Bi-stable mechanisms

Bi-stable compliant mechanisms experience nonlinear buckling and nonlinear post-buckling when operating, which is difficult to model. In this section, a typical type of lumped bi-stable compliant mechanisms is modeled where the

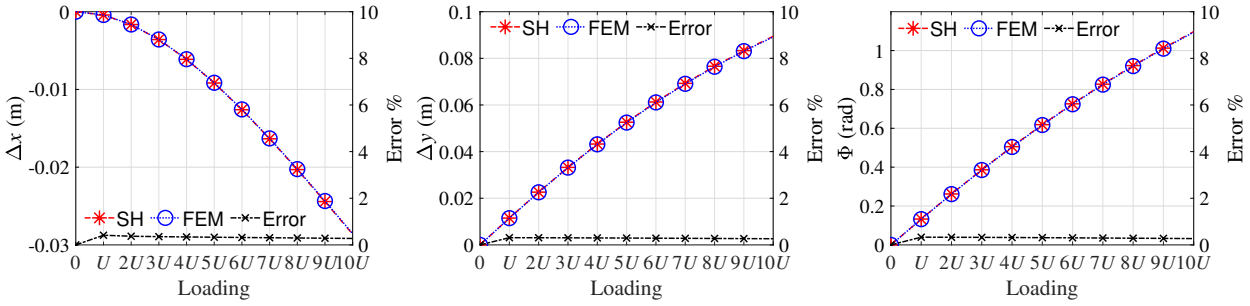

(A) $iU - \Delta x$ (B) $iU - \Delta y$ (C) $iU - \Phi$

FIGURE 5.9: Numerical results by shooting method (SH)

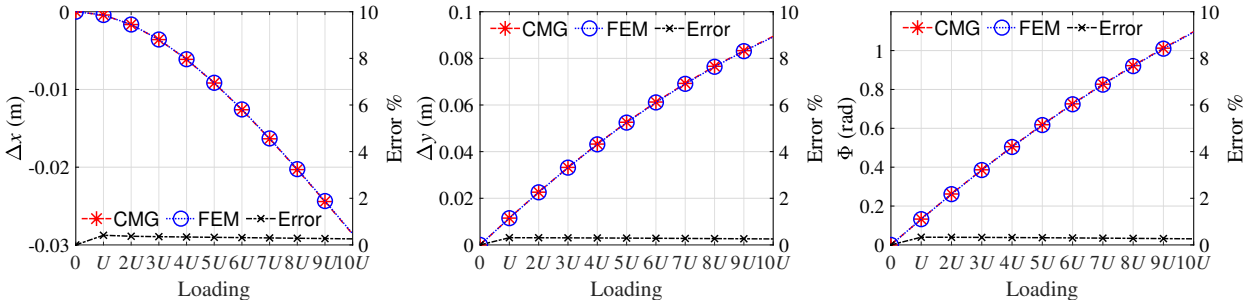

(A) $iU - \Delta x$ (B) $iU - \Delta y$ (C) $iU - \Phi$

FIGURE 5.10: Numerical results by globally-implemented collocation method (CMG)

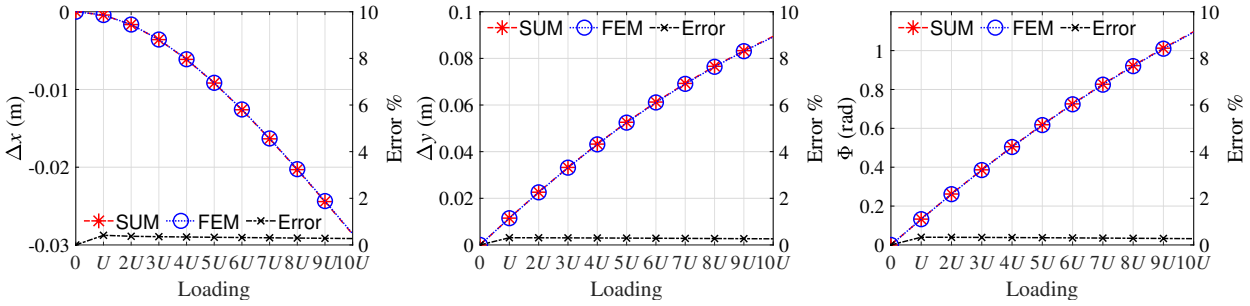

(A) $iU - \Delta x$ (B) $iU - \Delta y$ (C) $iU - \Phi$

FIGURE 5.11: Numerical results by subdomain method (SUM)

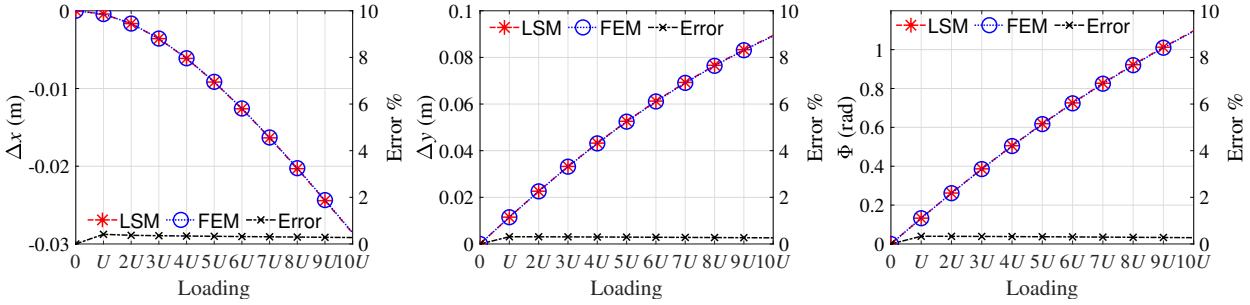

(A) $iU - \Delta x$ (B) $iU - \Delta y$ (C) $iU - \Phi$

FIGURE 5.12: Numerical results by least square method (LSM)

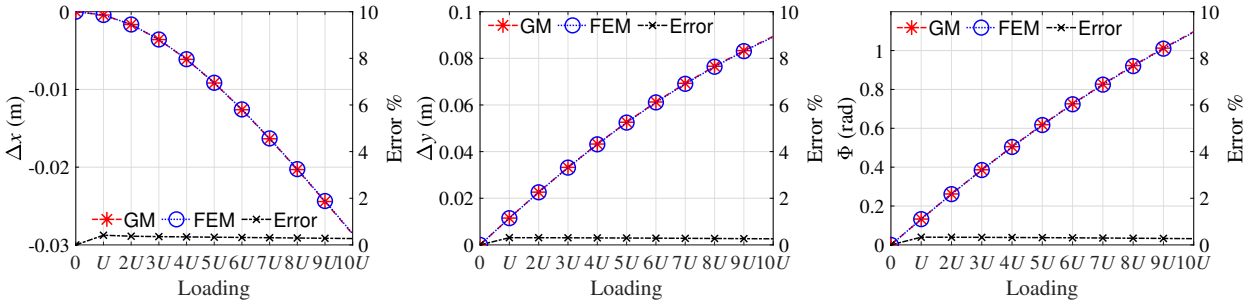

(A) $iU - \Delta x$ (B) $iU - \Delta y$ (C) $iU - \Phi$

FIGURE 5.13: Numerical results by Galerkin method (GM)

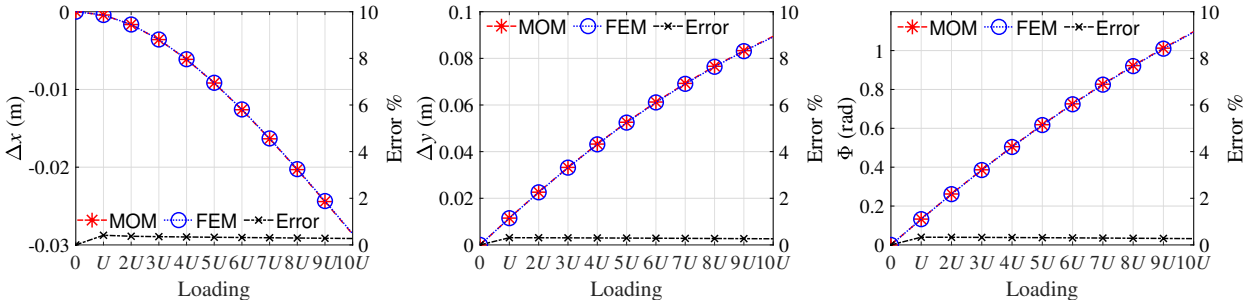

(A) $iU - \Delta x$ (B) $iU - \Delta y$ (C) $iU - \Phi$

FIGURE 5.14: Numerical results by method of moments (MOM)

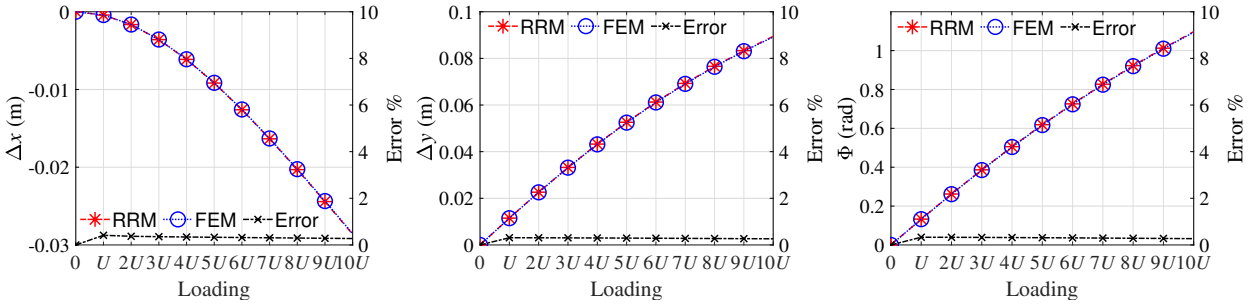

(A) $iU - \Delta x$ (B) $iU - \Delta y$ (C) $iU - \Phi$

FIGURE 5.15: Numerical results by Rayleigh–Ritz method (RRM)

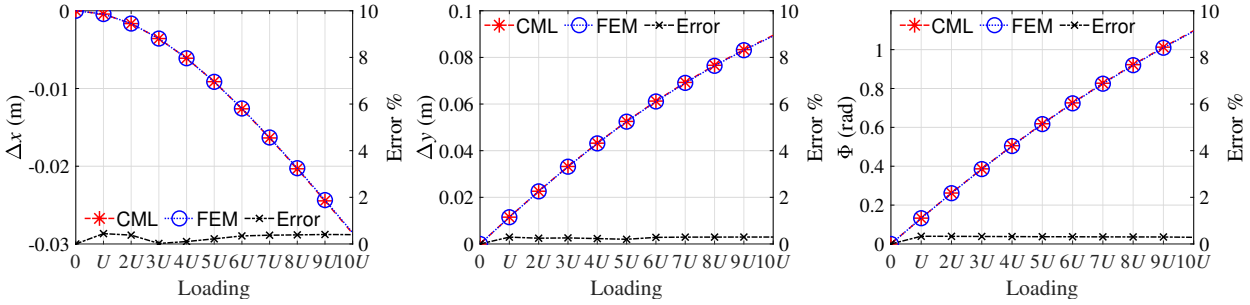

(A) $iU - \Delta x$ (B) $iU - \Delta y$ (C) $iU - \Phi$

FIGURE 5.16: Numerical results by locally-implemented collocation method (CML)

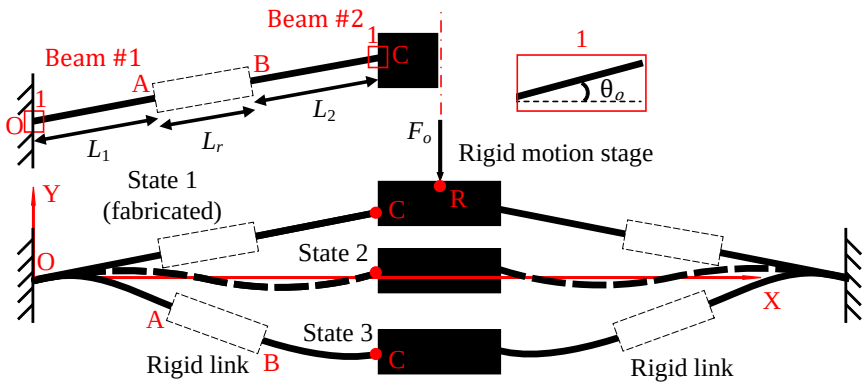

FIGURE 5.17: Schematic diagram of a bi-stable compliant mechanism

built-in flexible members are modeled via reduced-mode Cosserat rod model (COR), BVP (3.133). Note that we use Galerkin method to solve reduced-mode Cosserat rod model, noted as COR-GM. This means, besides bending, the axial and shear strains are both considered. As shown in Fig. 5.17, the bi-stable mechanism is composed of 2 rigid links, 1 rigid motion stage and 4 flexible beams. State 1 refers to its fabricated shape where the mechanism is symmetrically fabricated and fixed at the two sides. The detailed geometric parameters are all provided in Fig. 5.17. The mechanism has 3 states where State 1 and State 3 are the stable equilibrium states whereas State 2 is the unstable equilibrium state. Subjected to the external force F_o, the mechanism works from State 1 through State 2 finally arriving at State 3. Here, we are interested in the relationship between F_o and the displacement ΔY of the reference point R. Since the structure of the bi-stable mechanism is symmetrical, we can simplify the modeling by working on the half of it as shown in Fig. 5.18. Likewise, the static model can be divided into three parts: constitutive equations, force equilibrium equations and geometric compatibility equations.

- **Static modeling**

  1) **Constitutive relationships**
  Normally, we start with the constitutive equations of each flexible member first. According to BVP (3.133), we can write down the governing equation in complete form for Beam #1:

$$
\begin{aligned}
&\text{D.E. } EI\frac{\mathrm{d}^2\theta_1}{\mathrm{d}s^2}(s) = \\
&-F_{x1}[\sin\theta_1(s)(-\frac{\cos\theta_1(s)F_{x1}}{AE}+\frac{\sin\theta_1(s)F_{y1}}{AE}+1)+\cos\theta_1(s)(\frac{\sin\theta_1(s)F_{x1}}{AG}+\frac{\cos\theta_1(s)F_{y1}}{AG})] \\
&-F_{y1}[\cos\theta_1(s)(-\frac{\cos\theta_1(s)F_{x1}}{AE}+\frac{\sin\theta_1(s)F_{y1}}{AE}+1)-\sin\theta_1(s)(\frac{\sin\theta_1(s)F_{x1}}{AG}+\frac{\cos\theta_1(s)F_{y1}}{AG})] \\
&\text{B.C. } \theta_1(0) = \theta_o \\
&\qquad \frac{\mathrm{d}\theta_1}{\mathrm{d}s}(L_1) = \frac{M_{o1}}{EI}
\end{aligned}
\tag{5.10}
$$

  For Beam #2, we have a similar BVP as follows:

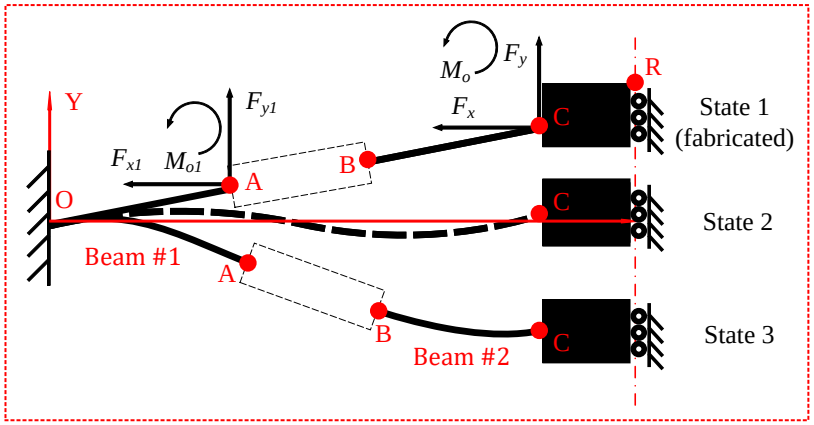

FIGURE 5.18: Detailed force diagram of the classic compliant bi-stable mechanism

$$
\begin{aligned}
&\text{D.E. } EI\frac{\mathrm{d}^2\theta_2}{\mathrm{d}s^2}(s) = \\
&-F_{x2}[\sin\theta_2(s)(-\frac{\cos\theta_2(s)F_{x2}}{AE}+\frac{\sin\theta_2(s)F_{y2}}{AE}+1)+\cos\theta_2(s)(\frac{\sin\theta_2(s)F_{x2}}{AG}+\frac{\cos\theta_2(s)F_{y2}}{AG})] \\
&-F_{y2}[\cos\theta_2(s)(-\frac{\cos\theta_2(s)F_{x2}}{AE}+\frac{\sin\theta_2(s)F_{y2}}{AE}+1)-\sin\theta_2(s)(\frac{\sin\theta_2(s)F_{x2}}{AG}+\frac{\cos\theta_2(s)F_{y2}}{AG})] \\
&\text{B.C. } \theta_2(0) = \theta_1(L_1) \\
&\qquad \theta_2(L_2) = \theta_o \\
&\qquad \frac{\mathrm{d}\theta_2}{\mathrm{d}s}(L_2) = \frac{M_o}{EI}
\end{aligned}
\tag{5.11}
$$

Then, we can characterize the deflected shapes of Beam #1 and Beam #2 in their local coordinate systems respectively according to Eq. (3.134):

$$
\begin{aligned}
x_1(s) &= \int_0^s \cos\theta_1(\xi)(-\frac{\cos\theta_1(\xi)F_{x1}}{AE}+\frac{\sin\theta_1(\xi)F_{y1}}{AE}+1)-\sin\theta_1(\xi)(\frac{\sin\theta_1(\xi)F_{x1}}{AG}+\frac{\cos\theta_1(\xi)F_{y1}}{AG})\mathrm{d}\xi \\
y_1(s) &= \int_0^s \sin\theta_1(\xi)(-\frac{\cos\theta_1(\xi)F_{x1}}{AE}+\frac{\sin\theta_1(\xi)F_{y1}}{AE}+1)+\cos\theta_1(\xi)(\frac{\sin\theta_1(\xi)F_{x1}}{AG}+\frac{\cos\theta_1(\xi)F_{y1}}{AG})\mathrm{d}\xi
\end{aligned}
\tag{5.12}
$$

and

$$
\begin{aligned}
x_2(s) &= \int_0^s \cos\theta_2(\xi)(-\frac{\cos\theta_2(\xi)F_{x2}}{AE}+\frac{\sin\theta_2(\xi)F_{y2}}{AE}+1)-\sin\theta_2(\xi)(\frac{\sin\theta_2(\xi)F_{x2}}{AG}+\frac{\cos\theta_2(\xi)F_{y2}}{AG})\mathrm{d}\xi \\
y_2(s) &= \int_0^s \sin\theta_2(\xi)(-\frac{\cos\theta_2(\xi)F_{x2}}{AE}+\frac{\sin\theta_2(\xi)F_{y2}}{AE}+1)+\cos\theta_2(\xi)(\frac{\sin\theta_2(\xi)F_{x2}}{AG}+\frac{\cos\theta_2(\xi)F_{y2}}{AG})\mathrm{d}\xi
\end{aligned}
\tag{5.13}
$$

2) **Force equilibrium**
Besides, we also have the following force-equilibrium relationships:

$$
\begin{aligned}
&F_x = F_{x1};\ F_y = F_{y1};\ F_o = 2F_y \\
&M_{o1} = M_o + F_y(L_r\cos\theta_1(L_1)+x_2(L_2)) + F_x(L_r\sin\theta_1(L_1)+y_2(L_2))
\end{aligned}
\tag{5.14}
$$

3) **Geometric compatibility relationships**
Then, the geometric relationships are presented below:

$$
\begin{aligned}
&(L_1+L_r+L_2)\cos\theta_o = x_1(L_1)+L_r\cos\theta_1(L_1)+x_2(L_2) \\
&\Delta Y = (L_1+L_r+L_2)\sin\theta_o - (y_1(L_1)+L_r\sin\theta_1(L_1)+y_2(L_2))
\end{aligned}
\tag{5.15}
$$

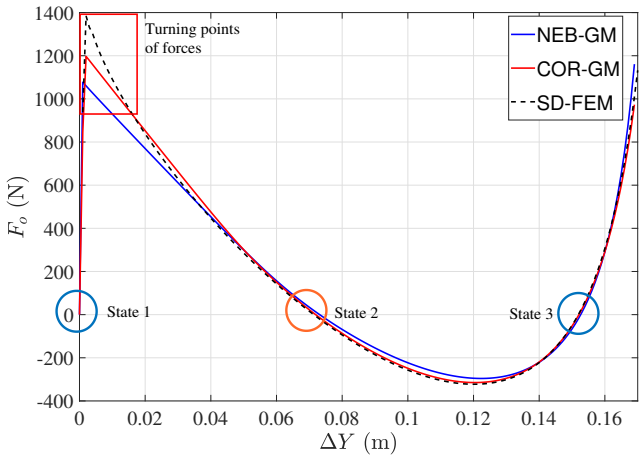

FIGURE 5.19: Force-displacement relationship of the studied bi-stable mechanism

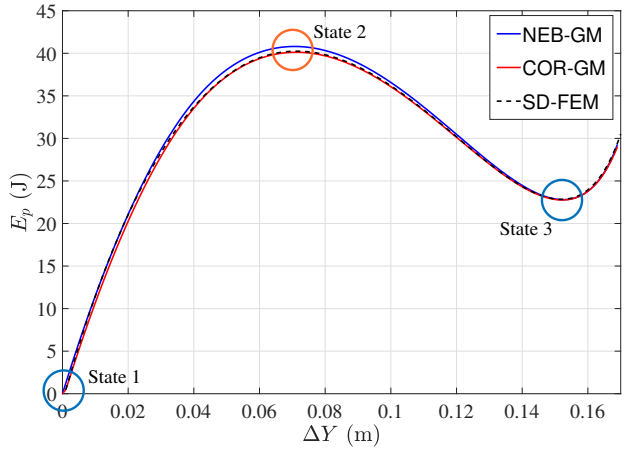

FIGURE 5.20: Stored elastic energy-displacement relationship of the studied bi-stable mechanism

where ΔY denotes the displacement of the reference point R. Finally, to calculate the energy stored in this mechanical system along its workspace, we just need to follow (3.135).

- **Numerical results**
  To verify the modeling methodology, we use solid-mechanics-based FEM (SD-FEM) as the reference. Euler Bernoulli beam theory, which is solved by Galerkin method as well (NEB-GM) presented in Section 4.5.3.4, is used to solve the constitutive equations for comparisons. Then, the geometric and material parameters chosen for the studied straight beam is shown in the following:

$$E = 200 \times 10^9 \text{ Pa};\ \nu = 0.30;\ w = 0.015 \text{ m};\ h = 0.005 \text{ m};$$
$$L_1 = 0.25 \text{ m};\ L_r = 0.25 \text{ m};\ L_2 = 0.25 \text{ m};\ \theta_o = 0.1266 \text{ rad};$$
$$k_t = \frac{12 + 11\nu}{10 + 10\nu};\ G = \frac{E}{2(1+\nu)};$$

  To analyze the mechanical performance of bi-stable mechanisms, the relationship between the force and the displacement of point of force is of great importance. Therefore, $F_o - \Delta Y$ is plotted in Fig.5.19 for further analysis. Besides, we also present the relationship between the elastic energy E_p stored in this system and the displacement ΔY as well (see Fig.5.20).

- **Results analysis**
  In Fig. 5.19 and Fig. 5.20, many interesting insights behind the plotting can be discovered. Clearly, the results in these 2 figures both verify the existence of 2 stable equilibrium states (State 1 and State 3) and 1 unstable

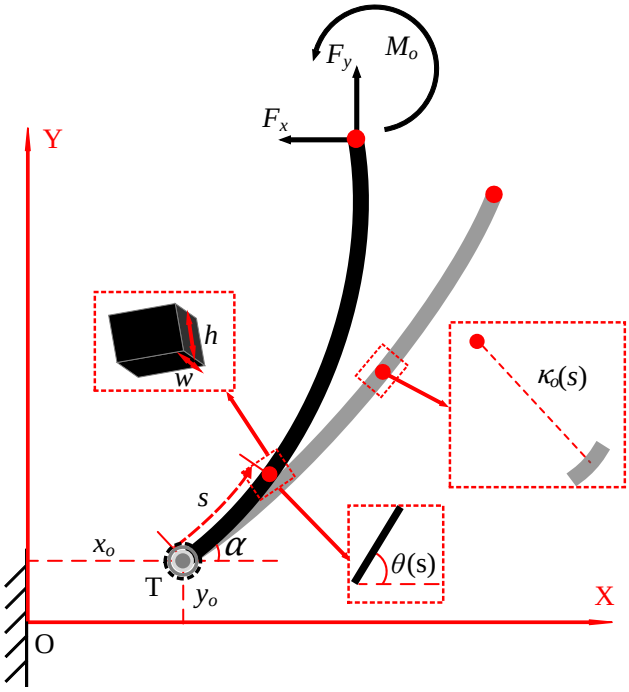

FIGURE 5.21: A slender beam subjected to beam-end loading and driven by prismatic joints and revolute joints

equilibrium state (State 2). In Fig. 5.19, 3 equilibrium states lie in the line $F_o = 0$ that implies at these 3 states the mechanism can stay equilibrium without external inputs. States 1 and 3 have positive stiffness while State 2 has negative stiffness, which means States 1 and 3 are stable whereas State 2 is not. According to the minimum total potential energy principle, the potential energy of States 1 and 3 reaches the local minimum as well as stay in a stable equilibrium state (Fig. 5.20). On the contrary, State 2 stays at the unstable state since its potential energy reaches the local maximum.

If we first take a look at the graphical results in Fig. 5.19 and Fig. 5.20, NEB-GM obviously is the most inaccurate one since it only considers bending. However, COR-GM takes into account shear and axial strains, and their curves share the same trend with limited errors except for the turning points of the forces at left top corner of Fig. 5.19. The errors may be due to the following reason. In pure-compliant bistable mechanisms, the involved slender beams experience large axial loading, resulting in highly nonlinear buckling and post-buckling behaviors. Therefore, in this special case, the beam theory used COR-GM may not be able to capture the whole characteristics of the deformation during the operation of the bi-stable mechanisms. This means the linearly elastic assumption in considering bending, shear and axial strains may not be accurate enough to handle this scenario. For example, axial stress stiffening is not quantitatively considered in the presented beam models.

5.2.4 Kinematic-joint-actuated compliant mechanisms

From the mechanical application point of view, compliant mechanisms can be mainly driven by two types of actuation systems: they can be driven by loading (force and torque), and they can also be driven by given (angular and translational) displacements. Logically, we can introduce the terminologies from the field of classic robotics, the first type is termed as force-control robotic system whereas the second type is termed as kinematic-control (or kinematic-joint-actuated) one. In this section, we are interested in modeling planar kinematic-joint-actuated compliant mechanisms, and normally we control the displacements of the beam tip T using kinematic joints (such as prismatic joints and revolute joints) as shown in Fig. 5.21. Therefore, we need to define these control inputs as follows:

$$\begin{aligned} &\text{Rotation angle: } \alpha \\ &\text{X-axis translational displacement: } x_o \\ &\text{Y-axis translational displacement: } y_o \end{aligned} \tag{5.16}$$

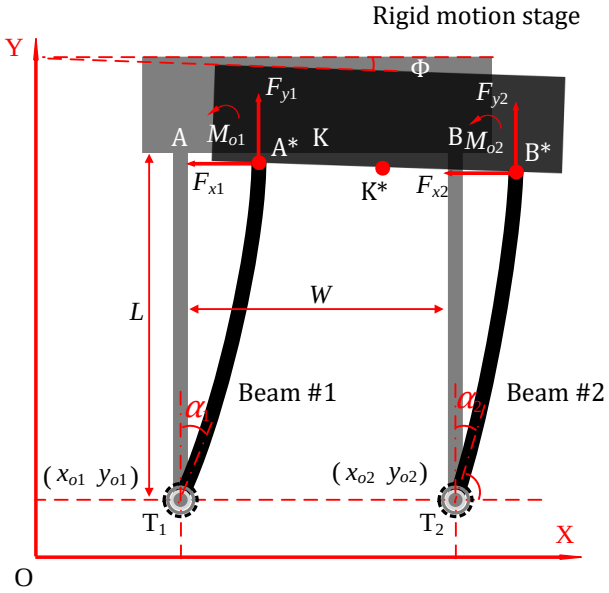

FIGURE 5.22: Schematic diagram of a kinematic-joint-actuated compliant parallelogram

Rearranging (3.30) with the boundary condition: $\theta(0) = \alpha$, we can rewrite the second-order nonlinear BVP:

$$\begin{aligned} \text{D.E.}\quad & \frac{\mathrm{d}^2\theta}{\mathrm{d}s^2} = -\frac{F_y}{EI}\cos\theta(s) - \frac{F_x}{EI}\sin\theta(s) + \frac{\mathrm{d}\kappa_o}{\mathrm{d}s}(s) \\ \text{B.C.}\quad & \theta(0) = \alpha \\ & \frac{\mathrm{d}\theta}{\mathrm{d}s}(L) = \frac{M_o}{EI} + \kappa_o(L) \end{aligned} \tag{5.17}$$

Therefore, we can characterize the beam shape (the exact coordinates of the beam in the global coordinate system) via

$$x(s) = x_o + \int_0^s \cos(\theta(\xi))\mathrm{d}\xi;\ y(s) = y_o + \int_0^s \sin(\theta(\xi))\mathrm{d}\xi,\ \ s \in [0, L] \tag{5.18}$$

5.2.4.1 Kinematic-joint-actuated compliant parallelograms

In all types of compliant mechanisms, compliant parallelogram mechanisms are the most popular one in different applications, such as MEMS (Kota et al., 2001) and positioning stages (Clark et al., 2015). In (Wu and Hao, 2020), the proposed compliant parallelogram mechanism is driven by force, which yields a bulky actuation system. Obviously, the mentioned work could be a lab prototype rather than a practical product. Therefore, as shown in Fig. 5.22, to simplify the actuation system, the inputs of the system are chosen as the translational and angular displacements of the revolute joints. That's why we term the studied mechanism as a kinematic-joint-actuated compliant mechanism. As the same as the classic compliant mechanisms, the static model has three parts: constitutive equations, force equilibrium equations and geometric compatibility equations.

- **Static modeling**

  1) **Constitutive relationships**
  For Beam #1 and #2, we have the following governing BVPs:

$$\begin{aligned} \text{D.E.}\quad & \frac{\mathrm{d}^2\theta_i}{\mathrm{d}s^2} = -\frac{F_{yi}}{EI}\cos\theta_i(s) - \frac{F_{xi}}{EI}\sin\theta_i(s) \\ \text{B.C.}\quad & \theta_i(0) = \frac{\pi}{2} - \alpha_i \\ & \frac{\mathrm{d}\theta_i}{\mathrm{d}s}(L) = \frac{M_{oi}}{EI} \end{aligned} \tag{5.19}$$

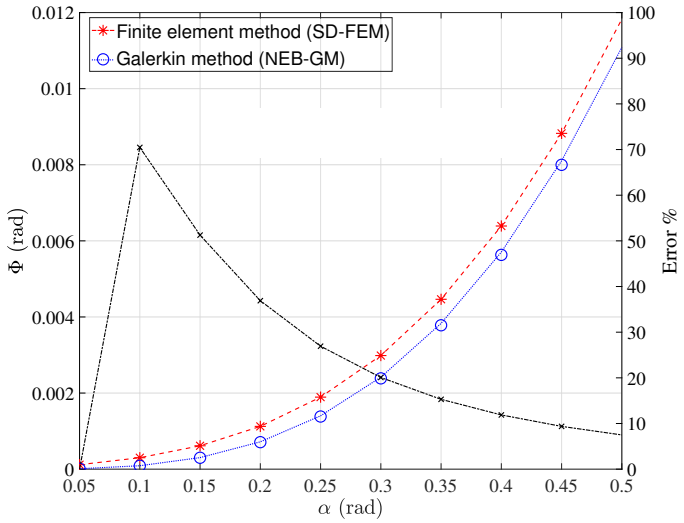

(A) Geometrically nonlinear Euler Bernoulli beam theory (NEB) as the constitutive law

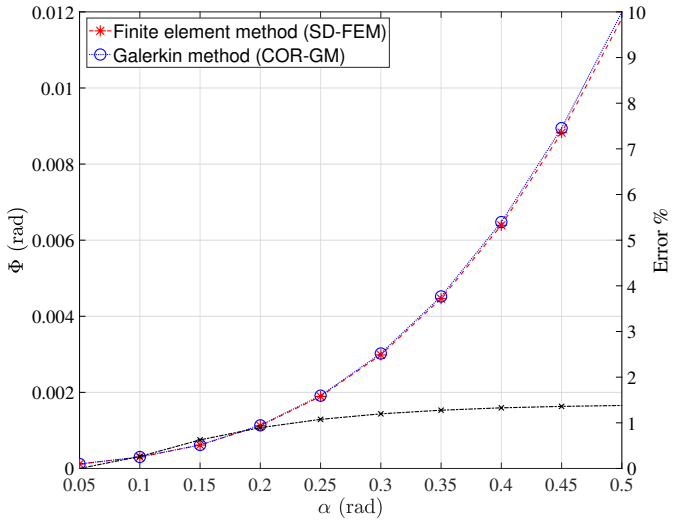

(B) Cosserat rod theory (COR) as the constitutive law

FIGURE 5.23: Results of Φ-α via FEM and GM

with

$$x_i(s) = x_{oi} + \int_0^s \cos\theta_i(\xi)\mathrm{d}\xi;\ y_i(s) = y_{oi} + \int_0^s \sin\theta_i(\xi)\mathrm{d}\xi,\ s \in [0, L],\ i = 1, 2 \tag{5.20}$$

where the two built-in flexible beams are assumed as straight beams with the same constant cross sections for modeling demonstration as shown in Fig 5.22.

2) **Force equilibrium**

$$\begin{aligned} &F_{x1} + F_{x2} = 0;\ F_{y1} + F_{y2} = 0; \\ &M_{o1} + M_{o2} + F_{y2} W\cos\Phi - F_{x2} W\sin\Phi = 0 \end{aligned} \tag{5.21}$$

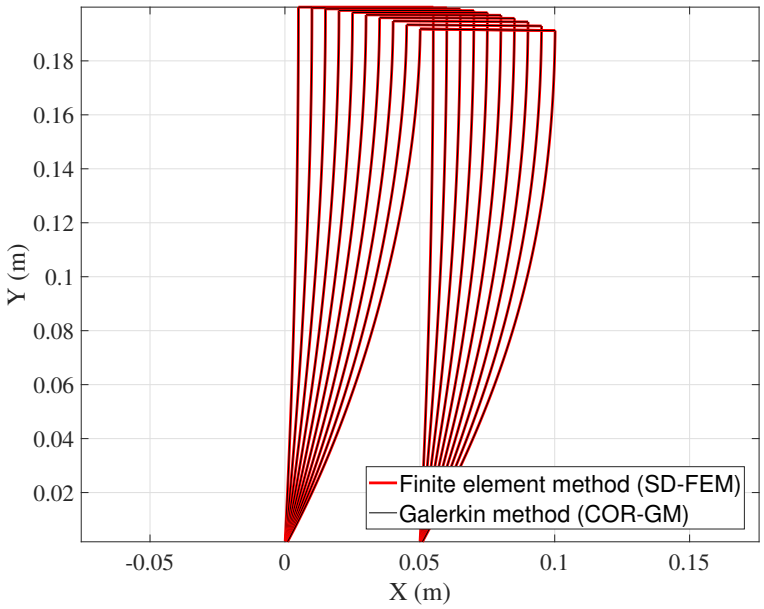

FIGURE 5.24: Graphical results of the deflected compliant parallelogram mechanism via SD-FEM and COR-GM

3) **Geometrical compatibility relationships**

$$\begin{aligned} &\alpha_{K*} = \Phi = \theta_1(L) - \frac{\pi}{2} = \theta_2(L) - \frac{\pi}{2}; \\ &|x_2(L) - x_1(L)| = W\cos\Phi;\ |y_2(L) - y_1(L)| = W\sin\Phi \\ &x_{K*} = \frac{1}{2}[x_1(L) + x_2(L)];\ y_{K*} = \frac{1}{2}[y_1(L) + y_2(L)]; \end{aligned} \tag{5.22}$$

In this model, we are interested in the resulting angular and translational displacements of the reference point K* due to the inputs of the system α_i, x_{oi} and y_{oi} $(i = 1, 2)$. In other words, we can formulate the whole group of equations (5.19) to (5.22) into a general formulation:

$$F(\alpha_i, x_{oi}, y_{oi}, x_{K*}, y_{K*}, \alpha_{K*}) = 0,\ i = 1, 2 \tag{5.23}$$

where α_i, x_{oi}, y_{oi} are the inputs whereas $x_{K*}, y_{K*}, \alpha_{K*}$ are the outputs of the static model. Besides, to analyze the mechanical interference during the operation of the studied mechanism, we can logically use (5.20) to characterize the deflected beam shapes.

- **Numerical validation**
  In this section, we use the following information for this numerical validation. We first use Euler Bernoulli beam theory as the constitutive law for the built-in slender beams. Secondly, the reduced-mode Cosserat rod model for planar deflection (3.133) is used as the constitutive law to compare the results of Euler Bernoulli beam theory. The material and geometry information is presented below:

$$\begin{aligned} &E = 200 \times 10^9 \text{ Pa};\ \nu = 0.30;\ w = 0.01 \text{ m};\ h = 0.004 \text{ m};\ L = 0.2 \text{ m};\ W = 0.05; \\ &I = \frac{h^3 w}{12};\ G = \frac{E}{2(1+\nu)};\ A = wh; \end{aligned}$$

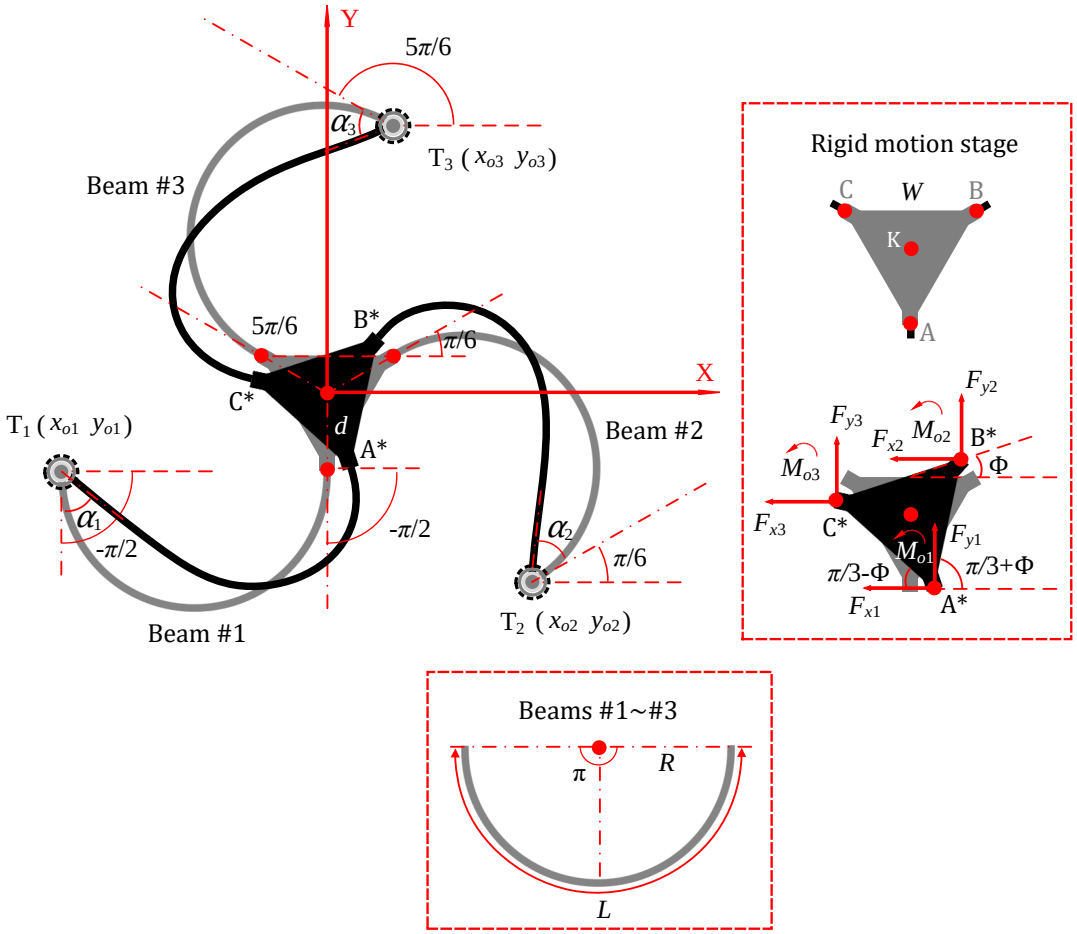

FIGURE 5.25: Schematic diagram of a kinematic-joint-actuated compliant parallelogram

Here, in this numerical testing, only the rotation angle of the kinematic joint of each slender beam (Beam # 1 and Beam # 2) is controlled:

$$\alpha_1 = \alpha_2 = \alpha = [0.05, 0.1, 0.15, 0.2, \cdots, 0.5]^\top$$

The results of Φ-α and the graphical results of deflected parallelogram are provided in Fig. 5.23 and Fig. 5.24 respectively where solid-mechanics-based Finite element method (SD-FEM) is used.

- **Mechanism analysis**
  Obviously, as shown in Fig. 5.23, Euler Bernoulli beam theory is not able to capture the accurate results compared to that of SD-FEM whereas the reduced-mode Cosserat rod model does. This is possibly because of the considerable contribution of axial and shear strains to total deflection of the studied kinematic-joint-actuated compliant parallelogram where only bending is considered in Euler Bernoulli beam theory whereas bending, axial and shear strains are all considered in the reduced-mode Cosserat rod model.

5.2.4.2 Kinematic-control-based compliant parallel mechanisms

As shown in Fig. 5.25, the studied mechanism is a compliant parallel mechanism where three circularly curved beams are utilized. The three flexible beams are actuated by three motor-driven revolute joints at their beam ends and evenly distributed around the origin O where AB=BC=CA=W. The geometrical and force-equilibrium explanation is presented in Fig. 5.25 in detail.

- **Geometrical characterization of the rest-state parallel mechanism**

At its **rest state** where the built-in flexible beams are not deformed, we have

$$\begin{aligned} &x_A = 0;\ y_A = -d;\ x_B = d\cos\frac{\pi}{6};\ y_B = d\sin\frac{\pi}{6};\ x_C = d\cos\frac{5\pi}{6};\ y_C = d\sin\frac{5\pi}{6} \\ &\alpha_1 = \alpha_2 = \alpha_3 = 0;\ d = \frac{W}{2\cos\frac{\pi}{6}} \end{aligned} \tag{5.24}$$

To characterize the exact coordinates of the circularly curved beams, we need to proceed to solve the following BVP:

$$\begin{aligned} &\text{D.E.}\ \ \frac{\mathrm{d}\theta_i}{\mathrm{d}s}(s) = \frac{1}{R} \\ &\text{B.C.}\ \ \theta_i(0) = \alpha_i - \frac{\pi}{2} + \frac{2\pi}{3}(i-1) \end{aligned} \tag{5.25}$$

where $i = 1, 2, 3$. Logically, for this linear ODE with the given boundary condition, we can write down the analytical solution right away:

$$\theta_i(s) = -\frac{\pi}{2} + \frac{2\pi}{3}(i-1) + \frac{s}{R} \tag{5.26}$$

along with the coordinate characterization:

$$x_i(s) = x_{oi} + \int_0^s \cos(\theta_i)\mathrm{d}\xi;\ y_i(s) = y_{oi} + \int_0^s \sin(\theta_i)\mathrm{d}\xi; \tag{5.27}$$

Equivalently,

$$x_{oi} = \int_0^s \cos(\theta_i)\mathrm{d}\xi - x_i(s);\ y_{oi} = \int_0^s \sin(\theta_i)\mathrm{d}\xi - y_i(s); \tag{5.28}$$

Therefore, in the rest state of the studied CM, we have the following geometrical relationships:

1) **Beam #1:**

$$x_{o1} = x_A - \int_0^L \cos(\theta_1)\mathrm{d}\xi;\ y_{o1} = y_A - \int_0^L \sin(\theta_1)\mathrm{d}\xi; \tag{5.29}$$

2) **Beam #2:**

$$x_{o2} = x_B - \int_0^L \cos(\theta_2)\mathrm{d}\xi;\ y_{o2} = y_B - \int_0^L \sin(\theta_2)\mathrm{d}\xi; \tag{5.30}$$

3) **Beam #3:**

$$x_{o3} = x_C - \int_0^L \cos(\theta_3)\mathrm{d}\xi;\ y_{o3} = y_C - \int_0^L \sin(\theta_3)\mathrm{d}\xi; \tag{5.31}$$

So far, we have all the geometrical information available in the rest state of the CM.

- **Static modeling**

1) **Constitutive relationships**
For Beam #1, #2 and #3, we have the following governing BVPs:

$$\begin{aligned} &\text{D.E.}\ \ \frac{\mathrm{d}^2\theta_i}{\mathrm{d}s^2} = -\frac{F_{yi}}{EI}\cos\theta_i(s) - \frac{F_{xi}}{EI}\sin\theta_i(s) \\ &\text{B.C.}\ \ \theta_i(0) = \alpha_i - \frac{\pi}{2} + \frac{2\pi}{3}(i-1) \\ &\qquad \frac{\mathrm{d}\theta_i}{\mathrm{d}s}(L) = \frac{M_{oi}}{EI} + \kappa_o(L) = \frac{M_{oi}}{EI} + \frac{1}{R} \end{aligned} \tag{5.32}$$

with

$$x_i(s) = x_{oi} + \int_0^s \cos\theta_i(\xi)\mathrm{d}\xi;\ y_i(s) = y_{oi} + \int_0^s \sin\theta_i(\xi)\mathrm{d}\xi;\ s \in [0, L];\ i = 1, 2, 3 \tag{5.33}$$

where the built-in flexible beams are assumed as circularly curved beams with constant cross sections for modeling demonstration as shown in Fig 5.25.

2) **Force equilibrium**

$$F_{x1}+F_{x2}+F_{x3}=0;\ F_{y1}+F_{y2}+F_{y3}=0;$$
$$M_{o1}+M_{o2}+M_{o3}+F_{x2}W\sin\Phi+F_{y2}W\cos\Phi-F_{x1}W\cos(\frac{\pi}{3}-\Phi)+F_{y1}W\sin(\frac{\pi}{3}-\Phi)=0 \tag{5.34}$$

3) **Geometrical compatibility relationships**

$$\begin{aligned}
&\alpha_{K*}=\Phi=\theta_1(L)-\frac{\pi}{2}=\theta_2(L)-\frac{7\pi}{6}=\theta_3(L)-\frac{11\pi}{6}\\
&|x_2(L)-x_1(L)|=W\cos(\frac{\pi}{3}+\Phi);\ |y_2(L)-y_1(L)|=W\sin(\frac{\pi}{3}+\Phi)\\
&|x_3(L)-x_2(L)|=W\cos(\Phi);\ |y_3(L)-y_2(L)|=W\sin(\Phi)\\
&|x_1(L)-x_3(L)|=W\cos(\frac{\pi}{3}-\Phi);\ |y_1(L)-y_3(L)|=W\sin(\frac{\pi}{3}-\Phi)\\
&x_{K*}=\frac{1}{2}[x_1(L)+x_2(L)+x_3(L)];\ y_{K*}=\frac{1}{2}[y_1(L)+y_2(L)+y_3(L)];
\end{aligned} \tag{5.35}$$

In this modeling, we are interested in the resulting angular and translational displacements of the reference point K* due to the inputs of the system α_i, x_{oi} and y_{oi} ($i=1,2,3$). In other words, we can formulate the whole group of equations (5.32) to (5.35) into a general formulation:

$$F(x_{oi},y_{oi},\alpha_i,x_{K*},y_{K*},\alpha_{K*})=0;\ i=1,2,3 \tag{5.36}$$

where α_i, x_{oi}, y_{oi} are the inputs whereas $x_{K*}, y_{K*}, \alpha_{K*}$ are the outputs of the static model. Besides, to analyze the mechanical interference during the operation of the studied mechanism, we can logically use (5.33) to characterize the deflected beam shapes.

- **Numerical validation**
  In this section, the following information is used for this numerical validation. Likewise, Euler Bernoulli beam theory is first used as the constitutive law for the built-in slender beams. Secondly, the reduced-mode Cosserat rod model for planar deflection (3.133) is used as the constitutive law to compare the results of Euler Bernoulli beam theory. The material and geometry information is presented below:

$$E=200\times10^9\ \text{Pa};\ \nu=0.30;\ w=0.01\ \text{m};\ h=0.004\ \text{m};\ R=0.08;\ \text{m};\ W=0.05\sqrt{3}\ \text{m};$$
$$L=\pi R;\ I=\frac{h^3w}{12};\ G=\frac{E}{2(1+\nu)};\ A=wh;\ d=\frac{W}{2\cos\frac{\pi}{6}}$$

Here, in this numerical testing, only the rotation angle of the kinematic joint of each slender beam (Beam # 1, Beam # 2 and Beam # 3) is controlled:

$$\alpha_1=\alpha_2=\alpha_3=\alpha=[0.1,0.2,0.3,0.4,\cdots,1]^\top$$

The results of Φ-α and the graphical results of deflected CM are provided in Fig. 5.26 and Fig. 5.27 respectively where solid-mechanics-based Finite element method (SD-FEM) is used.

- **Mechanism analysis**
  As shown in Fig. 5.26, it is clear that there's no big difference between the results of EB-GM and COR-GM respectively, which means bending of each built-in slender beams is the major contribution. Logically, the axial and shear strains can be neglected in the current actuation and configuration.

5.3 Mechanism optimization: an ICB-based compliant parallelogram

As demonstrated in Section 5.2, we have proved the feasibility of efficiently modeling CMs via the proposed methodology. In this section, based on the mentioned efficient and accurate modeling framework, we aim to show how the

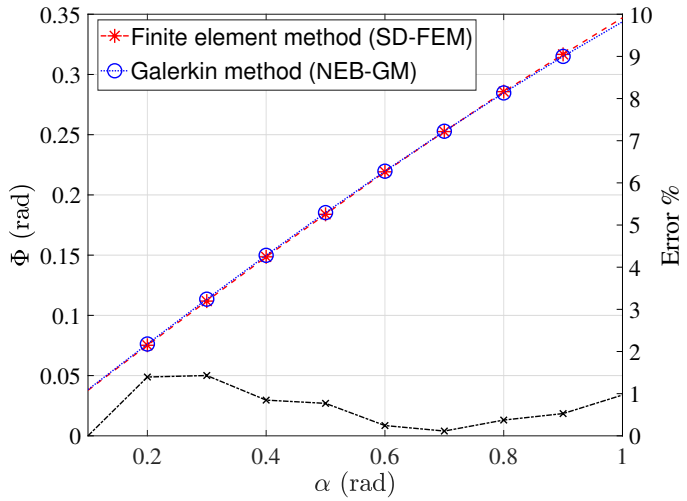

(A) Geometrically nonlinear Euler Bernoulli beam theory as the constitutive law

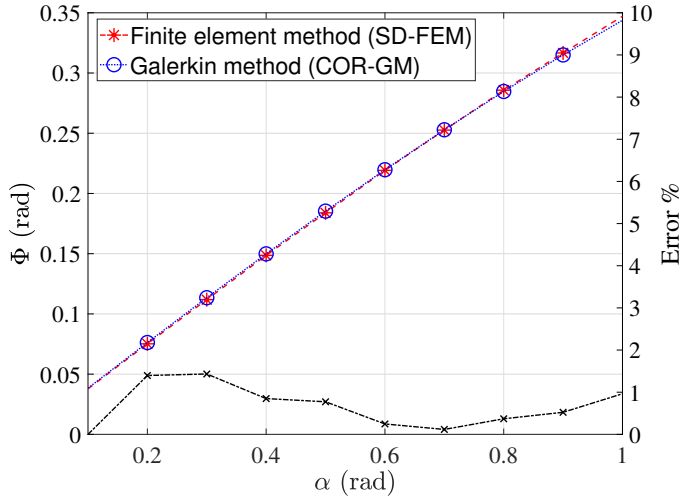

(B) Cosserat rod theory as the constitutive law

FIGURE 5.26: Results of Φ-α via FEM and GM

proposed modeling method can be used to optimize the designs of CMs. For this topic, we are going to work on compliant parallelograms where there are many geometric parameters that need to be optimized to fulfill some given design objective. As shown in Fig. 5.28, these geometric parameters are key ones of the design that can hugely influence that performance of of the CMs. In the following, we are going to demonstrate a model-based optimization process of an ICB-based compliant parallelogram followed by experimental validation.

5.3.1 Brief introduction and its background

Compliant parallelograms are a typical type of CMs, normally serving as positioning stages to transfer motion and energy (Howell, 2013a)(Awtar, 2003)(Lobontiu, 2002). However, the built-in flexible members tend to buckle under high axial loading, losing load-bearing ability and causing undesired parasitic motions (Chen, Ma, and Li, 2016)(Chen, Wilcox, and Howell, 2009)(Han et al., 2017)(Slocum, Kamrin, and Slocum, 2019). Studies on anti-buckling have been reported in the existing literature (Kong, Chen, and Hao, 2019)(Hao, Yu, and Liu, 2018)(Chen, Ma, and Li, 2016)(Wu and Hao, 2020) where most designs and applications convert compression into tension to avoid buckling of flexible members. However, most of the previously mentioned designs are only capable of uni-directional anti-buckling (Kong, Chen, and Hao, 2019)(Chen, Ma, and Li, 2016). In particular, a novel type of anti-buckling CM has been proposed in (Wu and Hao, 2020), presenting bidirectional anti-buckling capacity. Nevertheless, the design suffers from significant stiffness reduction when subjected to high payloads. To address these issues, we propose

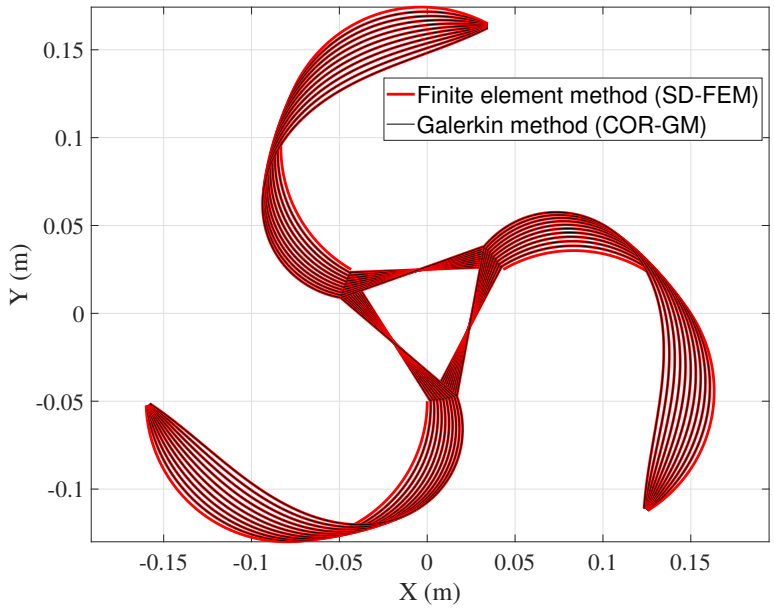

FIGURE 5.27: Graphical results of the deflected parallel CMs via SD-FEM and COR-WRM

a novel compliant planar parallelogram mechanism (CPPM) with bidirectional anti-buckling and bidirectional high load-bearing capacity where ICBs are involved. Based on the initial design of the ICB-based parallelograms proposed in (Wu, Zheng, and Hao, 2021), we extend the previous work by analyzing larger workspaces of the mentioned parallelograms. The overall structure and geometrical information of the CPPM are shown in Fig. 5.28. As depicted in Fig. 5.28a, the CPPM consists of a rigid motion stage, a rigid base and 4 legs, which are termed Leg 1 to Leg 4. Each leg has 1 rigid link and 2 circularly curved beams. P_o, F_o and M_o are the forces exerted at the reference point R which is also the geometrical center of the CPPM in its initial/undeformed state, and it's rigidly connected to the motion stage. Wherever the forces and moments are applied to the rigid motion stage, they can be transformed into the forces and moments exerted on the point R, which assists the performance analysis. It can be noted that there are two types of legs: Leg 1 and Leg 4 are inversely distributed, while Leg 2 and Leg 3 in the middle are non-inverted. One of the great advantages of this arrangement is that whether the motion stage is loaded in positive or negative X direction, there are always four circularly curved beams in tension and another four in compression to compensate for bidirectional stiffness reduction. Compared to an anti-buckling mechanism based on straight beam design (Wu and Hao, 2020)(Wu, Zheng, and Hao, 2021), the ICB-based design does not experience stiffness reduction under heavy payloads. The CPPM introduces some principal geometric parameters to better explain the mechanism illustrated in Fig.5.28b, which are also the main parameters for further optimization. Apply the Y-axis force F_o, X-axis force P_o, and moment M_o (compensation in abnormal loading cases) to the reference point O connected to the rigid motion stage, there will always be motion in three directions: X-axis translation, Y-axis translation and Z-axis rotation which are Δx_o, Δy_o and Φ. Here, in this section, we present a mechanism optimization process of this CPPM, followed by experimental testing as verification. (Chen et al., 2023) is recommended for readers who are interested in the details.

5.3.2 Model-based optimization

Based on the results in Section 5.2, modeling CMs lies in the following three aspects: constitutive equations, equilibrium equations and geometric compatibility equations. In particular, the constitutive equations are derived via geometrically nonlinear Euler Bernoulli beam theory in Section 3.3.1. To studied this CPPM, for simplicity, we can formulate the whole model in a compact form:

$$f(F_o, P_o, M_o, \Delta x_o, \Delta y_o, \Phi, D_a, D_b, K_a, K_b, W_a, W_b) = 0 \tag{5.37}$$

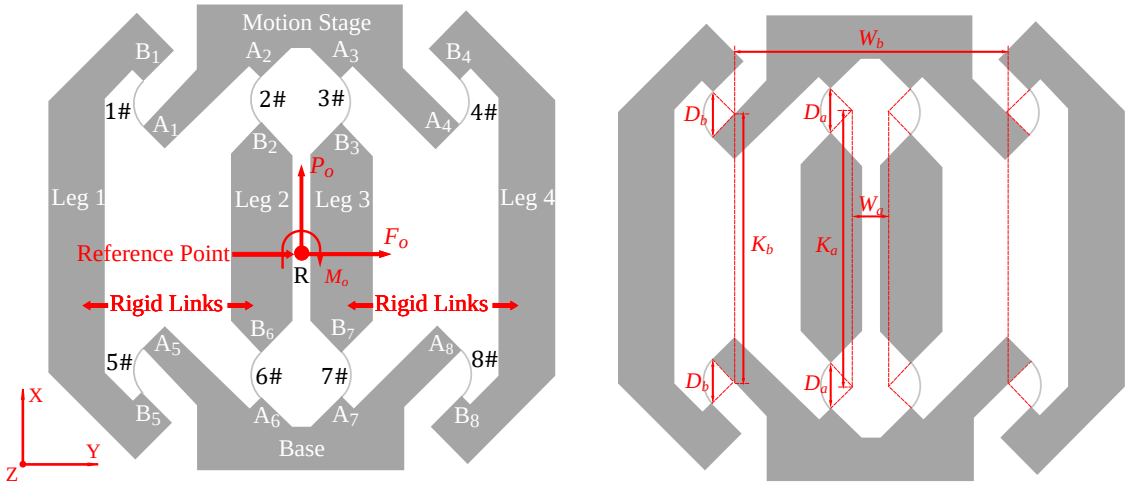

(A) Overall structure (B) Geometrical information

FIGURE 5.28: ICB-based compliant parallelogram

which explains the relationship between the inputs and outputs. The inputs can either be the exerted loading F_o, P_o, M_o or the resulting linear displacements and rotational angle $\Delta x_o, \Delta y_o, \Phi$ of the reference point R, and the rest group logically serves as the outputs. For the details of the modeling, (Chen et al., 2023) is recommended for readers. Obviously, we need to use Newton Raphson method to handle (5.37). For this studied positioning stage (CPPM), we are interested in the following two desired mechanical properties:

- **Constant stiffness along primary motion**: more constant stiffness leads to easier force actuation and control.
- **Minimum parasitic motion**: less parasitic motion results in more accurate primary motion.

As stated in (Wu and Hao, 2020)(Wu, Zheng, and Hao, 2021), the key geometric parameters are the ones shown in Fig. 5.28 that can influence the mentioned two properties since they can hugely change the state of overconstraint in the studied mechanism. Then, we can always formulate arbitrary objective functions for the CM as follows:

$$\mathbf{z} = F(D_a, D_b, K_a, K_b, W_a, W_b) \tag{5.38}$$

Therefore, the optimization problems logically yield:

$$\begin{aligned} &\min_{D_a, D_b, K_a, K_b, W_a, W_b} \quad \mathbf{z} \\ &s.t. \quad g(D_a, D_b, K_a, K_b, W_a, W_b) = 0 \end{aligned} \tag{5.39}$$

where $g(D_a, D_b, K_a, K_b, W_a, W_b) = 0$ is derived from the practical design constraints, such as the expected dimension of the design. As stated in Section 2.7, we can use Lagrange multiplier to solve (5.39). Here, we take the expected constant stiffness along the primary motion for example. In this case, $\mathbf{z}$ represents the stiffness along the primary motion K_y within its workspace $\Delta y_o \in [-0.015, 0.015]$ where international system of units is used. As graphically demonstrated in Fig. 5.29, the stiffness curves of the optimized ones are flatter that that of the original ones. This means subjected to the given constraints, the performance of the optimized design has presented more constant primary stiffness compared to that of the original one, which obviously satisfies our design needs.

However, so far, we have only theoretically proved the results using SD-FEM and NEB-WRM respectively, and we need to finally verify our results through experimental testing. Note that the following is the geometry information of the original design:

$$\begin{aligned} &K_a = 80\,\text{mm};\ K_b = 80\,\text{mm};\ D_a = 20\,\text{mm};\ D_b = 20\,\text{mm};\ W_a = 20\,\text{mm};\ W_b = 120\,\text{mm}; \\ &T = 1\,\text{mm};\ H = 3\,\text{mm};\ E = 69\,\text{Gpa};\ \mu = 0.33. \end{aligned} \tag{5.40}$$

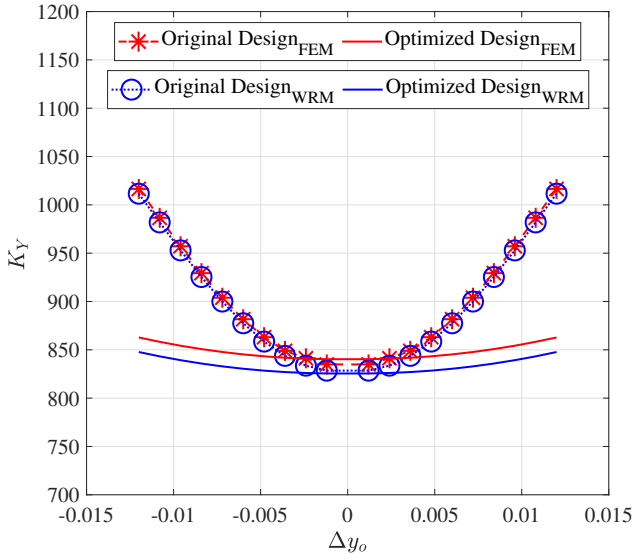

FIGURE 5.29: The plot of primary stiffness against displacement: K_Y-Δy_o

and the following is that of the optimized design:

$$K_a = 60\,\text{mm};\ K_b = 113\,\text{mm};\ D_a = 60\,\text{mm};\ D_b = 7\,\text{mm};\ W_a = 20\,\text{mm};\ W_b = 120\,\text{mm};\\ T = 1\,\text{mm};\ H = 3\,\text{mm};\ E = 69\,\text{Gpa};\ \mu = 0.33. \tag{5.41}$$

where D_a, D_b, K_a, K_b are the optimized parameters.

5.3.3 Experimental validation

5.3.3.1 Experimental setup

The fabricated CPPM for high-precision translational motion is shown in Fig. 5.30. The prototype is driven by a micrometer (213-102, SAN LIANG corporation) with an actuation range of more than 12 mm and the displacement resolution of 1 μm. The force applied to the motion stage is detected by a force sensor (RDF-TS6, RUILIDE corporation) with a 0.01 N resolution and up to 30 N measurement limit. The extension bar is connected to the motion stage and the force sensor. The displacement in the Y-axis of motion stage is measured by displacement sensor (ACE-121T, AICEYI corporation), which provides a resolution of 1 μm within a measurement range of 25 mm. The material and geometry information of the prototype follows the optimized design (5.41) from the last section.

5.3.3.2 Experimental procedure

As we are interested in the Y-axix stiffness of the optimized CPPM, only the force-displacement relation in Y axis was tested in this process.

1. **Initial setup**
   The displacement sensor tip was supposed to touch the flexure mechanism before conducting each experimental testing. Based on the home position of the flexure mechanism, the displacement sensor interface and the force sensor interface were both reset to zero initially. Then by turning the micrometer screw and monitoring the force sensor interface simultaneously, we made the force sensor probe just touch the motion stage where the reading of the force sensor was about one or two resolution of the force sensor.

2. **Measurement**
   We turned the micrometer screw while observing the reading (starting from zero) of the displacement sensor. The Y-axis displacement reading was set up at an equal incremental step of 0.6 mm starting from 0 mm and the corresponding force sensor measurement was recorded at each step. We stopped turning the micrometer

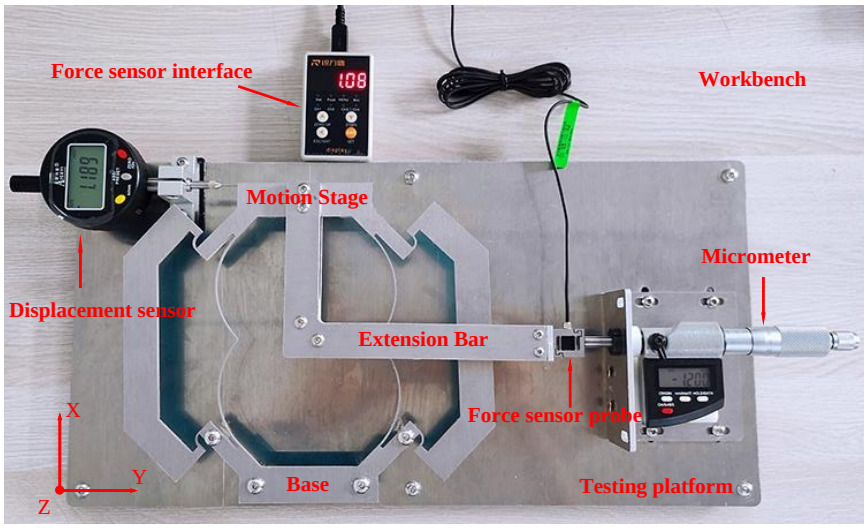

FIGURE 5.30: Experimental testing setup.

when the maximum Y-axis displacement of 12 mm was reached. We repeated the same procedure above three times with the average force plus the variance of measurements data presented in Fig. 5.31a.

5.3.3.3 Experimental results

Fig. 5.31a shows the force-displacement (F_o-Δy_o) relations in Y axis. The nearly constant stiffness as observed in Fig. 5.31b verifies the claim of the design discussed in the last section. The constant Y-axis stiffness also indicates the absence of overconstraint in this design, which is mainly due to the existence of ICBs and the optimized structure obtained in the optimization process.

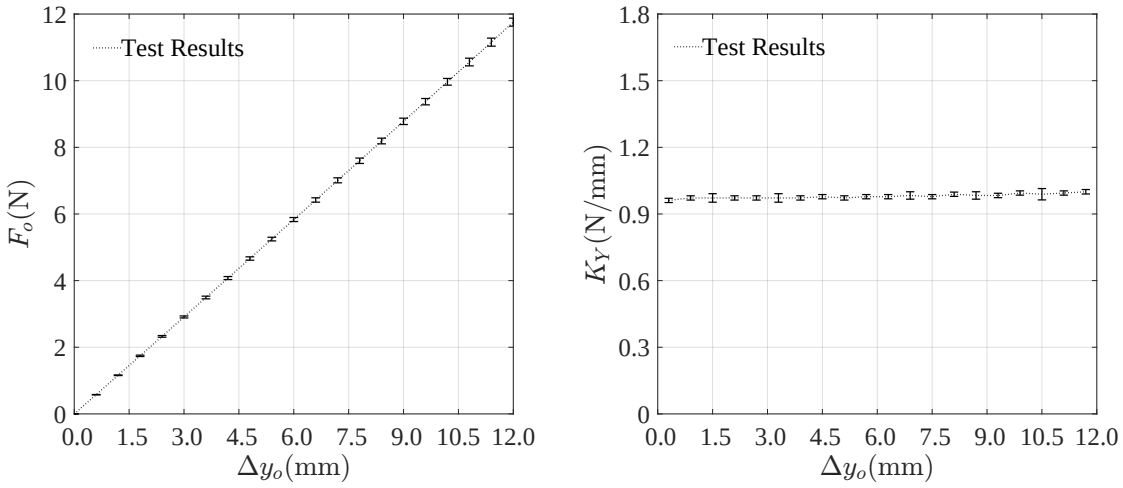

(A) F_o against Δy_o. (B) K_Y against Δy_o.

FIGURE 5.31: The testing results of the prototype

5.4 Conclusions

In this chapter, we have presented the methodology of modeling four representative compliant mechanisms where different models and numerical methods are used with the results verified by FEM. Base on the accurate efficient modeling methodology, we demonstrate a model-based optimization process of an ICB-based parallelogram where some key geometric parameters of the studied CM are optimized to fulfill the given performance objectives. The desired performance of the optimized design has been verified via experimental testing. Summarized above, this chapter

systematically introduces the modern optimization methodology for the design of CMs where both the constitutive theories (Geometrically Euler Bernoulli beam theory and Cosserat rod theory) and some efficient numerical methods are proposed to be used for the first time, to the best of our knowledge.

Chapter 6

Model-based Control and its Application

6.1 Introduction

Based on the proposed modeling methods for CMs in Chapter 5, in this chapter, we move onto the study on control objectives of the modeled CMs. Here, we take simple continuum manipulators driven by two in-extensible cables as an illustrative example. As is well-known, continuum manipulators are essentially a unique branch of slender-beam-based elastic systems which depend on their deflections to transfer motion, energy and force. They are able to present safe compliance and diverse maneuverability in interactions with the environment and human co-workers. As shown in Fig. 6.1, the slender continuum manipulator is driven by two inextensible cables which are placed in parallel along the robot body where the two cables are driven by two motors respectively. Under this actuation system, we have two standard control strategies for the cable-driven manipulator: force control F_1, F_2 and kinematic control $\Delta l_1, \Delta l_2$. In terms of force control, it's straightforward to develop a static or dynamic model if not considering friction. However, this may lead to huge errors in experimental testing since the friction is time-varying, highly nonlinear and therefore difficult to be precisely estimated. Kinematic control of the manipulator almost bypasses the influence of the existing friction but this control method still has drawbacks, such as not considering the dynamic characteristics of the robot. In this section, we present static and statics-based kinematic modeling of a planar continuum manipulator via geometrically nonlinear Euler Bernoulli beam theory based Newtonian and Lagrangian frameworks respectively, presented in Chapter 3.

6.2 Static, kinematic and inverse modeling

In this section, we present static, kinematic and inverse modeling respectively via Newtonian framework and Lagrangian framework. In Newtonian framework, we focus on the exact force details of the system whereas Lagrangian framework provides a more general and global view for this system using an energy-based points of view.

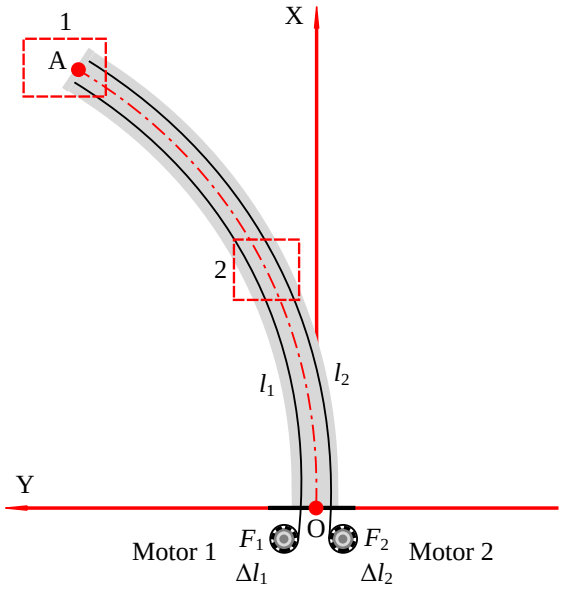

FIGURE 6.1: Schematic diagram of a cable-driven continuum manipulator

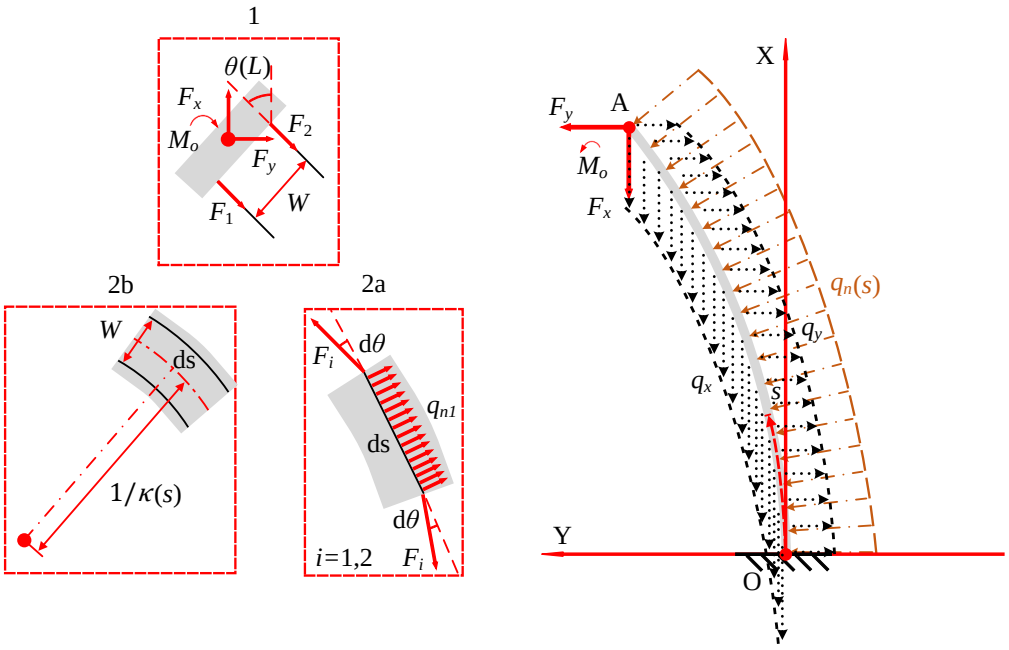

FIGURE 6.2: Detailed force diagram of the studied cable-driven continuum manipulator

6.2.1 Newtonian framework

Here, we aim to analyze the exact loading exerted on the beam by the cables where the friction is not considered. The backbone of the continuum robot is assumed as an inextensible beam. Therefore, we need to derive our model from the most fundamental representation of Euler Bernoulli beam theory (see BVP (3.18) in Section 3.3.1).

6.2.1.1 Modeling

We first take a look at box 1 in Fig. 6.1 and Fig. 6.2, and we can derive the following force equilibrium relationships for rigid cap at the tip of the manipulator:

$$\begin{aligned} &F_x + (F_1 + F_2)\cos\theta(L) = 0 \\ &F_y + (F_1 + F_2)\sin\theta(L) = 0 \\ &\frac{W}{2}(F_2 - F_1) + M_o = 0 \end{aligned} \tag{6.1}$$

where F_x, F_y, F_i, M_o as shown in box 1 in Fig. 6.2 represent vertical force, horizontal force, the cable forces and the moment generated by the cable forces exerted at the beam end. W denotes the distance between the twp parallel cables. Then, as shown in box 2a in Fig. 6.2, we have the following force-equilibrium relationship in the studied infinitesimal volume element of each cable where q_{ni} denotes the distributed pressure exerted by the cables to the beam body:

$$2F_i \sin \mathrm{d}\theta \approx 2F_i \mathrm{d}\theta = q_{ni}\mathrm{d}s \tag{6.2}$$

Logically, we will end up with:

$$q_{ni}(s) = 2F_i\kappa(s)_i;\ i = 1,2 \tag{6.3}$$

where $\kappa(s)_i$ is the curvature of the two cables at s, and $q_{ni}(s)$ stands for the distributed loading on the cables at s. As shown in box 2b in Fig. 6.2, we have the geometric information as follows:

$$\kappa_1(s) = \frac{1}{\frac{1}{\kappa(s)} - \frac{W}{2}};\ \kappa_2(s) = \frac{1}{\frac{1}{\kappa(s)} + \frac{W}{2}}; \tag{6.4}$$

where $\kappa(s)$ is the axis curvature of the continuum robot at s. Then, we have the following relationship for the cable lengths l_1 and l_2:

$$\begin{aligned} l_1 &= \int_0^{\theta(L)} \frac{1}{\kappa_1(s)} \mathrm{d}\theta = L - \frac{W}{2}(\theta(L) - \theta(0)) = L - \frac{\theta(L)}{2} W \\ l_2 &= \int_0^{\theta(L)} \frac{1}{\kappa_2(s)} \mathrm{d}\theta = L + \frac{W}{2}(\theta(L) - \theta(0)) = L + \frac{\theta(L)}{2} W \end{aligned} \tag{6.5}$$

Clearly, we have the relationship:

$$l_1 + l_2 = 2L \tag{6.6}$$

If we define:

$$\Delta l_1 = \frac{\theta(L)}{2} W;\ \Delta l_2 = -\frac{\theta(L)}{2} W \tag{6.7}$$

logically we will have

$$\Delta l_1 = -\Delta l_2 \tag{6.8}$$

where instead of l_1 and l_2, Δl_1 and Δl_2 are defined as the practical kinematic inputs of the manipulator. Due to this coupled relation (6.8), in the following, **we use Δl to denote** Δl_1 and $-\Delta l_2$.

According to Newton's third Law, we can formulate the exact loading exerting on the slender continuum robot into a simple ODE via (3.18):

$$\begin{aligned} EI(\frac{\mathrm{d}\theta}{\mathrm{d}s} - \kappa_o(s)) = &\int_s^L q_n(s)(x(\gamma) - x(s)) \cos\theta(\gamma)\mathrm{d}\gamma + \int_s^L q_n(s)(y(\gamma) - y(s)) \sin\theta(\gamma)\mathrm{d}\gamma + F_y(x(L) - x(s)) \\ &+ F_x(y(L) - y(s)) + M_o - \int_s^L q_y(s)[x(\gamma) - x(s)]\mathrm{d}\gamma + \int_s^L q_x(s)[y(\gamma) - y(s)]\mathrm{d}\gamma \end{aligned} \tag{6.9}$$

where q_x, q_y are distributed loading (such as gravity), $q_n(s) = q_{n1}(s) + q_{n2}(s)$, and $\kappa_o(s) = 0$ since the backbone of the robot is fabricated straight. Therefore, in order to remove these constant dependencies, by applying $\frac{\mathrm{d}x}{\mathrm{d}s} = \cos\theta$ and $\frac{\mathrm{d}y}{\mathrm{d}s} = \sin\theta$, we calculate the derivative of (6.9) with respect to s, which yields:

$$\begin{aligned} EI\frac{\mathrm{d}^2\theta}{\mathrm{d}s^2} = &-(F_y\cos\theta(s) + F_x\sin\theta(s)) + q_n(s)\cos\theta(s)\int_L^s \cos\theta(\xi)\mathrm{d}\xi + \frac{\mathrm{d}q_n}{\mathrm{d}s}x(s)\int_L^s \cos\theta(\xi)\mathrm{d}\xi \\ &+ \frac{\mathrm{d}q_n}{\mathrm{d}s}\int_s^L\int_0^\gamma \cos\theta(\xi)\mathrm{d}\xi\cos\theta(\gamma)\mathrm{d}\gamma + q_n(s)\sin\theta(s)\int_L^s \sin\theta(\xi)\mathrm{d}\xi \\ &+ \frac{\mathrm{d}q_n}{\mathrm{d}s}y(s)\int_L^s \sin\theta(\xi)\mathrm{d}\xi + \frac{\mathrm{d}q_n}{\mathrm{d}s}\int_s^L\int_0^\gamma \sin\theta(\xi)\mathrm{d}\xi\sin\theta(\gamma)\mathrm{d}\gamma + q_y(s)\cos\theta(s)(L-s) \\ &+ \frac{\mathrm{d}q_y}{\mathrm{d}s}x(s)(L-s) + \frac{\mathrm{d}q_y}{\mathrm{d}s}\int_L^s\int_0^\gamma \cos\theta(\xi)\mathrm{d}\xi\mathrm{d}\gamma + q_x(s)\sin\theta(s)(s-L) + \frac{\mathrm{d}q_x}{\mathrm{d}s}y(s)(s-L) \\ &+ \frac{\mathrm{d}q_x}{\mathrm{d}s}\int_s^L\int_0^\gamma \sin(\theta(\xi))\mathrm{d}\xi\mathrm{d}\gamma \end{aligned} \tag{6.10}$$

subjected to the following two boundary conditions:

$$\begin{aligned} &\text{B.C. } \theta(0) = 0 \\ &\frac{\mathrm{d}\theta}{\mathrm{d}s}(L) = \frac{M_o}{EI} \end{aligned} \tag{6.11}$$

Obviously, from (6.1) to (6.11), we can formulate the whole static-kinematic modeling as follows:

$$f(F_1, F_2, \Delta l, \theta(s)) = 0; \tag{6.12}$$

Since we are interested in the position and orientation of the end effector, termed as P_e:

$$P_\mathrm{e} = [x(L), y(L), \theta(L)]^\top \tag{6.13}$$

Thus, both for modeling and inverse modeling, we can characterize the shape of the manipulator via

$$x(s) = \int_0^s \cos(\theta(\xi))\mathrm{d}\xi;\ y(s) = \int_0^s \sin(\theta(\xi))\mathrm{d}\xi;\ s \in [0, L] \tag{6.14}$$

The following demonstrates the respect modeling purposes:

1) **Static modeling:** if F_1 and F_2 are known and the rest variables are unknown in (6.12), (6.12) yields a **static model**.

2) **Kinematic modeling:** if Δl is known and the rest variables are unknown in (6.12), (6.12) finally becomes a **kinematic model**.

3) **Inverse modeling:** if the reference position P_e^* of the end effector is known, then we have the following relationship:

$$P_e = P_e^* \tag{6.15}$$

where

$$P_e^* = [x_t, y_t, \theta_t]^\top \tag{6.16}$$

To calculate the corresponding force inputs (F_1 and F_2) or displacement input Δl, we need to develop an inverse model composed of (6.12) and (6.15) where only P_e^* is the input. Note that P_e^* here is assumed in the workspace of the manipulator's end-effector.

6.2.2 Lagrangian framework

In this section, we aim to analyze the deflection of the continuum manipulator from the energy point of view. For static modeling and the related statics-based geometrical modeling, the principle of minimum total potential energy is used as the key to govern the mentioned physical process. Basically, this is an optimization process since we are looking for a function to satisfy the minimum principle. Suppose that this unknown function is a differentiable one within an interval and therefore can be approximated by a polynomial of s with several unknown polynomial coefficients. In this context, we essentially look for a group of unknown polynomial coefficients to achieve this minimum condition where our target is transformed from the function to the group of coefficients, as presented in Section 4.6. Obviously, the parameterization is logically of great importance in this optimization process under this energy framework.

6.2.2.1 Static, kinematic and inverse modeling

1. **Parameterization**
   Parameterization is the prerequisite for energy framework due to the involved optimization process. Considering $\frac{\mathrm{d}\theta}{\mathrm{d}s}(s)$ denotes the current curvature caused by bending at s and $\kappa_o(s)$ denotes the initial curvature, we can formulate the stored elastic energy E_p via

$$E_p = \int_0^L \frac{1}{2} EI(\frac{\mathrm{d}\theta}{\mathrm{d}s} - \kappa_o(s))^2 \mathrm{d}s = \int_0^L \frac{1}{2} EI(\frac{\mathrm{d}\theta}{\mathrm{d}s})^2 \mathrm{d}s \tag{6.17}$$

   where the studied continuum robot has no initial curvature so $\kappa_o(s) = 0$ since the backbone is fabricated straight. As shown in Fig. 6.1, the two cables along the robot body are driven by two motors where the corresponding forces and displacements of the cables are represented by F_1, F_2, Δl_1 and Δl_2. Normally, the total potential energy due to the cable tension can be considered conservative. Besides, distributed loading ($q_x(s)$ and $q_y(s)$), such as gravity, is also considered. Therefore, the total potential energy due to the mentioned two can be formulated as follows:

$$\Pi = E_p - W_p = \int_0^L \frac{1}{2} EI(\frac{\mathrm{d}\theta}{\mathrm{d}s})^2 \mathrm{d}s - \Delta F \Delta l - \int_0^L q_x(s)(s - x(s))\mathrm{d}s + \int_0^L q_y(s) y(s) \mathrm{d}s \tag{6.18}$$

   where

$$\Delta F = F_1 - F_2 \tag{6.19}$$

2. **Functional minimization and optimization**
As stated in (6.18), the functional Π is a function of function $\theta(s)$. According to the principle of minimum total potential energy, we aim to search for a proper function $\theta(s)$ that minimizes the given functional Π, which is a classic problem in functional analysis. Mathematically speaking, it's always better to find the exact analytical function of $\theta(s)$ but this is always hard to achieve. Instead, from the perspective of engineering, we can bypass the difficulties of deriving the analytical one via using polynomials to approximate the desired function. According to Weierstrass's first theorem, we can then define an nth-order polynomial to approximate the desired function, i.e.,

$$\vartheta(s) = \sum_{i=0}^{n} c_i s^i;\ (i = 0, 1, 2, 3...n) \tag{6.20}$$

where there are $n+1$ unknown coefficients c_i noted as $c = [c_0, c_1, ..., c_n]^\top$.

1) **Static modeling:** the functional minimization problem stated in (6.18) for static modeling can be transformed into an optimization problem where the cost function yields

$$\Pi \approx \bar{\Pi} = f(c) = \int_0^L \frac{1}{2} EI(\frac{\mathrm{d}\vartheta}{\mathrm{d}s})^2 \mathrm{d}s - \Delta F \Delta l - \int_0^L q_x(s)(s - x(s))\mathrm{d}s + \int_0^L q_y(s) y(s) \mathrm{d}s \tag{6.21}$$

with the boundary conditions due to (6.11):

$$\begin{aligned} &\vartheta(0) = 0 \\ &\frac{\mathrm{d}\vartheta}{\mathrm{d}s}(L) = \frac{M_o}{EI} = \frac{\Delta F d}{2EI} \end{aligned} \tag{6.22}$$

and the constraints according to (6.7) and (6.8):

$$\Delta l = \frac{\vartheta(L)}{2} W \tag{6.23}$$

where for the modeled manipulator, the structure, the material and the driving forces are given so W, E, I, ΔF, q_x and q_y are known. Finally, we will end up with the following:

$$\begin{aligned} &\min_{c}\ \bar{\Pi} = f(c) \\ &s.t.\ \ (6.22)(6.23) \end{aligned} \tag{6.24}$$

Obviously, the functional minimization problem has been transformed into a classic optimization problem with linear equality constraints where the unknown variables are the polynomial coefficients c.

2) **Kinematic modeling:** likewise, from (6.18) that states the prerequisites for statics-based kinematic modeling, we have

$$\Pi \approx \bar{\Pi} = f(c, \Delta F) = \int_0^L \frac{1}{2} EI(\frac{\mathrm{d}\vartheta}{\mathrm{d}s})^2 \mathrm{d}s - \Delta F \Delta l - \int_0^L q_x(s)(s - x(s))\mathrm{d}s + \int_0^L q_y(s) y(s) \mathrm{d}s \tag{6.25}$$

with the boundary conditions due to (6.22) and the constraints (6.23) where W, E, I, Δl, q_x and q_y are known. Finally, we can arrive at the following optimization problem:

$$\begin{aligned} &\min_{c, \Delta F}\ \bar{\Pi} = f(c, \Delta F) \\ &s.t.\ \ (6.22)(6.23) \end{aligned} \tag{6.26}$$

likewise, (6.26) is also a classic optimization problem with linear equality constraints where the unknown variables are the polynomial coefficients c and ΔF.

3) **Inverse modeling:** finally, we normally need to take care of inverse modeling when it comes to control of the studied robot.

$$\begin{aligned}\Pi \approx \bar{\Pi} &= f(c, F_1, F_2, \Delta l) \\ &= \int_0^L \frac{1}{2} EI(\frac{\mathrm{d}\vartheta}{\mathrm{d}s})^2 \mathrm{d}s - (F_1 - F_2)\Delta l - \int_0^L q_x(s)(s - x(s))\mathrm{d}s + \int_0^L q_y(s)y(s)\mathrm{d}s\end{aligned} \tag{6.27}$$

with the boundary conditions due to (6.22) and the constraints (6.23) along with the constraints for the end effector according to (6.15) and (6.20):

$$x(L) = \int_0^L \cos(\vartheta(s))\mathrm{d}s = x_t;\ y(L) = \int_0^L \sin(\vartheta(s))\mathrm{d}s = y_t;\ \vartheta(L) = \sum_{i=0}^{n} c_i L^i = \theta_t \tag{6.28}$$

where x_t, y_t and θ_t are known targeted coordinates within the workspace and (6.28) is a nonlinear constraint. Finally, we can reach the following optimization problem.

$$\begin{aligned}&\min_{c, F_1, F_2, \Delta l} \quad \bar{\Pi} = f(c, F_1, F_2, \Delta l) \\ &s.t. \quad (6.22)(6.23)(6.28)\end{aligned} \tag{6.29}$$

likewise, (6.29) is also a classic optimization problem with nonlinear equality constraints where the unknown variables are the polynomial coefficients $c, F_1, F_2, \Delta l$.

6.2.3 Discussions

Noticed from (6.19), it is obvious that the inverse modeling and kinematic modeling both have multi solutions. Therefore, we need to add some constraints to get rid of some undesired results. For example, the force inputs F_1 and F_2 are always required to be as small as possible to save energy. In this context, it is simple to handle the constraints under Lagrangian framework where we just need to add terms like $F_1^2 + F_2^2$ into the objective function. However, under Newtonian framework, we will have to transform the problem into an optimization problem where the objective function is $f = F_1^2 + F_2^2$ with some nonlinear constraints which essentially are the model derived from Newtonian framework. All in all, for simplicity, no matter in Newtonian framework or Lagrangian framework, we can formulate the static model as

$$f(F_1, F_2, P_\mathrm{e}) = 0 \tag{6.30}$$

and kinematic model as

$$f(\Delta l, P_\mathrm{e}) = 0 \tag{6.31}$$

6.3 Model-based control

Since modeling of continuum manipulators provides predictions about their performances, model-based controllers including open-loop and closed-loop ones considerably contribute to stable operations of these manipulators. According to the kinematic model (6.31), the workspace $\mathcal{W}$ of the manipulator can be defined (Amehri, Zheng, and Kruszewski, 2022):

$$\mathcal{W} = \{P_\mathrm{e} \in \mathbb{R}^{3\times 1} \mid f(\Delta l, P_\mathrm{e}) = 0,\ \forall \Delta l \in \Delta L\} \tag{6.32}$$

where ΔL denote the group of all admissible kinematic inputs. Equivalently, the workspace $\mathcal{W}$ can be defined as well according to the static model (6.30). However, from the practical point of view, it is not handy to specify the bounds of the input forces F_1 and F_2 so we use (6.32) as the definition of the workspace. Due to the same reason, the kinematic model is used in the following demonstration of control methods. In the following sections, all the reference positions are assumed:

$$P_\mathrm{e}^* \in \mathcal{W} \tag{6.33}$$

Different from (6.16) where P_e^* is one targeted position and orientation of the end-effector, we can define it as a path chosen from the workspace $\mathcal{W}$:

$$P_\mathrm{e}^* = [P_{\mathrm{e}_1}^*, P_{\mathrm{e}_2}^*, P_{\mathrm{e}_3}^*, P_{\mathrm{e}_4}^* ..., P_{\mathrm{e}_n}^*] \tag{6.34}$$

where

$$P_{e_i}^* = [x_{t_i}, y_{t_i}, \theta_{t_i}],\ i = 1,2,3,4...n \tag{6.35}$$

6.3.1 Open-loop control

In terms of open-loop control, to follow the user-defined path P_e^*, we just need to solve the following series of equations:

$$f(\Delta l_i^*, P_{e_i}^*) = 0,\ i = 1,2,3,4...n \tag{6.36}$$

Logically, by applying the method of inverse modeling presented in Section 6.2.2.1, we will end up with the corresponding open-loop inputs:

$$\Delta l = \Delta l^* = [\Delta l_1^*, \Delta l_2^*, \Delta l_3^* ... \Delta l_n^*] \tag{6.37}$$

6.3.2 Closed-loop control

In practice, due to the model inaccuracy and other uncertainties, the error between the current position and the reference position always exists, which can be defined:

$$e = P_e^* - P_e \in \mathbb{R}^{3\times 1} \tag{6.38}$$

Then, via (6.31), we can calculate the Jacobian matrix J between Δl and P_e:

$$J(\Delta l) = \frac{\partial P_e}{\partial \Delta l} \tag{6.39}$$

Logically, we can design the closed-loop inputs:

$$\Delta l = \Delta l^* + k_p (J^\top J)^{-1} J^\top e \tag{6.40}$$

where k_p denotes the gain of the controller.

Remark 15 *As mentioned before, it's not straightforward to specify the bounds of the force inputs since several conditions need to be considered, such as the actuation system, the strength of the manipulator and so on. However, if the above issues are all settled, we can still develop open-loop and closed-loop controllers following the same manner from* (6.36) *to* (6.40).

6.4 Experimental validation

In this section, the purpose is to apply the proposed model-based controller to a continuum manipulator where the kinematic one is used. Beforehand, we conduct parameter identification to finalize the equivalent material property, and also verify the inverse kinematic model via experimental testing. The testing results of the proposed open-loop controller are presented in the end.

6.4.1 Introduction

In this section, we briefly introduce the experimental set-up of the testing platform. As demonstrated in Fig. 6.3, the platform is composed of two components: the continuum manipulator and the control and communication system.

6.4.1.1 Continuum manipulator

As shown in Fig. 6.4, the manipulator, which is driven by 4 parallelly mounted cables, is composed of 10 rigid disks that are chained by a compliant elastic backbone along its body. In Fig. 6.5a, the detailed cross-section geometry of the disk is demonstrated, and the distance W between the two cable holes is 32 mm. The total length of the robot is round 280 mm so each section is about 28 mm. The total mass of the manipulator is about 80.2 g.

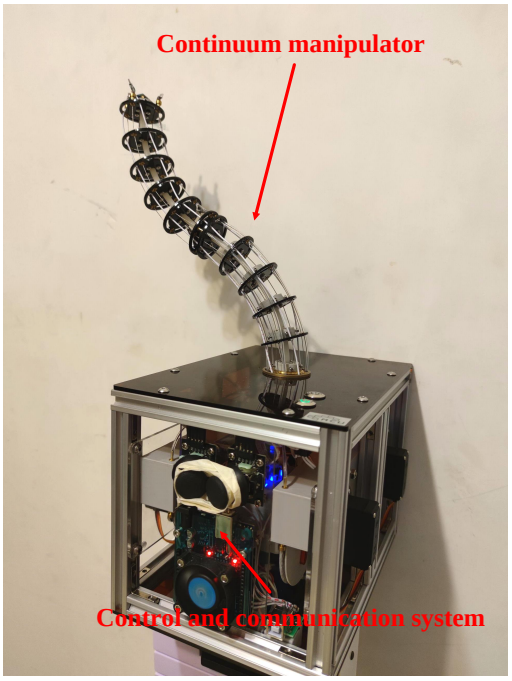

FIGURE 6.3: Overall demonstration of the testing platform

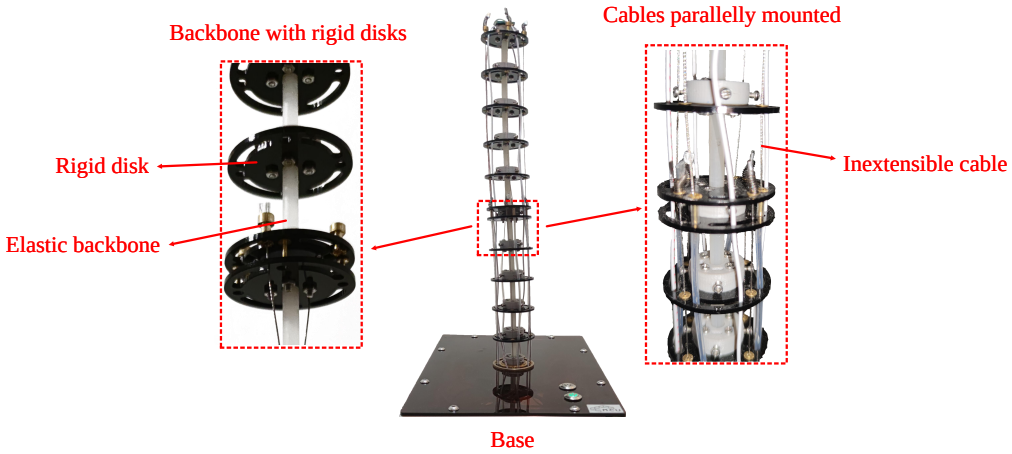

FIGURE 6.4: Prototype of the continuum manipulator

6.4.1.2 Control and communication system

As demonstrated in Fig. 6.6, the control and communication system is placed at the base of the manipulator in a compact black box. It is mainly composed of motors, a transmission system, an electronic board for communication and a manual controller. In this setup, the angular displacement of the motors is controlled so the displacement of the cables can be logically controlled via the transmission system. Note that there are 4 cables that can be driven for spatial manipulation of the manipulator but here, for demonstration, only 2 cables are used to achieve planar manipulation.

6.4.2 Parameter identification and verification

Generally speaking, the backbone of the continuum manipulator can be modeled by slender beam as shown in Fig. 6.4. Therefore, we need to identify the material properties of the equivalent beam that's used to model the manipulator. In Fig. 6.7, the manipulator bends only due to the gravity (the distributed loading q_y), and we use a physically equivalent beam to model this static behavior as well as finalizing the equivalent material properties via parameter identification. First, as shown in Fig. 6.7, we measure the coordinates of end effector highlighted in red, which are $x^*(\frac{Li}{10})$ and

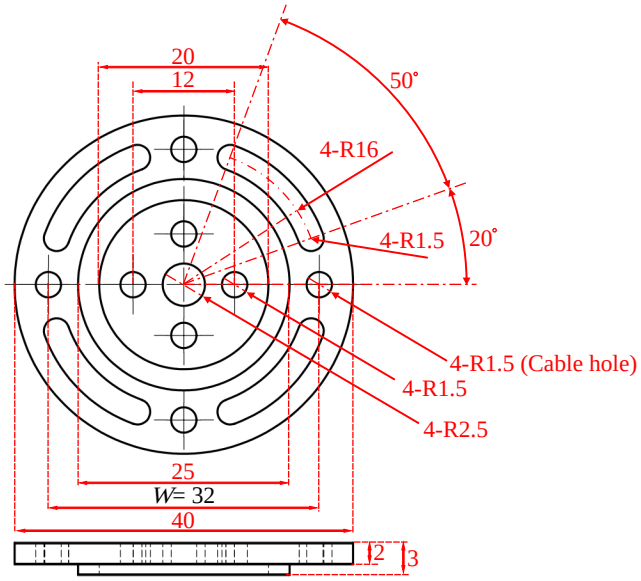

Unit: mm

(A) Detailed geometry of each rigid disk

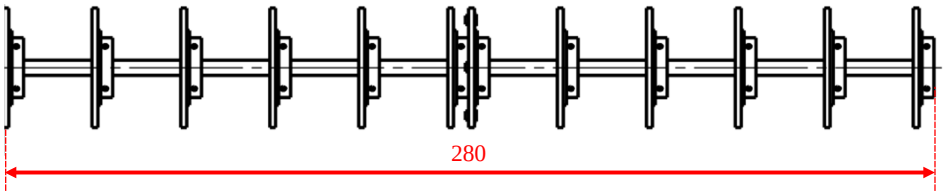

Unit: mm

(B) Overall geometry of the continuum manipulator

FIGURE 6.5: Detailed geometry information of the continuum manipulator

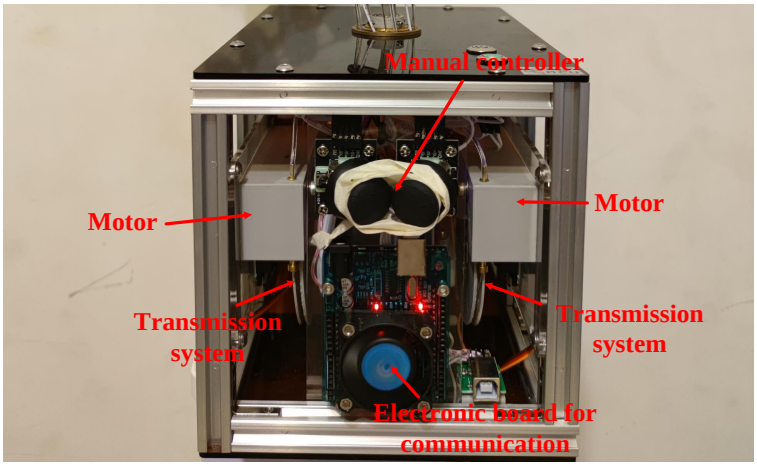

FIGURE 6.6: Demonstration of the control and communication system

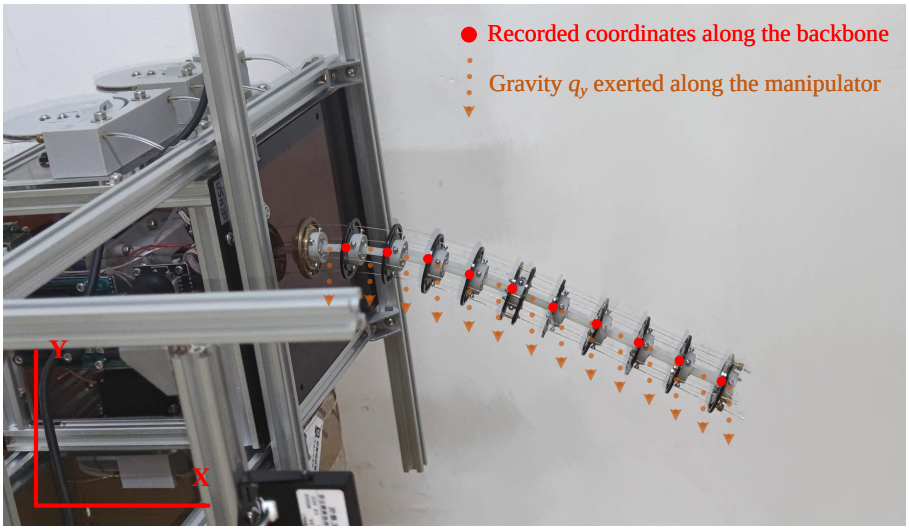

FIGURE 6.7: Manipulator bending only due to gravity (the distributed loading q_y)

$y^*(\frac{Li}{10})$ with $(i = 1, 2...10)$. According to (3.33), we can write down the BVP of the studied beam only due to gravity:

$$\begin{aligned} \text{D.E.} \quad & \frac{\mathrm{d}^2\theta}{\mathrm{d}s^2} = \frac{q_y \cos\theta(s)(L-s)}{EI} \\ \text{B.C.} \quad & \theta(0) = 0 \\ & \frac{\mathrm{d}\theta}{\mathrm{d}s}(L) = 0 \end{aligned} \tag{6.41}$$

where the unknown variable is EI (note that we don't need to handle EI as two separate variables). Then, we can set up the needed objective function as:

$$\mathbf{z} = f(EI) = \sum_{i=1}^{10} \{(x^*(\frac{Li}{10}) - x(\frac{Li}{10}))^2 + (y^*(\frac{Li}{10}) - y(\frac{Li}{10}))^2\} \tag{6.42}$$

Then, we can formulate the identification process as an optimization problem:

$$\begin{aligned} & \min_{EI} \ \mathbf{z} \\ & s.t. \ (6.41) \end{aligned} \tag{6.43}$$

Similarly, instead of formulating the analytical gradient, the numerical gradient can be calculated via finite difference method to meet the following condition:

$$\frac{\mathrm{d}\mathbf{z}}{\mathrm{d}EI}(EI) \approx \frac{f(EI+\varepsilon) - f(EI)}{\varepsilon} = 0 \tag{6.44}$$

where ε is an infinitesimal. As stated in Section 6.4.1.1, we can derive the length of the equivalent beam and the exerted gravity for this manipulator:

$$L = 0.28\,\mathrm{m};\ W = 0.032\,\mathrm{m};\ q_y = \frac{mg}{L} = 2.86\,\mathrm{N/m} \tag{6.45}$$

and the measured coordinates are all presented in Table 6.1. By solving the optimization problem (6.43), we can obtain the following value of EI:

$$EI = 0.0208\ \mathrm{Pa} \tag{6.46}$$

Finally, we plot the shape of the modeled beam to compare with the exact shape of the manipulator backbone as shown in Fig. 6.8. Clearly, the modeled beam with the identified value of EI in (6.46) provides quite accurate results compared to the real manipulator. With the identified material property ready, we aim to model the manipulator

TABLE 6.1: The recorded coordinates for parameter identification

	$i=1$	$i=2$	$i=3$	$i=4$	$i=5$	$i=6$	$i=7$	$i=8$	$i=9$	$i=10$
$x^*(\frac{iL}{10})$	1.39	6.49	13.45	21.79	32.6	44.19	56.25	68.23	80.67	95.05
$y^*(\frac{iL}{10})$	−27.68	−55.82	−82.6	−107.1	−132.97	−159.3	−185.62	−210.13	−234.63	−260.5

Unit: mm

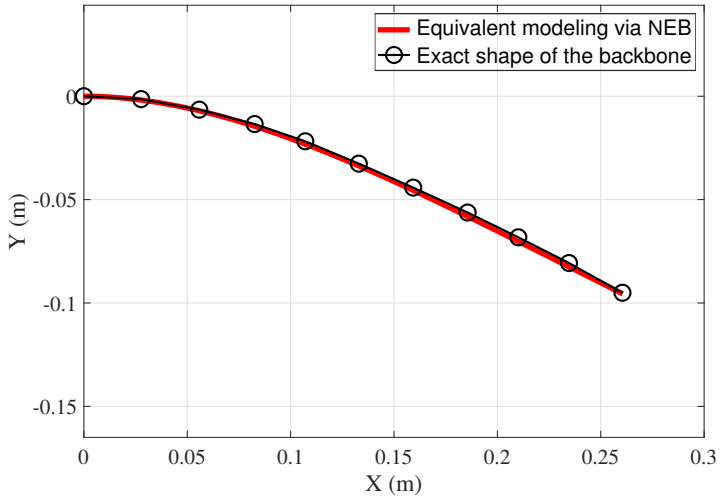

FIGURE 6.8: Manipulator bending only due to gravity (the distributed loading q_y)

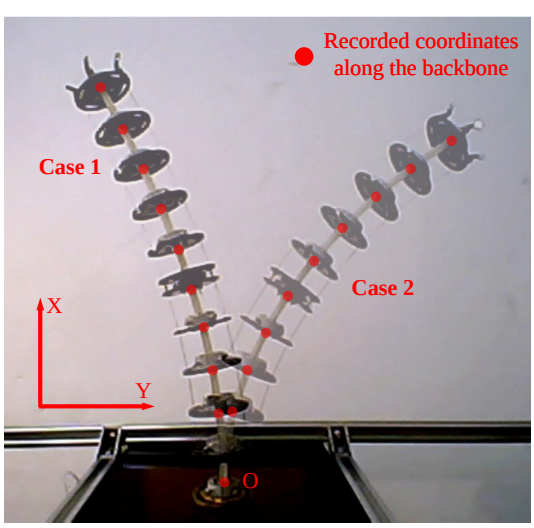

(A) Experimental testing

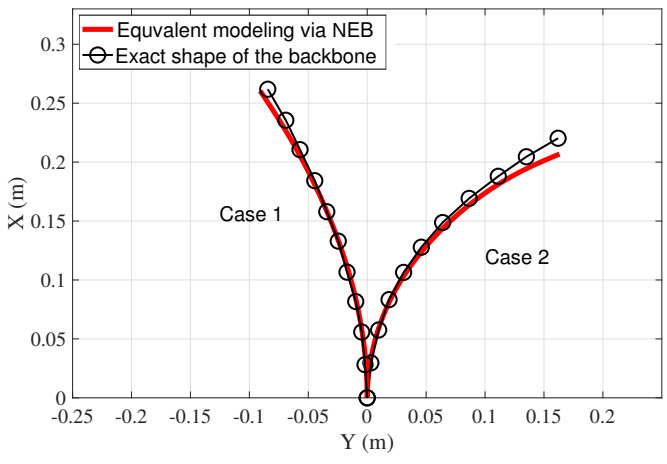

(B) Model verification via Geometrically nonlinear Euler Bernoulli beam theory (NEB)

FIGURE 6.9: Model verification via experimental testing

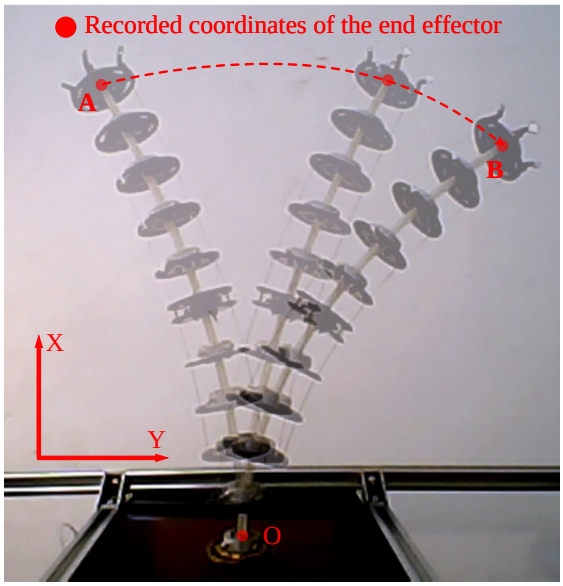

FIGURE 6.10: The reference path from point A to point B

actuated by the inextensible cables for verification as shown in Fig. 6.9. Note that in Fig. 6.9a, the manipulator is vertically placed in the actuation mode so the direction of gravity in the model is changed:

$$q_x = \frac{mg}{L} = 2.86\,\mathrm{N/m} \tag{6.47}$$

and the cable displacement is controlled:

$$\textbf{Case 1: } \Delta l = 3\pi \text{ mm}; \quad \textbf{Case 2: } \Delta l = -6\pi \text{ mm} \tag{6.48}$$

According to (6.25) and (6.26), we can logically characterize the final deflected backbone to compare the actual shape of the backbone as shown in Fig. 6.9b. It can be noticed that there's still some difference between the model and the actual manipulator, and the error may possibly come from the following parts:

1. **Model inaccuracy:** in the modeling, Euler Bernoulli beam theory is used, which means only pure bending of the backbone is considered. Shear and axial strains are ignored.

2. **Inaccurate assumption of actuation:** the assumption in (6.4) restricts the curvature of the two cables in the static-kinematic model, which may differ from the practical case of this continuum manipulator. The deducted conclusion (6.8) from the assumption in (6.4) may also lead to errors between the model and the practical manipulator.

6.4.3 Control implementation

Here, we demonstrate the closed-loop and open-loop control of the manipulator based on the inverse kinematic model (6.31). As shown in Fig. 6.10, the manipulator is controlled to follow the path from point A to point B which is corresponding to case 1 and case 2 as shown in Fig. 6.9a. As stated in the previous section, it is easy to calculate the targeted positions of point A, $P^*_{\mathrm{e}\,(\mathrm{A})} = P^*_{\mathrm{e}\,(\mathrm{AB})_1}$ and point B, $P^*_{\mathrm{e}\,(\mathrm{B})} = P^*_{\mathrm{e}\,(\mathrm{AB})_n}$ respectively via (6.48). Then, we choose the path from point A to point B that belong to the workspace of the manipulator $\mathcal{W}$:

$$P^*_{\mathrm{e}\,(\mathrm{AB})} = [P^*_{\mathrm{e}\,(\mathrm{AB})_1}, P^*_{\mathrm{e}\,(\mathrm{AB})_2}, P^*_{\mathrm{e}\,(\mathrm{AB})_3}, P^*_{\mathrm{e}\,(\mathrm{AB})_4} ..., P^*_{\mathrm{e}\,(\mathrm{AB})_n}] \in \mathcal{W} \tag{6.49}$$

where

$$P^*_{\mathrm{e}\,\mathrm{AB}_i} = x_{t_i},\ i = 1, 2, 3, 4...n \tag{6.50}$$

Note that here we are only interested in the X-axis coordinate of the end effector since in the current configuration the y_{t_i} and θ_{t_i} are implicitly determined by x_{t_i}. Besides, the kinematic model is used for designing the controller

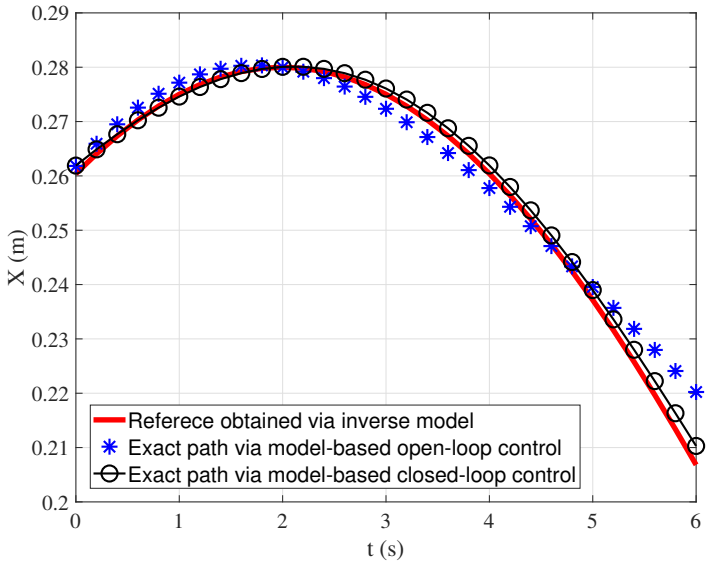

FIGURE 6.11: The X-axis reference from point A to point B

where the manipulator's dynamics is ignored. Therefore, the time constraint added for the path should not be too short, otherwise the dynamic characteristics of the robot may cause the failure of the controller. Here, the reference path is designed to be fulfilled within 6 seconds. Following (6.36) to (6.40), we can therefore design the closed-loop controller for this task. The actual coordinates of the end effector are recorded to compare the reference ones shown in (6.49) (see Fig. 6.11) where it can be noticed that the closed-loop control present better performance in following the reference path compared to that of the open-loop one. This is logical that the local PID part of the closed-loop controller contributes to reducing the errors.

6.5 Conclusions

In this chapter, to present the control method for compliant mechanisms, we demonstrate an experimental implementation of controlling a continuum manipulator. We start from presenting the static, kinematic and inverse modeling of the manipulator via geometrically nonlinear Euler Bernoulli beam theory to the design of a model-based controller. In terms of the modeling, Newtonian framework and Lagrangian framework are both presented where the former focuses on the detailed equilibrium state of the manipulator while the later aims to satisfy the minimum condition of the total potential energy. For the model-based controllers, we present both the closed-loop one and the open-loop one for the manipulator. In the end, to verify the proposed control strategy, we have conducted an experimental case on controlling a planar continuum manipulator where the results of the closed-loop controller and the open-loop one are compared. Basically, this chapter paves the way for the control of CMs, and also offers potential possibilities for controlling other types of CMs.

Chapter 7

Conclusions and Perspectives

7.1 Conclusions

In this thesis, we have investigated a comprehensive methodology of design, modeling, optimization and control of compliant mechanisms. As the core of compliant mechanisms, the built-in flexible members (flexures, slender beams and so on) serve as the functional parts to transfer motion, displacement and energy depending on the elasticity of the material. This thesis provides analysis of these flexible members from geometric definition, transformation of coordinate systems and (static) modeling of large deflections of the slender beams to (static or kinematic) modeling of CMs, optimization and model-based control where planar beams are mainly considered. Given specific design requirements or performance objectives, we can formulate the tasks into typical optimization problems via universal tools to avoid the procedure of trial-and-error process when designing compliant mechanisms. Among the above mentioned work, efficient modeling of large deflections of slender beams, which is the fundamental of the proposed methodology in this thesis, is of the most importance.

Therefore, in Chapter 1, we have reviewed the current state-of-the-art of CMs, including the existing CM-based mechanical applications and most importantly, the commonly-used methods for static and kinematic modeling of slender beams. In Chapter 2, we briefly introduce the mathematical tools used in this thesis to prepare for the following chapters. Then, in Chapter 3, we lay the stress on a focused area in CMs, static modeling of planar large deflections where we present the geometrical definition of slender beams and different modeling methodologies for large-deflection problems. Thirdly, the methods applied to solve the derived models in Chapter 4 are explained in detail. In Chapter 5, we demonstrate the modeling of some representative compliant mechanisms and a case study about mechanism optimization on an ICB-based compliant parallelogram. In Chapter 6, we present a practical case of modeling a continuum manipulator, design of the model-based controller and corresponding experimental testing, to verify the proposed methodology in this thesis.

In the following, we present a brief summary of the main contributions of this thesis: static modeling of planar large deflections and the corresponding numerical methods; model-based optimization and model-based control.

7.1.1 Static modeling of planar large deflections and the corresponding numerical methods

In this thesis, we present two modeling frameworks: Newtonian mechanics and Lagrangian mechanics. Under Newtonian framework, we study the deflection of slender beams from the perspective of moment balance along the beam axis where the force equilibrium is analyzed in detail. On the contrary, under Lagrangian framework, the deflection of slender beams is studied from an energy-based point of view where the total potential energy of the studied elastic system is focused instead of the force equilibrium along the beam axis. It is proved in physics that these two are equivalently to each other and also in this studied elastic system, the equivalence has also been proved in Remark 6 and Remark 7. Therefore, we can choose from the mentioned two frameworks based on the faced engineering scenarios. Here, we present Table 7.1 to demonstrate the differences between the two mentioned frameworks, including scope, modeling complexity, numerical solutions, closed-form solutions and focus.

7.1.2 Performance prediction, model-based optimization and model-based control of compliant mechanisms

The purpose of modeling the studied CMs is to predict their performances, model-based optimization and model-based control. In particular, the last two play a very important role in mechanical design and controller design. Normally,

TABLE 7.1: Comparisons between Newtonian framework and Lagrangian framework

Framework / Evaluation	Newtonian framework	Lagrangian framework
Scope	All types of external load	Conservative external load
Modeling complexity	Relatively complex ODEs	Simple optimization problems
Numerical solutions	Shooting method, Weighted residual methods, Taylor series method..	Lagrange multiplier
Closed-form solutions	Adomian decomposition method	N/A
Focus	Moment and force balance of every single point along the beam axis	Input work and stored energy of the elastic system

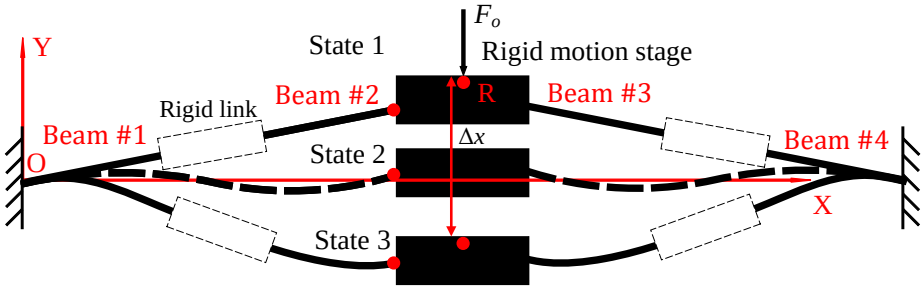

FIGURE 7.1: Analysis of bi-stable mechanisms from an energy point of view

numerical modeling is used to serve the optimization process and controller design since analytical solutions are hard to find. In Chapter 5, an ICB-based compliant parallelogram is designed through optimization followed by experimental validation. In the last chapter, we present a simple implementation of controlling a planar continuum manipulator where a model-based closed-loop controller is designed. Logically, the physics-based modeling helps designers avoid trial-and-error process, which hugely improves the efficiency of the process in mechanical design and controller design.

7.2 Perspectives

Based on the layout of the thesis, which is also the structure of my future work, I would like to present some potential areas and possible extensions of the presented results.

7.2.1 Defining the geometry of 3D beams and the transformation into body frame

In Chapter 3, we mainly discuss how to define a planar beam in different coordinate systems as well as the transformation to body frame for further analysis of large deflections. As stated in Section 3.2.6, we propose a similar idea of defining a 3D (spatial) beam in different coordinate systems and the transformation strategy to body frame as well. This is because, in compliant mechanisms, some spatial ICBs used for presenting more various mechanical properties, such as springs, are commonly used.

7.2.2 Analyzing multi-stable mechanisms from a Lagrangian (energy) point of view

As stated in Section 5.2.3 and Section 3.3.1.2, several types of bi-stable mechanisms (pure compliant bi-stable mechanisms and different pre-buckled bi-stable mechanisms) are analyzed from a Newtonian perspective where moment balance along the flexible beam is satisfied. In my future work, I would like to analyze the bi-stable mechanisms from an energy point of view (see Fig. 7.1) since it is simpler and straightforward, being directly formulated into an optimization problem without touching the governing ODEs. In Fig. 7.1, we can easily formulate the total potential energy as follows:

$$\Pi = f(\theta_i(s), \frac{\mathrm{d}\theta_i}{\mathrm{d}s}(s), s) = \sum_{i=1}^{4} \int_0^{L_i} \frac{1}{2} EI (\frac{\mathrm{d}\theta_i}{\mathrm{d}s}(s))^2 \mathrm{d}s - F_o \Delta x \tag{7.1}$$

where $i = 1, 2, 3, 4$. Constraint by some corresponding boundary conditions for $\theta_i(s)$, we just need to find the proper $\theta_i(s)$ that can minimize Π according to the principle of minimum potential energy. Then, transforming (7.1) into an optimization problem, we can use Lagrange multiplier to handle this problem.

7.2.3 Contact-aided compliant mechanisms

Different from the simple cases regarding contact problems stated in Section 3.3.1.3 and Section 3.4.1.2, my future focus will be the topic on more complex scenarios, such as flexible contact and irregular-shape contact. To handle this type of problems, the chained body-frame beam constraint model (CBBCM) needs to be utilized where each body-frame beam constraint model (BBCM) serves as the elementary one to analyze internal and external forces (stated in Section 4.4.2).

7.2.4 Efficient numerical methods for Full-mode Cosserat rod model

Cosserat rod theory is commonly used in modeling deformable manipulators but not widely used in modeling CMs. To solve Cosserat rod model, shooting method and its related ones are used. However, these methods are normally time-consuming to solve the BVP of the governing ODEs since it essentially transforms the BVP into a series of IVPs. Instead of being stuck with shooting strategies, we have presented the following two aspects to increase the efficiency of solving Cosserat rod model.

7.2.4.1 Newtonian framework: efficient numerical methods for ODEs

If we continue to handle the BVP of the governing ODEs of Cosserat rod model, we have multiple solutions since in applied mathematics there are many numerical or closed-form solutions to the mentioned problem. Essentially, the ODEs of Cosserat rod model have some unique properties due to the fact that the rotation matrix $\mathbf{R}$ has always to be in the group of $SO3$ ($\mathbf{R}^{-1} = \mathbf{R}^{\top}$). As long as the we define an unknown matrix that always has this property, the studied ODEs come back to a very normal set. Then, multiple methods like weighted residual methods can be used to solve the BVP in a more efficient manner.

7.2.4.2 Lagrangian framework: optimization problems

On the other hand, we consider the problem from the perspective of Lagrangian point of view. This is because the set of ODEs is basically the results of variation from the formulation of total potential energy according to the equivalency between Newtonian mechanics and Lagrangian mechanics. Therefore, we can solve the problem at the stage where total potential energy is formulated. Likewise, we can transform the problem into a classic optimization problem as well. Similarly, rotation matrix $\mathbf{R}$ needs to be defined in the group of $SO3$.

Appendix A

Detailed Deduction of Derivatives for Taylor Series Method

According to the governing equation (4.78), we can easily obtain the 2nd-order derivative at 0 as:

$$\frac{\mathrm{d}^2\theta}{\mathrm{d}s^2}(0) = -\frac{F_y}{EI}(\cos\theta(0) + \frac{F_x}{F_y}\sin\theta(0)) = -\frac{F_y}{EI}$$

which in fact is constant. Then, by differentiating (4.78) with respect to s and take the value $s = 0$, we can get the 3rd-order derivative at 0 as:

$$\frac{\mathrm{d}^3\theta}{\mathrm{d}s^3}(0) = -\frac{F_y}{EI}(-\sin\theta(0)\frac{\mathrm{d}\theta}{\mathrm{d}s}(0) + \frac{F_x}{F_y}\cos\theta(0)\frac{\mathrm{d}\theta}{\mathrm{d}s}(0)) = -\frac{F_x}{EI}\frac{\mathrm{d}\theta}{\mathrm{d}s}(0)$$

which indeed is a function of one unknown variable $\frac{\mathrm{d}\theta}{\mathrm{d}s}(0)$. Calculating again the twice differentiation of (4.78) with respect to s and take $s = 0$, we obtain the 4th-order derivative at 0 as:

$$\begin{aligned}\frac{\mathrm{d}^4\theta}{\mathrm{d}s^4}(0) &= -\frac{F_y}{EI}(-\cos\theta(0)(\frac{\mathrm{d}\theta}{\mathrm{d}s}(0))^2 - \sin\theta(0)\frac{\mathrm{d}^2\theta}{\mathrm{d}s^2}(0) - \frac{F_x}{F_y}\sin\theta(0)(\frac{\mathrm{d}\theta}{\mathrm{d}s}(0))^2 + \frac{F_x}{F_y}\cos\theta(0)\frac{\mathrm{d}^2\theta}{\mathrm{d}s^2}(0)) \\ &= \frac{F_y}{EI}(\frac{\mathrm{d}\theta}{\mathrm{d}s}(0))^2 - \frac{F_x}{EI}\frac{\mathrm{d}^2\theta}{\mathrm{d}s^2}(0)\end{aligned}$$

which can be implicitly regarded as a function of one unknown variable $\frac{\mathrm{d}\theta}{\mathrm{d}s}(0)$, since it has been shown in the former calculation that $\frac{\mathrm{d}^2\theta}{\mathrm{d}s^2}(0)$ is a function of the unknown variable $\frac{\mathrm{d}\theta}{\mathrm{d}s}(0)$. By iterating the above procedure, we can obtain the successive high-order derivatives $\frac{\mathrm{d}^i\theta}{\mathrm{d}s^i}(0)$, which gives the 5th-order derivative at 0 as:

$$\frac{\mathrm{d}^5\theta}{\mathrm{d}s^5}(0) = \frac{3F_y}{EI}\frac{\mathrm{d}^2\theta}{\mathrm{d}s^2}(0)\frac{\mathrm{d}\theta}{\mathrm{d}s}(0) - \frac{F_x}{EI}\frac{\mathrm{d}^3\theta}{\mathrm{d}s^3}(0) + \frac{F_x}{EI}(\frac{\mathrm{d}\theta}{\mathrm{d}s}(0))^3$$

the 6th-order derivative at 0 as:

$$\frac{\mathrm{d}^6\theta}{\mathrm{d}s^6}(0) = \frac{4F_y}{EI}\frac{\mathrm{d}^3\theta}{\mathrm{d}s^3}(0)\frac{\mathrm{d}\theta}{\mathrm{d}s}(0) + \frac{3F_y}{EI}(\frac{\mathrm{d}^2\theta}{\mathrm{d}s^2}(0))^2 - \frac{F_y}{EI}(\frac{\mathrm{d}\theta}{\mathrm{d}s}(0))^4 - \frac{F_x}{EI}\frac{\mathrm{d}^4\theta}{\mathrm{d}s^4}(0) + \frac{6F_x}{EI}\frac{\mathrm{d}^2\theta}{\mathrm{d}s^2}(0)(\frac{\mathrm{d}\theta}{\mathrm{d}s}(0))^2$$

the 7th-order derivative at 0 as:

$$\begin{aligned}\frac{\mathrm{d}^7\theta}{\mathrm{d}s^7}(0) &= \frac{5F_y}{EI}\frac{\mathrm{d}^4\theta}{\mathrm{d}s^4}(0)\frac{\mathrm{d}\theta}{\mathrm{d}s}(0) + \frac{10F_y}{EI}\frac{\mathrm{d}^3\theta}{\mathrm{d}s^3}(0)\frac{\mathrm{d}^2\theta}{\mathrm{d}s^2}(0) - \frac{10F_y}{EI}\frac{\mathrm{d}^2\theta}{\mathrm{d}s^2}(0)(\frac{\mathrm{d}\theta}{\mathrm{d}s}(0))^3 - \frac{F_x}{EI}\frac{\mathrm{d}^5\theta}{\mathrm{d}s^5}(0) + \frac{10F_x}{EI}\frac{\mathrm{d}^3\theta}{\mathrm{d}s^3}(0)(\frac{\mathrm{d}\theta}{\mathrm{d}s}(0))^2 \\ &\quad + \frac{15F_x}{EI}(\frac{\mathrm{d}^2\theta}{\mathrm{d}s^2}(0))^2\frac{\mathrm{d}\theta}{\mathrm{d}s}(0) - \frac{F_x}{EI}(\frac{\mathrm{d}\theta}{\mathrm{d}s}(0))^5\end{aligned}$$

the 8th-order derivative at 0 as:

$$\begin{aligned}\frac{\mathrm{d}^8\theta}{\mathrm{d}s^8}(0) = &\frac{15F_x}{EI}(\frac{\mathrm{d}^2\theta}{\mathrm{d}s^2}(0))^3 + \frac{6F_y}{EI}\frac{\mathrm{d}^5\theta}{\mathrm{d}s^5}(0)\frac{\mathrm{d}\theta}{\mathrm{d}s}(0) + \frac{15F_y}{EI}\frac{\mathrm{d}^4\theta}{\mathrm{d}s^4}(0)\frac{\mathrm{d}^2\theta}{\mathrm{d}s^2}(0) + \frac{10F_y}{EI}(\frac{\mathrm{d}^3\theta}{\mathrm{d}s^3}(0))^2 + \frac{F_y}{EI}(\frac{\mathrm{d}\theta}{\mathrm{d}s}(0))^6 \\ &+ \frac{15F_x}{EI}\frac{\mathrm{d}^4\theta}{\mathrm{d}s^4}(0)(\frac{\mathrm{d}\theta}{\mathrm{d}s}(0))^2 + \frac{60F_x}{EI}\frac{\mathrm{d}^3\theta}{\mathrm{d}s^3}(0)\frac{\mathrm{d}^2\theta}{\mathrm{d}s^2}(0)\frac{\mathrm{d}\theta}{\mathrm{d}s}(0) - \frac{15F_x}{EI}\frac{\mathrm{d}^2\theta}{\mathrm{d}s^2}(0)(\frac{\mathrm{d}\theta}{\mathrm{d}s}(0))^4 - \frac{20F_y}{EI}\frac{\mathrm{d}^3\theta}{\mathrm{d}s^3}(0)(\frac{\mathrm{d}\theta}{\mathrm{d}s}(0))^3 \\ &- \frac{45F_y}{EI}(\frac{\mathrm{d}^2\theta}{\mathrm{d}s^2}(0))^2(\frac{\mathrm{d}\theta}{\mathrm{d}s}(0))^2 - \frac{F_x}{EI}\frac{\mathrm{d}^6\theta}{\mathrm{d}s^6}(0)\end{aligned}$$

the 9th-order derivative at 0,

$$\begin{aligned}\frac{\mathrm{d}^9\theta}{\mathrm{d}s^9}(0) = &\frac{F_x}{EI}(\frac{\mathrm{d}\theta}{\mathrm{d}s}(0))^7 - \frac{F_x}{EI}\frac{\mathrm{d}^7\theta}{\mathrm{d}s^7}(0) - \frac{35F_y}{EI}\frac{\mathrm{d}^4\theta}{\mathrm{d}s^4}(0)(\frac{\mathrm{d}\theta}{\mathrm{d}s}(0))^3 + \frac{21F_y}{EI}\frac{\mathrm{d}^2\theta}{\mathrm{d}s^2}(0)(\frac{\mathrm{d}\theta}{\mathrm{d}s}(0))^5 + \frac{7F_y}{EI}\frac{\mathrm{d}^6\theta}{\mathrm{d}s^6}(0)\frac{\mathrm{d}\theta}{\mathrm{d}s}(0) \\ &+ \frac{21F_y}{EI}\frac{\mathrm{d}^5\theta}{\mathrm{d}s^5}(0)\frac{\mathrm{d}^2\theta}{\mathrm{d}s^2}(0) + \frac{35F_y}{EI}\frac{\mathrm{d}^4\theta}{\mathrm{d}s^4}(0)\frac{\mathrm{d}^3\theta}{\mathrm{d}s^3}(0) - \frac{105F_y}{EI}(\frac{\mathrm{d}^2\theta}{\mathrm{d}s^2}(0))^3\frac{\mathrm{d}\theta}{\mathrm{d}s}(0) + \frac{105F_x}{EI}(\frac{\mathrm{d}^2\theta}{\mathrm{d}s^2}(0))^2\frac{\mathrm{d}^3\theta}{\mathrm{d}s^3}(0) \\ &+ \frac{70F_x}{EI}(\frac{\mathrm{d}^3\theta}{\mathrm{d}s^3}(0))^2\frac{\mathrm{d}\theta}{\mathrm{d}s}(0) + \frac{21F_x}{EI}\frac{\mathrm{d}^5\theta}{\mathrm{d}s^5}(0)(\frac{\mathrm{d}\theta}{\mathrm{d}s}(0))^2 - \frac{35F_x}{EI}\frac{\mathrm{d}^3\theta}{\mathrm{d}s^3}(0)(\frac{\mathrm{d}\theta}{\mathrm{d}s}(0))^4 - \frac{105F_x}{EI}(\frac{\mathrm{d}^2\theta}{\mathrm{d}s^2}(0))^2(\frac{\mathrm{d}\theta}{\mathrm{d}s}(0))^3 \\ &+ \frac{105F_x}{EI}\frac{\mathrm{d}^4\theta}{\mathrm{d}s^4}(0)\frac{\mathrm{d}^2\theta}{\mathrm{d}s^2}(0)\frac{\mathrm{d}\theta}{\mathrm{d}s}(0) - \frac{210F_y}{EI}\frac{\mathrm{d}^3\theta}{\mathrm{d}s^3}(0)\frac{\mathrm{d}^2\theta}{\mathrm{d}s^2}(0)(\frac{\mathrm{d}\theta}{\mathrm{d}s}(0))^2\end{aligned}$$

the 10th-order derivative at 0 as:

$$\begin{aligned}\frac{\mathrm{d}^{10}\theta}{\mathrm{d}s^{10}}(0) = &\frac{168F_x}{EI}\frac{\mathrm{d}^5\theta}{\mathrm{d}s^5}(0)\frac{\mathrm{d}\theta}{\mathrm{d}s}(0)\frac{\mathrm{d}^2\theta}{\mathrm{d}s^2}(0) + \frac{280F_x}{EI}\frac{\mathrm{d}^4\theta}{\mathrm{d}s^4}(0)\frac{\mathrm{d}\theta}{\mathrm{d}s}(0)\frac{\mathrm{d}^3\theta}{\mathrm{d}s^3}(0) - \frac{560Fx}{EI}\frac{\mathrm{d}^3\theta}{\mathrm{d}s^3}(0)\frac{\mathrm{d}^2\theta}{\mathrm{d}s^2}(0)(\frac{\mathrm{d}\theta}{\mathrm{d}s}(0))^3 \\ &- \frac{420F_y}{EI}\frac{\mathrm{d}^4\theta}{\mathrm{d}s^4}(0)\frac{\mathrm{d}^2\theta}{\mathrm{d}s^2}(0)(\frac{\mathrm{d}\theta}{\mathrm{d}s}(0))^2 - \frac{840F_y}{EI}(\frac{\mathrm{d}^2\theta}{\mathrm{d}s^2}(0))^2\frac{\mathrm{d}\theta}{\mathrm{d}s}(0)\frac{\mathrm{d}^3\theta}{\mathrm{d}s^3}(0) + \frac{28F_x}{EI}(\frac{\mathrm{d}\theta}{\mathrm{d}s}(0))^6\frac{\mathrm{d}^2\theta}{\mathrm{d}s^2}(0) \\ &+ \frac{280F_x}{EI}(\frac{\mathrm{d}^3\theta}{\mathrm{d}s^3}(0))^2\frac{\mathrm{d}^2\theta}{\mathrm{d}s^2}(0) + \frac{210F_x}{EI}\frac{\mathrm{d}^4\theta}{\mathrm{d}s^4}(0)(\frac{\mathrm{d}^2\theta}{\mathrm{d}s^2}(0))^2 - \frac{420F_x}{EI}(\frac{\mathrm{d}^2\theta}{\mathrm{d}s^2}(0))^3(\frac{\mathrm{d}\theta}{\mathrm{d}s}(0))^2 + \frac{8F_y}{EI}\frac{\mathrm{d}^7\theta}{\mathrm{d}s^7}(0)\frac{\mathrm{d}\theta}{\mathrm{d}s}(0) \\ &+ \frac{28F_y}{EI}\frac{\mathrm{d}^6\theta}{\mathrm{d}s^6}(0)\frac{\mathrm{d}^2\theta}{\mathrm{d}s^2}(0) + \frac{56F_y}{EI}\frac{\mathrm{d}^5\theta}{\mathrm{d}s^5}(0)\frac{\mathrm{d}^3\theta}{\mathrm{d}s^3}(0) - \frac{280F_y}{EI}(\frac{\mathrm{d}^3\theta}{\mathrm{d}s^3}(0))^2(\frac{\mathrm{d}\theta}{\mathrm{d}s}(0))^2 + \frac{56F_y}{EI}\frac{\mathrm{d}^3\theta}{\mathrm{d}s^3}(0)(\frac{\mathrm{d}\theta}{\mathrm{d}s}(0))^5 \\ &+ \frac{210F_y}{EI}(\frac{\mathrm{d}^2\theta}{\mathrm{d}s^2}(0))^2(\frac{\mathrm{d}\theta}{\mathrm{d}s}(0))^4 + \frac{28F_x}{EI}\frac{\mathrm{d}^6\theta}{\mathrm{d}s^6}(0)(\frac{\mathrm{d}\theta}{\mathrm{d}s}(0))^2 - \frac{70F_x}{EI}\frac{\mathrm{d}^4\theta}{\mathrm{d}s^4}(0)(\frac{\mathrm{d}\theta}{\mathrm{d}s}(0))^4 - \frac{F_y}{EI}(\frac{\mathrm{d}\theta}{\mathrm{d}s}(0))^8 \\ &- \frac{56F_y}{EI}\frac{\mathrm{d}^5\theta}{\mathrm{d}s^5}(0)(\frac{\mathrm{d}\theta}{\mathrm{d}s}(0))^3 + \frac{35F_y}{EI}(\frac{\mathrm{d}^4\theta}{\mathrm{d}s^4}(0))^2 - \frac{105F_y}{EI}(\frac{\mathrm{d}^2\theta}{\mathrm{d}s^2}(0))^4 - \frac{F_x}{EI}\frac{\mathrm{d}^8\theta}{\mathrm{d}s^8}(0)\end{aligned}$$

$$\frac{\mathrm{d}^{11}\theta}{\mathrm{d}s^{11}}(0) = ...$$

In summary, according to (4.78), for a given order n, we can always deduce the analytic formulation of the nth derivative of θ at $s = 0$, and all those high-order derivatives are the functions of only one unknown variable $\frac{\mathrm{d}\theta}{\mathrm{d}s}(0)$. It is worth noting that those tedious deductions can be automatically obtained via symbolic computation software, such as Mathematica and Maple.

Bibliography

Abbasbandy, Saeid and C Bervillier (2011). "Analytic continuation of Taylor series and the boundary value problems of some nonlinear ordinary differential equations". In: *Applied Mathematics and Computation* 218.5, pp. 2178–2199.

Adomian, George (2013). *Solving frontier problems of physics: the decomposition method*. Vol. 60. Springer Science & Business Media.

Albanesi, Alejandro E, Victor D Fachinotti, and Martin A Pucheta (2010). "A review on design methods for compliant mechanisms". In: *Mecánica Computacional* 29.3, pp. 59–72.

Amehri, Walid, Gang Zheng, and Alexandre Kruszewski (2022). "Position-Access Workspace of Slender Soft Manipulators". In: *Journal of Mechanisms and Robotics* 14.6, p. 061001.

Antman, Stuart S (2005). *Nonlinear Problems of Elasticity*. Springer.

Armanini, Costanza et al. (2021). "Soft robots modeling: A literature unwinding". In: *arXiv preprint arXiv:2112.03645*.

Awtar, Shorya (2003). "Synthesis and analysis of parallel kinematic XY flexure mechanisms". PhD thesis. Massachusetts Institute of Technology.

Awtar, Shorya and Shiladitya Sen (2010). "A generalized constraint model for two-dimensional beam flexures: Nonlinear strain energy formulation". In: *Journal of mechanical Design* 132.8.

Awtar, Shorya, Alexander H Slocum, and Edip Sevincer (2007). "Characteristics of Beam-Based Flexure Modules". In: *Journal of Mechanical Design* 129.6.

Banerjee, A, B Bhattacharya, and AK Mallik (2008). "Large deflection of cantilever beams with geometric nonlinearity: Analytical and numerical approaches". In: *International Journal of Non-Linear Mechanics* 43.5, pp. 366–376.

Bergou, Miklós et al. (2008). "Discrete Elastic Rods". In: *ACM Transactions on Graphics (SIGGRAPH)* 27.3, 63:1–63:12.

Bergou, Miklós et al. (2010). "Discrete viscous threads". In: *ACM Transactions on graphics (TOG)* 29.4, pp. 1–10.

Bertails, Florence (2009). "Linear time super-helices". In: *Computer graphics forum*. Vol. 28. 2. Wiley Online Library, pp. 417–426.

Bertails, Florence et al. (2006). "Super-helices for predicting the dynamics of natural hair". In: *ACM Transactions on Graphics (TOG)* 25.3, pp. 1180–1187.

Bertails-Descoubes, Florence (2012). "Super-Clothoids". In: *Computer Graphics Forum*. Vol. 31. 2pt2. Wiley Online Library, pp. 509–518.

Bertsekas, Dimitri P (2014). *Constrained optimization and Lagrange multiplier methods*. Academic press.

Black, Caroline B, John Till, and D Caleb Rucker (2017). "Parallel continuum robots: Modeling, analysis, and actuation-based force sensing". In: *IEEE Transactions on Robotics* 34.1, pp. 29–47.

Boresi, Arthur Peter, Richard Joseph Schmidt, Omar M Sidebottom, et al. (1985). *Advanced mechanics of materials*. Vol. 6. Wiley New York.

Boyer, Frédéric, Shaukat Ali, and Mathieu Porez (2011). "Macrocontinuous dynamics for hyperredundant robots: application to kinematic locomotion bioinspired by elongated body animals". In: *IEEE Transactions on Robotics* 28.2, pp. 303–317.

Boyer, Frédéric, Mathieu Porez, and Wisama Khalil (2006). "Macro-continuous computed torque algorithm for a three-dimensional eel-like robot". In: *IEEE transactions on robotics* 22.4, pp. 763–775.

Boyer, Frédéric and Dominique Primault (2004). "Finite element of slender beams in finite transformations: a geometrically exact approach". In: *International Journal for Numerical Methods in Engineering* 59.5, pp. 669–702.

Brush, Don O, Bo O Almroth, and JW Hutchinson (1975). "Buckling of bars, plates, and shells". In.

Cardona, A and Mr Geradin (1988). "A beam finite element non-linear theory with finite rotations". In: *International journal for numerical methods in engineering* 26.11, pp. 2403–2438.

Carleo, Giuseppe et al. (2019). “Machine learning and the physical sciences”. In: *Reviews of Modern Physics* 91.4, p. 045002.

Charrondière, Raphaël et al. (2020). “Numerical modeling of inextensible elastic ribbons with curvature-based elements”. In: *Computer Methods in Applied Mechanics and Engineering* 364, p. 112922.

Chen, Guimin and Ruiyu Bai (2016). “Modeling large spatial deflections of slender bisymmetric beams in compliant mechanisms using chained spatial-beam constraint model”. In: *Journal of Mechanisms and Robotics* 8.4.

Chen, Guimin and Fulei Ma (2015). “Kinetostatic modeling of fully compliant bistable mechanisms using Timoshenko beam constraint model”. In: *Journal of Mechanical Design* 137.2, p. 022301.

Chen, Guimin, Yakun Ma, and Jiajie Li (2016). “A tensural displacement amplifier employing elliptic-arc flexure hinges”. In: *Sensors and Actuators A: Physical* 247, pp. 307–315.

Chen, Guimin, Daniel L Wilcox, and Larry L Howell (2009). “Fully compliant double tensural tristable micromechanisms (DTTM)”. In: *Journal of Micromechanics and Microengineering* 19.2, p. 025011.

Chen, Guimin et al. (2019). “Modeling large deflections of initially curved beams in compliant mechanisms using chained beam constraint model”. In: *Journal of Mechanisms and Robotics* 11.1.

Chen, Rui et al. (2023). “Design and optimization of a novel compliant planar parallelogram mechanism utilizing initially curved beams”. In: *Mechanism and Machine Theory* 179, p. 105092.

Chikhaoui, Mohamed Taha et al. (2019). “Comparison of modeling approaches for a tendon actuated continuum robot with three extensible segments”. In: *IEEE Robotics and Automation Letters* 4.2, pp. 989–996.

Chimento, Jairo, Craig Lusk, and Ahmad Alqasimi (2014). “A 3-D pseudo-rigid body model for rectangular cantilever beams with an arbitrary force end-load”. In: *International Design Engineering Technical Conferences and Computers and Information in Engineering Conference*. Vol. 46360. American Society of Mechanical Engineers, V05AT08A029.

Chow, S-N and Jack K Hale (2012). *Methods of bifurcation theory*. Vol. 251. Springer Science & Business Media.

Clark, Leon et al. (2015). “Development of a passive compliant mechanism for measurement of micro/nanoscale planar 3-DOF motions”. In: *IEEE/ASME Transactions on Mechatronics* 21.3, pp. 1222–1232.

Courrieu, Pierre (2008). “Fast computation of Moore-Penrose inverse matrices”. In: *arXiv preprint arXiv:0804.4809*.

Cowper, GR (1966). “The shear coefficient in Timoshenko’s beam theory”. In.

Craig, John J (2005). *Introduction to robotics: mechanics and control*. Pearson Educacion.

Dong, Xin et al. (2014). “Design and analysis of a family of snake arm robots connected by compliant joints”. In: *Mechanism and Machine Theory* 77, pp. 73–91.

Dupont, Pierre E et al. (2009). “Design and control of concentric-tube robots”. In: *IEEE Transactions on Robotics* 26.2, pp. 209–225.

Dym, Clive L, Irving Herman Shames, et al. (1973). *Solid mechanics*. Springer.

Euler, Leonhard (1744). *Methodus inveniendi lineas curvas maximi minimive proprietate gaudentes*. apud Marcum-Michaelem Bousquet.

— (1759). “Sur la force des colonnes”. In: *Memoires de l’Academie des Sciences de Berlin*, pp. 252–282.

Fan, Shixun, Hua Liu, and Dapeng Fan (2018). “Design and development of a novel monolithic compliant XY stage with centimeter travel range and high payload capacity”. In: *Mechanical Sciences* 9.1, p. 161.

Farhadi Machekposhti, D, N Tolou, and JL Herder (2015). “A review on compliant joints and rigid-body constant velocity universal joints toward the design of compliant homokinetic couplings”. In: *Journal of Mechanical Design* 137.3.

Fowler, RM, LL Howell, and SP Magleby (2011). “Compliant space mechanisms: a new frontier for compliant mechanisms”. In: *Mechanical Sciences* 2.2, pp. 205–215.

Gakhov, Fedor Dmitrievich (2014). *Boundary value problems*. Elsevier.

Han, Qi et al. (2017). “A novel fully compliant tensural-compresural bistable mechanism”. In: *Sensors and Actuators A: Physical* 268, pp. 72–82.

Hannan, Michael W and Ian D Walker (2003). “Kinematics and the implementation of an elephant’s trunk manipulator and other continuum style robots”. In: *Journal of robotic systems* 20.2, pp. 45–63.

Hao, Guangbo, Jingjun Yu, and Yufei Liu (2018). “Compliance synthesis of a class of planar compliant parallelogram mechanisms using the position space concept”. In: *2018 International Conference on Reconfigurable Mechanisms and Robots (ReMAR)*. IEEE, pp. 1–10.

Hatami, Mohammad (2017). *Weighted residual methods: principles, modifications and applications*. Academic Press.

Howell, Larry L (2013a). “Compliant mechanisms”. In: *21st century kinematics*. London: Springer.

— (2013b). “Introduction to compliant mechanisms”. In: *Handbook of Compliant Mechanisms*, pp. 1–13.

Howell, Larry L and Ashok Midha (1994). “A method for the design of compliant mechanisms with small-length flexural pivots”. In.

Hricko, Jaroslav and Štefan Havlík (2019). “Compliant mechanisms for motion/force amplifiers for robotics”. In: *International Conference on Robotics in Alpe-Adria Danube Region*. Springer, pp. 26–33.

Hutchinson, JR (2001). “Shear coefficients for Timoshenko beam theory”. In: *J. Appl. Mech.* 68.1, pp. 87–92.

Ibrahimbegović, Adnan and Mazen Al Mikdad (1998). “Finite rotations in dynamics of beams and implicit time-stepping schemes”. In: *International Journal for Numerical Methods in Engineering* 41.5, pp. 781–814.

Isbister, Andrew, Nicola Y Bailey, and Ioannis Georgilas (2021). “An Integrated Kinematic Modeling and Experimental Approach for an Active Endoscope”. In: *Frontiers in Robotics and AI*, p. 193.

Jahn, Johannes (2017). “Karush–Kuhn–Tucker conditions in set optimization”. In: *Journal of Optimization Theory and Applications* 172.3, pp. 707–725.

Jin, Mohui et al. (2020). “Large-deflection analysis of general beams in contact-aided compliant mechanisms using chained pseudo-rigid-body model”. In: *Journal of Mechanisms and Robotics* 12.3.

Jones, Bryan A, Ricky L Gray, and Krishna Turlapati (2009). “Three dimensional statics for continuum robotics”. In: *2009 IEEE/RSJ International Conference on Intelligent Robots and Systems*. IEEE, pp. 2659–2664.

Jones, Bryan A and Ian D Walker (2006). “Kinematics for multisection continuum robots”. In: *IEEE Transactions on Robotics* 22.1, pp. 43–55.

Jones, Robert Millard (2006). *Buckling of bars, plates, and shells*. Bull Ridge Corporation.

Kelley, Carl T (2003). *Solving nonlinear equations with Newton’s method*. SIAM.

Kong, Kejia, Guimin Chen, and Guangbo Hao (2019). “Kinetostatic modeling and optimization of a novel horizontal-displacement compliant mechanism”. In: *Journal of Mechanisms and Robotics* 11.6.

Kota, Satyanarayana et al. (2005). “Design and application of compliant mechanisms for surgical tools”. In.

Kota, Sridhar et al. (2001). “Design of compliant mechanisms: applications to MEMS”. In: *Analog integrated circuits and signal processing* 29.1, pp. 7–15.

Kota, Sridhar et al. (2003). “Design and application of compliant mechanisms for morphing aircraft structures”. In: *Smart structures and materials 2003: industrial and commercial applications of smart structures technologies*. Vol. 5054. SPIE, pp. 24–33.

Kuppens, PR et al. (2021). “Compliant mechanisms that use static balancing to achieve dramatically different states of stiffness”. In: *Journal of Mechanisms and Robotics* 13.2.

Lacarbonara, Walter (2008). “Buckling and post-buckling of non-uniform non-linearly elastic rods”. In: *International Journal of Mechanical Sciences* 50.8, pp. 1316–1325.

Lagrange, Joseph-Louis (1770). “Sur la figure des colonnes”. In: *Miscellanea Taurinensia* 5, pp. 123–166.

— (1853). *Mécanique analytique*. Vol. 1. Mallet-Bachelier.

Langer, Joel and David A Singer (1996). “Lagrangian aspects of the Kirchhoff elastic rod”. In: *SIAM review* 38.4, pp. 605–618.

Li, Haiyang (2016). “Approaches to the synthesis, modelling and optimisation of spatial translational compliant parallel mechanisms”. PhD thesis. University College Cork.

Liang, Haitong, Guangbo Hao, and Oskar Z Olszewski (2021). “A review on vibration-based piezoelectric energy harvesting from the aspect of compliant mechanisms”. In: *Sensors and Actuators A: Physical* 331, p. 112743.

Ling, Mingxiang et al. (2016). “Enhanced mathematical modeling of the displacement amplification ratio for piezoelectric compliant mechanisms”. In: *Smart Materials and Structures* 25.7, p. 075022.

Ling, Mingxiang et al. (2020). “Kinetostatic and dynamic modeling of flexure-based compliant mechanisms: a survey”. In: *Applied Mechanics Reviews* 72.3.

Lobontiu, Nicolae (2002). *Compliant mechanisms: design of flexure hinges*. CRC press.

— (2020). *Compliant mechanisms: design of flexure hinges*. Boca Raton: CRC press.

Ma, Fulei and Guimin Chen (2016). “Modeling large planar deflections of flexible beams in compliant mechanisms using chained beam-constraint-model”. In: *Journal of Mechanisms and Robotics* 8.2.

Ma, Xiaokun et al. (2016). “Efficient energy harvesting using piezoelectric compliant mechanisms: theory and experiment”. In: *Journal of Vibration and Acoustics* 138.2.

Mankame, Nilesh D and GK Ananthasuresh (2002). “Contact aided compliant mechanisms: concept and preliminaries”. In: *International design engineering technical conferences and computers and information in engineering conference*. Vol. 36533. American Society of Mechanical Engineers, pp. 109–121.

Megaro, Vittorio et al. (2017). "A computational design tool for compliant mechanisms." In: *ACM Trans. Graph.* 36.4, pp. 82–1.

Mehta, Vipul (2010). *Design, analysis, and applications of cellular contact-aided compliant mechanisms*. The Pennsylvania State University.

Meng, Lingda et al. (2020). "A mechanically intelligent crawling robot driven by shape memory alloy and compliant bistable mechanism". In: *Journal of Mechanisms and Robotics* 12.6, p. 061005.

Nikishkov, GP (2004). "Introduction to the finite element method". In: *University of Aizu*, pp. 1–70.

Oh, Young Seok and Sridhar Kota (2009). "Synthesis of multistable equilibrium compliant mechanisms using combinations of bistable mechanisms". In: *Journal of Mechanical Design* 131.2.

Oldfather, WA, CA Ellis, and Donald M Brown (1933). "Leonhard Euler's elastic curves". In: *Isis* 20.1, pp. 72–160.

Orekhov, Andrew L, Vincent A Aloi, and D Caleb Rucker (2017). "Modeling parallel continuum robots with general intermediate constraints". In: *2017 IEEE International Conference on Robotics and Automation (ICRA)*. IEEE, pp. 6142–6149.

Orekhov, Andrew L and Nabil Simaan (2020). "Solving cosserat rod models via collocation and the magnus expansion". In: *2020 IEEE/RSJ International Conference on Intelligent Robots and Systems (IROS)*. IEEE, pp. 8653–8660.

Osborne, Mike R (1969). "On shooting methods for boundary value problems". In: *Journal of mathematical analysis and applications* 27.2, pp. 417–433.

Pham, Huy-Tuan and Dung-An Wang (2011). "A constant-force bistable mechanism for force regulation and overload protection". In: *Mechanism and Machine Theory* 46, pp. 899–909.

Qi, Peng et al. (2015). "A novel continuum manipulator design using serially connected double-layer planar springs". In: *IEEE/ASME Transactions on Mechatronics* 21.3, pp. 1281–1292.

Qin, Yun et al. (2013). "Modelling and analysis of a rigid–compliant parallel mechanism". In: *Robotics and Computer-Integrated Manufacturing* 29.4, pp. 33–40.

Qiu, Jin, Jeffrey H Lang, and Alexander H Slocum (2004). "A curved-beam bistable mechanism". In: *Journal of microelectromechanical systems* 13.2, pp. 137–146.

Ramirez, Issa A and Craig P Lusk (2011). "Spatial-beam large-deflection equations and Pseudo-Rigid-Body Model for axisymmetric cantilever beams". In: *International Design Engineering Technical Conferences and Computers and Information in Engineering Conference*. Vol. 54839, pp. 43–49.

Rao, Singiresu S (2017). *The finite element method in engineering*. Butterworth-heinemann.

— (2019). *Engineering optimization: theory and practice*. John Wiley & Sons.

Rasmussen, Nathan O et al. (2006). "A 3d pseudo-rigid-body model for large spatial deflections of rectangular cantilever beams". In: *International Design Engineering Technical Conferences and Computers and Information in Engineering Conference*. Vol. 42568, pp. 191–198.

Renda, Federico et al. (2017). "Screw-based modeling of soft manipulators with tendon and fluidic actuation". In: *Journal of Mechanisms and Robotics* 9.4.

Renda, Federico et al. (2018). "Discrete cosserat approach for multisection soft manipulator dynamics". In: *IEEE Transactions on Robotics* 34.6, pp. 1518–1533.

Rubin, Mordecai B and AH Cardon (2002). "Cosserat theories: shells, rods and points. Solid mechanics and its applications, vol 79". In: *Appl. Mech. Rev.* 55.6, B109–B110.

Rucker, D Caleb, Bryan A Jones, and Robert J Webster III (2010). "A geometrically exact model for externally loaded concentric-tube continuum robots". In: *IEEE transactions on robotics* 26.5, pp. 769–780.

Rucker, D Caleb and Robert J Webster (2011). "Computing jacobians and compliance matrices for externally loaded continuum robots". In: *2011 IEEE International Conference on Robotics and Automation*. IEEE, pp. 945–950.

Rucker, D Caleb and Robert J Webster III (2011). "Statics and dynamics of continuum robots with general tendon routing and external loading". In: *IEEE Transactions on Robotics* 27.6, pp. 1033–1044.

Russell, RD and Lawerence F Shampine (1972). "A collocation method for boundary value problems". In: *Numerische Mathematik* 19.1, pp. 1–28.

Sadati, SM Hadi et al. (2017). "Control space reduction and real-time accurate modeling of continuum manipulators using ritz and ritz–galerkin methods". In: *IEEE Robotics and Automation Letters* 3.1, pp. 328–335.

Shampine, Lawrence F, Jacek Kierzenka, Mark W Reichelt, et al. (2000). "Solving boundary value problems for ordinary differential equations in MATLAB with bvp4c". In: *Tutorial notes* 2000, pp. 1–27.

Simo, Juan Carlos and Loc Vu-Quoc (1988). "On the dynamics in space of rods undergoing large motions—a geometrically exact approach". In: *Computer methods in applied mechanics and engineering* 66.2, pp. 125–161.

Slocum, Jonathan, Kenneth Kamrin, and Alexander Slocum (2019). "A buckling flexure-based force-limiting mechanism". In: *Journal of Mechanisms and Robotics* 11.4.

Song, Myeong-Gyu et al. (2010). "Development of small sized actuator with compliant mechanism for optical image stabilization". In: *IEEE Transactions on Magnetics* 46.6, pp. 2369–2372.

Song, Xi and Shi-Rong Li (2007). "Thermal buckling and post-buckling of pinned–fixed Euler–Bernoulli beams on an elastic foundation". In: *Mechanics Research Communications* 34.2, pp. 164–171.

Sonneville, Valentin, Alberto Cardona, and O Brüls (2014). "Geometrically exact beam finite element formulated on the special Euclidean group SE (3)". In: *Computer Methods in Applied Mechanics and Engineering* 268, pp. 451–474.

Spiegel, Murray R (1991). *Advanced mathematics*. Vol. 4. McGraw-Hill, Incorporated.

Stone, Marshall H (1948). "The generalized Weierstrass approximation theorem". In: *Mathematics Magazine* 21.5, pp. 237–254.

Tanık, Çağıl Merve et al. (2015). "Steel compliant Cardan universal joint". In: *Mechanism and Machine Theory* 92, pp. 171–183.

Tantanawat, Tanakorn, Zhe Li, and Sridhar Kota (2004). "Application of compliant mechanisms to active vibration isolation systems". In: *International Design Engineering Technical Conferences and Computers and Information in Engineering Conference*. Vol. 46954, pp. 1165–1172.

Thomas, Theodosia Lourdes et al. (2021). "Surgical applications of compliant mechanisms: a review". In: *Journal of mechanisms and robotics* 13.2.

Till, John, Vincent Aloi, and Caleb Rucker (2019). "Real-time dynamics of soft and continuum robots based on Cosserat rod models". In: *The International Journal of Robotics Research* 38.6, pp. 723–746.

Till, John et al. (2015). "Efficient computation of multiple coupled Cosserat rod models for real-time simulation and control of parallel continuum manipulators". In: *2015 IEEE international conference on robotics and automation (ICRA)*. IEEE, pp. 5067–5074.

Timoshenko, Stephen P and James M Gere (2009). *Theory of elastic stability*. Courier Corporation.

Todhunter, Isaac (1893). *A History of the Theory of Elasticity and of the Strength of Materials: pts. 1-2. Saint-Venant to Lord Kelvin*. Vol. 2. University Press.

Trease, Brian and Sridhar Kota (2009). "Design of adaptive and controllable compliant systems with embedded actuators and sensors". In: *Journal of Mechanical Design* 131.11.

Venkiteswaran, Venkatasubramanian Kalpathy and Hai-Jun Su (2016). "Pseudo-rigid-body models for circular beams under combined tip loads". In: *Mechanism and Machine Theory* 106, pp. 80–93.

Wazwaz, Abdul-Majid (2010). *Partial differential equations and solitary waves theory*. Springer Science & Business Media.

Webster III, Robert J and Bryan A Jones (2010). "Design and kinematic modeling of constant curvature continuum robots: A review". In: *The International Journal of Robotics Research* 29.13, pp. 1661–1683.

Wu, Ke and Guangbo Hao (2020). "Design and nonlinear modeling of a novel planar compliant parallelogram mechanism with general tensural-compresural beams". In: *Mechanism and Machine Theory* 152, pp. 1–23.

Wu, Ke and Gang Zheng (2022a). "A comprehensive static modeling methodology via beam theory for compliant mechanisms". In: *Mechanism and Machine Theory* 169, p. 104598.

— (2022b). "Insight into numerical solutions of static large deflection of general planar beams for Compliant Mechanisms". In: *Mechanism and Machine Theory* 172, p. 104757.

— (2022c). "Solutions to large beam-deflection problems by Taylor series and Padé approximant for compliant mechanisms". In: *Mechanism and Machine Theory* 177, p. 105033.

— (2022d). "Theoretical analysis on nonlinear buckling, post-buckling of slender beams and bi-stable mechanisms". In: *Journal of Mechanisms and Robotics* 14.3.

Wu, Ke, Gang Zheng, and Guangbo Hao (2021). "Efficient spatial compliance analysis of general initially curved beams for mechanism synthesis and optimization". In: *Mechanism and Machine Theory* 162, p. 104343.

Ypma, Tjalling J (1995). "Historical development of the Newton–Raphson method". In: *SIAM review* 37.4, pp. 531–551.

Yu, Yue-Qing, Zhong-Lei Feng, and Qi-Ping Xu (2012). "A pseudo-rigid-body 2R model of flexural beam in compliant mechanisms". In: *Mechanism and Machine Theory* 55, pp. 18–33.

Yu, Yue-Qing and Na Zhang (2019). “Dynamic modeling and performance of compliant mechanisms with inflection beams”. In: *Mechanism and Machine Theory* 134, pp. 455–475.

Yu, Yue-Qing et al. (2005). “Dynamic modeling of compliant mechanisms based on the pseudo-rigid-body model”. In.

Yuan, Ming (2010). “High dimensional inverse covariance matrix estimation via linear programming”. In: *The Journal of Machine Learning Research* 11, pp. 2261–2286.

Zirbel, Shannon A et al. (2016). “Bistable mechanisms for space applications”. In: *PloS one* 11.12, e0168218.

Titre en français
Résumé en français

Selon la littérature, il est clairement établi que dans le domaine des mécanismes conformes (MC), il n'existe aucun résultat sur la manière de définir géométriquement des poutres initialement courbées de forme aléatoire (ICB) et de modéliser efficacement la grande déflexion de ces structures élancées soumises à des conditions de chargement complexes. En particulier, la modélisation efficace du flambage non linéaire et du flambage postérieur pour servir à la conception de MC n'a pas été réalisée à notre connaissance. De plus, il existe également peu de résultats sur la conception basée sur des modèles (optimisation) et le contrôle basé sur des modèles de MC. Si les problèmes mentionnés ne sont pas résolus, les chercheurs peuvent encore souffrir du processus de conception fastidieux par essais et erreurs et se retrouver coincés avec un cadre de conception basé sur l'énumération globale ou des méthodes de conception purement empiriques. Pour traiter les préoccupations mentionnées, dans cette thèse, nous étudions le problème dans les chapitres suivants de la thèse.

Au chapitre 2, nous présentons en détail différents outils mathématiques utilisés pour résoudre les problèmes de valeur aux limites (PVL) d'équations différentielles ordinaires (EDO) et les problèmes d'optimisation, étant donné que les formulations de la modélisation des grandes déflexions sont des PVL et des problèmes d'optimisation, comme indiqué dans le chapitre 3.
Le chapitre 3 est principalement composé de trois aspects. Tout d'abord, nous introduisons la définition géométrique de poutres planaires arbitraires dans différents systèmes de coordonnées et la stratégie de transformation des coordonnées vers le repère corporel. Les avantages et les inconvénients de la conception de poutres planaires sont discutés, suivis des contributions potentielles à la définition géométrique de poutres spatiales et à la transformation des coordonnées via une stratégie similaire. Ce problème est formulé sous forme d'EDOs. Ensuite, nous présentons la modélisation des grandes déflexions sous différentes conditions aux limites via la mécanique newtonienne, où une poutre mince planaire arbitraire soumise à différentes conditions de chargement est étudiée. Cela peut être formulé comme un PVL d'une EDO. En particulier, la modélisation du flambage non linéaire et du post-flambage est également présentée. Enfin, nous introduisons la modélisation des grandes déflexions sous différentes conditions aux limites via la mécanique lagrangienne, et différentes conditions de chargement sont également discutées. Notez que dans le cadre lagrangien, le problème est formulé comme une minimisation fonctionnelle.

Au chapitre 4, avec les stratégies de modélisation et les outils mathématiques disponibles, nous utilisons ces outils pour résoudre efficacement les différents modèles développés au chapitre 3. En ce qui concerne la transformation des coordonnées, nous utilisons la méthode de collocation

pour approximer la solution (de l'EDO). Deuxièmement, pour les modèles (PVL) développés via la mécanique newtonienne, nous utilisons diverses méthodes numériques, des méthodes hybrides et des méthodes semi-analytiques pour analyser les problèmes de grandes déflexions. Ensuite, dans le cadre lagrangien, nous transformons le problème de minimisation fonctionnelle en un problème d'optimisation, et utilisons le multiplicateur de Lagrange pour résoudre numériquement le problème. Enfin, une étude de cas complète est présentée pour vérifier la méthodologie proposée.

Différent de la modélisation d'une seule structure élancée mentionnée au chapitre 4, le chapitre 5 précise d'abord la modélisation d'un mécanisme conforme où quatre types de MC représentatifs sont modélisés. Dans ces exemples illustratifs, l'efficacité élevée et la précision fiable des outils mathématiques pour résoudre les modèles constitutifs ont été prouvées. En fonction du cadre de modélisation efficace et précis, un processus de conception basé sur l'optimisation rapide d'un parallélogramme conforme à base de poutres initialement courbées est réalisé, suivi de la validation expérimentale.

Au chapitre 6, nous présentons enfin une mise en œuvre expérimentale du contrôle d'un manipulateur continu. La statique, la cinématique et la modélisation inverse sont d'abord démontrées respectivement à travers le cadre newtonien et le cadre lagrangien. Ensuite, le processus de conception d'un contrôleur basé sur le modèle est présenté, suivi de la validation expérimentale où les boucles fermées et les boucles ouvertes sont toutes testées.

Le chapitre 7 présente les conclusions de la présente thèse et expose les perspectives des travaux futurs, notamment la définition géométrique de poutres 3D (avec la transformation en repère corporel), l'analyse des mécanismes conformes à multi-stabilité du point de vue lagrangien et les méthodes numériques efficaces pour la théorie des tiges de Cosserat en mode complet. Les détails sont les suivants.

Sur la base de la structure de la thèse, qui est également la structure de mes futurs travaux, j'aimerais présenter quelques domaines potentiels et extensions possibles des résultats présentés.

Dans le chapitre 3, nous discutons principalement de la manière de définir une poutre plane dans différents systèmes de coordonnées, ainsi que de la transformation en repère corporel pour une analyse ultérieure des grandes déflexions. Par conséquent, nous proposons une idée similaire de définir une poutre 3D (spatiale) dans différents systèmes de coordonnées et la stratégie de transformation en repère corporel également. En effet, dans les mécanismes conformes, certaines poutres spatiales initialement courbées utilisées pour présenter des propriétés mécaniques plus variées, telles que des ressorts, sont couramment utilisées.

Comme indiqué au chapitre 5, plusieurs types de mécanismes bistables (mécanismes conformes bistables purs et différents mécanismes conformes préfléchis) sont analysés du point de vue newtonien, où l'équilibre des moments le long de la poutre flexible est satisfait. Dans mes travaux futurs, j'aimerais analyser les mécanismes bistables du point de vue énergétique, car

c'est plus simple et direct, se formulant directement en un problème d'optimisation sans toucher aux EDO régissant.

Contrairement aux cas simples concernant les problèmes de contact mentionnés au chapitre 3, ma future attention se portera sur des scénarios plus complexes, tels que le contact flexible et le contact de forme irrégulière. Pour traiter ce type de problèmes, le modèle de contrainte de poutre enchaînée en repère corporel (CBBCM) doit être utilisé, où chaque modèle de contrainte de poutre en repère corporel (BBCM) sert d'élémentaire pour analyser les forces internes et externes.

La théorie des tiges de Cosserat est couramment utilisée pour modéliser les manipulateurs déformables mais n'est pas largement utilisée pour modéliser les MC. Pour résoudre le modèle de tige de Cosserat, on utilise généralement la méthode de tir et les méthodes connexes. Cependant, ces méthodes sont généralement longues à exécuter pour résoudre le PVL des EDO régissant, car elles transforment essentiellement le PVL en une série de problèmes de valeur initiale (PVI). Au lieu de rester bloqué avec les stratégies de tir, nous avons présenté les deux aspects suivants pour augmenter l'efficacité de résolution du modèle de tige de Cosserat.

Si nous continuons à traiter le PVL des EDO régissant le modèle de tige de Cosserat, nous avons plusieurs solutions, car en mathématiques appliquées, il existe de nombreuses solutions numériques ou analytiques au problème mentionné. Fondamentalement, les EDO du modèle de tige de Cosserat ont des propriétés uniques en raison du fait que la matrice de rotation doit toujours appartenir au groupe SO3. Dès lors que nous définissons une matrice inconnue ayant toujours cette propriété, les EDO étudiées reviennent à un ensemble très normal. Ensuite, plusieurs méthodes comme les méthodes de résidus pondérés peuvent être utilisées pour résoudre le PVL de manière plus efficace.

D'autre part, nous considérons le problème du point de vue lagrangien. Cela s'explique par le fait que l'ensemble des EDO est essentiellement le résultat de la variation à partir de la formulation de l'énergie potentielle totale selon l'équivalence entre la mécanique newtonienne et la mécanique lagrangienne. Par conséquent, nous pouvons résoudre le problème à l'étape où l'énergie potentielle totale est formulée. De même, nous pouvons également transformer le problème en un problème d'optimisation classique. De manière similaire, la matrice de rotation doit être définie dans le groupe SO3.

Mots-clefs: Mathématiques appliquées; Théorie du contrôle; Robotique